Design Studies of Fixed and Tunable Frequency Gyrotron Oscillators

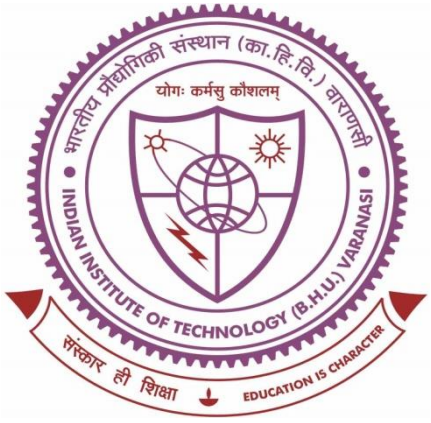

Thesis submitted in partial fulfillment for the Award of Degree

Doctor of Philosophy

By

Sivavenkateswara Rao V

DEPARTMENT OF ELECTRONICS ENGINEERING

INDIAN INSTITUTE OF TECHNOLOGY

(BANARAS HINDU UNIVERSITY)

VARANASI – 221005

INDIA

ROLL NO: 13091010

2019

CERTIFICATE

It is certified that the work contained in the thesis titled **"Design Studies of Fixed and Tunable Frequency Gyrotron Oscillators"** by **"Sivavenkateswara Rao V"** has been carried out under our supervision and that this work has not been submitted elsewhere for a degree.

It is further certified that the student has fulfilled all the requirements of Comprehensive Examination, Candidacy and SOTA for the award of Ph. D. Degree.

(Prof. Pradip Kumar Jain)
Supervisor
Department of Electronics Engineering
IIT (BHU), Varanasi

(Dr. M. Thottappan)
Co-Supervisor
Department of Electronics Engineering
IIT (BHU), Varanasi

DECLARATION BY THE CANDIDATE

I, Sivavenkateswara Rao V, certify that the work embodied in this thesis is my own bonafide work and carried out by me under the supervision of Prof. Pradip Kumar Jain, and Dr. M. Thottappan from"23/07/2013" to “27/12/2019”, at the Department of Electronics Engineering, Indian Institute of Technology (BHU), Varanasi. The matter embodied in this thesis has not been submitted for the award of any other degree/diploma. I declare that I have loyally acknowledged and given credits to the research workers wherever their works have been cited in my work in this thesis. I further declare that I have not willfully copied any other's work, paragraphs, text, data, results, *etc*., reported in journals, books, magazines, reports, dissertations, theses, *etc*., or available at websites and have not included them in this thesis and have not cited as my own work.

Date: **Signature of the Student**

Place: **Sivavenkateswara Rao V**

CERTIFICATE BY THE SUPERVISORS

It is certified that the above statement made by the student is correct to the best of our knowledge.

(Prof. Pradip Kumar Jain)
Supervisor
Department of Electronics Engineering
IIT (BHU), Varanasi

(Dr. M. Thottappan)
Co-Supervisor
Department of Electronics Engineering
IIT (BHU), Varanasi

Signature of Head of Department
"SEAL OF THE DEPARTMENT"

COPYRIGHT TRANSFER CERTIFICATE

Title of the Thesis: **Design Studies of Fixed and Tunable Frequency Gyrotron Oscillators**

Name of the Student: **Sivavenkateswara Rao V**

Copyright Transfer

The undersigned hereby assigns to the Indian Institute of Technology (Banaras Hindu University), Varanasi all rights under copyright that may exist in and for the above thesis submitted for the award of the Doctor of Philosophy.

Date: **Signature of the Student**

Place: **Sivavenkateswara Rao V**

Note: However, the author may reproduce or authorize others to reproduce material extracted verbatim from the thesis or derivative of the thesis for author's personal use provided that the source and the Institute's copyright notice are indicated.

ACKNOWLEDGEMENTS

First and Foremost, I would like to express my deep and sincere gratefulness to my supervisor, Prof. Pradip Kumar Jain for his valuable personal and professional support, consistence motivations and excellent guidance. I would like to thank to my Co-Supervisor, Dr. M.Thottappan, for his valuable support and guidance. The completion of this research work is truly an outcome of his immense knowledge, valuable ideas and suggestions that has provided a good basis for this work. His constant guidance, cooperation, motivation and support helped me in all the time of research and writing of this thesis.

Besides my supervisors, I would like to thank the members of the research performance evaluation committee, Prof. S. P. Singh and Prof. R. Mahanty, for their encouragement, detailed and constructive comments.

My sincere thanks go to all staff members, especially to Mr. Rajesh Kr. Rai, Mr. Achal Srivastava, Mr. Ajit, Mr. Punawasi, Mr. Jairam and Ranjan Singha for their kind co-operation.

My sincere appreciations and thanks goes to Mr. Rajan Agrahari and Co., Mr. Akhilendra and Co, Mr. Vikram Kumar, Mr. Anshusharan Singh, Mr. Vineet Singh, Mr. Veerababu, Mr. Arjun kumar and Co., Dr. Naresh Kumar Pilli, Dr, Ramesh Kalyan, Dr. Rajasekar Yerrasani, Mr. Raghuram, Mr. Vijaybabu, Mr. Vinod Kumar, Mr. Pankaj Kumar Jha, Mr. Gaurav Singh and Mrs. Garima Dubey, who stood behind me during my ups and downs and keeps motivate me to reach the target.

A special thanks to Mr. Jaya Krishna and Co, Mr. Kumar Raja, Mr. Mohan Rao, Mr. Govindha Rao K, Dr. Hemanth Kumar and Co., Mr. UmaMaheswarao Mr. KV Shiva Kumar, Mr. Sridhar Kumar Ch, Mr. Sundar B, Mr. Eswara Prasad, Mr. Dharma Shasta

During this work, I have collaborated with many of my colleagues for whom I have great regards and I wish my warmest thanks to, Dr. Gourav Modanwal, Dr. Subiman Chatterjee, Dr. Sudhir Bhaskar, Mr. Prabhakar Tripathi, Mr. G. Venkatesh, Mr. Soumjit, Mr. Ravinder Agrahari, Mr. M. A. Ansari, Mr. Rajneesh, Mr. Akash, Mr. V. V. Reddy, and Mr. S. G. Yadav for providing technical help in my research work and fun filled environment.

I am very much thankful to Dr. M. S. Chauhan, Dr. Gargi Dwivedi, Dr. Amit Arora, Dr. M. V. Swati and Co., Dr. Nallaswamy and Dr. Manpuran Mahto for their valuable motivation and assistance from personal to the technical level.

Finally, I hearty express sincere thanks to my family members SrinivasaRao V, Venkateswari K and Co. Mr. Lokeswara Rao U. I wish to express gratitude to them, for their unconditional love, extreme patience and constant support over the years. They provide me the strength and confidence to attain this task.

Last but not the least; I thank almighty God for providing me strength and courage in completing the work.

Date: ***(Sivavenkateswara Rao V)***

Dedicated To

Parents and My Guru
Shri Pradip Kumar Jain

TABLE OF CONTENT

LIST OF FIGURES

et al. (2006) and as per our modified design, respectively.

LIST OF TABLE

ABBREVIATIONS

Abbreviation	Details
A	Ampere
BWOs	Backward Wave Oscillators
CARM	Cyclotron Auto-Resonance Maser
CPI	Communication and Power Industries
CRM	Cyclotron Resonance Maser
CST	Computer Simulation Tool
CVD	Chemical Vapor Deposition
CW	Continuous Wave
DC	Direct Current
DNP	Dynamic Nuclear Polarization
ECR	Electron Cyclotron Resonance
ECRM	Electron Cyclotron Resonance Maser
EM	Electromagnetic
EPR	Electron Paramagnetic Resonance
FEL	Free Electron Laser
FFT	Fast Fourier Transform
FFT	Fast Fourier Transform
GCF	Gaussian Content Factor
GCF	Gaussian Content Factor
GHz	Gigahertz

GUI	Graphical User Interface
GW	Gigawatts
Gyro-BWO	Gyrotron Backward Wave Oscillator
Gyro-TWT	Gyrotron Travelling Wave Tube
HPM	High Power Microwaves
IAP	Institute of Applied Physics
IPRA	Iterative Phase Retrieval Algorithm
keV	Kilo Electron Volt
kV	Kilovolts
kW	Kilowatts
LSA	Large Signal Analysis
MHz	Megahertz
MIG	Magnetron Injection Gun
MIT	Massachusetts Institute of Technology
MMW	Millimeter-Wave
MW	Megawatt
NMR	Nuclear Magnetic Resonance
NRL	Naval Research Laboratory
OFHC	Oxygen free High conductivity
PBA	Perfect Boundary Approximation
PBG	Photonic Band Gap
PIC	Particle-in-Cell
PMS	Permanent Magnetic Systems

QOM	Quasi optical mode
QOMC	Quasioptical Mode converter
RF	Radio Frequency
T	Tesla
TD	Time Domain
TE	Transverse Electric
TEM	Transverse Electric Magnetic
THz	Terahertz
TM	Transverse Magnetic
TWTs	Travelling Wave Tubes
VEDs	Vacuum Electronic Devices
W	Watt

LIST OF SYMBOLS

$f(z)$	A function
$An\ ()$	Amplitude function of EM field
a_n	Amplitude of nth mode
A	Amplitude of the signal
ϕ	Angle of electron in gyrocenter coordinate system (r,ϕ)
ζ	Angle of the electron momentum vector about the gyro-center
ω_0	Angular frequency of RF wave
v_z	Axial electron velocity
p_z	Axial momentum of electrons
ς	Axial position variable
$h(z)$	Axial profile of the field along the cavity
k_z	Axial propagation constant
m, p	Azimuthal, and radial mode indices
φ, r, z	Azimuthal, radial, and axial cylindrical coordinates
m,p, q	Azimuthal, radial, and axial mode indices
I_b	Beam current
V_b	Beam voltage
$\Theta 0$	Beamlets phase in cavity centered coordinate system
$Jm()$	Bessel function of the ordinary type
q	Bunching parameter of the electron beam
Q	Cavity quality factor
r_w	Cavity wall radius
ε	Complex permittivity
σ	Conductivity
Cmp	Coupling coefficient
ωc	Cyclotron frequency
B_0	DC magnetic field
Δ	Detuning parameter
δ	Detuning parameter
Q_D	Diffractive quality factor
L	Effective cavity interaction length
η	Efficiency
E	Electric field
θ	Electron angle in cavity centered coordinate system
R_b	Electron beam radius
e	Electron charge

ω_c	Electron cyclotron frequency
ξ	Electron energy
p	Electron momentum
v	Electron velocity
η_{el}	Electronic efficiency
U_w	Energy stored in the cavity
μ_0	Free-space permeability
ε_0	Free-space permittivity
G	Geometrical factor
s	Harmonic number
r_L	Larmor radius
L	Length of cavity
I_L	Limiting current
$vz0$	Longitudinal electron velocity
βz	Longitudinal normalized velocity
B	Magnetic field
m_e	Mass of electron
f_n	Mode amplitude
ψ	Mode phase
J_m	m^{th} order ordinary Bessel function of first kind
$\beta_{\|\|}$	Normalized axial electron velocity
ζ	Normalized axial position
I	Normalized beam current
μ	Normalized cavity interaction length
u	Normalized energy
F	Normalized field amplitude
p	Normalized momentum of electrons
$\beta_{\perp 0}$	Normalized transverse electron velocity
β	Normalized velocity
N	Number of interacting modes
N	Number of modes
Q_{ohm}	Ohmic Q
ρ	Ohmic wall loss
λ	Operating wavelength
v_t	Perpendicular electron velocity
Λ	Phase of electron
ψ	Phase of electron
α	Pitch factor

P	Power dissipated
$h(z)$	Profile function
Q	Quality Factor
w	Relative energy variable
γ	Relativistic factor
E	RF Electric Field
v_g	RF Group velocity
B	RF Magnetic Field
v_p	RF Phase velocity
Λ	slow-time scale phase variable
$Vdep$	Space charge voltage depression
I_{st}	Start oscillation current
$B0$	Static magnetic field
χ	Susceptibility
t	Time
$P_n\{\tau\}$	Time–Dependent RF Output power
U	Total stored energy
Jt	Transverse AC current density
$\eta_\perp$	Transverse efficiency
p_t	Transverse momentum of electrons
βt	Transverse normalized velocity
k_{nt}	Transverse propagation constant
0	Used for initial values
c	Velocity of light in free space
ω	Wave frequency
k	Wave number
λ	Wavelength
$\vec{A}$	magnetic vector potential
$A_{1-3,}B_{1-3}$	constants
$A_{mn,}B_{mn}$	coefficients
$\alpha_{\triangle m}(z)$	amplitude of wall deformation in the waveguide
$\vec{B}, B_0$	magnetic flux density vector, magnetic flux density
$\vec{D}$	electric flux density vector
$\vec{E}$	electric field vector
$\vec{F}$	electric vector potential
f	frequency of an electromagnetic field or wave
G	Green's function

$\overrightarrow{H}$	magnetic field vector
$H_m^{(n)}$	Hankelfunctions of order m and kind n
J_m	Bessel function of first kind and order m
$J_m^{'}$	derivative of the Bessel function of first kind and order m
J	imaginary unit $\sqrt{-1}$
K_{ij}	coupling coefficients between mode i and mode j
$K_{\perp}$	wave number in transverse direction
L_B, L_{φ}	Brillouin length, ray length along the circumference
Δm	waveguide perturbation order, difference in azimuthal order
N_m	Neumann function of order m
R_0, R_c	Launcher radius, caustic radius
$\Delta R(\varphi, z)$	surface perturbation of launcher wall
$\overrightarrow{R}$	ray vector
ρ, φ, z	cylindrical coordinates
$\psi^{(1)}, \psi^{(2)}$	inward, outward traveling part of the scalar field
Ψ	Brillouin angle
$\chi_{mn}^{'}$	n-th root of the derivative of the Bessel function of order m
$\Delta\chi_{mn}^{'}$	difference in Bessel roots
∇	Nabla operator
R_{cr}	Caustic radius
L_{NLT}	Length of the nonlinear taper
R_0	Mean radius of the launcher
R_c	Radius of the interaction structure
R(z)	Axial radius profile
Vmp(z)	Cold cavity field profile
h(z)	Axial E field profile across interaction cavity at beam absent
h	Convective heat transfer coefficient
d_S	Shift in the beam axis
s_h	Shape factor of NLT section
f_h	Fin height
f_w	Fin width
s_f	Spacing between fins
η_f	Fin efficiency
A_f	Fin area
Tout	Tempertaure at outer surface of the cavty
ΔR_{rad}	Radial deformantion

δR	Cavity thickness from the inner uniform section
L_c	Length of the uniform section
L_{cut}	Launcher cut length
RG1,2,3	Rdial fin groups
WOG	Wtthout fins groups
L_{ds},L_{ups}	Parabolic smoothing section lengths
α_L	Taper angles
α_L	Taper angle of the launcher

PREFACE

The work of the present thesis focuses on the beam-wave interaction studies and thermal studies of the high power gyrotron oscillators. In addition, the beam wave interaction studies of low power tunable gyrotron device are presented. The thesis aims to develop RF and thermo mechanical studies on the fixed frequency, high power gyro-vacuum electron device, i.e. gyrotron oscillators to create a solid theoretical background for future experimental studies. Historical developments of gyrotrons, in addition to VEDs, is scrutinised to bring out the research gap and problems. A series of works have been done on the gyrotron oscillator, and the part of these works has been published in reputed Journals. Further, the aim, introduction and scope of the thesis are briefly discussed below.

As compared to solid state devices, Vacuum electron devices (VEDs) generate high RF power to serve the various applications from space exploration to nuclear researches. At higher frequencies, the fabrication difficulties and operational limitation of conventional microwave tubes, push the research and development activities towards Gyrotron devices. Gyrotron devices not only overcome the limitation of transverse dimension limitation for high harmonic but also allow the beam wave interaction at a half radius from the wall for fundamental harmonic. With high power generation/ amplification and handling capabilities, gyrotron devices find applications in plasma heating, ceramic sintering, RADAR and particle accelerator application. Gyrotron oscillator finds application in plasma heating in popularly known thermonuclear fusion reactors while its amplifier counterparts are found suitable for RADAR and particle accelerator applications.

For the medium and high power levels, due to the finite conductive nature of interaction cavity walls, in the process of beam wave interaction, the generated RF power results ohmic losses in the structure and thereby thermal effects comes into the picture and leads mechanical deformations. Since, the device is very sensitive to the geometrical perturbations; a proper incorporation of thermal system for optimized RF performance is needed. As well under practical

considerations, the misalignments and spreads in the beam limit the geometrical tolerances of the structure. Taking this, the operation of the 95GHz, 100kW gyrotron in a relative high order mode is investigated and its pros and cons are discussed. In addition, the beam wave interaction studies with the inclusion of the nonlinear taper regions which are derived by inspecting the axial mode field profiles, using the time dependent multimode theory are performed. As well the necessary modifications to the multimode theory for the study of beam wave interaction behaviour under the practical beam conditions i.e., axial beam shift and tilt are incorporated and compared with the PIC simulations. Considering the importance of the efficiency, the design and analysis of internal quasi optical mode launchers has been presented using a self-developed numerical code based on the coupled mode theory instead of using Commercial Tools like LOT and SURF3D. As well the design studies of low power tunable source for DNP NMR spectroscopy applications are discussed

CHAPTER 1

INTRODUCTION AND LITERATURE REVIEW

1.1. Introduction

The demonstration of Vacuum Electron Devices (VEDs) were first made in 1883, when Thomas Edison measured an electric current from a heated filament cathode to a positively- biased plate, or anode, in an evacuated bulb [Sobol *et al.* (1984)]. By exploiting this property Fleming developed a valve (diode) in 1904 which was used for detection of DC current. Later in 1906, Lee defrost introduced a grid to the Fleming's valve and developed a triode. These glass vacuum tubes were employed for the radio communication until the magnetron was invented [Collins *et al.* (1948)] that generates significant microwave radiation. The advent of World War II further served as a catalyst for the development of microwave tubes. The need for high power microwave signals used for radar detection systems brought about the 3GHz, 10kW magnetron in 1939 [Boot *et al.* (1946)], and the klystron, invented by the Varian brothers in 1937 [Bryant *et al.* (1886)].

Ever since then, microwave tube community has been rapidly advancing due to an ever increasing demand for higher powers, greater efficiency, and higher frequencies. New and varied applications for these devices have allowed the industry to evolve and thrive. Many nuclear fusion experiments require gyrotrons to provide high power microwaves over long pulses for heating plasmas to very high temperatures, as will be discussed. The proposed International Thermonuclear Experimental Reactor (ITER) will require many of these gyrotrons producing powers which have never been reached before. Gyrotrons are also being seriously considered for imaging in medical applications, such as Electron Paramagnetic Resonance (EPR) used in Dynamic Nuclear Polarization (DNP) spectroscopy. At MIT, a 250 GHz gyrotron has been demonstrated for use in DNP [Bajaj *et al.* (2003)], and a 460 GHz second-harmonic gyrotron is being developed to provide greater resolution [Hornstein *et al.* (2006)].

Microwaves are serving our society in almost every prospect of day-to-day life. Their use is omnipresent, from ground base to the deep space communications, for civilian as well as defence requirements, space exploration, scientific researches to medical applications, strategic to industrial applications, generation of thermonuclear energy, and so on [Amboss *et al.* (1980), Andronov *et al.* (1978), Barker *et al.* (2001), Chatterjee *et al.* (1999), Chu *et al.* (1978), Collin (1966), Curie (1989), Gandhi (1981), Gaponov *et al.* (1994), Gilmour (1986), Hirshfield *et al.* (1977), Liao (1988), Singh *et al.* (2011)]. With increasing demand of device operation at higher frequencies for new applications, the research are now pushed towards the development of millimeter and sub-millimeter wave sources [Chatterjee (1999), Chu (2004), Edgcombe (1993), Emerson (1997), Felch *et al.* (1999), Gaponov *et al.* (1994), Kartikeyan (2004), Nusinovich (2004)]. At these frequencies, microwave tubes (vacuum electron beam devices) are only capable to deliver high power at which their solid-state counterparts are not able to compete [Chu (2004), Kartikeyan *et al.* (2004), Liao (1988)].

The microwave tubes find its applications over wide range of areas, such as, communication systems, radars, electronic warfare weaponry, plasma heating in fusion research, material processing, medical imaging, advanced particle accelerators, and many more [Chu (2004), Gold *et al.* (1997), Kartikeyan *et al.* (2004), Smith *et al.* (1993), Thumm (1996)]. These applications span over variety of technologies, such as, ground base point-to-point communication, satellite communication, satellite-to-home communication, thermal reactors (heating of hydrogen isotopes at ignition temperature), military radars (missile tracking and guidance), civilian radars (remote sensing, weather detection, highway collision avoidance, airport traffic control, speed detectors, air-traffic control, mapping of ground terrain), medical applications (hyperthermia, lung water detection, monitoring of heartbeat), etc. Moreover, microwave tubes operating in

millimeter wave extends its applications including high resolution radar and high information density communication, deep space and specialized satellite communication, advanced high gradient RF linear particle accelerators in high energy physics, plasma diagnostics and chemistry, waste remediation, laser pumping, electron cyclotron resonance (ECR) heating of fusion plasmas, radar and imaging in atmospheric and planetary science, nonlinear spectroscopy, high power microwaves (HPM) electronic warfare, etc. [Barker *et al.* (2004), Benford (1992), Chu (2004), Feinstein *et al.* (1987), Felch *et al.* (1999), Flyagin *et al.* (1988), Gold *et al.* (1997), Grantstein *et al.* (1987), Kartikeyan *et al.* (2004), Nusinovich (2004), Sakmoto (2006), Singh *et al.* (2011), Thumm (2002, 2003, 2010)].

The broad sweep of progress in RF vacuum electronics across a variety of devices was proposed in terms of the evolution of a "power density" as a figure of merit by Nergaard in 1960 providing an insightful basis for comparing device types [Parker *et al.* (2002)]. The physical significance derives from the fact that the maximum beam or charge carrier power that can be transported through a device is proportional to the cross-sectional area of the circuit, i.e., inversely proportional to the operating frequency. As operating frequency increases, the power handling capacity of device reduces. These necessities along with the development of superconducting magnet gave birth to a new class of microwave devices, i.e., the fast wave devices. The fast wave devices includes gyromonotron, gyro-traveling-wave tube (gyro-TWT), gyroklystron, gyro-BWO, and gyrotwystron [Baird (1979), Chu (2004), Felch (1999), Nusinovich (2004)].

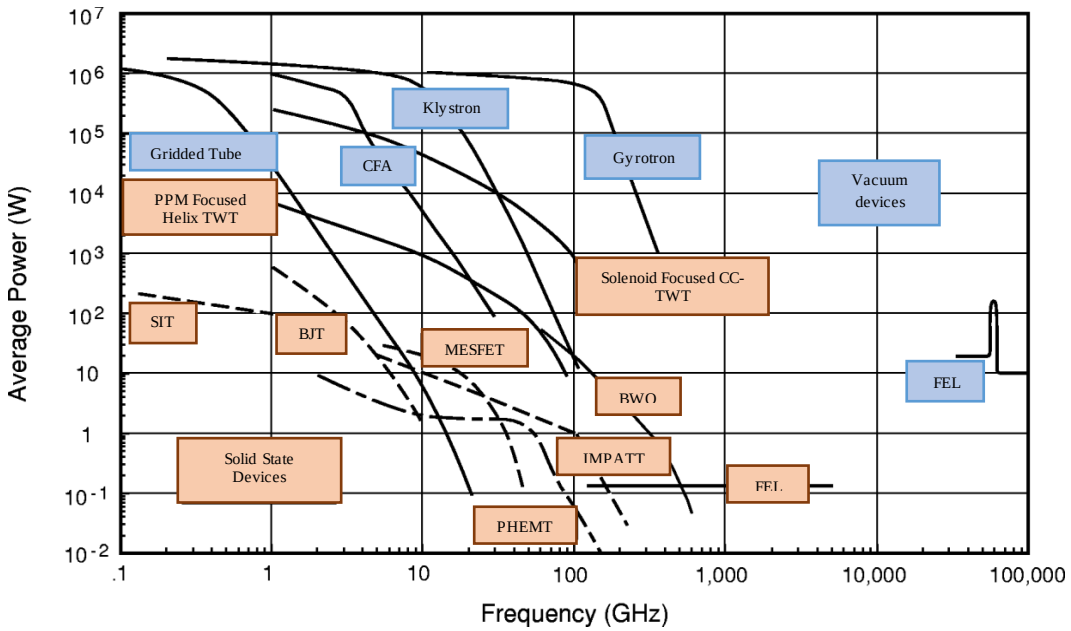

Figure 1.1: Comparison of average power versus frequency for various types of devices.

The gyro-devices and FEL surpassed the conventional slow-wave devices in the mid-1970 for high power at millimeter and sub-millimeter wave frequency range. A typical comparison of average power delivered by different devices has been represented in Fig. 1.1. In fact, microwave tubes faced stiff competition from their solid state counterpart at some stage since the later was based on the highly developed semiconductor technology. Afterwards around seventies the technology would be replaced by the semiconductor technology. However, the scenario has been changed in eighties with the growth of the microwave tubes in terms of the performance [Baird *et al.* (1979), Symons *et al.* (1986), Kartikeyan *et al.* (2004), Nusinovich (2004), Thumm (2010)]. Since, only microwave devices are capable to produce thousand times or more output power at higher frequency regime compared to the semiconductor based devices. Miniaturised size of semiconductor devices at higher frequencies limits the power handling capability whereas in case of vacuum devices, size restriction is not an issue at the higher frequencies and they can deliver high output power with considerable power handling capability [Kartikeyan *et al.* (2004), Nusinovich (2004)].

1.2. Fast-Wave Gyro-Devices

The performance of quantum-mechanical devices, like, laser degrades in terms of average output power level with decreasing frequencies and that of conventional microwave tubes with increasing the frequencies of operation [Edgcombe (1993), Gilmour (1986), Nusinovich (2004), Thumm *et al.* (2005)]. These results a technological gap in the millimeter-wave ranges to achieve substantial device performances. This happens due to the reduction in energy of each quantum with the frequency and simultaneously it is difficult to retain the population inversion in a quantum-mechanical device. On the other hand, with increase in the operating frequencies, transverse dimension of microwave devices shrinks rapidly, thereby reducing the power handling capability. Hence, with increasing operating frequency of conventional microwave tubes, the RF output power decreases due to the various limiting factors arise such as DC power dissipation, RF losses, electron current density, material breakdown, etc. This has motivated the search for the new electron beam devices that fulfills the gap in terms of appreciable power level in the microwave and millimeter wave regions, for instance, gyrotron devices based on cyclotron resonance maser (CRM) instability [Baird (1979), Barker (2001), Basu (1996), Edgcombe (1993), Felch *et al.* (1999), Gilmour (1986), Nusinovich (2004)].

In gyro-devices, a hollow gyrating electron beam interacts with the transverse electric mode supported by a fast-wave-guiding structure, like, a cylindrical waveguide or cavity. In these devices, basically the electron beam is made periodic rather than the interaction structure that supports a fast waves. In a gyrotron, transverse kinetic energy of electrons is converted into electromagnetic energy rather than axial kinetic energy (as in a TWT) or potential energy (as in a magnetron) during the beam-wave interaction mechanism. The Doppler-shifted frequency is made nearly equal to the cyclotron

frequency or any of its harmonics for the cyclotron resonance takes place, unlike in a device like TWT where the electron DC beam velocity is made synchronous with the RF phase velocity.

Similar to the slow-wave devices, transverse dimension of the interaction structure of fast-wave devices also decreases with the increase of frequency. However, in gyrotron device operation at the higher-order modes lead to a further increase in the waveguide transverse dimension [Kartikeyan *et al.* (2004), Liu (2000), Nusinovich (1999)]. This increase in transverse dimension of the interaction structure reduces the power loss density at the cavity or waveguide wall of the devices. Another advantage of a fast-wave gyro-device structure is that the electron beam can be placed far from the interaction structure wall to realize larger interaction field. This also reduces the problem of beam interception caused by the metallic boundaries.

The fast-wave gyro-devices, e.g., gyrotron are based on CRM instability and electrons bunching is relativistic. The electron bunches are kept in the decelerating RF phase which yields that most of the electrons interacting with RF waves transfer their energy to RF instead of taking energy from the later. This can be obtained by slightly detuning the cyclotron resonance condition while in a slow-wave device, this is done by slightly offsetting the synchronism between the DC beam velocity and RF phase velocity [Basu (1996), Edgcombe (1993), Gilmour (1986), Kartikeyan *et al.* (2004)]. Further the classification of gyrotron devices are done on the basis of their interaction mechanism. The synchronism between beam mode line and waveguide mode curve for beam-wave interaction of different gyrotron devices are discussed through the dispersion curve in Section 1.2.1.

1.2.1 Dispersion relation

The operational characteristic of the device is governed by the dispersion relation and device synchronism condition can be obtained at the grazing intersection between the beam mode and waveguide mode dispersion curve. In a gyrotron device, the condition of synchronism between the fast cyclotron wave and electron beam motion, transverse to a DC magnetic field, leads to a beam-mode dispersion relation of a gyro-device as described below [Basu (1996), Chu (2004), Edgcombe (1993), Gaponov-Grekhov *et al.* (1994), Gilmour (1986), Kartikeyan *et al.* (2004), Nusinovich (2004), Thumm (2010)].

1.2.1a Beam-mode dispersion relation

The beam mode dispersion relation can be obtained using the concept that over a cyclotron period, one or more RF cycles are completed [Basu (1996)]. Considering a gyrating electron beam that completes its one gyration in time T_c. The RF phase of the electric field component can be given as $\omega t - \beta z$ where ω is the wave frequency, β the propagation constant or wavenumber. After one gyration time period, the initial phase will change and can be given as $\omega(t+T_c)-\beta(z+v_z T_c)=\omega t+\omega T_c-\beta z-\beta v_z T_c$, where s is the beam mode or harmonic number, and v_z is axial beam velocity. Now, putting $s(2\pi)=(\omega-\beta v_z)T_c$, the initial phase change can be written as $\omega t-\beta z+s(2\pi)$. Considering,

$$s(2\pi)=(\omega-\beta v_z)T_c \tag{1.1}$$

$$s(2\pi)/T_c=\omega-\beta v_z\ . \tag{1.2}$$

The cyclotron frequency is $\omega_c = 2\pi/T_c$, so (1.2) can be written as

$$s\,\omega_c=\omega-\beta v_z \tag{1.3}$$

$$\omega - \beta v_z - s\,\omega_c = 0 \quad , \tag{1.4}$$

where, $$\omega_c = eB_0 / m_e \tag{1.5}$$

B_0 is the axial DC magnetic field, e and m_e are the magnitude of electron charge and mass at the rest, respectively. Since, gyro-devices are relativistic devices, so including relativistic mass factor (γ) into equation (1.4), it can be written as:

$$\omega - \beta v_z - s\,\omega_c / \gamma = 0. \tag{1.6}$$

The equation (1.6) is the beam-mode dispersion equation.

1.2.1b Waveguide-mode dispersion relation

Waveguide-mode dispersion relation can be determined by considering a TE_{mn} mode propagating in axial direction (*z*-direction) of a cylindrical waveguide. For TE_{mn} mode, *z*-component of electric field intensity would be zero, i.e., $E_z = 0$. The axial component of magnetic field intensity in the cylindrical waveguide can be given by [Liao (1988), Kartikeyan *et al*. (2004)]:

$$H_z = C_{mn}\, J_m(\gamma_n r) \exp\{ j(\omega t - \beta z - m\theta) \} \quad . \tag{1.7}$$

Here, r, θ, z are cylindrical coordinates, *m* and *n* are the azimuthal and radial index of a mode, γ_n is the radial phase propagation constant, J_m is the m^{th} order ordinary Bessel function of first kind. Field constant (C_{mn}) can be given by

$$C_{mn} = \frac{1}{J_m(v_{mn})\sqrt{\pi\left(v_{mn}^2 - m^2\right)}} \tag{1.8}$$

and

$$\gamma_n = \left(k_0^2 - \beta^2\right)^{1/2} = \left(\omega^2 / c^2 - \beta^2\right)^{1/2} = \chi_{mn} / r_w \ , \tag{1.9}$$

where, $k_0 = \omega(\mu_0 \varepsilon_0)^{1/2} = \omega / c$ is the free-space propagation constant; c is velocity of light in free space, μ_0 and ε_0 are permeability and permittivity of the vacuum,

respectively. Now, considering the axial magnetic field intensity H_{z0} at axis of the guide, i.e., r = 0. For the azimuthally symmetric mode $(m=0)$, $J_0(0)=1$. Consequently,

$$H_z\big|_{r=0} = C_{mn} = H_{zo}. \tag{1.10}$$

Therefore, (1.7) can be written as

$$H_z = H_{z0} J_m(\gamma_n r)\exp\{j(\omega t - \beta z - m\theta)\} \quad . \tag{1.11}$$

The azimuthal components of electrical field can be written as

$$E_\theta = \left(\frac{j\omega\mu_0}{\gamma_n}\right) H_{z0}\, J'_m(\gamma_n r)\, \exp j\left(\omega t - \beta z - m\theta\right) \quad . \tag{1.12}$$

For the perfectly conducting waveguide wall, the azimuthal component of electric field intensity would be zero at the wall $(r = r_W)$, i. e., $E_\theta(r = r_W) = 0$. Consequently, Bessel derivative must be zero. Hence,

$$J'_m(\gamma_n r) = 0. \tag{1.13}$$

This yields

$$\Rightarrow \qquad \omega^2 - \beta^2 c^2 - \omega_{cut}^2 = 0 \quad , \tag{1.14}$$

here, $\omega_{cut} = \gamma_n c$. Equation (1.14) represents the waveguide mode dispersion plot which is a hyperbola. The intersection of the beam mode line and waveguide mode curve described by (1.6) and (1.14) provide the synchronism condition. These dispersion relations for the various gyro devices are given in Fig. 1.2 which provides the information about their operating conditions.

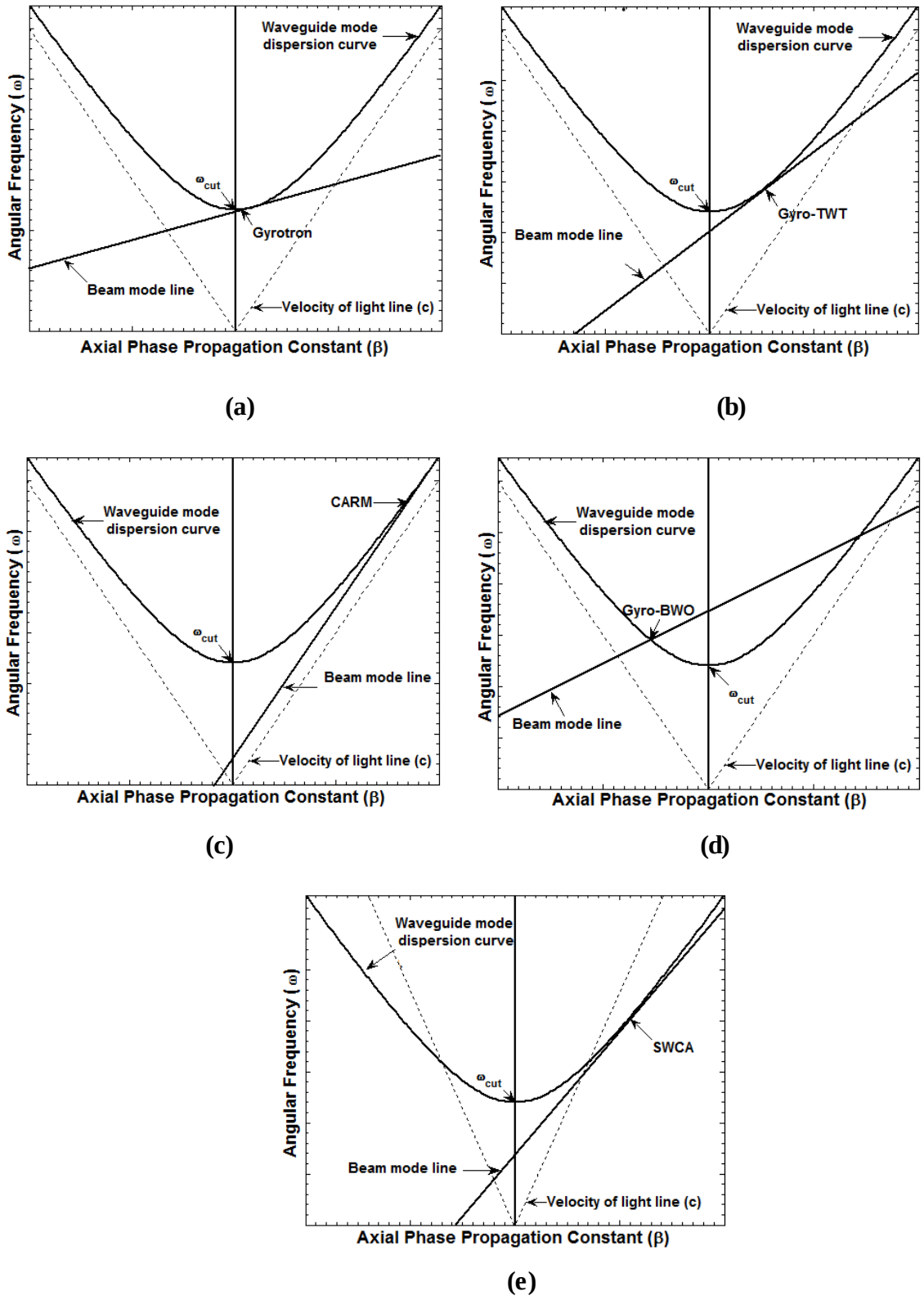

Figure 1.2: Dispersion diagrams showing the operating regions of interaction for **(a)** gyrotron, **(b)** gyro-TWT, **(c)** CARM, **(d)** gyro-BWO, and **(e)** SWCA.

In Fig. 1.2(a), the beam mode and waveguide mode dispersion relation for the gyrotron oscillators are given. Gyrotrons operate close to the waveguide cut-off frequency, at near-zero group velocity. This makes the beam velocity slow enough to maintain electromagnetic energy in the waveguide resonator cavity for interaction with the electron beam [Basu (1996), Gilmour (1986), Jain *et al*. (1994), Kartikeyan *et al*. (2004)], Symons *et al*. (1986)].

In a gyro-TWT amplifier, the grazing situation between the two curves provides the operating bandwidth of the device (Fig. 1.2 (b)). The broadband operation of gyro-TWT is desirable for the various applications that can be achieved by tuning the DC axial magnetic field to the value of grazing magnetic field. At the grazing condition, the group velocity of the beam mode and RF wave are identical that results in a high gain amplifier [Agrawal *et al*. (2001), Basu (1996), Chu *et al*. (1988), Ferguson *et al*. (1981)].

The CARM has attracted interest due to its potential for high efficiency operation, resulting from the further extended operating region of interaction where the resonance between the beam and wave is automatically maintained (Fig 1.2**(e)**). This favourable frequency shift from the cut-off frequency is caused by a large Doppler shift term associated with the large axial wave number and axial velocity [Bratman *et al*. (1981), Pendergast *et al*. (1988), Petelin (1974), Wang *et al*. (1991)].

The gyro-BWO operates at a point where both the phase and group velocities of the RF waves contain negative values (Fig 1.2(d)). By controlling either the DC axial magnetic field or the DC beam voltage, frequency tuning over a wide range of operating frequencies can be achieved in the gyro-BWO [Park *et al*. (1984), Nusinovich *et al*. (1996)].

In a slow wave cyclotron amplifier (SWCA), the axial non-relativistic bunching takes place. Additionally, the slow waveguide-mode is destabilized in such a way that the waveguide-mode dispersion characteristics is depressed below the beam-mode dispersion characteristics (Fig. 1.2**(e)**) [Baird *et al*. (1980), Choe *et al*. (1982), Ganguly *et al*. (1990)].

1.2.2 CRM interaction mechanism

The instabilities in a beam-wave system can be of different types. Their operation is mainly explained the interaction between slow and fast space charge waves on the electron beam and the electromagnetic waves in an interaction structure. The process of energy extraction is distinctive in all instabilities. The energy is extracted from the longitudinal component of the electron velocity in Cherenkov interaction [Pierce (1965)]. The interaction between a gyrating electron beam and an electromagnetic wave in the background of DC magnetic field leads to extraction of the transverse kinetic energy of the electrons. This interaction is known as the CRM instability [Chu (2004)] which occurs in the gyrotrons. In the CRM interaction, phase bunching of electrons occurs due to the change in relativistic mass as they lose or gain energy from the transverse electric field in the circuit. Another instability, which has the similar operating conditions to CRM interaction but inherently different, is termed as Weibel instability [Chu *et al*. (1978)]. In Weibel mechanism, phase bunching of electrons occurs due to axial movement of the electrons perpendicular to the cyclotron orbit as it occurs in SWCA (slow wave cyclotron amplifier) [Grantstein *et al*. (1987)]. Another instability, which is known as peniotron instability, differs significantly from that of CRM and Weibel instabilities. In peniotron interaction, energy is not extracted by the phase bunching process rather the drift of the electron guiding center causes the energy loss from each electron to the transverse electric field. The CRM, Weibel and

peniotron instabilities do not have limited domains and hence they interact with each other under certain conditions [Basu *et al.* (1996)].

The typical arrangement of CRM interaction is revealed in Fig. 1.3. Considering an annular gyrating electron beam drifting through a waveguide immersed in a background axial static magnetic field B_0 [Kartikeyan *et al.* (2004)].

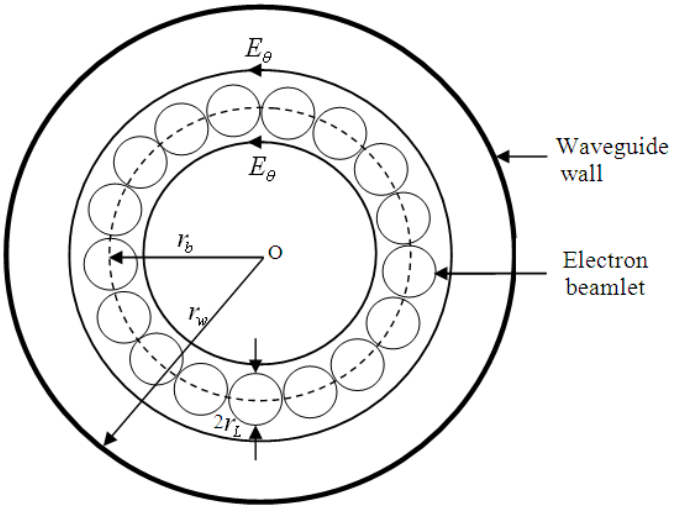

Figure 1.3: TE_{0n} mode RF electric field in a waveguide with electron beamlets.

In the figure, r_w is the radius of waveguide and r_b is the average beam radius, which is also the guiding center radius of the beamlets. The field orientation of a TE_{0n} mode is shown in the figure. The thickness of the beam is equal to twice of the Larmor radius (r_L) defined as

$$r_L = c\, v_t / \omega_c \tag{1.15}$$

where, v_t is transverse velocity of the electron, ω_c is the angular cyclotron frequency for electrons. The relativistic mass factor (γ) in terms of axial velocity (v_z) and transverse velocity (v_t) of the electron beam is as

$$\gamma = \left(1 - \left(v_t^2 + v_z^2\right)/c^2\right)^{-1/2} \quad . \tag{1.16}$$

The relativistic cyclotron frequency of the electrons can be specified as

$$\omega_c = e B_0 / (\gamma m_e) \ . \tag{1.17}$$

The azimuthal component of RF electric field (E_θ) interacts with the electrons in transverse plane. The relativistic cyclotron frequency of electrons is changed due to the alteration in the relativistic factor in this interaction. The change in cyclotron frequency established the instability that is known as Cyclotron Resonance Maser (CRM) instability. Cyclotron frequency of some electrons will increase whereas for some it decreases causing energy transfer and consequently, results in phase bunching of electrons [Chu (2004)].

1.2.2a Phase bunching

The phase bunching process can be understood easily assuming zero axial velocity. To understand this, one of the beamlets is captured to analyze the process of phase bunching as shown in Fig 1.4(a) where, B_0 is the axial DC magnetic field.

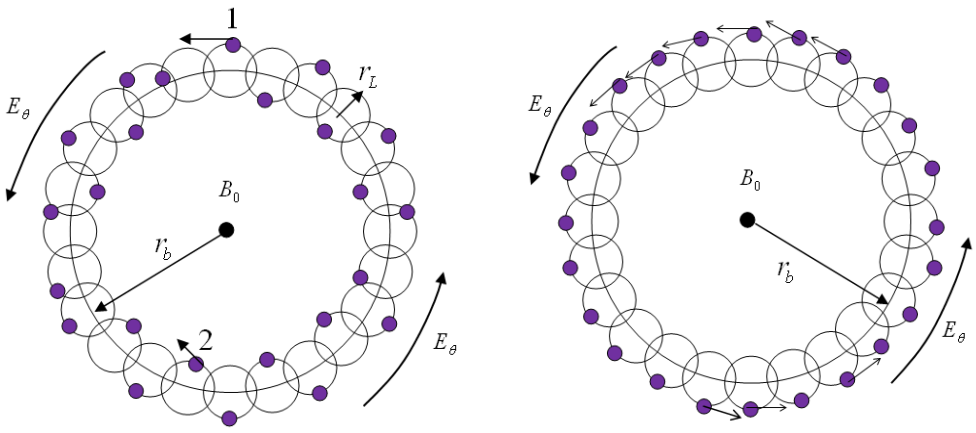

Figure 1.4: Illustration of phase bunching phenomenon in an annular electron beam **(a)** random distribution, and **(b)** phase bunched electrons in their cyclotron orbits.

The electrons are arranged in annulus circular orbits with radius r_L, typically $r_L << r_b$. From Fig. 1.4(a), initially, the phase of the electrons in their cyclotron orbits is

random. The presence of a transverse RF electric field in TE_{mn} mode will cause the electrons to be accelerated or decelerated. Obviously, with the random phasing, there is no net energy exchange [Basu (1996), Chu (2004), Kartikeyan *et al.* (2004)]. Bunching mechanism can be understood by considering two electrons assigning as 1 and 2 in the Fig. 1.4(a). Due to the azimuthal electric field, electron 1 will be decelerated and lose energy whereas, electron 2 will be accelerated and hence gain an equal amount of energy. Since, the cyclotron frequency of an electron is inversely proportional to its relativistic mass γm_e (from 1.17) therefore, electrons gaining energy from the RF field gyrate slower due to increased mass while the other ones that losing energy gyrate faster due to decreased mass. As a result, the electrons form a bunch in Larmor radius. This bunch of electrons transfer energy to RF wave if the wave frequency is slightly larger than the initial value of the cyclotron frequency as

$$\omega' - \frac{eB_0}{m_e \gamma_0'} > 0 \ . \tag{1.18}$$

Here, subscript 0 refer initial value and prime denotes the reference frame in which electron axial velocity vanishes. Since, electron 2 is in the opposite direction to the electric field, energy will enhance. This causes decrease in cyclotron frequency due to increase in relativistic mass and hence, this electron moves down farther from resonance. On the other hand, electron 1, which initially loses energy, experiences an increasing value of cyclotron frequency and comes closer to exact resonance. Hence, electron 2 gaining less energy and electron 1 losing an increasing amount of energy on each successive cycle. With time, instability develops in which the wave energy grows in time and the electrons bunch in phase within their cyclotron orbits as shown in Fig. 1.4(b). Furthermore, the Larmor radii of faster gyrating electrons decreases, while those of slower gyrating electrons increases, resulting in a change in the shape of each beamlet [Chu (2004), Kartikeyan *et al.* (2004)].

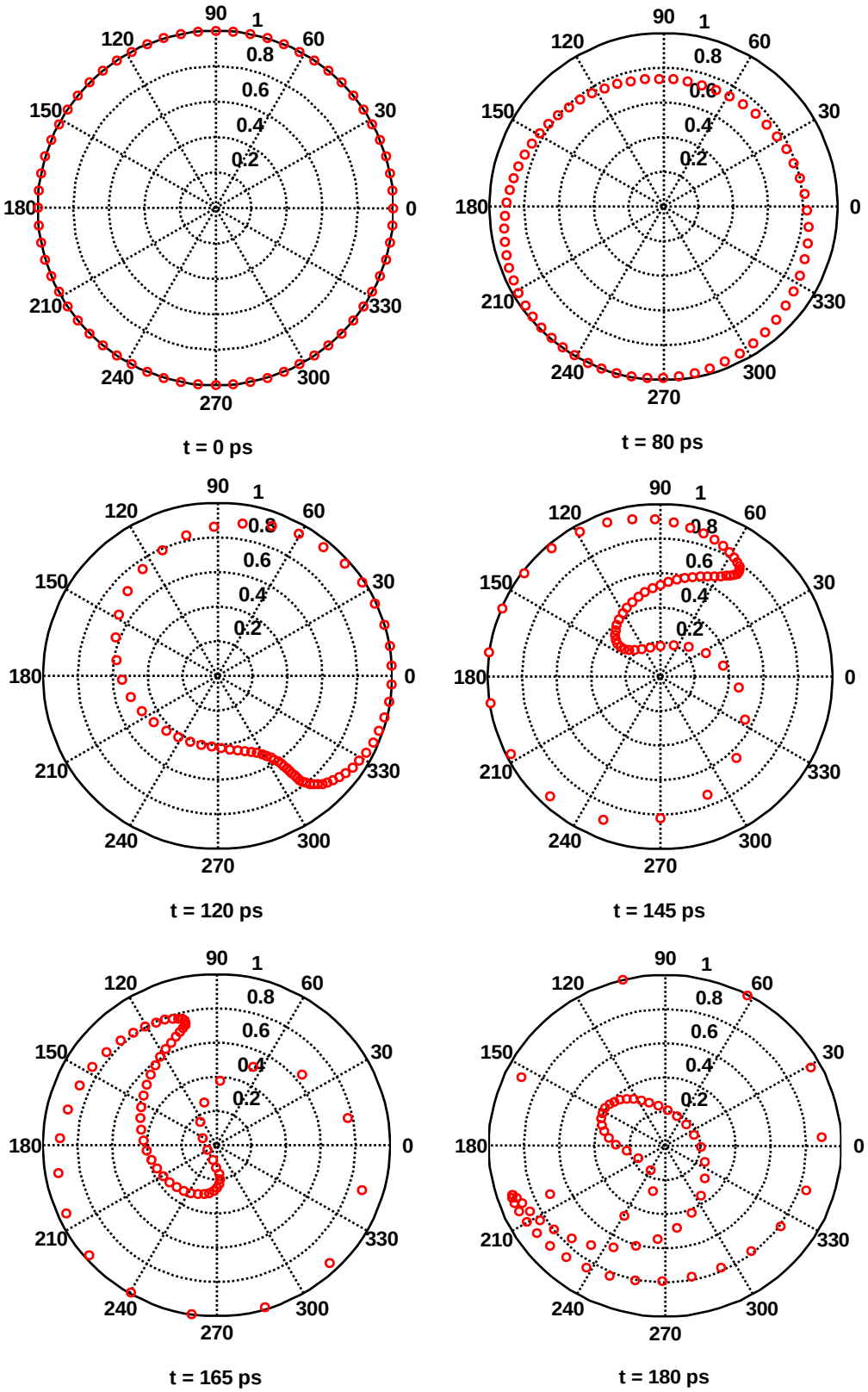

Figure 1.5: Time evolution of electrons phase distribution (shown as O) in the Larmor orbit [taken permission from Ashutosh *et al.* [2012].

The phase bunching of the electrons in CRM interaction is shown in Fig. 1.5. These figures demonstrate the Larmor radii of electrons in the phase space as a function of time. The number of representative electrons in the beamlet is taken as 64, which are initially uniformly distributed around a Larmor orbit (Fig. 1.5, at t = 0). The figures show the transverse position of electrons in the background electric field. The bunch of electrons follows the azimuthally rotating RF electric field. Obviously, Larmor radius of each electron altered and a bunch formation takes place. Finally, this bunch slips in phase to the RF and energy transfer phenomena takes place.

1.2.3 Operating principle

For the beam-wave interaction in all gyro-devices, an electron beam is emitted from a cathode and helically gyrated towards the RF interaction structure such as an open-ended cavity, series of cavities, or a long waveguide section in a background DC magnetic field. As, it has been discussed earlier that the electron beam consists of many electrons gyrating around the magnetic field lines in a small helical path with a cyclotron frequency close to the operating frequency of the device as they traverse from cathode to collector side. With such small helices, called beamlets, form a hollow annular beam in a specific beam radius. If Larmor radius of the electrons is smaller than the guiding centre radius, then device is called a small orbit device. On the other hand, if Larmor radius is greater than or equal to the guiding center radius, the device is called a large orbit device. Magnetron injection guns (MIG) are used to produce a small orbit beam. As discussed previously, the energy is extracted from the beam during the beam-wave interaction through relativistic CRM instability in gyro-devices. Bunches develop along the interaction length with time evolution. If operating frequency is slightly higher than the cyclotron frequency of the electrons, bunches slips to the phase of the

RF field and it falls in decelerating phase, consequently energy transfer takes place from beam to RF wave [Grantstein *et al.* (1987)]. In CRM interaction, the transverse energy of the electron beam is extracted to convert into RF energy. After interaction, electron beam lose its energy to the RF field in the cavity and is finally collected at a thermally cooled collector. The output RF radiations are sent through waveguides for the required application. Gyro-devices, such as, gyro-TWT, gyroklystron, gyrotwystron, gyro-BWO, and gyrotron oscillator, incorporate different types of the RF interaction structures.

1.3. Gyrotron Oscillator and its sub-assemblies

Gyrotron (gyromonotron) is an efficient high power microwave and millimeter wave coherent radiation source (oscillator) and based on CRM instability [Chu (2004)]. Gyrotron RF behavior has been extensively investigated through both theory as well as experiments in the past [Gaponov *et al.* (1981), Gilmour (1986), Grimm *et al.* (1993), Hirshfield *et al.* (1977), Kartikeyan *et al.* (2004), Kartikeyan *et al.* (2008), Kreischer *et al.* (1990), Nusinovitch (2004), Spira-Hakkarai *et al.* (1990), Thumm (2009, 2010)]. A schematic of gyrotron oscillator with axial and radial output couplings are shown in Figure. 1.6.

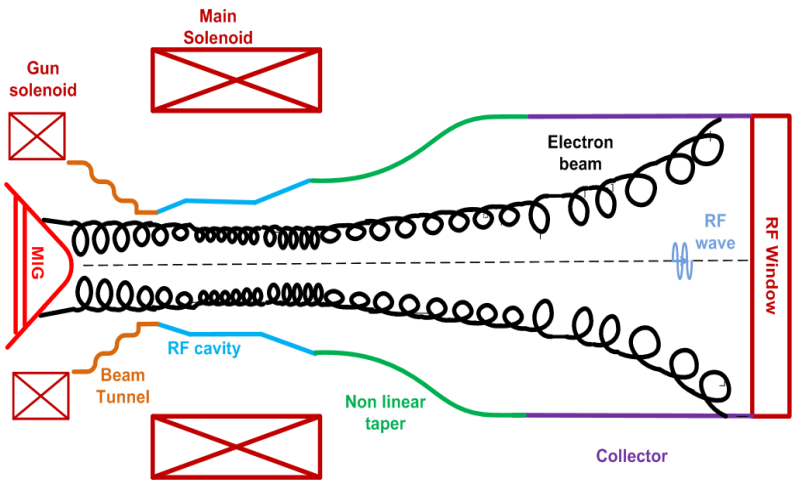

(a)

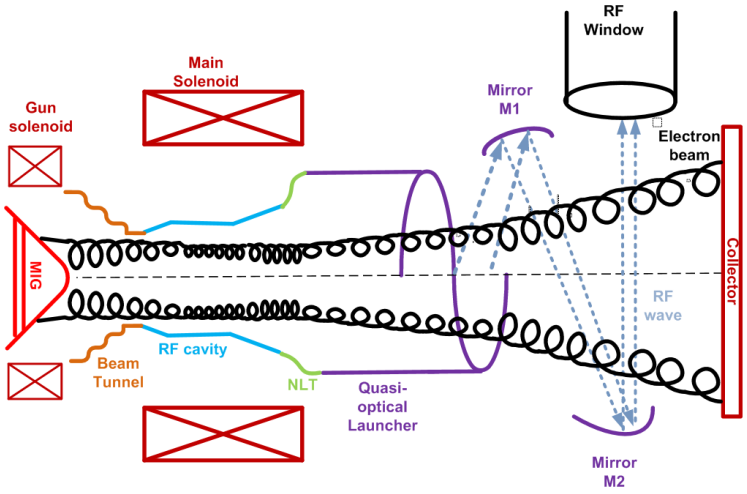

(b)

Figure. 1.6: Schematic of conventional gyrotron with (a) axial output RF coupling and (b) radial output RF coupling.

As we knew, energy has neither be created nor be destroyed, but only conversion from one form to other is possible. For this conversion, a collection of various sub-assemblies are needed. A device performance depends upon the collective performances of their sub-assemblies.

The RF source generates RF energy from a DC electron beam source with the help of a group of sub systems that allows interaction between RF wave and electron beam. For the RF source, the main goal is to convert the DC electron beam energy into RF energy with minimum losses and more efficiency. The functions of sub-assemblies of the RF device are as follows; emission and guiding of the electron beam, beam-wave interaction, and transmission of RF energy with minimum losses.

Figure. 1.6 shows the schematic diagram of the conventional tapered gyrotrons with axial and radial output RF coupling that includes its typical sub-assemblies. In the following paragraphs, the significance of various subassembly in the RF generation along with its feature are briefly described.

1.3.1 MIG gun and Beam tunnel

The source for RF generation by any microwave device is the DC electron beam. The electron beam is a bunch of electrons which are emitted from a component known as cathode in a system called as electron gun**.** The electron gun used in a gyrotron is usually magnetron injection gun (MIG) type. The conical shaped cathode emits gyrating electron beams with the electrons having small cyclotron orbits under the influence of a magnetic field, as required for the cyclotron resonance condition [Baird *et al.* (1986)].

The electrons emitted from the cathode in an electron gun of a microwave tube forms an electron beam of suitable parameters, namely, beam diameter, beam perveance, beam density, etc. and pass through the region for interaction with the RF wave. However, the beam-wave interaction in a gyrotron, the transverse electron energy is needed and thus the velocity ratio between the transverse velocity and the axial velocity is another important parameter in a function of a MIG [Baird *et al.* (1986)].

The beam tunnel is incorporated in between the electron gun and RF interaction cavity. It assists as a region where the electron beam gets stabilized. The design of the beam tunnel should be such that it should have some lossy material to absorb RF power and ensures the no backward wave propagation towards the electron gun.

1.3.2 RF interaction cavity

The RF interaction cavity mainly responsible for the generation of RF quantity with desired qualities like power and frequency, i. e., at single, step tunable and broadband frequencies. The RF waves generated in the cavity interact with gyrating electron beam emitted by MIG gun under external magnetic field. The cavity walls are made of by metals having finite conductivities. Due to this, the beam wave interaction mechanism causes ohmic losses based on the amount of RF generation in the structure which leads to thermal losses and results deformation in the cavity structure. Hence, a proper cooling

system to be designed for the reliable and longer performance of the RF cavity thereby device.

Various types of the RF interaction structures, such as, tapered cylindrical cavity of simple and complex type, coaxial cylindrical cavity, photonic bandgap (PBG) type and confocal cavity type are the typically used in the millimeter and submillimeter frequency range for high power as well as low power levels. A brief discussion on the pros and cons of various interaction cavities are discussed below.

A 2-D axis symmetric model view of conventional tapered cylindrical structure view is shown in Fig. 3. It consists of three sections, first a down taper section for RF isolation of length L_d, with an angle θ_d, followed by a uniform middle section where active beam-wave interaction takes place, of length L_c and at the end, an up-taper section where RF standing waves get converted into travelling waves to extract out RF energy, of length L_u with angle θ_{up}. Usually, parabolic smoothing section of lengths L_{ds} and L_{us} at down-taper and up-taper transitions, respectively, are used to minimize the unwanted mode conversions [Edgcombe (1993)].

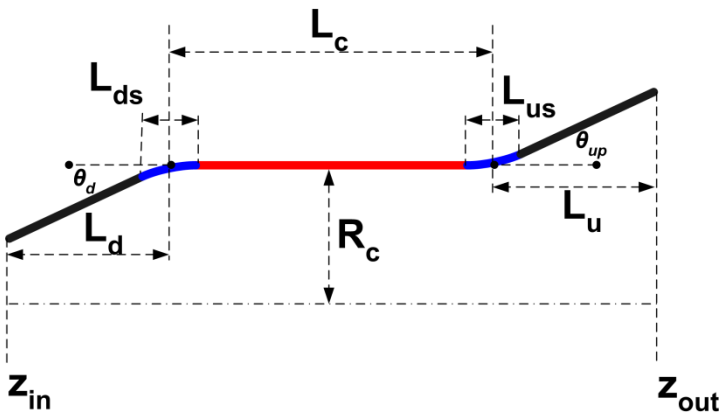

Figure 1.7: A 2D axial symmetric view of tapered cylindrical RF interation cavity.

It is fundamental, simple and conventional type of interaction cavity used for various power levels generation, i.e., all high power, medium power and low power level. Considering the high power level generation at high frequency devices, it needs

to operate in the high order mode that scales the transverse dimensions as well applying high beam parameters, makes the significant presence of voltage depression also mode competition which needs a careful design of the system.

In order to ease the mode competition and voltage depression effects, coaxial resonators type cavities are being considered as the interaction structure. Basically it is a combination of tapered cylindrical cavity along with a smooth and or corrugated center conductor. A 140GHz coaxial gyrotron was experimentally demonstrated in 1999 at MIT Dammertz *et al.* (2005), and researchers at FZK are planning to use a coaxial cavity for a 2 MW, 170 GHz gyrotron [Thumm (2004)]. Apart from the lesser mode competition, considering the practical aspects, it is somewhat challenging to maintain an off beam optical axis. Beam misalignment with the cavity axis is significant in these structures that lead to degradation of the performance of the system. A careful design and machining techniques are required. Photonic Band Gap based interaction cavity, is a novel methods for mode suppression in gyrotron oscillators and amplifiers are being investigated at MIT. A photonic bandgap (PBG) structure consisting of an array of metallic rods has been successfully demonstrated in a 140 GHz gyrotron experiment [Kartikeyan *et al.* (2004)]. Even though it supports selected modes but allows more tunable bandwidth.

Confocal waveguide, a type of quasi-optical open waveguide, performs a much lower mode density than conventional cylindrical waveguide, so that it could be stably operated at high-order mode with high frequency and high power. The confocal cavity utilized in gyrotron was initially proposed by R. J. Temkin *et al.* , Lindsay (1981), and it has been successfully used in 140-GHz fundamental gyrotron oscillator and traveling wave amplifier in MIT [Lindsay (1981), Lindsay (1981), Gaponov *et al.* (1975), Flyagin *et al.* (1977)]. Due to the good mode-selective characteristics, confocal

waveguide would greatly suppress the mode competition in harmonic gyrotron. A 140 GHz gyro-TWT amplifier using an open-edged confocal cavity to suppress competing modes has also been recently tested [Barker *et al.* (2005)]. Complex cavities, formed by a group of cylindrical tapered sections and the generation of RF power achieved by operating in two different modes.

1.3.3 Non -linear taper section

A short waveguide propagating section that acts as a connecting module between RF interaction cavity and collector for axial output coupling, or the QOM converter for radial output coupling device and allows RF transmission with minimum mode conversion by providing the proper impedance matching between them. It should allow the transmission of generated RF power with minimum mode conversion from the RF cavity end to the collector end which is at different radii thereby matching different impedances. Various taper designs such as exponential taper, triangular taper, Chebyshev taper, Klopfenstein taper, and Hecken taper can be employed for matching purposes. Flügel and Kühn considered modified Dolph-Chebychev tapers for the analysis and design of circular waveguide tapers [Thumm and Kasparek (2002), Edgcombe (1993), Benford and Swegel (19920, Kartikeyan *et al.* (2004), Barker *et al.* (2005)]. Out of all, a raised cosine type taper where a uniform profile at the start and end of the taper and a non-uniform type middle profile provide better agreement with short length. Ideally, the transmission coefficient of the taper should be maximum and the reflection coefficient should be minimum with low insertion loss [Edgcombe (1993), Lawson *et al.* 1990, Goldstein *et al.* 1984].

Usually, by scattering matrix calculations, the nonlinear tapers used in the gyro devices are designed and optimized. CASCADE tool is also used for the analysis and design of the nonlinear taper. Various Optimization techniques, like, genetic algorithm

(GA), swarm optimizations, etc. are widely used for the optimization of the taper profile that leads maximum transmissions while minimum mode conversions among various modes.

1.3.4 Quasi optical mode converter

A quasioptical mode (QOM) converter, is a combination of a mode launcher, a waveguide section with a cut at its end followed by a group of beam shaping and focusing mirrors, and is incorporated in between nonlinear taper and the collector of the device to allow the conversion of cavity interaction mode TE_{mn} into a free space Gaussian beam mode TEM_{00} that low loss transmission. Incorporation of QOM converter allows separation of electron beam from the RF wave after interaction, i. e., radial output coupling and improves the overall efficiency of the device [Vlasov *et al.* (1975), Denisov *et al.* (1992), Edgcombe *et al.* (19993), Kartikeyan *et al.* (2004)]. Usually, commercially available software, such as, LOT and SURF 3D tools are popularly used for the design and optimization of QOM converters [Calcabazas creek reseach, CA] and are very much expensive for the educational institutions. There are basically two types of quasi optical mode converters are used, namely, Vlasov type and Denisov type converter. Denisov converter is a modified Vlasov converter due to improvements in the launcher structure as well improvement in the conversions efficiency [Thumm and Kasparek (2002), Edgcombe (1993), Benford and Swegel (1992), Kartikeyan *et al.* (2004), Barker *et al.* (2005)].

1.3.5. Collector

After the transfer of the kinetic transverse energy to the RF signal through effective power growth in the RF interaction structure, the spent gyrating electron beam collides at the collector and safely dissipates the remaining beam energy. In addition,

the collected beam power can feed to the system as a power supply thereby enhancement in the efficiency. The overall device efficiency can be increased by incorporating depressed collector techniques, and is more suitable in the radial output couplings gyro devices. In addition, thermal studies of the collector are also important to analyze and optimize the collector efficiency as well as reliability of the system through proper cooling system design [Thumm and Kasparek (2002), Edgcombe (1993), Benford and Swegel (1992), Kartikeyan *et al.* (2004), Barker *et al.* (2005)].

1.3.6. RF window

An RF window is another crucial subassembly of the gyrotron, which ensures maximum transmission of internal generated RF power to the outer transmission. It provides a vacuum sealing between two pressure differences, typically the two pressures are 1 atm and 10^{-9} mbar (the ultra-high vacuum inside the gyrotron envelope) with low insertion loss. It should also have the capabilities of handling high peak/average power, and therefore the window material need to have high thermal conductivity and low RF loss tangent. In addition, for broadband applications, the impedance matching with rest of the RF transmission line is needed over a wideband frequencies. The desired features of an ideal RF window are as follows: low insertion loss, low reflection, wide bandwidth, high power handling, high mechanical strength, low loss tangent, i. e., low RF power absorption [Thumm and Kasparek (2002), Edgcombe (1993), Benford and Swegel (1992), Kartikeyan *et al.* (2004), Barker *et al.* (2005)].

Single disc, double disc, Brewster window, chemical vapor deposited diamond windows are the different variants of the RF window used in various fixed, high power, tunable gyrotron devices. Boron Nitride (BN), Silicon Nitride composite, diamond, Sapphire, Beryllia, Cryogenic Sapphire, Au-doped silicon and so on are the most used window materials for the gyro devices. The recent use of CVD (chemical vapor

deposition) diamond RF window has significantly increased the RF output power capability of gyrotrons [30]. The Brewster windows are usually preferred for high power multi frequency operated devices as well tunable gyrotrons [Thumm and Kasparek (2002), Edgcombe (1993), Benford and Swegel (19920, Kartikeyan *et al.* (2004), Barker *et al.* (2005)].

1.3.7 External DC magnetic field

In the gyro-devices, the generation of RF with desired quantities, i.e., power and frequency in the device is attained by providing a synchronous condition between the electron beam and the RF wave in the interaction cavity. This is accomplished by the tailoring of external axial DC magnetic field profile B (z) along the device with the peak at the interaction region. The values of B (z) are primarily depending on the targeted RF frequency, f and s harmonic operation of the device [Edgcombe (1993), Kartikeyan *et al.* (2004), Barker *et al.* (2005)].

In addition to RF generation, the propagation and the guiding of the spent beam to collector and transmission of the generated RF wave is depended by the magnetic profile. The gyration of annular electron beam emitted from the MIG gun, is achieved by use of an external magnetic field and that leads the electron to oscillate with the cyclotron frequency. A tapered magnetic field, from the MIG gun to the collector with peak at the interaction cavity is maintained for guiding the electron beam and controlling the interaction with the RF wave. Cryogenic magnets, super conducting magnets as well permanent magnets are used for the facilitation of external magnetic fields required by the gyrotron. By allowing the operation of the device at second or higher harmonic frequencies, a less magnetic field is used that allows the usage of permanent magnet instead of bulky super conducting magnet with the cost of efficiency

of the device [Thumm and Kasparek (2002), Edgcombe (1993), Benford and Swegel (19920, Kartikeyan *et al.* (2004), Barker *et al.* (2005)].

1.4. Applications

Gyrotron oscillators are capable of generating CW, long pulse and pulse power from few watts to few megawatts in the frequency range of millimeter, sub millimeter and THz wave at single, step tunable as well as broadband frequencies, respectively. Based on the range of power levels as well as operating frequencies and tunable frequency bands, gyrotron oscillators are suitable to use in several applications, like, plasma fusion, material processing, industrial heating, spectroscopic, medical sciences, communications (at the atmospheric window) and security application, like, in active denial systems, electronic warfare systems.

Since the ability of gyrotron to generate various ranges of CW and Pulse power at single, step tunable and continuous tunable frequencies makes its suable for use in wide variety of systems applications. A brief note on some of the areas where gyrotrons are used as the potential RF sources discussed as follows.

1.4.1 Plasma heating for fusion

The radio frequency electromagnetic waves are used for plasma heating. One kind of plasma heating method is Electron Cyclotron Resonance Heating (ECRH) which requires the sources in the frequency range of 100-200 GHz. At present, gyrotron oscillators are successively used as high power sources for ECRH applications and for plasma diagnosis of magnetically confined plasmas in controlled thermonuclear fusion research. The latest and ambitious international joint effort in the field of energy production by the controlled nuclear fusion is started in the form of ITER project with an aim to solve the problem of future energy generation to a great extent. ITER is the

biggest plasma fusion machine under construction. 170 GHz gyrotron with 1 MW of output power would be used in the ITER for ECRH and ECDD (Electron Cyclotron Current Drive). High efficiency, high output power and long pulse width are the key requirements for the development of fusion gyrotrons [Kumar *et al*. (2011), Gaponov *et al.* (1994), Kasugai *et al.* (2008)].

1.4.2 Industrial heating

Development of the gyrotrons exposes new possibilities of the potential technologies for industrial material processing [Edgcombe (1993)]. Microwave or millimeter wave heating is a kind of dielectric heating in which the radiations between the frequencies ranges from 300 MHz to 300 GHz are used [Kumar *et al.* (2012)]. The utilization of microwave has been taken on in the numerous industrial heating applications, like, rubber technology, ceramic sintering, chemical processing, composite fabrication, food processing, etc. In addition to the heating and sintering of the ceramics, the millimeter wave heating is used for surface hardening, drying, removal of the organic binders and moistures from the surface, growth of nanostructure ceramics, etc. [Idehara *et al.* (2006), Abe *et al.* (2005)]. Mostly gyrotrons of the frequency range 20 GHz to 35 GHz are used in the millimeter wave industrial applications [Bykov *et al*. (2004), Litvak *et al*. (2012)]. Microwave heating mechanism energy coupling directly depends on the frequency of the radiation. By taking this aspect into consideration, the low frequency gyrotrons are suitable for heating purpose.

1.4.3 Communication, Security and atmospheric science

The presence of narrow frequency band of atmospheric windows centered at 35 GHz and 95 GHz motivates the design and development of various RF sources used in the (millimeter wave radar) communication, security and the detection applications [Kumar *et al.* (2011), Liebe *et al.* (1989)]. The advantage of having small skin depth at

95 GHz frequency compared to the other commercial microwave frequencies like 2.45 GHz or 915 MHz [Kumar *et al.* (2012)], allows design RF source based active denial system (ADS) for security applications.

The radiation can reach upto $1/64^{th}$ inch in the human skin and create burning sensation. The blood vessels and nerve system are located beneath this skin depth and thus the radiation is not harmful. An Active Denial System (ADS) developed by Raytheon for the US Air Force Research Labs is a non-lethal, counter-personnel, directed energy weapon system which can be used against human targets at a distance beyond the effective range of small arms. The ADS launches a focused millimeter wave energy beam which induces unbearable heating sensation on an challenger's skin so that individual might be resisted without injury [Bratman *et al.* (2009), Kumar *et al.* (2012), LeVine *et al.* (2009)]. 95 GHz millimeter-wave radiation in the ADS also helps because of the natural atmospheric window at this frequency causing less atmospheric attenuation [Liebe *et al.* (2009), Neilson *et al.* (2009)]. This system can focus the 95 GHz millimeter wave effectually upto few kilometers. The 95 GHz gyrotron with the output power of 100 kW or more is an effective source of millimeter wave for ADS system [Hermitte *et al.* (1988)]. The radiation is non-ionizing and has small photonic energy to affect the cellular structure. Though, 95 GHz radiation creates some harmful effect on human eyes [Baird *et al.* (1986)]. The heating sensation of 95 GHz is intense but not burning because the heating sensation ends when the exposure to the radiation ends.

The facility of generation of high power at millimeter wave sources open the technological possibilities for the various kinds of atmospheric diagnosis such as measurement of humidity, turbulence structure determination, cloud monitoring, etc. 94

GHz radar system is used in the atmospheric diagnosis because of the natural atmospheric propagation window at this frequency [Mead *et al.* (1994)].

It was suggested by Manheimer Braz *et al.* (1997) that the gyrotron oscillator of 183 GHz can be effectively used in humidity detection because the water absorption rate is maximum at this frequency. The air turbulence is the major cause of air accidents. The radar system of 35 GHz as well as 94 GHz frequency can be used for air turbulence detection. The use of high power millimeter wave has also been proposed for the ozone conservation by the Wong *et al.* [Liao (2001)] and Askaryan *et al.* [Singh *et al.* (1998)]. The millimeter wave energy is capable to break the C-X bond, where X is the halogen in the upper part of the atmosphere. To paint the whole sky by the millimeter wave, thousands of gigawatt of RF energy would be required and thus hundreds of antenna station would be built on the earth. This is very expensive and huge geo-engineering project and still in research proposals.

1.4.4 Spectroscopy and medical science

One of the most significant properties of THz radiation also called submillimeter wave radiation (300 GHz to 3 THz) is its penetration through the several kinds of non-polar and non-conducting materials, like, papers, cloth, wood, etc. and can be used in the security systems [Litvak *et al.* (2012), Hornstein *et al.* (2005), Kartikeyan *et al.* (2007)]. The THz frequency fall in the spectral range of subatomic particle (like, electron spin system) and useful to characterize the materials via subatomic particles resonance [Bratman *et al.* (2009), Idehara *et al.* (2008)]. It is non-ionizing radiation (due to small energy of photon) and does not damage the tissues and DNA unlike X-ray. THz radiation shows unique spectral properties for several materials and used in the form of time domain spectroscopy [Bratman *et al.* (2009)]. In the medical science and structural biology, a THz radiation source emerged as a key component in the form of DNP /

NMR / ESR spectroscopy [Bratman *et al.* (2009), Kumar *et al.* (2011), Tatsukawa *et al.* (2005)]. The major areas of applications of THz gyrotrons are ESR and solid state NMR spectroscopy [Mehdi *et al.* (2004)].

Rather than the applications discussed above, the gyrotron is being explored for use in various new applications on the laboratory scale. Japanese groups are using gyrotron as a high power sources in the microwave rocket experiments [Piosczyk *et al.* (1996)]. G.S. Nusinovich has reported the radioactive material detection by using the THz gyrotron [Litvak *et al.* (2011)]. Gyrotrons are emerging as novel devices in various applications requiring high power RF sources.

1.5. Motivation and Objective

Observing the several advantages and emerging applications of the gyrotron oscillators over conventional microwave sources (i. e., slow-wave microwave tubes) as well as the possibilities of the stable high-power RF radiation in the millimetre and sub-millimetre wave regime, we focussed to pursue the our research in the gyrotron area. Considering the crucial role of gyrotrons in the area of, security domain as well as the spectroscopies, in the present work, we investigated the design studies of the gyrotrons that generates medium power level as well low power in the fixed and tunable frequency, respectively.

In addition, witnessing various advantages of radial output couplings of gyrotrons, like, enhancement of overall efficiency of the device, generation of practical low-loss Gaussian-like output beam modes and elimination of the long transmission line system; the design and analysis of the QOM launchers are also kept in the present research interest.

Since, the radiation of the RF energy results from the electron-beam and RF-wave interaction process which takes place in the interaction structure of the device which is a tapered cylindrical metallic cavity region. Due to finite electrical conductivity of the metallic walls of the cavity, there is ohmic losses that leads to thermo-mechanical effects on the cavity stricture and often cause structure deformations, if due care is not taken in its design. Since, the RF radiation is highly depends on cavity geometrical parameter and such ohmic losses will lead to degradation of the RF performance as well as shift in oscillation of the device. Hence its needs proper thermo-mechanical investigation and to mitigate the thermal issues, as required, an optimized cooling system has to be designed. Hence, the study of thermo-mechanical effects due to the RF power generation as well design of the optimized thermal system is essential to investigate for the gyrotron oscillators.

After the successful generation of RF power inside the device, its post-cavity subassembly, NLT section as well as the QOM launcher and RF Window transmit this RF power to the external RF transmission line. To achieve this process with minimum mode conversion and low attenuation losses; it is necessary to properly design and analyze performance of these components.

Time dependent multimode nonlinear analysis, as reported by Fliflet *et al.* (1991), is a widely accepted theory for observing the temporal growth of the RF power in the presence of various modes in the uniform section of the cylindrical cavity structure of gyrotrons. But, to guarantee the stable operation of the device, the after-cavity interactions are also need to observed. As well as the beam wave interactions under practical device considerations, like, velocity spread and the beam misalignments in the beam axis has not been explored using Fliflet *et al.* (1991) as of our knowledge.

The design of the nonlinear taper (NLT) section can be confirmed with the help of scattering matrix analysis in the structure by calculating the transmission and reflection coefficients versus frequency of the interaction cavity modes. A Commercially available CASCADE tool has been used for this purpose in general In addition, due to the irregularities in the dimpled mode launchers, the main interaction mode coming from the cavity is coupled to several modes and the optimized dimpled launcher results a Gaussian beam like mode on the launcher cut with a Gaussian content factor (GCF) of more than 99%. Now a days, people are using the commercially available LOT and SURF 3D tools from Calcabazas Creek Research, CA which is an expensive for the educational purpose. Hence, design and optimization of the QOM launchers through analysis is still a challenge.

Since, the determination of probable interaction cavity dimensions are determined from the cold cavity analysis by solving the single mode Vlasov approximation. As well, the parameters are optimized through beam wave interactions with the use of Gaussian field profiles in the case of single axial mode variation. Considering these two, we can design the NLT section by inspecting the field profile at the beam absent condition through the Vlasov approximation theory and the design in confirmed by incorporating calculated field profile in the beam wave interaction studies. As well, by developing a numerical code based on the coupled mode theories and using the wave equations in the launcher domain, the study of Denisov launchers are planned to be carried out.

1.6. Plan and Scope

Gyrotron oscillator is a well-established compact, stable and efficient fast-wave device, radiating high-power in the millimetre and sub millimetre frequency regime and

have numerous potential applications. In the present dissertation, its design methodology and analytical & simulation investigations of the single frequency as well as tunable frequency gyrotrons are planned to be carried out. Design studies of the gyrotrons using tapered cylindrical cavity type RF interaction structures operating for the single frequency, generating medium power level gyrotrons, operating in whispering gallery mode and volumetric mode are investigated. The device design methodology, RF and beam parameter selection, electron-beam and RF-wave interaction behaviour as well as thermo-mechanical performance are to be studied through rigorous analysis and to be verified through simulation studies.

For the first time, we have used single simulation tool for the gyrotron beam wave interaction and thermal studies. We have also suggested modified device design to mitigate the thermo-mechanical effect and its effect on the device RF performance are investigated. Followed by, the design and analysis of the post interaction cavity components, like, the nonlinear taper (NLT) section, quasi optical mode (QOM) launcher and the output RF windows for transmission of the generated power in the interaction cavity to the external transmission line are described. An afetrcavity interaction study for single frequency gyrotron oscillator is also carried by considering uniform axial DC magnetic field profiles. In addition, the design and frequency tuning studies of low power, tunable frequency gyrotrons for DNP enhanced NMR spectroscopies with electrical and magnetic tunings are described. Necessary steps required for the device parameters selection, tapered cavity RF interaction structure design of the tunable frequency gyrotrons are discussed. Further, the RF window used for the tunable frequency RF extraction is also presented.

In Chapter 1, with the introduction of gyro-devices evolution and literature review of high and low power gyrotrons operating in the single frequency and tunable

frequency, respectively. Operating principle, and sub-assemblies of the gyrotron oscillators are presented. Thereafter, various output couplings used in the gyrotrons and their advantages as well challenges are briefly described. The applications of various power level gyrotrons generating RF radiation at single and tunable frequency are discussed. The motivation of the present research and the organization of the thesis are drawn at the end of this chapter.

In Chapter 2, the post interaction components, i.e., quasi optical mode (QOM) converters that are responsible the radial coupling output for the device are investigated for its design and performance study. The basic theory and the design equations for the conventional Vlasov and Denisov types of QOM launcher are presented. The design parameters of the Vlasov launchers for the 95GHz, 100kW TE_{62} and $TE_{10,4}$ modes gyrotrons, a single frequency medium power level rating, to be presented in the Chapter 3 and 4 of this thesis are determined. Then observing the practical limitations and design considerations of Vlasov type converters, in the present work, Denisov type launchers are designed. A brief notes on the coupled mode theory used for the analysis of Denisov type launchers are also described. Usually, the QOM converters are designed and optimized by widely accepted commercial software's LOT and SURF3D developed Calabaza's Creek. Considering its unavailability with respect to cost with researcher, we developed our own numerical code in the Matlab domain based on the theoretical concepts. Developed code validation as well as the optimization of the Denisov's launchers for the $TE_{10,4}$, 95GHz 100kW by inspecting the mode variation profiles along the launcher section followed by wall field intensity profiles are described in this chapter. Further, the analysis and design of single disc type output RF windows for various type of operating modes, i. e., TE_{mn}, TM_{mn} and TEM_{00} are

discussed followed by the design of the RF windows for the proposed structure are presented.

In Chapter 3, design methodology, analysis and simulation of a tapered cylindrical cavity 100kW gyrotron oscillator operating in $TE_{6,2}$ at 95GHz is presented. The basic theory, design constraints, methodology and the analysis used for design of fixed frequency tapered interaction cavity are described. Non-linear, time dependent, multimode theory proposed by Fliflet *et al.* [1991] are used to develop indigenous code and used for the analysis of the designed gyrotron device. By investigating the electron-beam and RF-wave interaction behaviour using this analytical code is got verified by comparing the results with those obtained through PIC simulation reconfiguring a Commercial PIC code "CST Studio Suite". The device design is further optimized at a uniform axial DC magnetic field profile. The device performance is further investigated under practical considerations, namely, velocity spread and beam misalignments. The thermo-mechanical analysis of the designed RF cavity structure is also carried out. Also, the design of an optimized cooling system is presented and the system performance got verified through simulation using "COMSOL Multiphysics" commercial code.

Considering the challenges and issues related to deformations and misalignments caused due to thermo-mechanical effect, in Chapter 4, we designed, analyzed and simulated the same rating gyrotron device (100kW, $TE_{6,2}$ mode, 95GHz) as discussed in Chapter 3 is now proposed to investigate while working at a relatively higher order mode $TE_{10,4}$. which would allow a larger transverse dimensions thereby more relaxation regarding thermal issues as well as it could also be upgraded to higher power levels too. After the RF interaction cavity structure design, to ensure stable device operation, the beam wave interaction studies of the cavity structure by adding a raised cosine type non-linear taper (NLT) is carried-out for an axial uniform DC

magnetic profile. Since, the time dependent multimode analysis is used so far considering the uniform section of the cavity with ideal gaussian type field profile. In the present work, we have now extended studies till NLT end section by incorporating the actual field profiles calculated by solving the Vlasov approximation equation to the combined RF cavity and NLT geometry. The beam wave interaction studies, as well as the effect of beam misalignments on the beam coupling to the TE_{mn} mode and the effect off offset in the beam axis with respect to the cavity axis are studies. Instead of performing the thermo-mechanical behaviour simulation using a now code, COMSOL Multiphysics, for the present case, the thermo-mechanical analysis is also simulated using the same code used for beam-wave interaction simulation. For the first time we have used a single commercial code "CST Studio Suite" and its Steady state thermal solver as well Mechanical solver tool sucessfully applied for the gyrotron.

In Chapter 5, the design and analysis of low power tunable gyrotrons for the DNP enhanced NMR applications are presented. Various tuning techniques used in gyrotrons are discussed. In the present work, we have described the design methodology and designed an RF interaction structure that is able to generate a minimum RF power of 20W over a band of 2.4GHz for $TE_{5,3}$, 263GHz gyrotron for the 400MHz DNP NMR spectroscopy applications. Here also, by allowing the actual field profiles calculated for the RF interaction cavity geometry from the Vlasov approximation for the high order axial modes, the time dependent multimode analysis is carried out at several beam currents via electrical and magnetic tunings and the RF power output are described. Then considering a SiO_2, as window material, the design of single disc type RF window is also presented.

With acquired knowledge from Chapter 5, that longer integration cavities lower the start oscillation current of mode excitation as well as it also allows the excitation of

high order axial modes. In Chapter 6, an experimentally demonstrated low power tunable gyrotron operating in $TE_{0,3}$ at 140 GHz, is revisited and the reported RF interaction cavity tailored such that excitation of the higher order mode via magnetic tuning leads to device frequency tunability. The enhancement in the tuning bandwidth of modified device is also demonstrated.

In the last chapter, Chapter 7, the work embodied in the present thesis are summarized and the significant conclusions are drawn from the major findings. The limitations of the present study are discussed pointing out the scope for the future work.

--- XXX ---

CHAPTER 2

ANALYSIS AND DESIGN OF THE QUASI-OPTICAL MODE LAUNCHERS AND RF WINDOW FOR GYROTRON

2.1. Introduction

One of the main advantages of the gyrotron oscillators is ability to operate the device in the higher order TE_{mnq} modes, thereby accruing the advantages of wide transverse dimension and generation of higher power levels at the high frequencies. However, the higher order mode interaction is not suitable due to long path transmission, plasma heating, etc. For the effective transport and controlled heating, the radiation must be converted to suitable low order waveguide modes TE_{0n}, linearly polarized HE_{11} mode, Gaussian modes in free space i.e., TEM_{00}.

Conversion of higher order modes using conventional waveguide converters is complex and lossy due to several stages of intermediated mode conversion are involved that leads longer transmission lines as well generation of the unwanted modes. In addition, these conventional mode converters are external to the device that makes the design of the collector complex; since it has to collect the spent electron beam as well as to guide the generated RF power to RF window through it. Hence, the overall efficiency of the device limited in case of high order interaction cavity modes which can be improved. This limitation causes the incorporation of axial output coupling, discussed in the Chapter 1.

In 1975, Vlasov *et al.* proposed a novel mode conversion technique that uses an internal waveguide section followed by a cut and a group of curved mirrors for the conversion of interaction mode into a small, Gaussian focused free space mode TEM_{00}. The component collectively called as quasi optical mode converter.

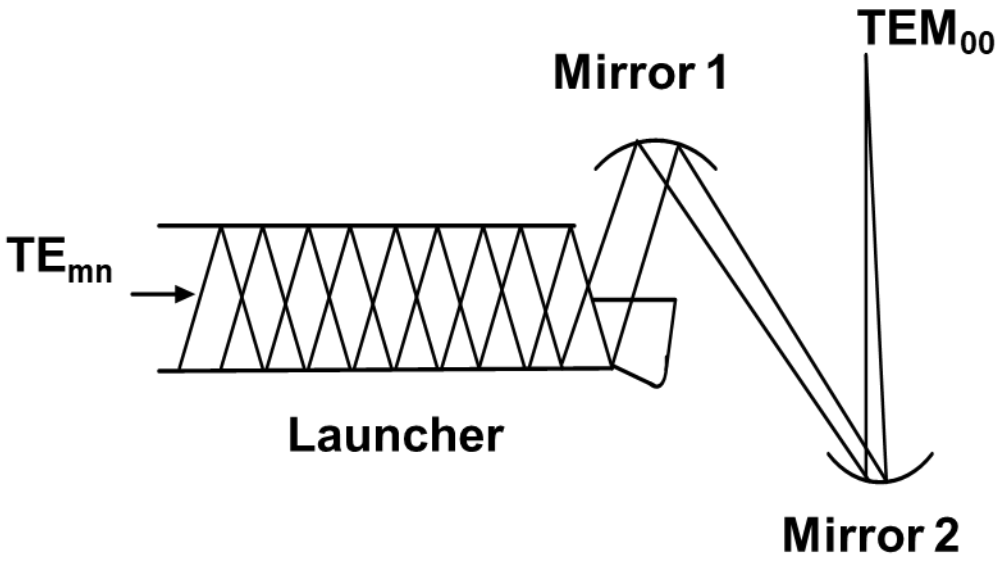

Figure 2.1: A schematic view of quasi optical mode converter system.

A Schematic view of conventional QOM Converter as shown in Figure 2.1, consists of two sections, the prime section is a Launcher, a kind of cylindrical waveguide followed by a spiral cut at its end used for launching the interaction cavity modes as a paraxial beam of radiation, and the subsequent section is mirror system used for beam focussing and shaping the launched beam into a beam of desired characteristics at the output RF window.

There are basically two types of converters which are differentiated based on the type of launcher profile, namely, Vlasov type converter, is the basic and fundamental quasi optical mode converter presented by Vlasov *et al.* and Denisov type is a modified Vlasov type converter and presented by Denisov *et al.*

Due to compactness of QOM converter over conventional mode converters, permits the incorporation of mode converter in the device and allows the separation of RF wave towards RF window and electron beam towards collector thereby

improvement of the overall efficiency of the device by depressed collector technique. An experimental investigations of the original device in which the transformation of $TE_{10,1}$ cylindrical waveguide mode to a narrow beam in free space mode was achieved with a modest power transfer efficiency of 80% using the Vlasov converter [Vlasov *et al.* (1975)].

The fundamental designs of the launcher and reflector, proposed by Vlasov *et al.* in 1975, are rooted in the geometric optics approximation. Using this theory, the propagation of the TE_{mn} mode is represented into group of rays and thereby calculation of the launcher parameters for the suitable radiation into mirrors. As well using, a rigorous vector diffraction theory was developed to calculate the radiated fields onto mirrors as well optimization of reflector/mirror surface parameters has done by the determination of Stratton Chu integrals.

Considering the conversion efficiency and the practical issues with mirror surface designs for high order TE_{mn} modes, in 1992, Denisov *et al.* proposed *a pre-bunching or pre-shaping or dimpled or rippled or Denisov converter* by modifying the launcher section of the Vlasov converters. By allowing a very small irregularities (far less than the mean radius of the launcher) on the launcher walls, the cylindrical waveguide mode coming from the cavity section is couples its power to several modes whose modes mixture gives an almost a small and Gaussian focussed beam at the launcher itself. Hence, it allows the beam shaping and focussing issues of mirrors simple and reduces the losses in the launcher section thereby more conversion efficiency.

The rippled wall waveguide is usually optimized using coupled mode theory, and the analysis used for it is described in the following sections. Various theories that

help for design, analysis of Vlasov and Denisov launchers and mirror sections are reported in the literature. AS well Launcher Optimization Tool (LOT) and SURF3D tools by J Neilson Calabazas Creek Res., Saratoga, CA, USA l [2004] are the computer codes been developed for analysis and optimization of QO launchers used in high power gyrotrons and are commercially available.

Accompanied by mode conversion, the inclusions of QOMC give numerous advantages and are follows:

I. Incorporation of depressed collector technique thereby increase in the overall efficiency of the device

II. Collection of radial output coupling, that makes collector design exclusively.

III. Reliability and protection of the device from the back propagation of RF by Vacuum RF window.

IV. Directly connect to the transmission line and reduces large dimensional transmission line system.

In the present work, with the help of the geometric optics and the coupled mode theory, the launchers used for the mode conversion of 95GHz 100kW gyrotron operating in high order $TE_{10,4}$- mode is designed and design and analysis of RF structures described in Chapter 4 of this thesis. The launchers are studied using coupled mode theory however its mirror section design is not kept within the scope of the work embodied in the present thesis. As well followed by QOMC, an RF window which is responsible for the transmission of generated power in the RF device to the transmission line is designed for the various popular window materials. Even though, the mirror is not designed here, since the design of RF window mainly dependents on the window

disc thickness and the dielectric properties of the material, using the available literature, the RF window design is attempted for a few window materials, as a tutorial exercise.

Chapter 2 is organized as follows: Starts with the importance of the quasi-optical mode converters, the analysis used for the design of Vlasov launcher is presented. Then the coupled mode theory is used for the design of the dimpled wall launcher and the theory required for the calculations of mode contents in various modes along with theory used for wall field intensities is presented briefly. Followed by the design and analysis of the Denisov launchers for $TE_{10,4}$ mode for 95GHz, 100kW is discussed. Then, the analysis and design of the RF window for the present gyrotron designs reported in the Chapters to follow are presented.

2.2. Vlasov Type Mode Launcher

For the design and analysis of quasi optical mode converters, the study of wave propagation inside an overmoded waveguide are explored by using a ray model (Fig. 2.2) that results from geometrical optics theory. We give a summary of the geometric optical parameters, a more detailed derivation can be found in [Drumm (2002), Michel (1998), and Wien 1995].

2.2.1. Geometric-optical field representation in cylindrical waveguides

We can use the scalar potential from equation to describe the wave propagation. By separating the Bessel function in into the Hankel functions of first and second kind with order *m*, we represent the standing wave in radial direction with two traveling waves.

$$J_m(x)=\frac{1}{2}\left(H_m^1(x)+H_m^2(x)\right), \tag{2.1}$$

$$\psi=\psi^{(1)}+\psi^{(2)}=\frac{1}{2}\left[H_m^{(1)}\left(k_\rho\rho\right)+H_m^{(2)}\left(k_\rho\rho\right)\right]e^{\mp jm\varphi}\,e^{\mp jk_z z}\ . \tag{2.2}$$

Furthermore, we take an adapted form of the approximation from [Morse *et al.* (1953)] for the two Hankel functions, that is valid for $x = \chi_{mn} > m$ and large arguments x and hence valid on the waveguide wall:

$$H_m^{(1),(2)}(x) \approx \sqrt{\frac{2}{\pi\sqrt{x^2 - m^2}}}\, e^{\pm j\left(\sqrt{x^2-m^2} - m.\cos^{-1}\left(\frac{m}{x}\right) - \frac{\pi}{4}\right)}, \tag{2.3}$$

where the upper sign belongs to superscript (1) and the lower sign belongs to superscript (2).

By using,

$$H_m^{(1)}(x) = \left(H_m^{(2)}(x)\right)^* . \tag{2.4}$$

If we now take the gradient of the phase function of the radially outgoing wave (2) and use (2.3), we get an equation that is similar to the Eikonal equation found in [Born et al. (2009)]. This gradient vector $\vec{R}$ is perpendicular to the phase front and represents the direction of the rays. For a wave propagating in positive *z*-direction and in positive φ-direction this results in:

$$\begin{aligned} \vec{R} &= \nabla\left(\arg\left(\psi^2(R_0, \varphi, z)\right)\right) \\ &= \nabla\left(-\sqrt{(k_\rho \rho)^2 - m^2} + m\cos^{-1}\left(\frac{m}{k_\rho \rho}\right) + \frac{\pi}{4} - m\varphi - k_z z\right)\Bigg|_{k_\rho \rho = \chi'_{mn}} \end{aligned} \tag{2.5}$$

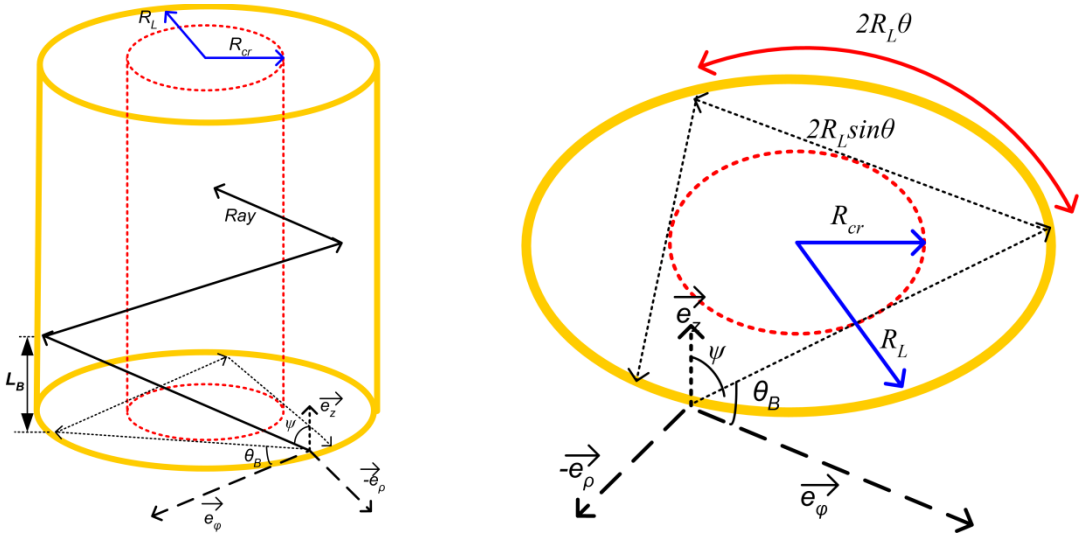

(a) (b)

Figure 2.2: Geometric optical description of a wave beam in a cylindrical waveguide (a) Side view; (b) top view.

Considering figure 2.2 and projecting this ray $\vec{R}$ onto $\vec{e}_z$, we get the so-called Brillouin angle, θ_B:

$$\cos\theta_B = \frac{k_z}{k} \quad . \tag{2.6}$$

The wave-number along the ray $\vec{R}$ is the free space wavenumber k. The distance the ray $\vec{R}$ travels in z-direction is called Brillouin length L_B shown in the left part of figure 2.2. This distance can be calculated from the TE mode's parameters as follows

$$L_B = 2R_0 \sin\alpha \cot\theta_B \quad . \tag{2.7}$$

The projection in the transverse plane onto $\vec{e}_\varphi$ yields the spread angle α as

$$\cos\alpha = \frac{m}{\chi_{mn}} = \frac{R_{cr}}{R_0} \quad , \tag{2.8}$$

where R_{cr} is the so called caustic radius [Weinstein (1969)] and the corresponding distance travelled in transverse direction, L_{trans} is defined a

$$L_{trans} = 2R_0 \sin\alpha \tag{2.9}$$

Along the circumference of the waveguide this length corresponds to:

$$L_{\varphi} = 2R_0\,\alpha \tag{2.10}$$

The wave propagation can be described as follows: An outgoing ray represented by (2) traveling towards the waveguide wall gets reflected from the metal surface and transforms into an ingoing ray represented by (1). The ingoing ray experiences a phase jump, when reaching the caustic at R_{cr}. This can be regarded as "transformation" of the ingoing ray into the outgoing ray, then the ray gets reflected again and so on. In this way the ray travels forward through the waveguide. To describe the whole field, we have to consider all rays traveling inside the waveguide.

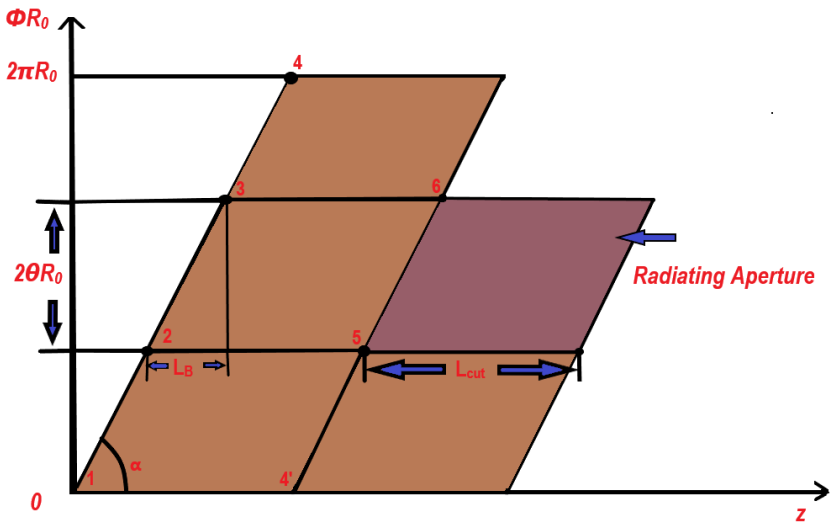

Figure 2.3: The unrolled waveguide surface at a constant radius R_0 and the Vlasov launcher cuts are highlighted.

Figure 2.3 shows the unrolled waveguide surface at a constant radius R_0. Here, we can see that all rays starting on the same helical line end on that line. So the ray

starting at point 1 travels to point 2, then to point 3, then to point $4 \equiv 4'$ and so on. It can be shown [Wien (1995)], that all rays touch the area contained within the parallelogram 2, 3, 5, 6, with size $L_{cut} \times 2\alpha R_0$ once. This area is called Brillouin zone. If we cut the waveguide open at a constant angle of ’ with length L_C, we radiate all rays as was stated before and therefore radiate all electromagnetic energy from the waveguide. As can be seen from [Wien (1995)], the cut length of a waveguide antenna in order to radiate all rays can be calculated as

$$\begin{aligned} L_{cut} &= \frac{2\pi R_0}{\tan\tau} \\ &= 2\pi R_0 \frac{\sin\alpha}{\alpha} \cot\theta_B \end{aligned} \tag{2.11}$$

with

$$\tan\tau = \frac{2R_0\,\theta_B}{L_B}\ . \tag{2.12}$$

The waveguide antenna with this type of cut achieves the separation of the electron beam from the electromagnetic wave. Thus the design of the collector of the gyrotron can be made independent of the RF output system, which is important when going to megawatt power levels.

In the geometrical optic limit, the flow of energy in a cylindrical waveguide mode can be represented by a set of rays travelling tangent to a caustic surface with an azimuthal bounce angle, α and a helical pitch angle, θ_B.

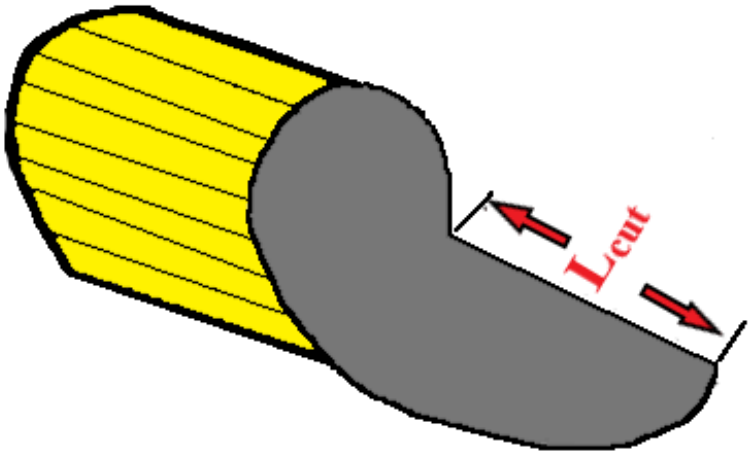

Figure 2.4: Vlasov launcher with a spiral cut of length L_{cut}.

The Stratton Chu vector diffraction theory was used to calculate the near field pattern on a plane perpendicular to the propagation direction of the launched beam. This near field pattern is determined by using the aperture fields calculated by the coupled mode theory, as the source terms in the Stratton Chu formula.

In the present Chapter, the design and analysis of converters are limited to the launcher sections only. The design and analysis of the launcher parameters for the case of single frequency gyrotron operating at 95GHz $TE_{10,4}$- mode for 100kW gyrotrons are done. In the following section, the Vlasov launcher design parameters for the current gyrotron are calculated with the help of above theories.

2.2.2. Calculations of Vlasov Launcher parameters

A Vlasov type converter is generally used for the whispering gallery interaction mode case where the radial variations of the field are upto 2. Even the role of the reflector section is very huge in this case for the beam shaping and conditioning towards the desirable beam generation. For whispering gallery modes the Vlasov type converter with a geometric optics reflector design is practical and can achieve conversion efficiencies in excess of 80%.

In the present work, the gyrotron designs are performed for TE_{62}, 95GHz, 100kW as well $TE_{10,4}$, 95GHz, 100kW which are discussed in Chapters 3 and 4, respectively. As well a low power tunable gyrotron operating in $TE_{5,3q}$ at 263 GHz presented in Chapter 6. The Vlasov launcher parameters are evaluated from the above theory and the parameters are tabulated in the Table 2.1. The dimensions of the Vlasov type launcher for the high power gyrotrons considered in the present work are tabulated in the following table.

Table 2.1: Vlasov launcher parameters

Parameter	**$TE_{6,2}$**	**$TE_{10,4}$**
Launcher radius (mm)	10	13.134
Bounce length L_B (mm)	36.1395	10.913
Bounce angle θ_B (^{o})	36.1395	65.3932
Minimum Launcher Cut length L_{cut}(mm)	71.363	30.154
Caustic radius R_{cr}(mm)	5.113	5.528
Azimuthal expansion angle 2α (^{0})	118.4955	130.2186

With the above launcher parameters the TE_{mn} mode coming from the interaction cavity is radiated as a paraxial beam on to the mirror section by providing the Vlasov cut of length L_{cut} with a azimuthal expansion angle of α. Then launched beam is guided and focussed by using the reflector section that subtend a minimum of 2α degrees, for the better conversion and focussing. In the present work, we limited our study upto launcher dimension only, not for the reflector part.

It is observed that Vlasov type converter has inherent properties that make it undesirable for converting certain classes of modes. Since the reflector must subtend a minimum of 2α degrees, the mirror for volume mode Vlasov type converters is large. Another limitation is the substantial diffraction from the Vlasov type launcher. Since,

the strong field near the cut leads larger diffraction losses and hence lowers the conversion efficiency. Even though, this smooth wall type launcher is suitable for whispering gallery mode ($m > n, n = 1, 2$), but considering the larger reflector dimensions as well lower conversion efficiency, the research has been shifted/focuses for the modified Vlasov launcher that can deliver a better conversion efficiency as well minimum diffraction losses. The modified launcher design and analysis are discussed in the following section.

2.3. Denisov Launchers

As discussed, in the Vlasov type converter, the fields are needed to radiate from the cut for the beam shaping and propagation towards reflector surfaces. But the strong fields near the cut leads severe diffraction losses and results a limited mode conversion thereby degradation of the efficiency and so not suitable for higher power sources where the efficiency matters. In addition, the requirement of the reflector surface increased as the bounce angle of the beam increases that leads the complexity and large dimensional surfaces that makes the realisation impractical. Thus, Vlasov launchers find limited use as well not potential for the conversion of high order volumetric modes. The fields along the helical cut and straight edges are very strong in Vlasov converter and that leads to strong diffraction losses there by reduction in the overall efficiency. One key idea to increase the conversion efficiency as well some decrement in the reflector dimensions is by modifying or reshaping the mode into desired mode before radiating from the cute that has very low field nearby cut in the launcher itself. Later on, by using reflector section, the radiated beam is shaped into desired form. In 1992, Denisov have proposed a technique to reduce the fields along the helical and straight cut edges by deforming the waveguide walls. The deformations of the waveguide walls allow the

coupling of the main mode energy into several modes and the interference of these modes on the launcher walls allows Gaussian bundles mixture formation since the Gaussian bundles have less or almost no fields at the edges of Brillouin regions and causes less or no diffraction achieves maximum conversion efficiency.

An ideal TE_{mn} mode converted into a perfect Gaussian beam mode through a profiled launcher by allowing the mixture of several modes in desired proportions of power as tabulated in the Table 2.2 at the launcher end.

Table 2.2: Ideal proportions of satellite mode mixture of a dimpled launcher

$TE_{m+2,n-1}$ (3%)	$TE_{m+3,n-1}$ (11%)	$TE_{m+4,n-1}$ (3%)
$TE_{m-1,n}$ (11%)	**$TE_{m,n}$ (44%)**	$TE_{m+1,n}$ (11%)
$TE_{m-4,n+1}$ (3%)	$TE_{m-3,n+1}$ (11%)	$TE_{m-2,n+1}$ (3%)

The interference of the nine wave guide modes creates an RF field bunching in the longitudinal and azimuthal directions. Selection of these modes are depends on the caustic radii, interference length of modes close to the cut length L_{cut} and similar Bessel zeros close to the interaction cavity mode $TE_{m,n}$.

Followings are the most common used Denisov launcher profiles for the reshaping of the cavity mode into Gaussian beam mode in the launcher itself.

$$R(\phi, z) = R_0 + \alpha_L z + \delta_1(z)\cos(\Delta\beta_1 z - L_1\phi) + \delta_2(z)\cos(\Delta\beta_2 z - L_2\phi) \tag{2.13}$$

$$R(\phi, z) = R_0 + \alpha_L z + \delta_1(z)\cos(\Delta\beta_1 z + L_1\phi) + \delta_2(z)\cos(\Delta\beta_2 z + L_2\phi) \tag{2.14}$$

$$R(\phi, z) = R_0 + \alpha_L z + \delta_1(z)\sin(\Delta\beta_1 z - L_1\phi) + \delta_2(z)\sin(\Delta\beta_2 z - L_2\phi)\,. \tag{2.15}$$

Here the parameters $\Delta\beta_{1,2}$ and $L_{1,2}$ are dependents on the selection satellite modes that are responsible for the Gaussian mode formation by azimuthal and radial bunching of the modes [Kartikeyan *et al.* (2004)]. Values of $\alpha, \delta_1(z), \delta_2(z)$ are chosen such that the desired proportions of couplings between the modes are achieved with minimum lengths and α_L is the small taper angle added to the radius of the launcher profile to avoid counterfeit oscillations in the launcher.

The overall bunching of Gaussian beam formed by superposition of azimuthal bunching , caused by the satellite modes that have equal caustic radii (R_{cr}) and similar Bessel zeros (χ_{mn}) and longitudinal bunching by the satellite modes that have equal caustic radii (R_{cr}) and an interference length close to the Launcher cut length L_{cut}, along the launcher section. L_1 and L_2 are the differences in the azimuthal indices of the main and satellite modes [Blank (1994)].

Practically, it is difficult to achieve the above said mode mixture with accuracy, but keeping it as our target, the profile has been optimized such that it results a Gaussian content at the cut of more than 99%. The theory required for mode variations and calculations of Gaussian content factor due to a dimpled mode waveguide sections are discussed below.

The parameters of several Denisov launcher profiles used and implemented in the literature are mentioned in Table 2.3 [Flamm (2012)].

Table 2.3: Various dimpled profiles [Flamm (2012), Blank (1994)]

f (GHz), mode	R_0/L (mm)	α_L	Type	L_1/L_2	$\delta_1(z)$,mm	$\delta_2(z)$,mm
118, $TE_{22,6}$	20/200	2e-3	2.13	1/3	$\begin{cases} 0\,to\,0.05, & 0<z<10 \\ 0.05, & 10<z<80 \\ 0.05\,to\,0, & 80<z<90 \\ 0, & else \end{cases}$	$\begin{cases} 0\,to\,0.05, & 10<z<20 \\ 0.05, & 20<z<90 \\ 0.05\ to\,0, & 90<z<100 \\ 0, & else \end{cases}$
110, $TE_{22,6}$	20/152	0	2.14	1/3	0.0399	0.0399
140, $TE_{28,8}$	21.9/250	4e-3	2.13	1/3	$\begin{cases} 0\,to\,0.041, & 0<z<10 \\ 0.041, & 10<z<60 \\ 0.05\,to\,0, & 60<z<70 \\ 0, & else \end{cases}$	$\begin{cases} 0\,to\,0.041, & 17<z<27 \\ 0.041, & 27<z<77 \\ 0.041\,to\ 0, & 77<z<87 \\ 0, & else \end{cases}$

2.3.1. Analysis of the dimpled launcher

Since the launcher waveguide walls have deformations that allow the coupling between modes, so cannot represent the energy through one normal mode. The study of coupling of energy between modes in these waveguides can be handled well with the help of coupled mode theory which gives the variations of the modes along the direction of the propagation. It is the goal of the pre bunching waveguide section to improve the radiation characteristics of the launched beam by illuminating the launching region (B') with a Gaussian ray distribution rather than a uniform distribution. The fields radiated into free space are coming from the Brillouin region just before the Brillouin region removed for launching the beam. Radiating aperture is the portion of the waveguide that is responsible for launching the beam. Hence, with the help of fields on the

Brillouin region just before the cut, the radiated fields at an observation point can be studied. Hence, in the study of the launchers, need to achieve good Gaussian content factors at two successive Brillouin regions for efficient conversion.

Hence, now days almost all the gyrotron device incorporate Denisov type converter as an internal part considering high order operating mods as well requirement of no power loss in the mode conversion.

Generally, the profile of Denisov launcher is a deformed one. Since the wall shapes are changing continuously, the fields in the waveguide cannot be represented through one normal mode and the deformations allows coupling of energy between different normal modes of the waveguide. This peculiar situation can be handled with the help of coupled mode theory which calculates the coupling coefficients of mode due to deformations in the structure. Coupled mode theory tells the coupling among the modes due to variations in the structure. If the amount of perturbation is very small compared to the mean radius of the waveguide, then can neglect the backward wave propagation.

In general, the coupling between forward travelling modes are given by the following expressions:

$$\frac{dA_i^+}{dz} = -ik_{zi}A_i^+ + \sum_u c_{iu}A_u^+ + \sum_v c_{iv}A_v^+, \tag{2.16}$$

$$\frac{dA_j^+}{dz} = -ik_{zj}A_j^+ + \sum_u c_{ju}A_u^+ + \sum_v c_{jv}A_v^+, \tag{2.17}$$

where the subscripts i and u deals for TE modes and the subscripts j and v for TM modes. A is the complex amplitude of the mode. For weak waveguide deformations of

the form $R(\phi, z) = R_0 + \delta(\phi, z)$ previously reported methods [Blank *et al.* (1994)] can be used determine the coupling coefficients for mild perturbations. The coupling coefficients, c_{iu}, c_{iv}, c_{ju}, and c_{jv} can be represented as follows:

$$c_{iu} = \frac{1}{2}\left[Q_{iu} \frac{\omega\mu}{\sqrt{k_{zi} k_{zu}}} + R_{iu} \sqrt{\frac{k_{zu}}{k_{zi}}} \right], \tag{2.18}$$

$$c_{iv} = \frac{1}{2} S_{iv} \frac{\omega}{c\sqrt{k_{zi} k_{zv}}} \ , \tag{2.19}$$

$$c_{ju} = \frac{1}{2}\left[T_{ju} c \sqrt{\frac{k_{zj}}{k_{zu}}} + U_{ju} \frac{1}{c} \sqrt{\frac{k_{zu}}{k_{zj}}} + V_{ju} \frac{c}{\omega} \sqrt{k_{zj} k_{zu}} \right] \ , \tag{2.20}$$

and

$$c_{jv} = \frac{1}{2}\left[W_{jv} \sqrt{\frac{k_{zj}}{k_{zv}}} + X_{jv} \frac{\omega\varepsilon}{\sqrt{k_{zj} k_{zv}}} \right] . \tag{2.21}$$

The term c_{mn} gives the coupling coefficient from the n^{th} mode of, TE or TM type to m^{th} mode of TE or TM type.

For a small amplitude perturbation of first order, $\delta(\phi, z)$, the eight unknowns in coupling coefficient expressions, (2.18) to (2.21) can studied with the help of [Doane (1985), Doane (1986) and Garin *et al.* (1987)]. Here, considering , the subscripts *i, u, j*, and *v*, refer to mode *i, u, j,* and *v*, where mode *i* is the $TE_{m_1 n_1}$, mode *u* is the $TE_{m_2 p_2}$, mode *i* is the $TM_{m_1' p_1'}$ and mode *v* is the $TM_{m_2' n_2'}$. The unknowns in equations. (2.18) to (2.21) are determined from the following expressions:

$$Q_{iu} = \frac{i\left(\frac{\nu_{m_2 p_2}}{R_0}\right)^2}{R_0 \pi \omega \mu \sqrt{\nu_{m_2 p_2}^2 - m_2^2}} \int_0^{2\pi} \left[\frac{i m_1 e^{i m_1 \phi}}{\sqrt{\nu_{m_1 p_1}^2 - m_1^2}} \frac{\partial \delta(\phi, z)}{\partial \phi} + \delta(\phi, z) e^{i m_1 \phi} \sqrt{\nu_{m_1 p_1}^2 - m_1^2} \right] e^{-i m_2 \phi} d\phi \tag{2.22}$$

$$R_{iu} = \frac{m_1 m_2}{R_0 \pi \sqrt{\nu_{m_1 p_1}^2 - m_1^2} \sqrt{\nu_{m_2 p_2}^2 - m_2^2}} \int_0^{2\pi} e^{i m_1 \phi} e^{-i m_2 \phi} \frac{\partial \delta(\phi, z)}{\partial z} d\phi \tag{2.23}$$

$$S_{iv} = \frac{i m_1}{R_0 \pi \sqrt{\nu_{m_1 p_1}^2 - m_1^2}} \int_0^{2\pi} e^{i m_1 \phi} e^{-i m_2^l \phi} \frac{\partial \delta(\phi, z)}{\partial z} d\phi \tag{2.24}$$

$$T_{ju} = \frac{i\left(\frac{\nu_{m_2 p_2}}{R_0}\right)^2}{R_0 \pi \omega \mu \sqrt{\nu_{m_2 p_2}^2 - m_2^2}} \int_0^{2\pi} \left[e^{i m_1^l \phi} \frac{\partial \delta(\phi, z)}{\partial \phi} + i m_1^1 e^{i m_1 \phi} \delta(\phi, z) \right] e^{-i m_2 \phi} d\phi \tag{2.25}$$

$$U_{ju} = \frac{m_2}{R_0 \pi \omega \varepsilon \sqrt{\nu_{m_2 p_2}^2 - m_2^2}} \left(\frac{\mu_{m_1^1 p_1^1}}{R_0} \right) \int_0^{2\pi} e^{i m_1^l \phi} e^{-i m_2 \phi} \delta(\phi, z) d\phi \tag{2.26}$$

$$V_{ju} = \frac{-i m_2}{R_0 \pi \sqrt{\nu_{m_2 p_2}^2 - m_2^2}} \int_0^{2\pi} e^{i m_1^l \phi} e^{-i m_2 \phi} \frac{\partial \delta(\phi, z)}{\partial z} d\phi \tag{2.27}$$

$$W_{jv} = \frac{1}{R_0 \pi} \int_0^{2\pi} e^{i m_1^l \phi} e^{-i m_2^1 \phi} \frac{\partial \delta(\phi, z)}{\partial z} d\phi \tag{2.28}$$

$$X_{jv} = \frac{i}{R_0 \pi \omega \varepsilon} \left(\frac{\mu_{m_1^1 p_1^1}}{R_0} \right) \int_0^{2\pi} e^{i m_1^l \phi} e^{-i m_2^l \phi} \delta(\phi, z) d\phi \tag{2.29}$$

Here R_0 is the mean radius of the waveguide, μ_{mp} and ν_{mp} are the p^{th} zero of $J_m(x)$ and $J_m^1(x)$, respectively.

The set of equations from 2.16 -2.29, gives the complete study of mode coupling caused by the irregularities whose amplitudes are of the order $\delta << R_0$ successfully. Though, in the gyrotrons the oscillation of TM_{mn} modes are not feasible in the interaction as well considering the amount of dimples, only coupling between TEmn are happens. Hence, using equation 2.16, 2.18, 2.22, and 2.23 together, the mode variations along the dimpled launcher can be determined successfully.

Observing the mode variation profiles the probable set of dimple launcher can be selected and will be confirmed by calculating the correlation coefficient of the Gaussian content of the wall field intensity near cut. The necessary theories are presented below.

2.3.2. Calculation of waveguide field components

The energy in the waveguide cannot sufficiently represent by single normal mode field components if the waveguide walls are changing continuously, i. e., nonuniform waveguide. Because of non-uniformity, there is always coupling of energy among several modes. If the amount of perturbations are mild, i. e., very small compared to mean radius of the waveguide, then the coupling between different kind of modes can be neglected, i. e., between TE and TM modes. Since, our Denisov type converter is used as an internal component of the gyrotrons which generates power in the TE_{mp} cavity modes. Hence, the calculation of TM mode effects is irrelevant here. Because of small non-uniformities, the overall field components can be calculated as a superposition of the forward travelling modes which assume propagate in the waveguide. The overall E and H fields in deformed waveguide walls are calculated with the following expression [Zhang *et al.* (2015)]:

$$H = \sum_i A_i^+(z)\, h_i\, e^{-j\int_0^z \beta_i z^1 dz}, \tag{2.30}$$

$$E = \sum_i A_i^+(z)\, e_i\, e^{-j\int_0^z \beta_i z^1 dz}, \tag{2.31}$$

and,
$$\iint_s e_i \times h_j \, ds = \pm\delta_{ij}, \tag{2.32}$$

where A_i^+ amplitude of the TE_{mp}, and it carries attenuation term with it but does not have the oscillation term. e_i and h_j are the orthogonal fields in the circle waveguide, s is the cross section and δ_{ij} is Dirac's delta function. And the term $e^{-j\int_0^z \beta_i z^1 dz}$ is the oscillation term and it is z dependent because the waveguide radius under consideration is varying with the z.

When the amplitude of the deformation is very smaller compared to mean radius of the waveguide, the TE_{mn} components in the circular waveguide for right hand rotating wave can be written as:

$$T_i = \frac{k}{\sqrt{\pi\beta_m}\sqrt{\chi_{mp}^2 - m^2 J_m(\chi_{mp})}} J_m\left(\frac{\chi_{mp} r}{R_0}\right) e^{-im\phi}. \tag{2.33}$$

Here k is free space wavenumber, r and φ are the radial and azimuthal coordinates, R_0 is the mean waveguide radius, β_m is the transverse wavenumber, χ_{mp} is the n^{th} root of the Bessel function, $J_m^l(\chi_{mp}) = 0$. With the help of T_i, the orthogonal fields can be expressed as follows:

$$e_i = \sqrt{\frac{\mu\omega}{\beta}}\left(\frac{1}{r}\frac{\partial T}{\partial \phi}\, a_r + \frac{\partial T}{\partial r} a_\phi\right), \tag{2.34}$$

$$h_i = \sqrt{\frac{\beta_m}{\mu\omega}}\left(\frac{\partial T_i}{\partial r} a_r + \frac{1}{r}\frac{\partial T_i}{\partial \phi} a_\phi + j\frac{\chi_{mp} m^2 T_i}{k^2 R_0^2} a_z\right). \tag{2.35}$$

Here a_r, a_φ, and a_z are the orthogonal unit vectors in radial, azimuthal and axial directions. With the help of equations (2.30) to (2.35), the fields on the deformed waveguide walls can be determined if the amplitudes of the modes are known. Hence, by the combination of coupled mode theory and super position concepts, the mode variation profiles along the axial direction as well as the field components of the deformed waveguide walls can be studied.

The following section is dedicated to the derivation of the required theory, necessary to describe the wave propagation in launchers.

Since the goal is to radiate the electromagnetic wave from the waveguide cut in the form of a Gaussian beam (Section 2.2), we need to obtain a mixture of different modes to form the Gaussian field profile. Consequently the electromagnetic wave will not consist of one single electromagnetic mode, but a linear combination of different modes. This can be achieved by summing over the azimuthal indices m and integrating over the longitudinal wave numbers k_z, see [Harrington (1961)]:

$$\psi(\rho,\varphi,z)=\sum_m \int_{k_z} A_{mn}(k_z)\, J_m\left(\sqrt{k^2-k_z^2}\,\rho\right) e^{-jm\varphi}\, e^{-jk_z z}\, dk_z . \qquad (2.36)$$

The previous derivations were made for TE as well as TM modes. However in the following only TE modes will be considered. The only source for TM modes is mode conversion, which will be neglected due to the smooth change in the waveguide surface.

The quality of launcher performance is analyzed by calculating the Gaussian beam content at the launcher cut. The generated Gaussian beam is compared with an ideal Gaussian beam and the content factor is measured and is given by

$$\eta_{scalar} = \frac{\left(\iint_S |u_1|.|u_2| \, dS \right)^2}{\iint_S |u_1|^2 dS . \iint_S |u_2|^2 dS}, \tag{2.37}$$

$$\eta_{vector} = \frac{\left| \iint_S u_1^* . u_2 \, dS \right|^2}{\iint_S |u_1|^2 dS . \iint_S |u_2|^2 dS} \tag{2.38}$$

where S is the aperture surface that contains the radiated Gaussian beam. Equation 2.36 compares the amplitudes of two field components u_1 and u_2 with respect to power, whereas equation 2.37 includes the phase of the field component in the comparison.

With the sufficient knowledge of the coupled mode theory and the concepts required for the calculation of the wall field intensities, the analysis and design of the dimpled mode launchers for the proposed gyrotron $TE_{10,4}$- 95 GHz and 100kW designs are carried out by developing a numerical code in the Matlab domain.

2.4. Field Computations, Results and Discussion of Denisov launchers

As per the coupled mode theory presented above, we developed a numerical code for calculation of the mode variation profiles as well wall field intensities on the launcher walls.

2.4.1. Validation of Dimpled Launcher design for $TE_{22,6}$ mode at 110GHz

In the present work, starts with the reported values given by Blank (1994), for a Denisov launcher at 110 GHz $TE_{22,6}$ mode, the mode variation profiles and the corresponding wall field intensities are determined. It was reported that, the author has shown the mode variation calculation by considering a 4 satellite modes for the launcher

profile calculation and left the consideration second category satellite modes ($TE_{m-4,n+1}$, $TE_{m-4,n-1}$, $TE_{m-4,n+1}$, and $TE_{m-2,n+1}$) though these modes generates in the launcher section and participates in the mode coupling. As well it is advised to consider more number of modes for better accuracy and optimized design.

The profile details are taken from Blank (1994) are also tabulated in Table 2.3, the mode variation profile for 4 satellite modes are done initially. Due to the irregularities in the launcher also allows coupling with the second order satellite modes, mode coupling in the structure is determined by considering more satellite modes.

As mentioned in the several occasions that LOT and SURF3D tools are used for the design and optimization of converters which are commercially available and financially expensive. In the present work, using the above mentioned theories, i.e., coupled mode theories and fied calculations in the waveguide launchers, we developed a numerical code using Matlab tool, that calculates the mode couplings across the dimpled launchers for various deformed profiles and using this mode coupling coefficients, the wall field intestines are calculated. Followed by calculation of the Gaussian content available at the launcher cut has been done for the optimization of the launcher profile. The decision on the optimization deformed surface has been taken by observing the amount of mode couplings at the end of the structure as well the Gaussian content factor at the launcher cut. All the analysis has been done by a self-numerical code in the Matlab environment.

After a successful understanding of the theories and by developing numerical code, a reported dimpled launcher profile for $TE_{22,6}$ 110GHz given by Blank (1994) has been validated.

2.4.1a. With four satellite modes

It has been observed that the mode variation profiles and the wall field intensities calculations along the launcher wall had been shown for the four primary satellite modes i.e., $TE_{19,7}$, $TE_{25,5}$, $TE_{21,6}$,and $TE_{23,6}$. At first, using self-developed code, the calculated results are plotted in Figure 2.5 and 2.6 and the results are found in good agreement with almost 100% match with the reported results.

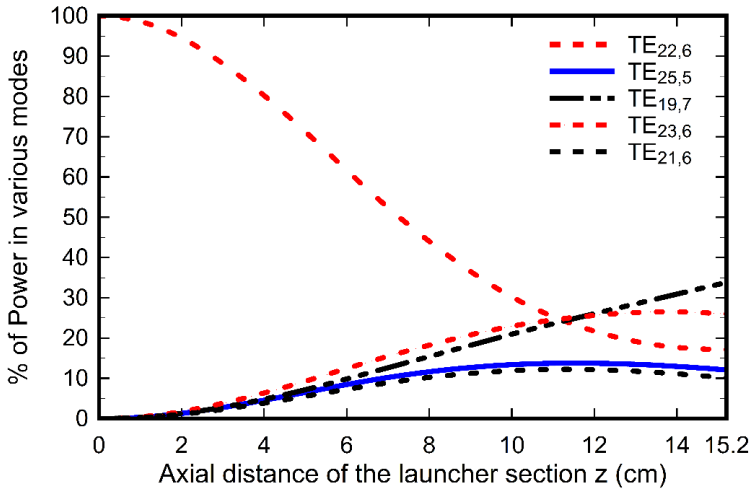

Figure 2.5: Mode variations profile along the length of the $TE_{22,6}$ mode at 110GHz launcher for eight satellite modes.

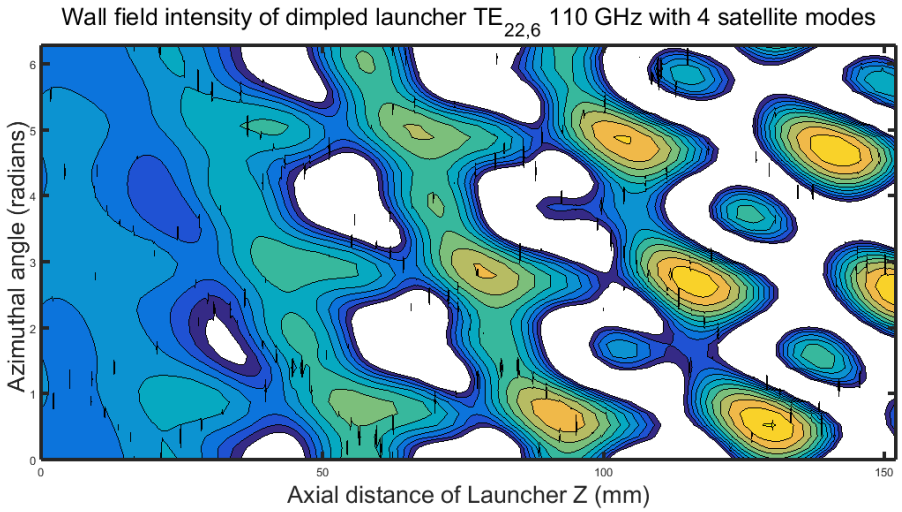

Figure 2.6: Wall field intensities on the dimple launcher of $TE_{22,6}$ mode at 110GHz for four satellite modes.

2.4.1b. With Eight satellite modes

Since, the amplitude of the deformation profiles are based on the primary satellite modes and the chosen 4 satellite modes certainly helps the growth of several modes and specially other four satellite modes ($TE_{26,5}$, $TE_{24,5}$, $TE_{23,7}$,and $TE_{18,7}$) as mentioned in Table 2.2.

We have re-calculated the mode variation profiles and the wall field intensities allowing other 4 satellite modes for more accurate study and are plotted in figures 2.7 and 2.8.

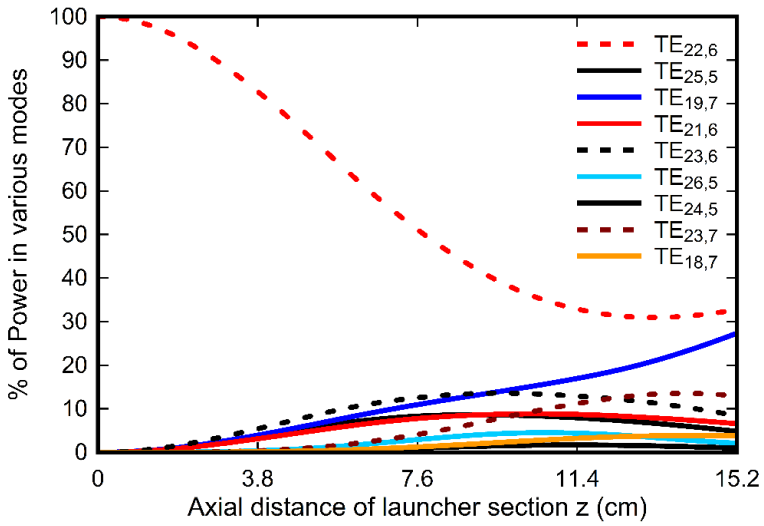

Figure 2.7: Mode variations profile along the length of the TE22,6 mode at 110GHz launcher for eight satellite modes.

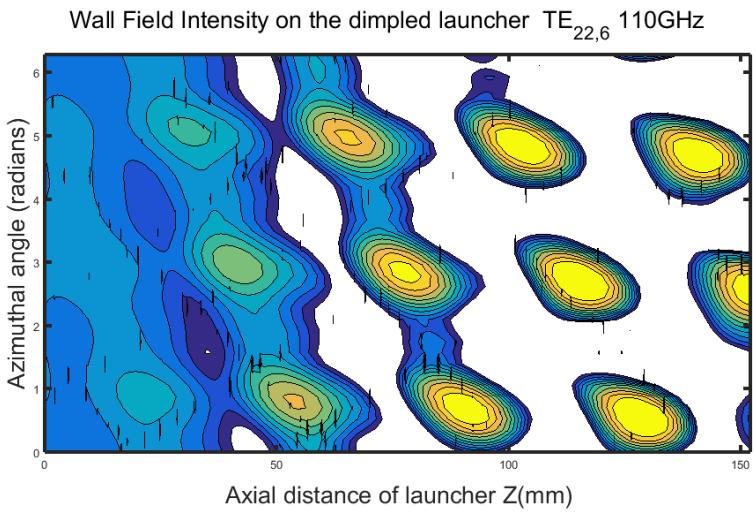

Figure 2.8: Wall field intensities on the dimple launcher of $TE_{22,6}$ mode at 110GHz for eight satellite modes.

It is observed that allowing more satellite modes in the calculations gives a different variation profile than earlier one but both cases leads to a good Gaussian beam formation at the launcher cut (on Brillouin regions). All the variations have been show pictorially.

It is perceived from figures 2.5 - 2.8 that due to second order satellite modes consideration, the amount of power in the various modes are differed significantly specially, main mode has a mode content of ~31% over 18% in the initial calculations. As well, a clear Gaussian beam can be observed in the latter case. Though, the design was the optimized and most suitable, but consideration of more satellite modes in the optimization of launcher profiles improves more accuracy and visualization of mode coupling that results a good Gaussian beam.

Further from figures 2.5 and 2.7, that even though ideal mode mixture content do not results but the optimized profiles gives a good Gaussian content near the cut. Though, it was reported that the author has allowed more satellite mods while optimizing surface but mode variations has been shown for 4 satellite modes case.

Though ideal combination of mode mixture is not realizable all the time but close to it for the optimized performance is sufficient.

2.4.2. Dimpled Launcher design for $TE_{10,4}$ mode at 95GHz

For our present design, a Denisov mode launcher design for the 95GHz, $TE_{10,4}$ mode is performed manually changing the launcher profile and confirming by observing the mode variation profile and Gaussian content at the launcher cut, since we do not have access to LOT code. Instead applying the constant dimples throughout launcher, an individual deformation profiles that results azimuthal and longitudinal bunching along with a small taper angle α_L is also, thereby Gaussian beam like mode at the launcher surface are considered for the present design. As well, the profiles are optimized by observing the mode coupling contents at the end of the launcher followed by wall field intensities. The optimized deformation profiles are plotted in figure 2.9.

The optimized dimpled profile is of nature represented by 2.13, with α_L =0.0015 and the deformed surfaces are shown in figure 2.9.

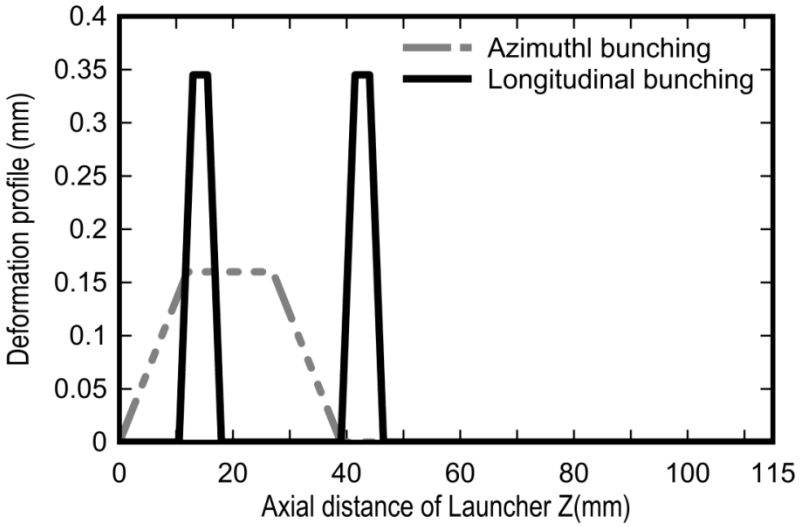

Figure 2.9: Wall Deformation profiles for the $TE_{10,4}$ mode at 95GHz launcher.

The mode variation profiles as well wall field intensities for the optimized launcher are plotted in figure 2.10-2.11.

Table 2.4: Dimpled Launcher parameters for 95GHz, $TE_{10,4}$

Parameter	**Value**
Operating mode	$TE_{10,4}$
Frequency	95GHz
Launcher Radius R_0	13.134 mm
Taper angle α_L	0.0015
Axial length of launcher	115.2 mm

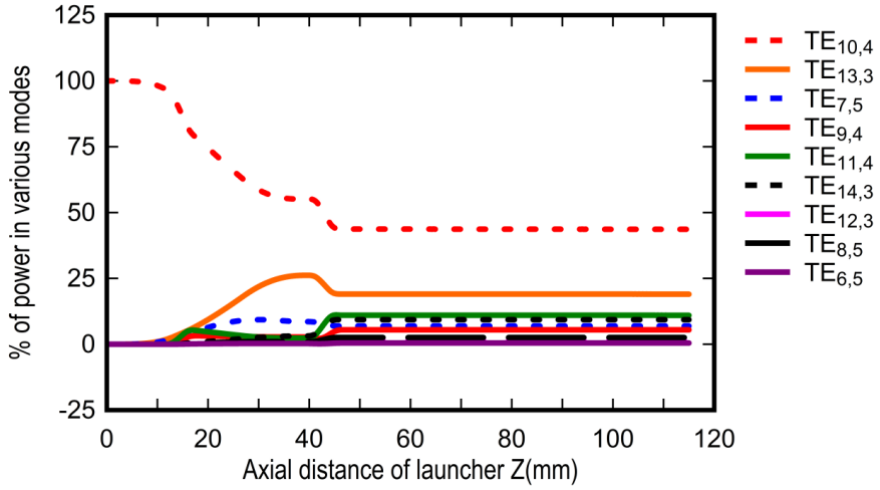

Figure 2.10: Mode variations profile along the length of the $TE_{10,4}$ mode at 95GHz launcher.

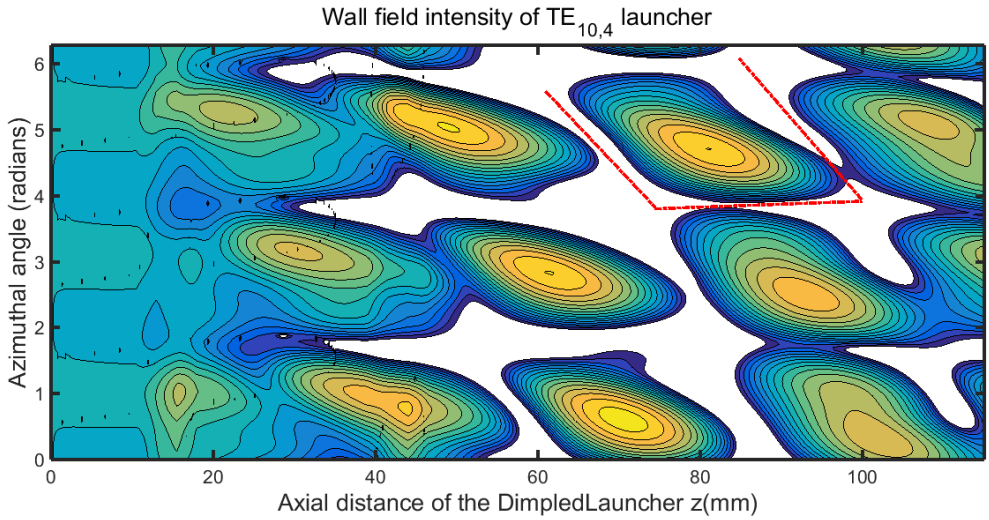

Figure 2.11: Wall field intensities on the dimple launcher of $TE_{10,4}$ mode at 95GHz.

The optimized launcher results a scalar Gaussian of more than 99% and with launcher cut has been highlighted in the figure 2.11.

2.5. Analysis and Design of Output RF Window

The RF window is an essential component of the output system of the gyrotrons and serves as a barrier between the vacuum side of the device and the external transmission line system. The desired features of an RF window are high power handling capability, high thermal conductivity and good mechanical strengths, as well large bandwidth, low reflection loss, etc.

Therefore, a proper window material with suitable geometrical and material properties is crucial for a gyrotron oscillators operating at high power and high frequencies. Usually, a low loss tangent (tan δ), high thermal conductivity, moderate mechanical strength are preferred.

In the high power Gyrotrons, materials, such as, Sapphire, Chemical vapor deposited (CVD) diamond, Silicon nitride composite, BeO, Au-doped silicon etc., are commonly used for window applications. The CVD diamond is the foremost choice for the MW power levels due to its excellent dielectric and mechanical properties. Coming

to the types of RF windows based on the construction, Disc type and Diamond windows for single and step tunable frequencies whereas Brewster windows for broadband frequencies.

In the present work, taking several materials individually, the RF window parameters are determined for the TEM_{00} mode, which is coming from the Denisov launcher that converts the $TE_{10,4}$ mode at 95GHz for 100kW power levels. The basic analytical concept used for the optimization of RF window for fixed frequency based on scattering matrix for disc type windows id briefly described here followed by the numerical calculations of the reflection and transmission characteristics for window discs of many thicknesses [Nickel *et al.* (1995)]. These results are discussed in the results and discussion section at the end of this current section.

2.5.1. Disc Type Windows

An RF window of disc type is usually characterized by disc thickness, loss tangent, disc diameter, and spacing between disc for multi disc type windows. For the disk type window, the thickness d_w is obtained by $d_w = n\lambda / 2(\varepsilon_r)^{1/2}$.

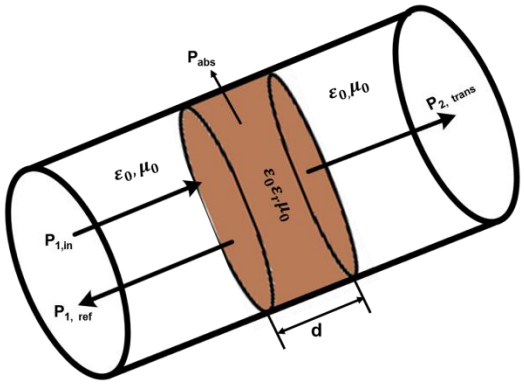

Figure 2.12: Schematic diagram of single disc type window of thickness d_w.

Figure 2.12 shows a homogeneous waveguide of arbitrary cross section with ideal conductive walls of section of the plane-parallel window of thickness *d*. The window surfaces are transverse to the waveguide axis and the disk edge is flush with the

waveguide wall. The disc is considered as it consists of one lossy homogeneous and isotropic dielectric material with the complex relative permittivity $\varepsilon_r = \varepsilon_r^{'} - j\varepsilon_r^{''} = \varepsilon_r^{'}(1 - j\tan\delta)$ and complex relative permeability $\mu_r = 1$. Nowadays, multi disc type windows where the dielectric materials are separated by a space s_d are used for the broadband applications.

Analysis of the disc type waveguide windows for gyrotrons is developed on the scattering matrix formulation and described in terms of the incident, reflected and transmitted waves. The basic formalism for disc type windows explained as follows:

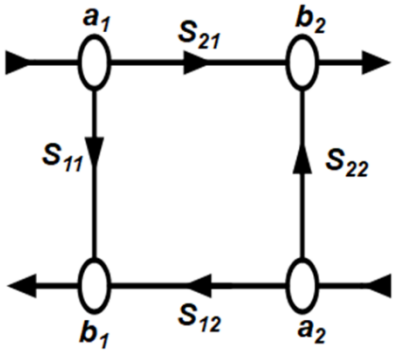

Figure 2.13: Equivalent Two port scattering matrix network.

Figure 2.13 shows an single disc waveguide window with its equivalent two-port scattering matrix network representation illustrating the incident and reflected waves a_k and b_k (k = 1, 2), respectively. The incident and reflected waves at the window plane are represented by a set of equations in matrix form as

$$[S] \equiv \begin{bmatrix} S_{11} & S_{12} \\ S_{21} & S_{22} \end{bmatrix} \equiv \begin{bmatrix} \left.\frac{b_1}{a_1}\right|_{a_2=0} & \left.\frac{b_1}{a_2}\right|_{a_1=0} \\ \left.\frac{b_2}{a_1}\right|_{a_2=0} & \left.\frac{b_2}{a_2}\right|_{a_1=0} \end{bmatrix} \tag{2.39}$$

$$\begin{aligned} b_1 &= S_{11}a_1 + S_{12}a_2 \\ b_2 &= S_{21}a_1 + S_{22}a_2 \end{aligned} . \tag{2.40}$$

The reflection, transmission and absorption coefficients in terms of the S-parameters of the network are related as:

$$R = |S_{11}|^2 = \frac{|b_1|^2}{|a_1|^2}\Big|_{a_2=0} = \frac{P_{1,refl}}{P_{1,in}}\Big|_{P_{2,in}=0} \tag{2.41}$$

$$T = |S_{21}|^2 = \frac{|b_2|^2}{|a_1|^2}\Big|_{a_2=0} = \frac{P_{2,trans}}{P_{1,in}}\Big|_{P_{2,in}=0} \tag{2.42}$$

$$A = 1 - |S_{11}|^2 - |S_{21}|^2 = \frac{P_{1,in} - P_{1,refl} - P_{2,trans}}{P_{1,in}}\Big|_{P_{2,in}=0} = \frac{P_{abs}}{P_{1,in}}\Big|_{P_{2,in}=0}. \tag{2.43}$$

The scattering matrix [S] of a dielectric region filled by material of length d_w and permittivity $\mathcal{E}$ is given by:

$$[S] = \frac{1}{1-\rho_v^2 e^{-2\gamma_{\varepsilon v} d_w}} \begin{bmatrix} \rho_v(1-e^{-2\gamma_{\varepsilon v} d_w}) & (1-\rho_v^2)e^{-\gamma_{\varepsilon v} d_w} \\ (1-\rho_v^2)e^{-\gamma_{\varepsilon v} d_w} & \rho_v(1-e^{-2\gamma_{\varepsilon v} d_w}) \end{bmatrix}, \tag{2.44}$$

where, the propagation constant $\gamma_{\varepsilon v} = \alpha_{\varepsilon v} + j\beta_{\varepsilon v} = \sqrt{k_{cv}^2 - \varepsilon_r k_0^2}$, the complex permittivity is given by $\varepsilon_r = \varepsilon_r^{'} - j\varepsilon_r^{''} = \varepsilon_r^{'}(1 - j\tan\delta)$.

$$\beta_{\varepsilon v} = \sqrt{k_0^2 \varepsilon_r{}' - k_{cv}^2} \cdot \sqrt{\frac{1}{2} + \frac{1}{2}\sqrt{\left(\frac{\varepsilon_r{}' \tan\delta}{\varepsilon_r{}' - (k_{cv}/k_0)^2}\right)^2 + 1}} \overset{\tan\delta << 1}{\approx} \sqrt{k_0^2 \varepsilon_r{}' - k_{cv}^2} \tag{2.45}$$

$$\alpha_{\varepsilon v} = \frac{k_0^2 \varepsilon_r{}' \tan\delta}{2\beta_{\varepsilon v}} \overset{\tan\delta << 1}{\approx} \frac{k_0 \varepsilon_r{}' \tan\delta}{2\sqrt{\varepsilon_r{}' - (k_{cv}^2/k_0)^2}} \quad . \tag{2.46}$$

The complex reflection coefficient due to the wave impedance discontinuity at the single dielectric transition plane for TE_{mn}, TM_{mn} and TEM_{00} modes are given by

$$\rho_v = \frac{\sqrt{1-(k_{cv}/k_0)^2} - \sqrt{\varepsilon_r - (k_{cv}/k_0)^2}}{\sqrt{1-(k_{cv}/k_0)^2} + \sqrt{\varepsilon_r - (k_{cv}/k_0)^2}}, \tag{2.47}$$

$$\rho_v = \frac{\sqrt{\varepsilon_r - (k_{cv}/k_0)^2} - \varepsilon_r\sqrt{1-(k_{cv}/k_0)^2}}{\sqrt{\varepsilon_r - (k_{cv}/k_0)^2} + \varepsilon_r\sqrt{1-(k_{cv}/k_0)^2}}, \tag{2.48}$$

$$\rho_v = \frac{1-\sqrt{\varepsilon_r}}{1+\sqrt{\varepsilon_r}}. \tag{2.49}$$

With the help of above equations, one can obtain transmission, reflection and absorption coefficients for the disc type window as follows:

$$T = \frac{T_0(1-2R_0\cos(2\Phi)+R_0^2)}{1-2R_0T_0\cos(2\beta_{\varepsilon v}d_w-2\varphi)+R_0^2T_0^2}, \tag{2.50}$$

$$R = \frac{R_0(1-2T_0\cos(2\beta_{\varepsilon v}d_w)+T_0^2)}{1-2R_0T_0\cos(2\beta_{\varepsilon v}d_w-2\varphi)+R_0^2T_0^2} \tag{2.51}$$

$$A = \frac{1-R_0-T_0-R_0T_0^2-R_0^2T_0+R_0^2T_0^2-2R_0T_0(\cos(2\beta_{\varepsilon v}d_w-2\Phi)-\cos(2\beta_{\varepsilon v}d_w)-\cos(2\Phi))}{1-2R_0T_0\cos(2\beta_{\varepsilon v}d_w-2\varphi)+R_0^2T_0^2}. \tag{2.52}$$

Here, $R_0 = |\rho_V|^2, \Phi = \arg\rho_v, T_0 = e^{-2\alpha_{\varepsilon v}d_w}$. By using the above mentioned analysis, one can easily design an RF window operating at the single or multiple frequencies for any of the incoming modes, either TE/TM or TEM_{00} mode. In some cases, multi dielectric regions are used for improvement in the performance, for such cases, the net scattering matrix of the system is obtained by cascading the individual matrixes.

2.5.2. Results and Discussion

In the present work, considering various window materials, the RF window is designed. In all the designs, a single disc of dielectric material is considered as well the incident mode is chosen as Gaussian beam mode, i.e., TEM_{00}. Since, for the TEM_{00} mode, the radius of window does not affect the window characteristics, hence a window of radius 32 mm is selected. The material properties are tabulated in Table.2.5. The

reflection and transmission characteristics versus frequency for various disc thicknesses *d* are determined and plotted in Figures. 2.14 -2.16.

Table2.5: Material properties used for RF window design [Link *et al.* (1993)]

Material	Frequency	Permittivity	Loss tangent
Born nitride (BN)	95GHz	4.7	115×10^{-5}
Sapphire	95GHz	9.4	20×10^{-5}
CVD	95GHz	5.67	2×10^{-5}

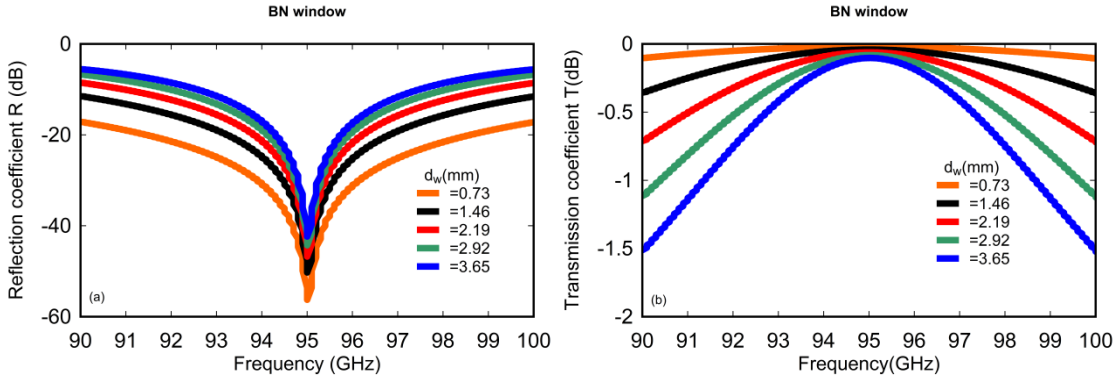

Figure2.14: (a) Reflection characteristics versus frequency (b) Transmission characteristics versus frequency for BN Window at various disc thicknesses d_w.

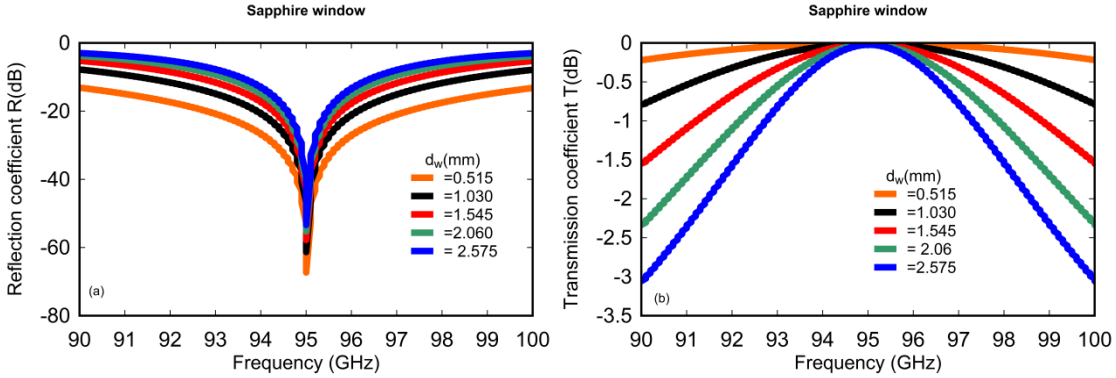

Figure2.15: (a) Reflection characteristics versus frequency (b) Transmission characteristics versus frequency for Sapphire Window at various disc thicknesses d_w.

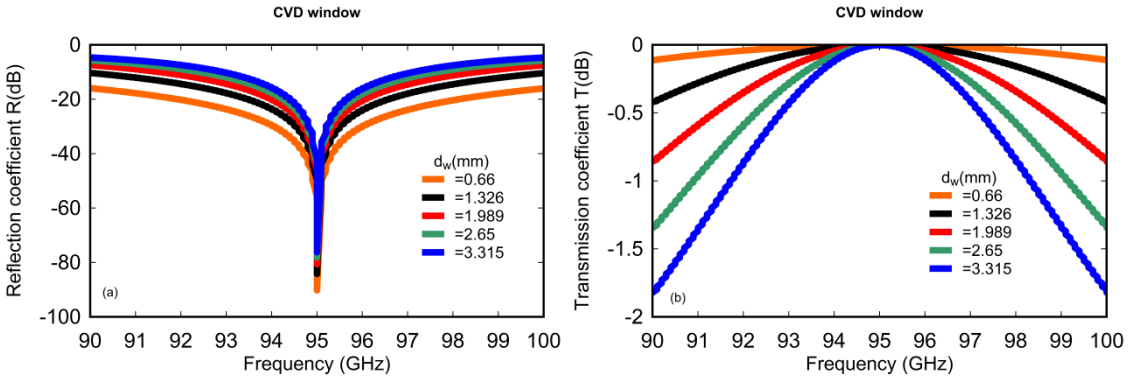

Figure 2.16: (a) Reflection characteristics versus frequency (b) Transmission characteristics versus frequency for CVD Window at various disc thicknesses d_w.

It can be observed that, in all the designs, as the thickness of the window d increases, the amount of reflection increases as well as the frequency range of maximum transmission coefficient also reduces that leads to the increment of the absorption coefficient. Though, all the designs show good reflection and transmission characteristics but depends on the range of power levels and optimum cost, the window material has to be selected. By studying the thermo mechanical behaviour of these windows, the final call can be taken based on the values of heat load (due to RF power absorption) and deflection, and higher tensile stress. Though this is kept out of the scope of the present study.

2.6. Conclusions

In the present chapter, Chapter 2, the advantages of an internal quasi-optical mode converter at high power high frequency gyrotrons are discussed. The basic theory used for the design, analysis of Vlasov mode launchers is described. Then, using the presented theory, the Vlasov type quasioptical mode launcher design parameters for the 95GHz $TE_{6,2}$ and 95GHz, $TE_{10,4}$ mode are calculated. Considering the presence of strong fields near the Vlasov cut, it has been shown that this leads to the severe

diffraction losses which in turn effects the conversion efficiency as well as the requirement of larger reflector geometries, limits the usage of Vlasov launcher to the whispering gallery modes. Then, design and analysis of modified Vlasov launcher, i.e., Denisov launcher has been also presented. The coupled mode theory used for the calculations of mode couplings due to irregularities as well the calculations of wall field intensities has been presented.

Using the analytical method proposed by Blank *et al.* (1994) the performance of the 110GHz, $TE_{22,6}$ mode gyrotron QOM launcher performance has been studied by considering four and eight satellite modes. It is found that consideration of more satellite modes gives better view of mode couplings due to dimples/irregularities in the launcher. Then, a computer code using MATLAB has been developed using the analytical approach developed here for the dimpled launcher. For the $TE_{10,4}$ 95GHz gyrotron, Denisov mode launcher design is performed manually using this code and by changing the launcher profile and confirming by observing the mode variation profile and Gaussian content at the launcher cut, since we do not have access to the popular LOT code generally used for this purpose. And the wall field's intensity profiles show a good Gaussian beam on the launcher cut has been observed.

Furthermore, the analysis and design of the disc type output windows used in gyrotrons are presented. Using the standard analytical approach and expressions, considering various window materials, the reflection and transmission versus frequency characteristics have been determined for the various cavity thicknesses. It has been found that as the thickness increases the amount of refection and the transmission coefficients are going against to the desired qualities of a window. Based on the amount of input power, the thickness of the material is needs to be chosen so that it can with

stand for the heat load generated by the RF power. However, thermo mechanical analysis of the windows has been kept out of the scope of the present work.

CHAPTER 3

DESIGN, ANALYSIS AND BEAM-WAVE INTERACTION STUDIES OF FIXED FREQUENCY (95 GHZ 100kW CW, $TE_{6,2}$ MODE) GYROTRON OPERATED IN THE WHISPERING GALLERY MODE

3.7. Conclusions

3.1. Introduction

As discussed in the Chapter 1, gyrotron oscillators are potential RF sources in several applications based on its power level and spectrum of generated frequencies. In the present work, we aimed to study the design of the medium power level gyrotrons used for security applications in the W band regime. As a part, we have selected the design goals of an RF source that able to generates an RF power of more than 100kW power, with efficiency >35% at 95GHz frequency, the beam parameters are taken from the a datasheet of the CPI gyrotron labelled with **VGB8095** so in the rest of the work, it is referred by [VGB8095].

In the literature, various gyrotrons of 100kW, 95 GHz operated in $TE_{6,2}$-, $TE_{7,3}$- and $TE_{10,4}$- are reported [VGB8095, Kumar *et al.* (2013), and Krishna *et al.* (2011)]. Out of which, TE_{62}- based gyrotrons have designed and tested experimentally reported by CPI, $TE_{7,3}$- mode based gyrotron has been reported by [Kumar *et al.* (2013)] and the initial studies mode selection of $TE_{10,4}$- operated device has been reported by [Krishna *et al.* (2011)] whereas the complete design studies that includes the beam wave interaction RF behaviour and thermal studies and the post RF interaction cavity component design are not presented.

As a first step towards our present research work in the field of gyrotron oscillators, considering the operating specifications and design goals of 95 GHz, 100 kW, $TE_{6,2}$ mode gyrotron by Communication and Power industries [VGB8095], the RF interaction cavity design, analysis and the beam wave interaction mechanisms are studied using the linear and non-linear theories reported in the literature. In addition, 3D PIC simulations for the beam present conditions are performed reconfiguring a commercial code "CST studio suite". Later, considering practical values of the electron

beam velocity spreads, the design is investigated for the various beam parameters. Also, the effect of misalignments condition in the beam source on the gyrotron performance is studied. After an intensive RF study of the gyrotron interaction structure, the thermal effects due to the RF power generation in the RF interaction cavity are explored. Design of the required thermal system and its needed suitable optimization to achieve the desired performance of the RF interaction structure is presented. We have further explored and validated our thermal system design using a commercial PIC tool, which is so far not reported in the published literature approachable to the authors. We have used commercial tool "COMSOL Multiphysics" for this purpose and analysed the designed, optimized cooling system for the gyrotron.

The present chapter, Chapter 3 is organized as follows. A brief introduction about various design constraints and the limiting factors required of the gyrotron design are presented. Then by the cavity design using linear theory along with study of beam wave interaction mechanisms under various modes in gyrotrons using precise theory of nonlinear, time dependent, multimode analysis developed by [Fliflet *et al.* (1991)] are presented. Then, the gyrotron RF interaction structure (tapered cylindrical cavity) model is simulated in the commercial CST Studio suite environment, using PIC simulation code the beam wave interaction mechanisms are also investigated. Followed by the thermo-mechanical studies that are essential due to the ohmic losses which leads deformations in the cavity thus degradation of device performance is studied. Using the commercial COMSOL Multiphysics, the optimized cooling system design for the present gyrotron is investigated in depth.

3.2. Design constraints and operating mode selection of Gyrotron

As we know, for any device design, it has to obey certain design requirements as well constraints. Similarly, for the gyrotron oscillators, it has to obey parameters, like, voltage depression (V_{dep}), limiting current (I_L), ohmic losses (dP/dA), fresnel parameter (C_F), etc. Gyrotrons operates at near cut-off frequency of the RF interaction cavity and radiate desired power at the targeted frequencies in $TE_{m,p}$ modes where m and p represents number of full wave and half wave variations in the azimuthal and radial directions. Based on the values of m and p values, in gyrotrons, the modes are classified as axisymmetric modes (m = 0), whispering gallery modes (where $m >> n$, p = 1, 2), volumetric modes (where $m >> n$, $p > 2$) [Edgcombe (1993), and Kartikeyan *et al.* (2013)].

Based on the operating mode and frequency of operation, the probable interaction cavity radius R_c and electron beam radius R_b are given by [Nusinovich (2004)]:

$$R_c = \frac{\chi_{mp}\lambda}{2\pi} = \frac{\chi_{mp}c}{2\pi f_c} \text{ and } R_b = \frac{\chi_{m\pm s,i}R_c}{\chi_{mp}} = \frac{\chi_{m\pm s,i}\lambda}{2\pi} = \frac{\chi_{m\pm s,i}c}{2\pi f_c} \tag{3.1}$$

where χ_{mp} is the p^{th} root of m^{th} order Bessel function of the first kind $J'_m(x) = 0$, c is the velocity of light in free space, f_c is the frequency of operation and where s is the harmonic number and i indicates the number maximum position of the field where the beam is to be launched in the interaction structure. The above stated relations give a probable radius values and sometimes needs a mild variations for optimized performance of the design.

Selection of suitable operating mode followed by optimization of interaction cavity dimension and beam parameter for achieving the design goal is two major steps

for the device design. The design goal and technical constraints of the present design are tabulated in the following Table 3.1.

Table 3.1: Design goal and technical constraint values

Parameter	Value
Frequency f	95±0.1 GHz
Output power P_{out}	> 100 kW
Diffractive quality factor Q_{diff}	800-900
Beam current	5 A
Beam voltage V_b	50 kV
Magnetic field at the cavity B	3.60±0.3 T
Pitch factor α	1.4-1.5
Harmonic number, s	1
Interaction efficiency η	>35%
Wall losses dP_{loss}/dA	< 2 kw/cm^2

Gyro-devices have to satisfy the design constraints while reaching the targeted goal for longer life as well reliable operation. Likewise, gyrotron oscillator has to obey design constraints under a limit like voltage depression V_{dep}, limiting current I_L, ohmic losses dP_{loss}/dA, along with significant frequency separation of operating mode from the competing modes [Edgcombe (1993), and Kartikeyan *et al.* (2013)]. In the following sub-sections, a brief description of the major design constraints and its role on the gyrotrons performance are presented.

3.2.1. Voltage Depression (V_{dep})

Owing to the space charge in the beam, the potential within the beam is reduced with respect to the wall potential. This phenomenon is called the voltage depression. The depression in the potential produces spread in the electron beam causes poor beam quality as well as reduction in efficiency. Lower values of voltage depression V_{dep} is

always desirable and in the cylindrical interaction cavity of gyrotrons, it is given by [Edgcombe (1993), and Kartikeyan *et al*. (2013)].

$$V_{dep} \approx 60 \frac{I_b}{\beta_z} \ln\left(R_c / R_b\right), \tag{3.2}$$

where R_c , R_b ,I_b, β_z are the interaction cavity radius, beam radius, beam current, normalized axial velocity of electrons, respectively.

3.2.2. Limiting Current (I_L)

The limiting current I_L is defined as the current beyond which the voltage depression becomes so large that the axial beam velocity tends to zero and the beam no longer propagates but is reflected [Edgcombe (1993), and Kartikeyan *et al*. (2013)]. The limiting current I_L can be given by:

$$I_L = \frac{2\pi\varepsilon_0 m_e c^3}{q_e}\left[\frac{\gamma_0\left(1-\left(1-\beta_{z0}^2\right)^{1/3}\right)^{3/2}}{\ln\left(R_c / R_b\right)}\right] \text{ where } \gamma_0 = 1 + \frac{q_e V_b}{m_e c^2} \ . \tag{3.3}$$

Here V_b is the beam voltage, q_e is the charge of the electron, m_e is the mass of the electron, γ_0 is the Lorentz factor or relativistic mass factor of the electron. Generally limiting current should be at least twice as large as the operating current of the device.

3.2.3. Ohmic Wall losses (dP_{loss}/dA)

The finite conductive nature of the interaction cavity walls of the device results losses in the cavity region in terms of ohmic losses. These losses are related by amount of targeted power P_{out}, quality factor Q_{diff}, operating mode and the dimensions of the structure. Ohmic losses plays critical role in the stable operation of the device due to thermo-mechanical dependency of the cavity materials that causes deviations in the RF

behaviour. The peak of the ohmic losses in the gyrotron oscillator can be given as [Edgcombe (1993), and Kartikeyan *et al.* (2013)]:

$$\left(\frac{dP_{loss}}{dA}\right)_{\max} \approx \sqrt{\frac{1}{30\sigma}}\left[\frac{f^{3/2}P_{out}Q_{diff}}{c^{3/2}L_c}\right]\left[\frac{1}{\chi_{mp}^2 - m^2}\right] \tag{3.4}$$

where Z_0 = 377 Ω is the intrinsic impedance for the vacuum, effective length of the interaction cavity L_c, σ is electrical conductivity of the cavity material. It is a limiting factor and generally should be kept below 2 KW/cm^2 for high power devices. Lower ohmic losses are desirable for stable frequency of operation and longer device life, and yields simple, efficient thermal management system design.

Since gyrotron operates in the high order mode that leads to presence of dense mode spectrum, hence, in addition to the above design constraints, knowledge of the frequency separations between the main operating mode and the competing modes also becomes important. The frequency of separation should be as wide as possible to avoid mode competition. For a TE$_{m,p}$ mode, the most competing modes are TE$_{(m-1),p}$ and TE$_{(m-3),(p+1)}$ and theoretically the frequency separation from these modes are determined by [Kumar *et al.* (2014)]:

$$\Delta f_1(\%) = \frac{\chi_{m,p} - \chi_{m-1,p}}{\chi_{m,p}} \times 100 \; and \; \Delta f_2(\%) = \frac{\chi_{m,p} - \chi_{m-3,p+1}}{\chi_{m,p}} \times 100 \tag{3.5}$$

Considering the design constraints and requirements of the device, a suitable operating mode selection is required for the achievement of the targeted goals. Sometimes, it is not feasible for modes to maintain all the design constraint within the limits and a trade-off among constraints needs to be considered. In the present chapter,

we have taken the operating mode and beam parameters from the CPI-VGB 8095, so no need of mentioning a detailed procedure to choose the operating mode. Hence, we moved with design, analysis and simulation of the RF structure that is able to meet the targeted goals. Considering several compete modes, the design constraints have been calculated for the beam parameters listed in Table 3.2. Considering effective length of the interaction cavity as 20 mm, at the design parameters listed in Table 3.1, using expressions 3.1-3.5, the design constraints for various modes are calculated and tabulated in the Table 3.2.

Table 3.2: Design constraints values for different modes

m	**n**	X_{mp}	R_c **(mm)**	R_b **(mm)**	V_d **(kV)**	I_L **(A)**	dP/dA_{max} **(kW/cm^2)**	m/X_{mp}	Δf_1	Δf_2
1	4	11.7048	5.8828	1.9256	1.4059	22.443	0.1639	0.0854	13.8210	39.653
1	4*	11.7048	5.8828	1.5348	1.6915	18.654	0.1639	0.0854	13.8210	39.653
2	4	13.1692	6.6187	0.9252	2.4771	12.738	0.1316	0.1518	11.1193	12.856
2	4*	13.1692	6.6187	2.1113	1.4385	21.9358	0.1316	0.1518	11.1193	12.856
3	3	11.345	5.7019	1.5348	1.6522	19.098	0.1862	0.2644	12.1323	17.431
3	3*	11.345	5.7019	2.6723	0.9541	33.072	0.1862	0.2644	12.1323	17.431
4	2	9.28171	4.6649	2.1113	0.9980	31.615	0.3179	0.4309	13.6517	8.0398
4	2*	9.28171	4.6649	3.2242	0.4650	67.854	0.3179	0.4309	13.6517	8.0398
4	3	12.6809	6.3733	2.1113	1.3909	22.686	0.1540	0.3154	10.5350	7.6970
4	3*	12.6809	6.3733	3.2242	0.8579	36.781	0.1540	0.3154	10.5350	7.6970
5	2	10.5191	5.2868	2.6723	0.8589	36.736	0.2603	0.4753	11.7635	5.2338
5	2*	10.5191	5.2868	3.7698	0.4257	74.112	0.2603	0.4753	11.7635	5.2338
6	**2**	**11.7341**	**5.8975**	**3.2242**	**0.7602**	**41.5076**	**0.2193**	**0.5113**	**10.3546**	**3.3165**
6	2*	11.7341	5.8975	4.3109	0.3945	79.978	0.2193	0.5113	10.3546	3.3165
6	3	15.2671	7.6731	3.2242	1.0915	28.907	0.1131	0.39300	8.3902	4.4703
6	3*	15.2671	7.6731	4.3109	0.7259	43.4698	0.1131	0.3930	8.3902	4.4703
10	1	11.7702	5.9156	5.3832	0.1187	265.737	0.5786	0.8496	9.0006	9.8668
10	1*	11.7702	5.9156	6.4461	0.1081	291.82	0.5786	0.8496	9.0006	9.8668

Inspecting the design constraints of various mode, it is found that $TE_{6,2}$ is possessing desired qualities at the given parameter. The limiting current I_L and voltage depression V_{dep} curves for the $TE_{6,2}$- mode over a range of normalized beam radius values are calculated for beam parameters listed in Table 3.1 and plotted in Figure 3.1

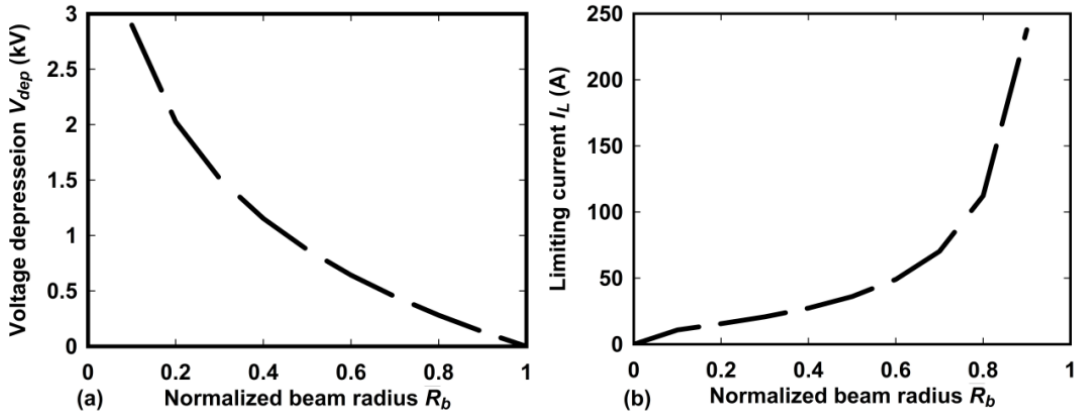

Figure 3.1: (a) Voltage depression V_{dep} (kV) versus normalized beam radius $\overline{R_b}(=R_b/R_c)$, and (b) Limiting current I_L (A) versus normalized beam radius $\overline{R_b}(=R_b/R_c)$ for $TE_{6,2}$- mode.

The RF interaction cavity that provides space for the beam wave interaction is to be designed. The role of the interaction structure is to allow the growth of the operating mode at desired frequency of oscillation while suppressing the mode conversion when subjected to the beam parameters. The background analysis required for the RF cavity design and the selection of the cavity dimensions are presented in the following subsection.

3.3. Design of RF Interaction structure

A conventional tapered cylindrical structure as RF interaction cavity is taken in the present design and its 2-D axis symmetric model view is shown in Figure 3.2. It consists of three sections, first a down taper section for RF isolation of length L_d, with an angle θ_d, followed by a uniform middle section where active beam-wave interaction

takes place, of length L_c and at the end, an up-taper section where RF standing waves get converted into travelling waves to extract out RF energy, of length L_u with angle θ_{up}. Usually, parabolic smoothing section of lengths L_{ds} and L_{us} at down-taper and up-taper transitions, respectively, are used to minimize the mode conversions [Edgcombe (1993), Kartikeyan *et al.* (2013)].

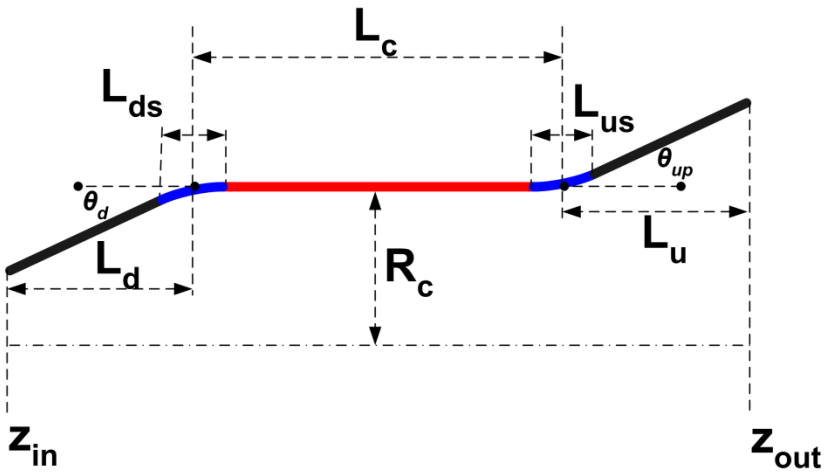

Figure 3.2: 2-D axis symmetric view of the tapered RF interaction cavity of the gyrotron.

Design of interaction cavity requires knowledge of axial RF field profile $V_{mp}(z)$, resonating frequencies f_{res}, and its quality factor Q_{diff}. If the taper angles are small (< 10^0), it is appropriate to use the single mode Vlasov approximation in which only single $TE_{m,p}$ mode is retained in the expansion of coupled equations and coupling due to the other modes due to cavity tapers can be neglected. Thus, in single mode approximation, the RF field profile $V_{mp}(z)$ in the interaction structure can be given by [Edgcombe (1993)]:

$$\frac{d^2V_{mp}}{dz^2}+\left(\frac{\omega^2}{c^2}-k_{mp}^2(z)\right)V_{mp}\simeq+i\omega J_{mp}, \tag{3.6}$$

where $J_{mp} = \int d\phi \int_0^{R_c} \mathrm{Re}^{*}_{mp} . JdR.$ is the source term, the complex RF frequency $\omega = \omega_{res}\left(1 + i/2Q_{diff}\right)$, ω_{res} resonant frequency and the transverse wave number $k_{mp}(z) = \chi_{mp} / R(z).$ The functions $V_{mp}(z)$ must satisfy radiation boundary conditions at the ends of the interaction cavity and can be written as:

$$\left.\frac{dV_{mp}}{dz}\right|_{z_{in}} = ik_z(z_{in})V_{mp}(z_{in}),\ and\ \left.\frac{dV_{mp}}{dz}\right|_{z_{out}} = -ik_z(z_{out})V_{mp}(z_{out}). \tag{3.7}$$

Here, k_z is the axial wave number and given by $k_z(z) = \sqrt{(\omega/c)^2 - k_{mp}^2(z)}$, z_{in} and z_{out} are the down taper and up taper axial ends of the interaction structure. The solution of expression (3.6) using the boundary conditions (3.7) is best carried out with the Numerov algorithm when the source term is set as: J_{mp}=0 [Numerov (1927)]. With a systematic cavity design procedure calculations are performed for various cavity geometry combinations. The suitable combinations and the corresponding cavity parameters in the cold condition (beam absent) i.e., J_{mp}= 0 are tabulated in Table 3.3.

Table 3.3: RF cavity parameter for various cavity combinations

Parameter	**Set#1**	**Set#2**	**Set#3**
L_d (mm)	13	13	13
L_c (mm)	20	20	20
L_{up}(mm)	23	23	23
θ_d	2.2^0	2.2^0	2.2^0
θ_{up}	2.8^0	2.8^0	2.8^0
L_{ds} (mm)	0	4	6
L_{us}(mm)	0	4	6
f_{res}(GHz)	95.004	95.01	95.033
Q_{diff}	1110	924	735

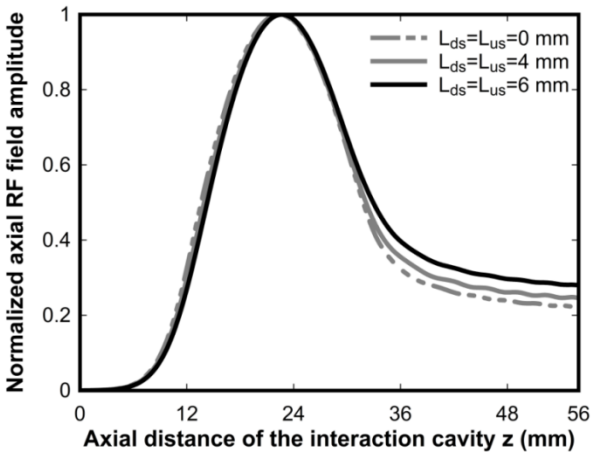

Figure 3.3: Normalized axial RF field amplitude profiles for various smoothing transition combinations at 0 mm, 4 mm, 6mm of lengths: L_d = 13 mm, L_c = 20 mm and L_{up} = 26 mm.

The normalized axial RF field amplitude profiles for various parabolic smoothing transition combinations for fixed cavity lengths (L_d, L_c *and* L_{up}) are plotted in Figure 3.3. It is observed that for increasing smoothing transitions, leads lower diffractive quality factor along with slight rise of reflection in the up taper region.

Table 3.4: Optimized tapered RF cavity dimensions

Parameter	**Value**
Cavity radius R_c	5.90 mm
Down taper length L_d	13 mm
Middle section Length L_c	20 mm
Up taper length L_u	23 mm
Parabolic smoothing L_{ds}	4 mm
Parabolic Smoothing L_{us}	4 mm
Down taper angle θ_d	2.2^0
Up Taper angle θ_{up}	2.8^0
Resonant Frequency f_{res}	95.01 GHz
Diffractive quality factor Q_{diff}	924

Following the determination of probable RF cavity dimensions, the designed beam parameters need to be optimized such that accomplishment of desired operation

with the minimum mode competition is achieved. The optimum radius and possible operating modes are determined by the calculations of the beam coupling coefficient as well the start oscillations currents of the several modes. A brief theory and its calculations for the current design are presented below.

3.3.1. Coupling Coefficient (C_{mp})

The optimum beam radius that results high beam wave coupling is estimated by coupling coefficient C_{mp} curves and can be obtained using the following expression [Edgcombe (1993), and Kartikeyan *et al.* (2013)]:

$$C_{mp}^2 = \frac{J_{m\pm s}^2\left(\chi_{mp} R_b / R_c\right)}{\left(\chi_{mp}^2 - m^2\right) J_m^2\left(\chi_{mp}\right)} \tag{3.8}$$

These curves are mode dependent and provide the amount of beam wave coupling value with respect to normalized beam radius for the uniform cavity radius R_c. The optimum beam radius is taken, such that, achieving maximum coupling and have significant distance away from both the walls as well axis of the structure. Considering various modes, the coupling coefficient C_{mp} curves for various modes with respect to normalized beam radius $\overline{R_b} = R_b / R_c$ are shown in Figure 3.4. It can be observed that the maximum coupling for the desired mode $TE_{6,2}$- occurs at normalized beam radius $\overline{R_b}$ = 0.545, accordingly electron beam radius is selected as 3.224 mm. It can be observed that the coupling coefficient for $TE_{3,3}$- mode is high compared to operating mode, but its stays to far from the cavity.

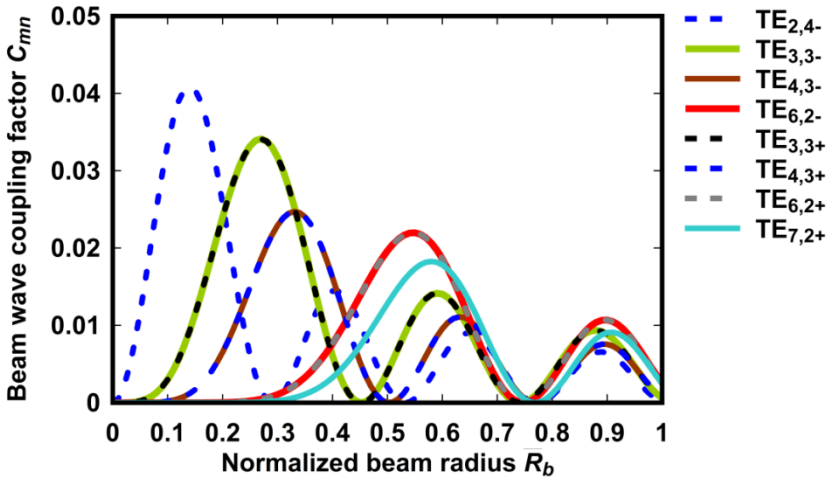

Figure 3.4: Beam wave coupling factor C_{mp} curves versus normalized beam radius($\overline{R_b}$) for various modes

3.3.2. Start Oscillation Current (I_{soc})

Though, the present design is for $TE_{6,2-}$, it is very important to determine the nearby and compete modes that can resists the mode growing. In high order operating mode devices, the competition from the nearby modes is inevitable and draws significant power from the electron beam causes power loss as well as reduction in device efficiency. Hence, identification of the competing modes is necessary and determined by the start oscillation current I_{soc} curves. It is defined as the minimum amount of current that allows the mode to oscillate significant and starts growing. The start oscillation current I_{soc} are calculated using linearized single-mode gyrotron theory and can be given as [Edgcombe (1993), and Kartikeyan *et al.* (2013)]:

$$I_{start}(\Delta,\mu) = 8.56x10^4 \frac{\exp\left((\mu\Delta)^2/8\right)}{\mu^2\left(\mu^2\Delta - 4s\right)} \frac{L_c\gamma_0}{Q\lambda}\left(\frac{\beta_{t0}^{2(3-s)}}{C_{mp}^2}\right) \tag{3.9}$$

where C_{mp} is the coupling coefficient and given by expression (3.9), and μ is normalized length of the interaction cavity, Δ is frequency mismatch or detuning parameter which are defined as [Edgcombe (1993), and Kartikeyan *et al.* (2013)]:

$$\mu = \frac{\pi \beta_{t0}^2 L_c}{\beta_{z0} \lambda} \; and \; \Delta = \frac{2}{\beta_{t0}^2}\left(1 - \frac{s\omega_{c0}}{\omega}\right) \quad . \tag{3.10}$$

Here, s is the harmonic number, β_{t0} is the normalized transverse velocity at the entrance of the interaction region, ω_{c0} is the non-relativistic cyclotron frequency [Kartikeyan *et al.* (2013)]. Considering the beam parameter as mentioned in Table 3.1 and for the cavity parameter as per Table 3.2, by varying the background DC magnetic field from 3.4 T to 3.7T, the start oscillation current I_{soc} values for various modes are calculated and plotted in Figure 3.5. In the I_{soc} calculation we considered the modes whose Eigen values are in the range of difference 3 from the desired mode Eigen value, i. e., $\chi_{mp} \pm 3$.

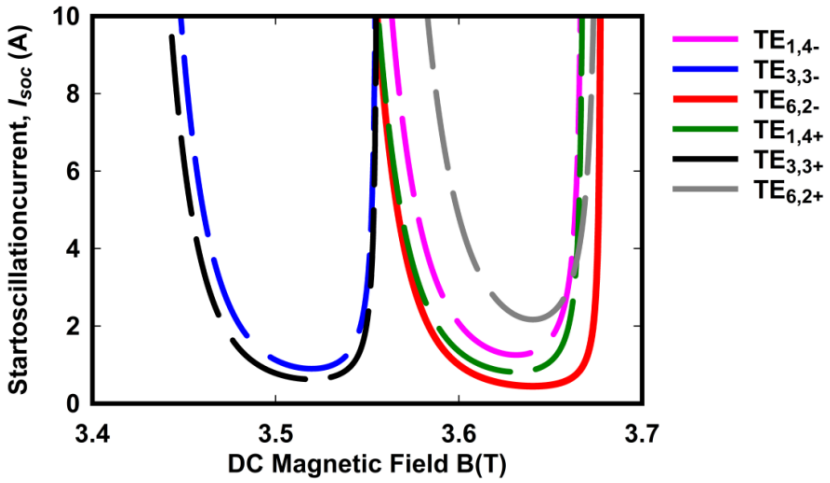

Figure 3.5: Start oscillation current Isoc (A) versus DC magnetic field B in (T) plots for different operating modes.

From the start oscillation current I_{soc} curves, it can be observed that $TE_{3,3+}$ and $TE_{1,4+}$ are some potential competing modes, however a suitable selection of DC magnetic field can reduce its significance. The role and significance of compete modes at various beam parameters in the beam wave interaction analysis and simulation are discussed in the following sections.

3.4. Beam-wave interaction study

Taking the probable set of beam parameters and cavity dimension as obtained from Section 3.2, by studying the electron beam and RF wave interaction mechanism for operating mode along with competing modes, the design is to be confirmed with the optimized parameters. In the present section the beam wave interaction mechanism is studied analytically using time dependent multimode analysis as well as the interaction cavity is simulated using commercial CST studio suite. The time dependent theory and the procedure for simulations in the CST studio suite environment is described in the coming sections.

3.4.1. Time-Dependent Multimode Theory

A self-consistent time-dependent multimode nonlinear analysis developed by Fliflet *et al.* (1991) is widely accepted for the study of the electron-beam and RF-wave interaction mechanism in the gyro devices. This theory is implemented in our work to study beam wave interaction behaviour of the gyrotron device. Space charge effects are neglected. A brief theory about the various set of coupled differential equations that governs the calculations of electron trajectories in the interaction structure as well the temporal behaviour of several modes are presented below.

In a highly overmoded gyrotron cavities, the mode spectrum is very dense and electron is likely to interact several modes in the cavities which leads to unstable the device and lower the efficiencies. Hence, for a high efficiency gyrotron, it is a challenging task to avoid the mode competition. Mode interaction theory has been presented by many of authors in the past [Bondeson *et al.* (1983), Kreischer *et al.* (1984)]. However, the single mode operation is indeed possible if the design of interaction structure is appropriate and the start oscillation current criteria are properly

analysed for the designed cavity. To study the performance of the overmoded cavities in the presence of several nodes, a multimode theory is presented here based on the formulation done by [Fliflet *et al.* (1991)].

In the analysis, a thin gyrating beam of electrons is considered. The arrangement of gyrating electron beam in a cylindrical cavity with all its coordinates is shown in Figure 3.6. Electrons move on a helical path gyrating about the guiding centre radius r_b. It is considered that electron beam interacts with the one or more competing modes closely spaced in the cavity.

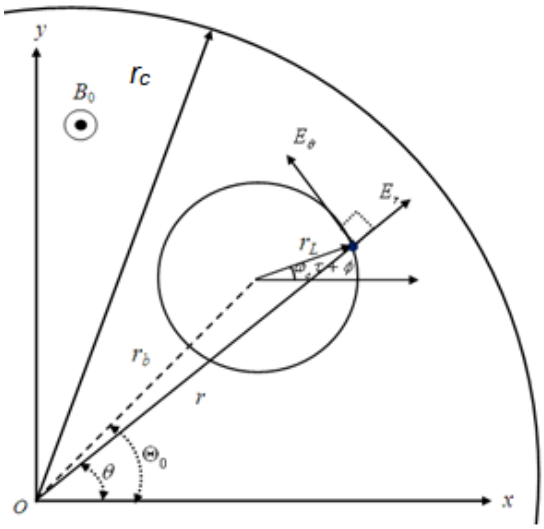

Figure 3.6: Arrangement of the gyrating electrons in Larmor orbit in the Cartesian as well as cylindrical coordinate systems.

The Lorentz's force equation governing motion of electrons in the presence of perturbing RF fields is given by

$$\frac{dP}{dt} + \frac{|e|}{\gamma m_e} P \times B_0 = -|e|(E + \frac{1}{\gamma m_e} P \times B) \equiv a' \quad , \qquad (3.11)$$

where, B_0 is the applied magnetic field $(B_0 = B_0\hat{z})$, P is the momentum of the electron, E and B are the electric and magnetic fields, and γ is the relativistic mass factor defined as $\gamma = [1 + p^2/(m_e c)^2]^{1/2}$.

Electrons interaction with RF fields result in perturbations in their momentum and phase, i. e., their momentum and phase deviate from the normal values they would have possessed if there were no interaction. To facilitate tracking of changes in the momentum and phase of electrons and with an observation on the most suitable co-ordinate system, the cylindrical co-ordinate system in this context is considered. Hence, the representing transverse momentum can be written in the form

$$p_x + ip_y = ip_t \exp[i(\omega_c \tau + \varphi)] \quad , \tag{3.12}$$

where, p_t and φ are slow time scale magnitude and phase of transverse momentum. The term slow time scale indicates those temporal derivatives of the two, momentum and phase, are quiet less than operating frequency (ω_0) or the reference cyclotron frequency (ω_c). Before interaction, the above equation (3.12) can be written as

$$p_x + ip_y = ip_t \exp[i(\omega_c \tau + \varphi_0)] \ , \tag{3.13}$$

where φ_0 and p_t are constants, the initial gyro-phase of an electron in a beam let and $\left[p_x^2 + p_y^2\right]^{1/2}$, respectively.

Hence, finally one can get the expressions for the momentum and phase of the particles [Fliflet *et al.* (1991)] as,

$$\frac{dp_t}{d\bar{z}} = \frac{\gamma}{p_z} \sum_{n=1}^{N} f_n J_s'\left(\bar{k}_{nt}\bar{r}_L\right) \mathrm{Re}\left\{\left[h + i\frac{p_z}{\gamma\omega_0}\frac{dh}{d\bar{z}}\right] e^{-i\left(\Lambda + \bar{\psi}_n + (m_n - s)\Theta_0\right)}\right\} \tag{3.14}$$

$$\frac{d\Lambda}{d\bar{z}} = \varpi_0\left[1-\frac{s\varpi_c}{\varpi_0\gamma}\right] - \frac{s\gamma}{p_z p_t}\sum_{n=1}^{N} f_n \frac{J_s^{'}\left(\bar{k}_{nt}\bar{r}_L\right)}{\bar{k}_{nt}\bar{r}_L}\mathrm{Re}\left\{\left[h + i\frac{p_z}{\gamma\bar{\omega}_0}\frac{dh}{d\bar{z}} - \frac{\varpi_{n0}^2 p_t^2}{s\varpi_c\varpi_0\gamma}h\right]e^{-i\left(\Lambda+\bar{\psi}_n+(m_n-s)\Theta_0\right)}\right\} \tag{3.15}$$

$$\frac{dp_z}{d\bar{z}} = \frac{p_t}{p_z\varpi_0}\sum_{n=1}^{N} fnJ_s^{'}\left(\bar{k}_{nt}\bar{r}_L\right)\mathrm{Re}\left[i\frac{dh}{d\bar{z}}e^{-i\left(\Lambda+\bar{\psi}_n+(m_n-s)\Theta_0\right)}\right] \quad , \tag{3.16}$$

where, γ is updated as

. The linearized mode phase parameter can be given as $\bar{\psi}_n(z) = \psi_n(t_0) + \left.\frac{d\psi_n}{dt}\right|_{t_0} z/v_z$.

Variables with bar are the normalized and are given as $\bar{r}_L = \frac{r_L}{r_{co}}, \overline{\omega_c} = \frac{\omega r_{co}}{c}, \bar{k}_{nt} = k_{nt}r_{co}, \bar{z} = \frac{z}{r_{co}}, \bar{\omega}_0 = \frac{\omega r_{co}}{c}$, and the slow time variations of azimuthal momentum phase with respect to the reference wave is given by, $\Lambda = (\omega_0 - s\omega_c)\tau + \omega_0 t_0 - s\varphi - (m_n - s)\theta_0$.

The normalized RF field amplitude and phase can be obtained from (3.17) and (3.18) as [Fliflet *et al.* (1991)] :

$$\frac{df_n}{d\tau} = -\frac{f_n}{2Q_n} + \bar{I}_n\int_0^L d\bar{z}h(\bar{z})\left\langle J_s^{'}\left(k_{nt}\bar{r}_L\right)\frac{p_t}{p_z}\cos\left(\Lambda+\bar{\psi}_n+\left(m_n-s\right)\Theta_0\right)\right\rangle_{\Lambda_0,\Theta_0} \tag{3.17}$$

$$\frac{d\Psi_n}{d\tau} = -\frac{\omega_0-\omega_{n0}}{2Q_n} - \frac{\bar{I}_n}{f_n}\int_0^L d\bar{z}h(\bar{z})\left\langle J_s^{'}\left(k_{nt}\bar{r}_L\right)\frac{p_t}{p_z}\sin\left(\Lambda+\bar{\psi}_n+\left(m_n-s\right)\Theta_0\right)\right\rangle_{\Lambda_0,\Theta_0}$$

(3.18)

where f_n and I_n are given by equation (3.19) and (3.20).

$$f_n = \frac{|e|}{m_e c^2}x_n^{'}C_n J_{m_n-s}\left(k_{nt}r_b\right)a_n\left(t_0\right), \tag{3.19}$$

$$I_n = \frac{|e|Z_0}{m_e c^2 \overline{\omega_o}} \frac{J^2_{m_{n-s}}\left(k_{nt} r_b\right)}{\pi\left(1-\frac{m_n^2}{x'^2_{m_n l_n}}\right) J^2_{m_n}\left(x'^2_{m_n l_n}\right)\overline{W}} I_0 \tag{3.20}$$

For co-rotating modes, $m_n > 0$, and for counter rotating modes, $m_n < 0$. Therefore, the time-dependent output power in the mode n can be obtained as,

$$P_n(\tau) = \frac{\pi m_0 c^4}{2Z_0|e|^2} \frac{\left(1-m_n^2/x'^2_{m_n l_n}\right) J^2_{m_n}\left(x'_{m_n l_n}\right)}{J^2_{m_{n-s}}\left(k_{nt} R_0\right)} \varpi_0 \overline{W} \left| f_n(\tau) \right|^2, \tag{3.21}$$

and the total interaction efficiency can be obtained by the energy distribution of all the particles as

$$\eta = \frac{\gamma_0 - \left\langle \gamma(z=L) \right\rangle_{\Delta_0,\Theta_0}}{\gamma_0 - 1} \quad , \tag{3.22}$$

where, $\langle \quad \rangle_{\Delta_0,\Theta_0}$ denotes the average over all the initial phase of all the particles.

3.4.2. Computational results and discussion

Using this multimode theory, the beam-wave interaction behaviour in the interaction cavity region, considering several modes can be studied on the time basis. The calculation is starts by assigning a small amplitudes and random phases to a set of modes. Then, solving the coupled, nonlinear, differential equations describing the electron momentum and phase equations along with the coupled time-dependent equations describing the mode amplitude and phase equations at each time step, the time varying behaviour of various modes are determined. Consequently, with the help of mode amplitudes and phases, the temporal growth of power levels in the modes and the electronic efficiency are calculated.

In the present study, considering a uniform background DC magnetic field profile along the interaction length, the coupled equations are numerically integrated using fourth order Runge-Kutta method. Considering a ramp type of DC beam voltage source from 35 kV to 50 kV with a period of rise time 200 ns is taken and a 5amps of DC currents is assigned to an electron beam that are generated with a pitch factor 1.414. The generated electron beam is injected into interaction region and is guided by external uniform DC magnetic field. In the calculation, the electrons are uniformly distributed gyrating with 32 beamlets with 32 electrons in each beamlets. With the space step size of 0.1 mm (< λ/30) as well a time step size of 5ps, the time dependent multimode analysis are done. For the operating and its neighboring modes, like, $TE_{3,3+}$, $TE_{3,3}$-, $TE_{10,1+}$, $TE_{10,1}$-, $TE_{6,2}$-, and $TE_{6,2+}$ beam-wave interaction behaviour are observed and its temporal power growth P_m are determined versus simulation time and are plotted in the Figure 3.7. Efficiency of the device is shown in Figure 3.8.

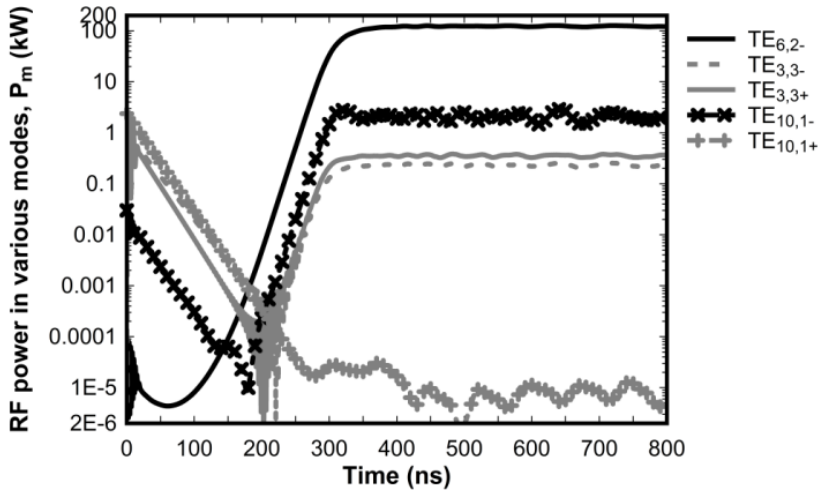

Figure 3.7: Temporal growth of output RF powers P_m (kW) in various modes through time dependent multimode analysis.

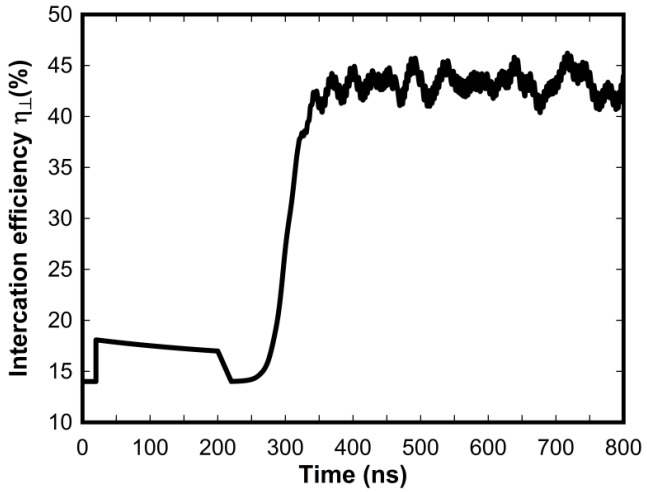

Figure 3.8: Interaction efficiency η versus time (ns).

It can be observed here that initially $TE_{3,3,}$+ mode dominates and after 300 ns it the desired operating mode $TE_{6,2}$- starts growing up to a stable RF power of ~123 kW; while all the competing modes reaches to a minimal value after 320 ns. An electronic efficiency of 40% is achieved at DC magnetic field of 3.60 T. Further, a parametric study is also performed analytically for range of applied DC magnetic fields and is discussed at the end.

3.5. 3D Particle in Cell (PIC) Simulation Studies

Various particles-in-Cell (PIC) codes are available for the study of beam wave interactions in high power microwave sources, like, MAGIC and CST Studio Suite are familiar. Since using MAGIC the beam wave interaction analysis is carried out by assigning a single mode means investigation under more than single mode is not possible. Whereas, using Commercial "CST Studio Suite", the beam wave interaction behaviour of the RF device can be investigated under more than one mode also. Various works [Swati *et al.* (2015), and Singh *et al.* (2013)] are reported in the field of microwave sources that uses CST studio suite for the investigations of beam wave interaction behaviour use in the devices.

In the present work, a 3D Particle in Cell simulation of the electron-beam and RF-wave interaction region of the device is performed reconfiguring a commercial code "CST Studio Suite." In the present study, taking OFHC copper as the cavity material with conductivity of 5.8×10^7 S/m, the RF interaction structure of the device is modeled. A particle circular source is taken for forming the gyrating electron beam with designed beam parameters with rise time of 1ns, that allows to run the simulation for less time than in the analysis, and an external axial magnetic field profile $B(z)$ is applied. To observe the temporal behaviour of modes, various 2D and 3D field monitors are placed with suitable boundary conditions.

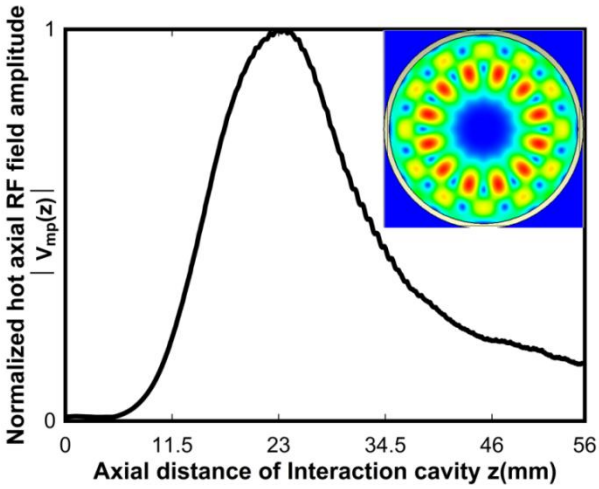

Figure 3.9: PIC simulation results: Normalized axial RF field amplitude profiles hot conditions along with vector field distribution.

3.5.1. Device performance under ideal condition

After the RF interaction cavity design, the desired axial electric field profile and mode excitation inside the cavity in the cold condition (absence of the electron beam) is ensured. Thereafter, by introducing the electron beam, the beam wave interaction behaviour is investigated. The simulated interaction cavity axial RF electric field profile versus axial cavity position in hot (beam present) conditions, and the as vector plot of field pattern of operating mode is shown in Figure 3.9. The time varying field

amplitudes of various modes are monitored using 3D *E*-field monitors and the significant mode amplitudes of the interaction are plotted in Figure 3.10. The operating $TE_{6,2-}$ mode and the main competing modes $TE_{3,3+}$ and $TE_{10,1-}$, at magnetic field B = 3.60T. Here, one can observe that for $TE_{6,2-}$ operating mode RF signal growth stabilizes in 200 ns and competing $TE_{3,3+}$ mode ad $TE_{10,1-}$decay to a minimal value in ~ 210 ns. The '+' and '-' assigned to the modes are confirmed by the orientation of field at particular location in the CST. If the mode rotates in clockwise wise then it is '+' and else it is '-'.

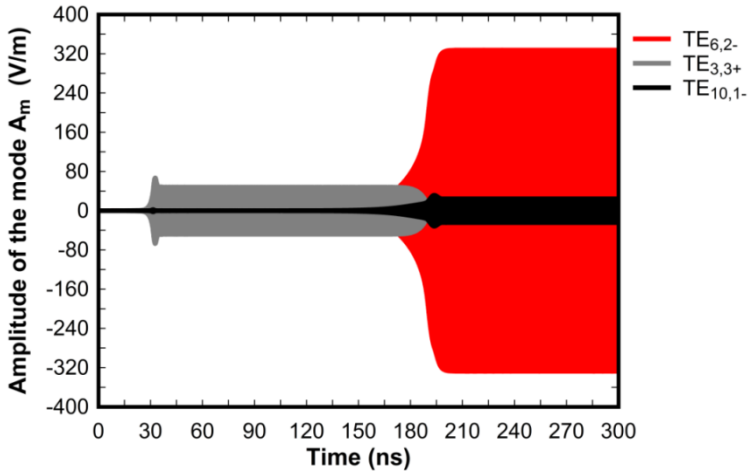

Figure 3.10: Temporal growth of operating and competing mode amplitudes A_m (V/m) from PIC Simulation study.

By post processing the results, the oscillation frequency as well RF power developed across various modes are determined. The temporal power growth is performed for the $TE_{3,3+}$, $TE_{10,1-}$ and $TE_{6,2-}$ modes. The frequency response of the modes is determined by performing Fourier Transform (FFT) action on the mode amplitude signals and the resultant frequency response for the modes are shown in the Figures 3.11 and 3.12. It is observed that the FFT responses of the main mode $TE_{6,2-}$ is at 94.987 GHz . As well from the peaks of the amplitudes of the FFT signals confirms that the $TE_{6,2-}$ is dominant. The temporal power growth in the gyrotron device for $TE_{3,3+}$ and

$TE_{6,2}$- modes are shown in Figure 3.12, where one can readily observe that power transfer from the electron-beam to the RF-wave in different modes with time during device operation.

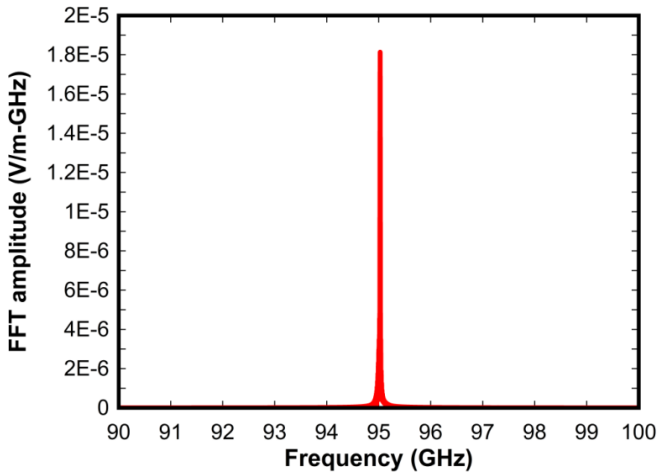

Figure 3.11: Frequency response of the operating and competing modes from PIC simulation study.

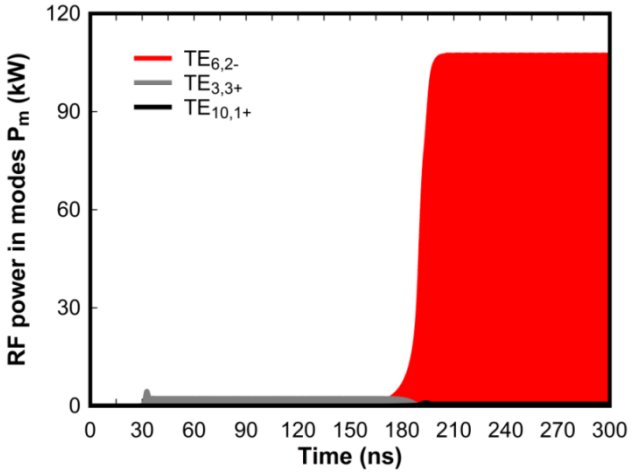

Figure 3.12: CST PIC simulation results- Temporal growth of RF powers in the operating and competing modes.

Around 107 kW stable RF power is generated at oscillation frequency 94.987 GHz in at the desired operating $TE_{6,2}$- mode, while RF power generated in all the competing modes is less than a percent. To strengthen the design study, a parametric analysis of device operation is also carried out for a range of the applied DC magnetic field. The RF output power generated versus applied DC magnetic field is performed

both analytically and also compared for its validation with PIC simulated values as shown in Figure 3.13. As magnetic field increases the RF power levels in the main mode are decreases in both analytical and simulated resulted results. Furthermore, an agreement within 7% is observed between the analytical and PIC simulation results. The discrepancy in the comparisons is because of the consideration of several assumptions in the analysis. Starts with ideal Gaussian type cavity axial E-field profile $h(z)$, zero velocity spreads in the beam and the calculations are limited to uniform section only. Conversely in the PIC simulations, the calculations are performed by including the uptaper section and a practical cavity axial E-field profile $h(z)$ (shown in Figure 3.9).

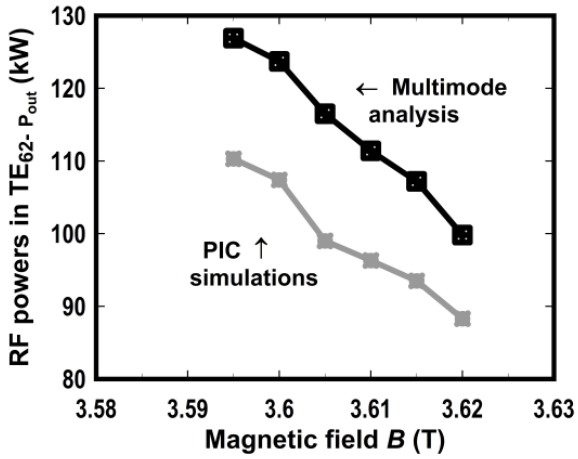

Figure 3.13: Comparisons of output RF powers in the main mode $TE_{6,2}$- by multimode analysis and PIC simulations for magnetic fields .

3.5.2. Device performance under practical conditions

So far, the beam wave interaction studies are carried out by using time dependent multimode theory as well CST studio suite under ideal conditions of beam parameters, i.e., no beam spread in terms of velocity as well beam alignment axis. But, the device performance is often required to be evaluated under non-ideal, i.e., in practical situations like at the presence of beam spreads and due to asymmetry of the beam axis with respect to the cavity axis. Though, these two situations arises from the

MIG gun part, but our study is considered only for interaction cavity, considering some possible spread values and misalignment situations, the beam wave interaction studies have been done using CST studio suite.

Velocity spread in the gyrating electron beam is usually present in the electron-beam devices and causes deviations of the beam characteristics and affects device performance [Dumbrajs *et al.*(2013) and Singh *et al.*(2014]. Even though, in present days, the device fabrication and beam launching technologies as well facilities are considerably improved that results a smaller variations in the quality of beam. The amount of velocity spreads and the misalignments are very small but certain amounts are always present in the practical devices. In our study considering velocity spreads of 0%, 5% and 8%, the device performance is analyzed and also evaluated through PIC simulation. Now, for misalignments of beam axis, there is no updated analysis with time dependent multimode theory [Fliflet *et al.* (1991)] and hence, the effects are investigated by simulation CST Studio Suite. The RF power and frequency of oscillations are calculated and tabulated in the Table 3.5 for velocity spreads. It is observed that the velocity spread effects much on the power level but its effect on oscillation frequency deviation is mild.

Table 3.5: RF power and frequencies for different velocity spreads

Velocity spread	RF power (kW)	Frequency (GHz)
0 %	107	94.987
5 %	102.4	94.988
8%	97.8	94.984

With a parallel shift of beam axis from the cavity axis of the interaction structure, in CST Studio suite environment, the design performance has been carried out. The calculated power levels and frequencies of the operating modes are done through PIC simulation. The possibility of beam misalignment happens at the time of

device fabrication and machining the beam source. Since, the complete analysis has been made by assuming the concentric relation between beam and cavity axis geometry. Even though, with the advancements of device machining and fabrication technologies, still there is a mild chance of misalignment can occurs. The effects have been studied in the simulation domain by taking a parallel shift of beam axis from cavity axis with steps, like, d = 0.1 mm, 0.2 mm and 0.3 mm. Similarly, the beam tilt is considered of at most 1^0 in steps of 0.2^0. The RF powers and the oscillation frequency of the device in the TE_{62}- mode at various beam shifts and tilts are simulated and tabulated in Table 3.6 and Table 3.7.

Table 3.6: RF power and frequencies for different beam shifts

Beam shift *d*	**RF power (kW)**	**Frequency (GHz)**
0.1 mm	107	94.987
0.2 mm	101.3	94.985
0.3 mm	96.8	94.984

Table 3.7: RF power and frequencies for different beam tilts

Beam tilt	**RF power (kW)**	**Frequency (GHz)**
0.2^0	101.3	94.973
0.4^0	97.6	94.973
0.6^0	94.7	94.971
0.8^0	94.3	94.97
1.0^0	92.1	94.97

By this, the RF behaviour of interaction cavity designed for 95 GHz, 100kW operating $TE_{6,2}$ mode is studied under ideal beam and various practical conditions . In addition to velocity spreads, accounting misalignment of beam axis with respect to the cavity geometry, the RF behaviour under various modes is done through CST Studio suite. In the high power high frequency RF sources, the ohmic losses generated in the cavity due to metallic nature of walls leads to structural deformation in the cavities

thereby degradation of the system performance. Since, for any RF source the desired characteristics are RF power and its operating frequency. Meanwhile, the microwave devices are majorly dependent on the cavity dimensions, so variations in it causes variations in the RF behaviour and its needs to be e analysed. This leads to study of thermos mechanical effects due to ohmic losses for RF sources are mandatory. In the next section, the calculations of ohmic profile in the gyrotron cavity as well the effect of cavity deformation on the RF performance are discussed in detail. Consequently, a thermal system has been designed by using various extended heat surface elements, i. e., fins. After considering all, the thermo-mechanical behaviour is investigated by using commercial PIC code "COMSOL Multiphysics".

3.6. Thermo-Mechanical Analysis and Optimized Cooling System Design

In gyrotron devices, apart from beam parameters, the RF structure dimension and its material properties also plays crucial role in the RF behaviour of the device. Any changes in structural dimension and material property of the RF interaction cavity not only causes deviation in its oscillation frequency but also degrades the RF output power as well as efficiency of the device apart from additional heating of the device structure. In the beam-wave interaction process, due to the finite electrical conductivity of the cavity walls, some part of the RF waves gets dissipated as the ohmic loss [Edgcombe (1993), and Kartikeyan *et al.* (2013)]. This leads to structure heating which may results in the RF cavity deformations, thereby changes in the oscillation frequency as well as decrease in the RF power output. Hence, an efficient thermal management system needs to be designed and ensured for stable operation of the gyrotron device [Edgcombe (1993), Kartikeyan *et al.* (2013), and Nusinovich *et al.* (2014)]. Thermo-mechanical

studies and its effect on RF behaviour of 1 MW power gyrotrons at 140 GHz, 170 GHz and 240 GHz are investigated using computational fluid domain softwares, like, ANSYS, STAR CCM and COMSOL Multi-physics in [Kumar *et al.* (2012), Liu *et al.* (2018), Q. Liu, Y. Liu, Z. Chen, X. Niu, H. Li, and J. Xu (2018), and Koner *et al.* (2009)] have carried out thermal analysis of RF interaction cavity of a 200kW CW, 42GHz gyrotron using ANSYS code for different coolant flow rate with the axial fins provided on its outer surface. Kumar *et al.* (2012) extended this work for 170 GHz gyrotron with axial as well as radial cooling fins. Q Liu *et al.* (2018) also carried out heat transfer analysis of the RF interaction cavity for the 140 GHz and 240 GHz gyrotrons using ANSYS code and shown the effect of cavity deformations on the multi-mode beam-wave interaction of the device. However, cooling fins and thermal system design and its optimization for the RF cavity of the device is not reported in the published literature accessible with us using COMSOL Multiphysics.

In the present work, the thermal and structural analysis of a tapered cylindrical RF interaction cavity of the gyrotron is carried out. With the help of design relationships, radial cooling fins design on the outer jacket of the middle section of the RF interaction cavity is presented. An optimum thermal system is designed and simulated using "COMSOL Multiphysics" code. Implementation of commercial code "COMSOL Multiphysics" is simpler than those used in previously reported work though equally accurate for this purpose and not explored earlier [Salvi *et al.* (2010)]. For the designed cooling system with different convective heat transfer coefficients, deformations in cavity profile are obtained through this simulation. Nonlinear time-dependent multimode theory is used further to obtain the RF output behaviour of the gyrotrons [Kartikeyan *et al.* (2013), Danly *et al.* (1986), Fliflet *et al.* (1991), and Singh *et al.* (2012)]. An optimum thermal system design thus obtained with maximum possible

deformation in the inner dimension of the RF cavity ensures the gyrotron oscillator RF frequency and power output variations within the specified tolerance limit of the device.

The thermal work is organized as follows: starts with evaluation of the effects of the RF cavity deformations on the resonant frequency of the device, the ohmic loss analysis of tapered interaction cavity that acts as wall load, radial cooling fins design, and role of cooling fins in the heat transfer enhancement and the heat transfer mechanisms of RF structure are presented. The thermo-mechanical analysis simulation set-up without fins and with radial fins using commercial code COMSOL Multiphysics are explained. Later, the simulated results of the RF structure for various convective heat transfer coefficients for different fin groups under optimized values of thermal system parameters are presented followed by its effects on the RF performance of the device due to changed scenario of the electron beam and RF wave interaction are also presented.

3.6.1. Analysis: Calculation of Ohmic Losses and Fin Design

As discussed in Sections 3.1 and 3.2, the RF fields are mainly confined in the middle section of cavity of radius R_c. The heat loading of the cavity walls are differential as per cavity RF field profile. Hence, for stable frequency radiation from gyrotron, we have to provide an efficient cooling system so that its deformation remains minimum so as to keep the oscillation frequency, RF output power and efficiency deviation remains within the tolerance limit of the device.

3.6.1a Effects of radial deformation on resonant frequency

Gyrotron oscillators operate near to cut-off region of its RF interaction cavity. The cavity radius plays a crucial role in governing the radiation frequency of the RF

wave. Using expression (3.1), the dependence of cavity cutoff frequency *fc* with the variations in cavity radius is plotted in Figure 3.14.

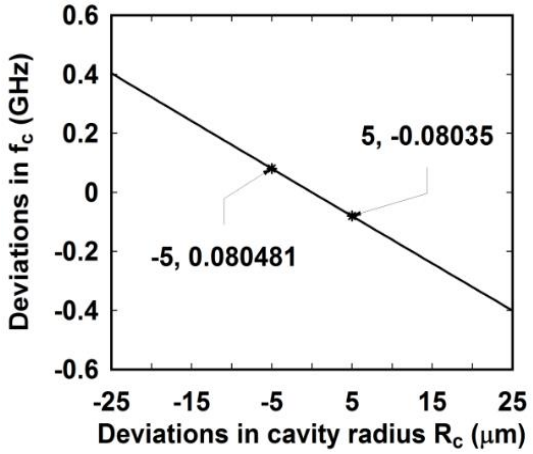

Figure 3.14: Variations in the cavity cut-off frequency fc due to changes in the RF cavity radius R_c.

We can observe from this plot that there is a change in the RF cavity radius, which will result in a significant change in the cavity cutoff frequency thereby will cause significant change in the gyrotrons oscillation frequency. Typically, a 5 μm change in cavity radius results in 80 MHz shift in the device oscillation frequency.

3.6.1.b Wall loss calculation

The Ohmic loss generated in the structure acts as a wall load or heat flux on the structure, and may cause structural deformations. The Ohmic wall losses P_Ω are connected to the Ohmic quality factor Q_Ω of the interaction structure by the well-known relation [Edgcombe (1993)]:

$$P_\Omega = \frac{2\pi f W}{Q_\Omega}, \tag{3.23}$$

with frequency f and stored energy W. A similar expression can be obtained for the diffraction loss P_{diff} as well:

$$P_{diff} = \frac{2\pi fW}{Q_{diff}}. \tag{3.24}$$

Combining equations (3.22) and (3.23), one obtains an expression for the Ohmic loss as a function of the output power $P_{out} = P_{diff}$ as:

$$P_{\Omega} = \frac{P_{diff} Q_{diff}}{Q_{\Omega}}. \tag{3.25}$$

Under the condition of normal skin effect, one gets:

$$P_{\Omega} \approx \frac{Q_{diff}\left(\pi f \mu_o \sigma\right)}{1-\left(m/\chi_{mp}\right)^2} \frac{P_{diff}}{R_c}, \tag{3.26}$$

where, σ is the electrical conductivity of the cavity material, m is the azimuthal mode index and μ_0 is the permeability of free space. Dividing equation (3.25) by the surface area A, gives the power loss density of the middle cavity section as [Nusinovich *et al.* (2014)]:

$$\frac{dP_{loss}}{dA} \approx \sqrt{\frac{1}{30\sigma}} \left(\frac{f^{3/2} P_{out} Q_{diff}}{c^{3/2} L_c} \right) \left(\frac{1}{\chi_{mp}^2 - m^2} \right). \tag{3.27}$$

The above wall load expression (3.26) is for a uniform profile and limited to the middle cavity section of length L_c only. Practically, the power loss density in the cavity is of non-uniform nature and also exists at the up-taper section as well. Thus, the ohmic loss profile along the interaction structure can be written as [Kartikeyan *et al.* (2013)]:

$$\frac{dP_{loss}(z)}{dA} \simeq \left(\frac{\delta}{4\pi\mu_0\omega} \right) \left[\frac{1}{\chi_{mp}^2 - m^2} \right] \left(\frac{\chi_{mp}^4}{R^4(z)} \left| V_{mp} \right|^2 + \frac{m^2}{R^2(z)} \left| \frac{dV_{mp}}{dz} \right|^2 \right). \tag{3.28}$$

Here, m is azimuthal mode index, *R(z)* is the cavity radius at axial position z, V_{mp} is the axial electric field profile of the interaction structure resulted from beam wave interaction analysis and δ is the skin depth. The surface roughness effects of interaction cavity can be accounted by replacing δ with $\delta_{eff} \simeq 2\delta$ [Kartikeyan *et al.* (2013)].

3.6.1c. Cooling Fins Design

For gyrotrons, due to thermal dependency of the materials, efficient heat transfer from the structure is always desired. Generally heat transfer rate can be increased by increasing the temperature gradient between the object and the environment, or by increasing the convection heat transfer coefficient or by increasing the surface area of the object. Here, the concept of increasing the surface area is achieved by incorporating fin surfaces.

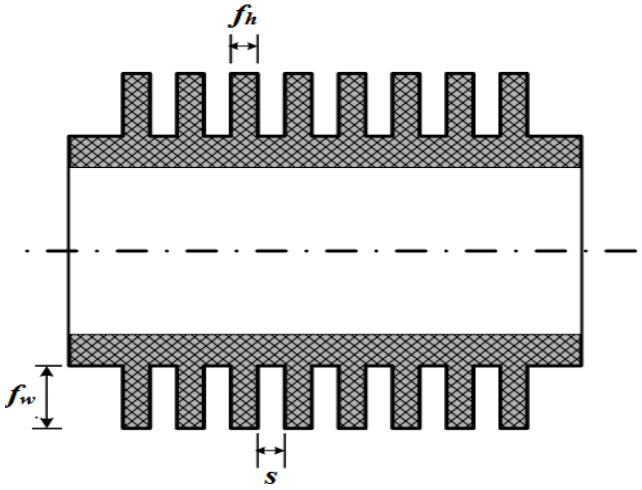

Figure 3.15: Schematic diagram of typical radial cooling fins on a cylindrical surface (f_h = fin height, f_w = fin width and s_f = spacing between fins).

Cooling fins provide an extended surface from the object intended to enhance the heat transfer rate to or from the environment through convection by increasing surface area of the object. In the present study, radial fins type as shown in Figure 3, is considered for the thermal system design.

With radial fins in place, the heat transfer rate q_t, is given by [Incropera *et al.* (2013)]:

$$q_t = hA_t\left[1-\frac{NA_f}{A_t}(1-\eta_f)\right]\theta_b \quad , \tag{3.29}$$

where, h is the convective heat transfer coefficient, A_t is the total surface area associated with the fins and the object, N is the fins number, each fin surface area A_f , single fin efficiency η_f , and θ_b is the temperature gradient between outer surface of the object and environment.

Keeping the goal as less fin area for optimum heat transfer rate; by varying fin geometries, such as, width f_w, height f_h, number of fins N with spacing between fins s_f is achieved, as shown in Figure 3.15.

3.6.1d. Heat Transfer Modes in the RF cavity

Heat transfer, defined as the transmission of thermal energy from one region to another as a result of the temperature gradient. It generally takes place by three different modes: Conduction, convection and radiation. The modes of heat transfer are quantified by the appropriate rate equations which give the heat transfer per unit area.

In the present problem, heat transfer through the conduction and forced convection modes are chosen to analyze the system. For heat transfer by conduction, the rate equation is known as Fourier's law, and the convective heat transfer process is described by the rate equation known as Newton's law of cooling [Incropera *et al.*(2013)]. The heat transfer from the inner surface to the outer surface of the cavity occurs in the conduction mode and from there on by convection mode to the fluid. The effects of the heat transfer on the cavity due to wall loading can be assessed in terms of

surface temperature and radial deformation at the inner and outer walls of the cavity. Heat transfer and structural analyses can be performed using computational fluid domain simulation software, like, ANSYS, STAR-CCM and COMSOL. In the present work, the thermal and structural analysis of the tapered cylindrical RF interaction cavity is carried out adapting a commercial code "COMSOL Multiphysics" whose GUI is more users friendly and simpler to implement than those of ANSYS, used in previously reported work, though is equally accurate [Salvi *et al.* (2010)].

3.6.2. Heat Transfer Analysis Using "COMSOL MULTIPHYSICS"

A commercial code "COMSOL Multiphysics" is adapted here for the structure thermo-mechanical effect investigation. This code is a cross-platform finite element analysis solver and multi-physics simulation software. It allows conventional physics-based user interfaces and coupled systems of partial differential equations. In the present study, the heat transfer module and solid mechanics module in COMSOL is chosen for the thermo-mechanical analysis of the interaction structure.

3.6.2.a COMSOL Multiphysics simulation modeling

In general the investigation process of a problem in COMSOL simulation domain process consists of four steps: 1) modeling of the geometry and assigning materials with given electrical and thermal properties; 2) based on problem investigations, selection of suitable physics modules, assigning the same to the geometry by updating it with the given input conditions, like, type of domain, type of boundaries and initial values, etc.; 3) initializing the study step: by selecting type of study either steady state or time dependent, and coupling between physics modules if necessary; and then 4) Define the mesh distribution by setting sequence type and type of element used for calculations.

In the present problem, considering the symmetry nature of the interaction cavity, for geometry realization 2D axis symmetric model in COMSOL is selected and interaction cavity is modeled as per the parameters listed in Table 3.4. From the material library, the OFHC copper with various material properties at 293.5 K as listed in Table 3.8 are assigned. In the work for both RF and Thermal calculations, the electrical conductivity of the cavity material has been chosen as 5.8e7 S/m. The modeled interaction cavity structures without and with radial fins in the COMSOL Multiphysics are shown in the Figure 3.16.

Table 3.8: Interaction cavity material properties at 293.5 K

Material properties	**Value (units)**
Cavity Material	(OFHC/OF) copper
Density	8939 (kg / m^3)
Electrical conductivity	$5.8*10^7$ S/m
Thermal conductivity	401 (W / (m. K))
Specific heat	383 J / (kg. K)
Elasticity modulus	126 (GPa)
Coefficient of Thermal expansion	$1.6719*10^{-5}$ (1/K)
Poisson ratio	0.3351

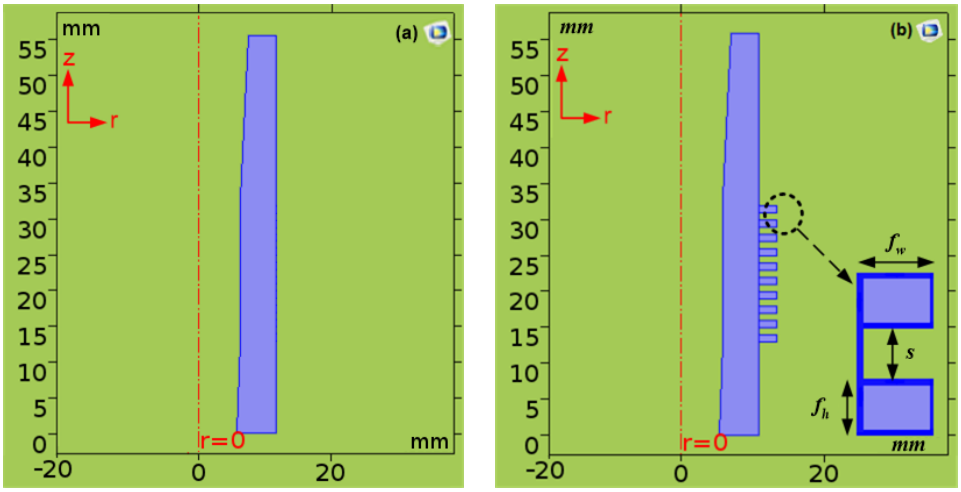

Figure 3.16: 2D axis symmetric interaction cavity models (a) without and (b) with radial fins simulated in COMSOL (fh = fin height, f_w = fin width and s_f = spacing between fins).

Heat transfer in solids and solid mechanics physics modules have been selected for the thermal and structural investigations of the interaction structure respectively and both physics are coupled. Coming to the assigning of boundary conditions, in the heat transfer in solids physics module, the wall loading profile (ohmic power loss density) calculated from expression (3.27) and shown in Figure 3.17, is loaded as the heat flux at the inner wall surface of the structure which causes the thermal effects and leads to structural deformations.

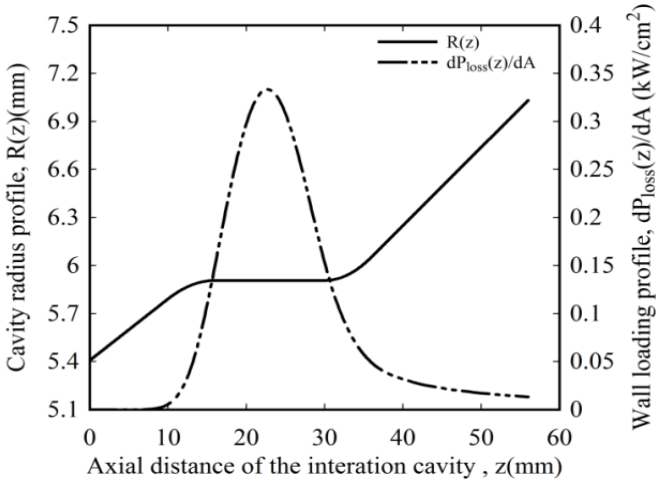

Figure 3.17: Wall loading profile (ohmic power loss density) for operating $TE_{6,2}$ mode of the gyrotron(electrical conductivity σ = 5.8x107 S/m).

Since our goal is to study the thermal effects and thereby designing the optimized cooling system, so the heat flux at the outer cavity walls is chosen in convective heat flux mode that transfers heat from inside to outside surface and thereby restricts the structural deformations, and is explained as:

$$q_o = h(T_{ext} - T_\infty) \quad , \tag{3.29}$$

where T_{ext} is the outer surface temperature of the structure and T_∞ is the ambient temperature. Since, the heat transfer takes from high temperature to low temperature so in the present problem it occurs from inner surface to outer surface that allows surface deformation from inner to outer surface [Incropera *et al.* (2013)]. In the present study, by fixing ambient temperature T_∞ at 293.5 K, for various convective heat transfer coefficient h (W/m^2.K) values the simulations are carried out. The axial end surfaces of the interaction cavity not subjected to heat flux are thermally insulated for the study.

The temperature distribution of the interaction cavity resulted from the heat transfer in solids physics module is coupled to the solid mechanics physics module as thermal load for the deformations study. Maintained fixed constraints on the axial end surfaces and free to move constraints on the radial surfaces of the interaction cavity, the structural deformations have been calculated. A steady-state, with coupling between physics modules study and sequence type of physics controlled mesh with extremely fine element type is selected for the simulations.

Firstly, the thermo-mechanical analysis using COMSOL Multiphysics code is performed by considering various thickness values of the interaction cavity from the middle section, δR = 3 mm to 7 mm at different values of heat transfer coefficient h of the coolant under no fins condition. Then, by considering radial fins over the middle section with various fin width $f_{w,}$ fin height f_h, spacing between fins s, and different number of fins N, the thermo-mechanical analyses on interaction cavity are also carried out.

In the present work, considering radial fins along the middle section of the cavity (L_c), the thermal system is optimized by maintain the temperature of coolant at room temperature. The allowed tolerances of radial deformations (increase) at the inner

cavity radius is upto 6 μm such that oscillation frequency shifts at maximum upto 0.1 GHz [Kartikeyan *et al.* (2013)] with average outer surface cavity temperature ~ 300 K. For this purpose, different convective heat transfer coefficient *h* values are chosen which solely describe the fluid dynamics parameters [Incropera *et al.* (2013)], such as, fluid flow rates, hydraulic diameter, etc. Generally, in forced convection mode, for liquids, heat transfer coefficient *h* lies in the range between 100-20000 ($W/m^2.K$) and for convection with phase change boiling or condensation; the heat transfer coefficient *h* lies in the range of 2500-100000 ($W/m^2.K$) [Incropera *et al.* (2013)]. In the present problem, the study is limited with heat transfer coefficient *h* from 4000 to 20000 ($W/m^2.K$), means no boiling or condensation of the fluid in the cooling system design is allowed.

The impact of thermal system parameters on the RF interaction cavity under the ohmic wall loss are assessed in terms of cavity outer surface temperatures by thermal analysis and radial deformations at cavity inner surfaces by structural analysis and are discussed in detail. Subsequently, the thermo-mechanical effects on the RF behaviour of the interaction cavity at optimized cooling system parameters are investigated using the nonlinear time-dependent multimode theory [Fliflet *et al.* (1991)].

3.6.3 Result and Discussion

The thermo-mechanical effect of ohmic loss generated due to the microwave power radiated in the tapered cylindrical interaction cavity of the gyrotron has got investigated. The structure is modeled and simulated using commercial code "COMSOL Multiphysics". Considering various cavity thickness δR values at different convective heat transfer coefficient *h* values, for without fins and with radial fins groups are studied. Initially, investigations are carried out for structure without fins, labeled as

"WOG" group. As described in above, the effects are measured in terms of radial deformations (increase) ΔR_{rad} at inner and temperatures T_{out} at outer surface of the interaction cavity.

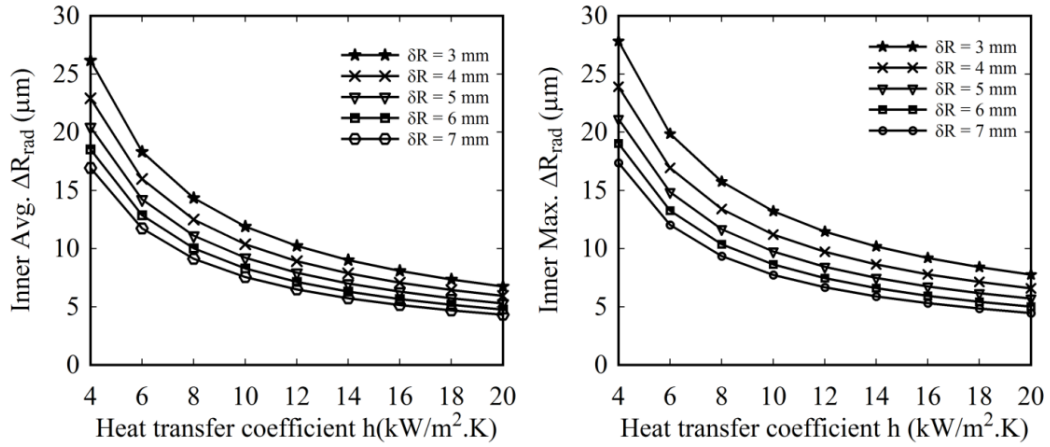

Figure 3.18: Radial deformation ΔR_{rad} at the cavity inner surface for various heat transfer coefficient h and cavity thickness δR values (a). Average and (b) Maximum.

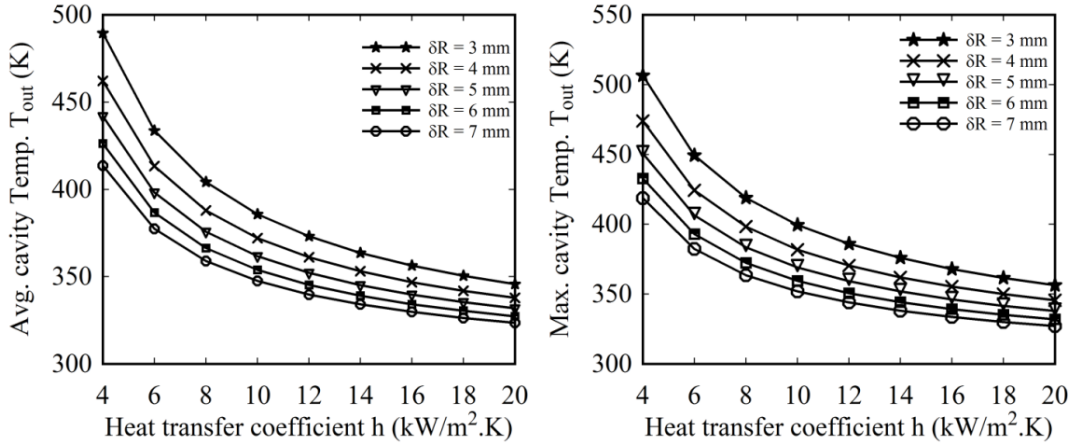

Figure 3.19: Temperature at the cavity outer surface Tout for various heat transfer coefficient h and cavity thickness δR values (a) Average and (b) Maximum.

Since, due to the non-uniform nature of the heat flux, for the initial study, both the average and maximum values of inner ΔR_{rad} and T_{out} at inner and outer surfaces are plotted as Figures 3.18 -3.19, respectively.

As expected, it can be easily observed from the Figures 3.19-3.20 that for higher values of convective heat transfer coefficient *h*, the amount of radial deformations (increase) and the temperature values of the cavity are decreasing monotonically with increasing of cavity thickness δR means increment in the heat transfer rate. In order to restrict the magnitudes of radial deformations (increase) ΔR_{rad} and the cavity temperatures T_{out} under the desired values, radial type fins have been introduced on the outer surface of the interaction cavity. From the preliminary studies without fins (WOG group), the probable range of convective heat transfer coefficient *h* and cavity thickness δR are suitable for the optimum thermal system design of cavity structure are selected. Secondly, there is a nominal variation in the average and maximum levels of radial deformations ΔR_{rad} at the inner surface, as well as considering the temperatures at the outer surface the average surface T_{out} are of important for the optimization of the thermal design. Thus, the variations of maximum inner radial deformations (increase) ΔR_{rad} and average outer surface temperatures T_{out} for the fin groups are shown in the rest of the analysis.

For achieving the desired performance of the thermal system with minimum fins area is always desired and, the fins area is increased by varying the fins geometrical parameters in a systematic way and simultaneously observing the maximum radial deformations (increase) and average temperature values of the interaction cavity by using COMSOL Multiphysics. Considering moderate power levels in the interaction cavity, the radial fin groups labeled as RG1, RG2, RG3, and RG4 are placed in the middle part region (L_c) on the outer surface of the RF interaction cavity. Different geometrical parameters of the fin groups are listed in Table 3.9 with uniform spacing s = 1 mm between the fins.

Table 3.9: Dimension of various radial fin groups

Fin group	Fin width f_w (mm)	Fin height f_h (mm)	Number of fins N
WOG	0	0	0
RG1	2	1	10
RG2	2.5	1	10
RG3	3	1	10
RG4	3.5	1	10

The thermo-mechanical simulations are carried out with the various fins groups for the range of convective heat transfer coefficient h from 8000 to 16000 (W/m^2.K), and cavity thickness δR=3 mm to 5 mm. Maximum inner radial deformation (increase) ΔR_{rad} and average cavity outer surface temperatures T_{out} for the fin groups are tabulated in Table 3.10 and Table 3.11.

Table 3.10: Maximum values of radial deformations (increase) ΔR_{rad} at cavity inner surface for various radial fin groups (RG1, RG2, RG3, RG4) at various heat transfer coefficient h and thickness δR values.

Heat transfer coefficient, h (W/m^2.K)	δR, mm	WOG ΔR_{rad} (µm)	RG1 ΔR_{rad} (µm)	RG2 ΔR_{rad} (µm)	RG3 ΔR_{rad} (µm)	RG4 ΔR_{rad} (µm)
8000	3	15.752	6.920	6.070	5.424	4.907
8000	4	13.384	6.186	5.084	4.554	4.135
8000	5	11.672	5.608	4.416	3.967	3.614
10000	3	13.211	5.774	5.474	4.921	4.483
10000	4	11.205	5.164	4.584	4.137	3.782
10000	5	9.742	4.682	3.986	3.609	3.311
12000	3	11.465	5.000	5.011	4.582	4.297
12000	4	9.717	4.476	4.200	3.853	3.625
12000	5	8.433	4.061	3.657	3.365	3.174
14000	3	10.182	4.441	4.807	4.405	4.151
14000	4	8.629	3.980	4.010	3.716	3.521
14000	5	7.479	3.614	3.484	3.254	3.097
16000	3	9.193	4.016	4.653	4.248	4.016
16000	4	7.794	3.605	3.900	3.599	3.421

16000	5	6.751	3.277	3.402	3.163	3.020

Table 3.11: Average cavity outer surface temperatures of various radial fin groups (RG1, RG2, RG3, RG4) at various convective heat transfer coefficient *h* and cavity thickness δR values.

Heat transfer coefficient *h* (W/m2.K)	***δR* mm**	**WOG T_{out} (K)**	**RG1 T_{out} (K)**	**RG2 T_{out} (K)**	**RG3 T_{out} (K)**	**RG4 T_{out} (K)**
8000	3	404.2	339.9	333.3	328.1	323.9
8000	4	387.8	334.4	328.8	324.3	320.6
8000	5	375.7	330.1	325.1	321.2	318.0
10000	3	385.8	331.0	325.5	321.2	317.8
10000	4	372.0	326.5	321.8	318.1	315.2
10000	5	361.7	323.0	318.9	315.6	313.0
12000	3	373.0	325.0	320.3	316.7	313.8
12000	4	361.1	321.2	317.2	314.0	311.5
12000	5	352.2	318.2	314.7	311.9	309.7
14000	3	363.6	320.6	316.5	313.4	310.8
14000	4	353.0	317.3	313.8	311.1	308.9
14000	5	345.1	314.7	311.7	309.3	307.3
16000	3	356.3	317.3	313.7	310.9	308.7
16000	4	346.8	314.4	311.3	308.9	307.0
16000	5	339.7	312.1	309.4	307.3	305.6

For the radial fin groups RG3 and RG4, the range of *h* from 14000 to 16000 with δR = 5 mm, the maximum inner radial increase is less than 3.25 μm which is of our design constraint and the average cavity outer surface temperature is at 310 K.

For the optimum range of heat transfer coefficient *h* values, considering water as a coolant with T_{fluid} at 293.15 *K*, the range of various thermal system parameters, like, hydraulic diameters (D_h) through which the coolant is flown, at different water flow rates are calculated and are shown in the Figure 3.20 [Incropera *et al.* (2013)].

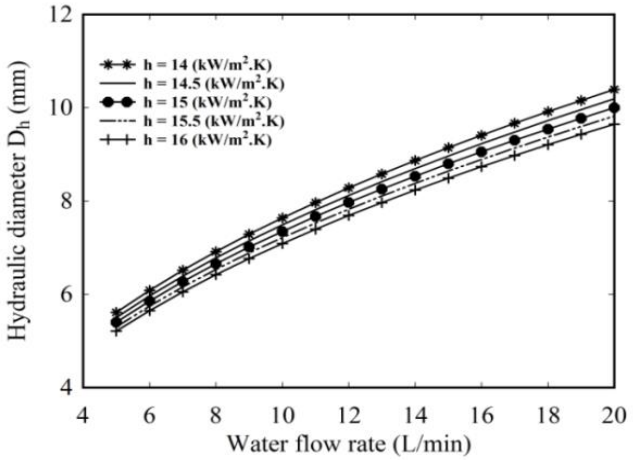

Figure 3.20: Range of hydraulic diameter D_h and water flow rates of the thermal system for the optimized convective heat transfer coefficient h values.

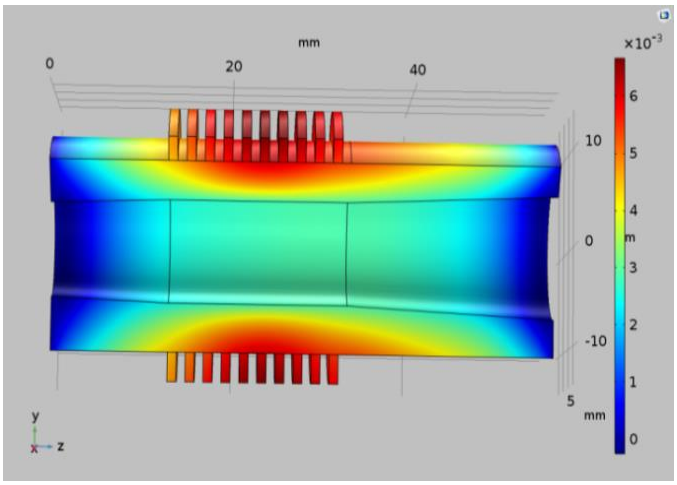

Figure 3.21: 3D view of the radial deformation distribution for heat transfer coefficient h=15000 (W/m2.K) and δR=5 mm of RG3 group.

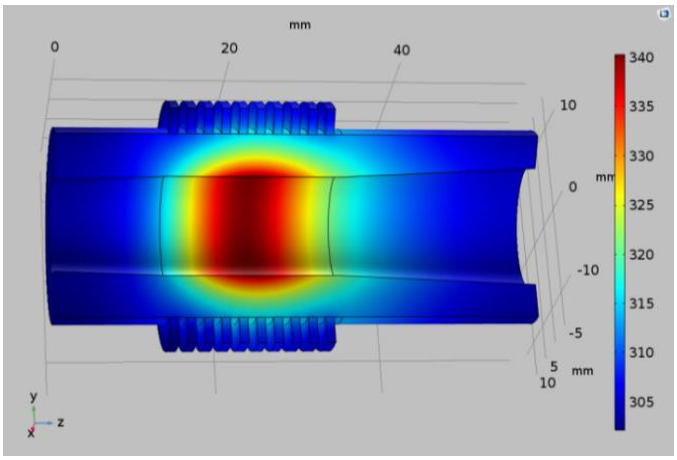

Figure 3.22: 3D view of temperature distribution for heat transfer coefficient h=15000 (W/m2.K) and cavity δR= 5 mm of RG3 group.

The 3D view of temperature distribution and the radial deformation (increase) distribution of interaction cavity for optimized heat transfer coefficient h as 15000 ($W/m^2.K$) and cavity thickness δR = 5 mm, for RG3 fins group, are shown in Figures 3.21 and 3.22.

It can be observed that the average value of cavity outer surface temperature T_{out} is around $308K$ and the maximum radial increase ΔR_{rad} at the inner surface of the cavity is ~3.2µm that is within tolerable limits of the targeted design parameters. The deformations occurring around the outer surface is of maximum 6 µm, a collective one from inner to outer surface. Comparatively, the surface deformation at the inner walls is more because of the presence of heat source which causes larger temperature rise than the coolant temperature. Due to the coolant, the heat transfers faster to the outer surface thereby maintaining desired operation. The cavity radius profiles of initial and the deformed cavity with in tolerable limits at the optimized cooling system parameters are shown in Figure 3.23.

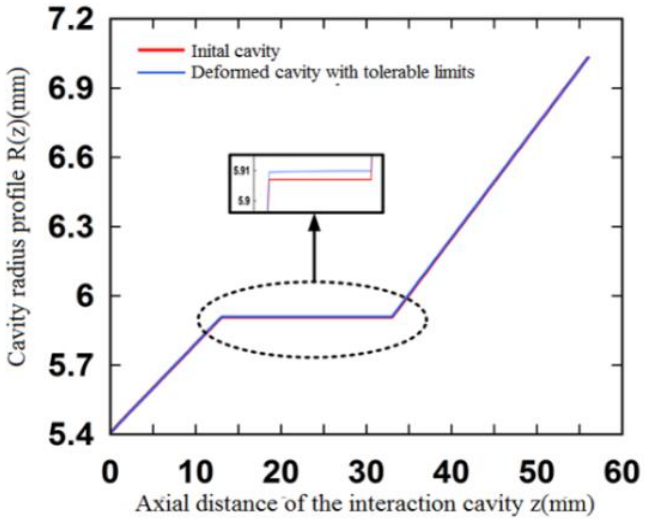

Figure 3.23: Initial (red colour) and deformed cavity (blue colour) due to ohmic loss at optimized thermal system parameters.

Now, the study is further extended to investigate thermo-mechanical effects on the RF behaviour of the deformed cavity with tolerable limits at initial and final (steady state) conditions. RF behaviour of the device under both conditions, cold (in absence of electron beam) as well as hot (in presence of electron beam) are investigated. At cold condition, the axial RF field profile and the resonant frequency and quality factors of the cavity are calculated by solving the wave equation in the cavity at radiation boundary conditions that leads minimum reflection mentioned in Section 3.2. The comparisons of cavity field amplitudes with resonance frequency and quality factors of both initial and deformed conditions (with RG3 fins, h =15000 W/m^2.K, δR = 5 mm) are plotted in Figure 3.24. It can be observed that with designed cooling system, maximum reduction in the resonant frequency f_{res} is 48 MHz and a decrement of 20 in the diffractive quality factor Q_{diff} occurred from the initial cavity values (cold condition).

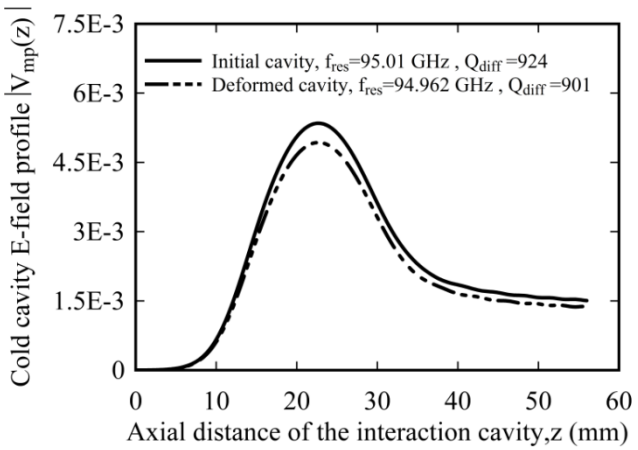

Figure 3.24: Cold cavity field amplitude profiles for the initial and deformed cavity.

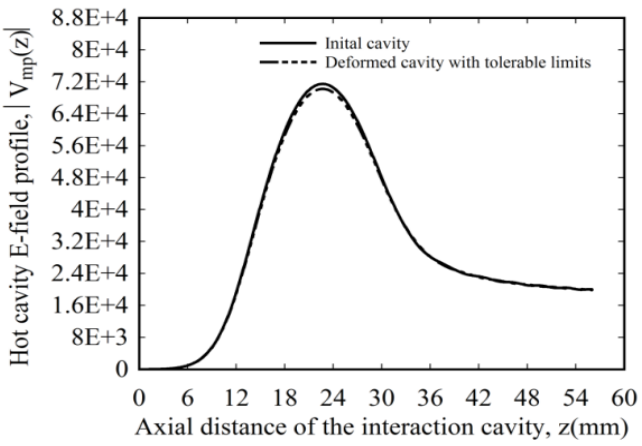

Figure 3.25: Hot cavity electric field profiles of initial and deformed cavity.

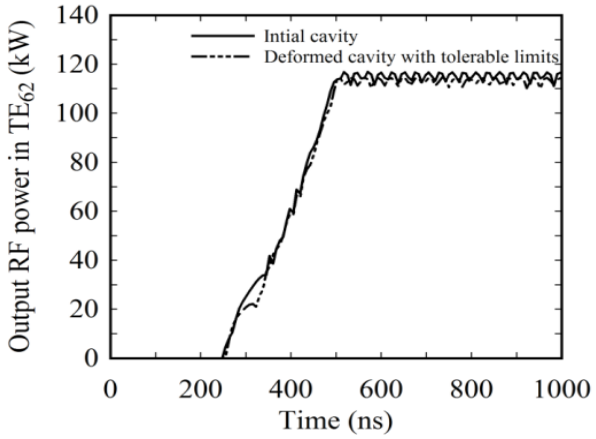

Figure 3.26: Comparisons of power levels in the $TE_{6,2}$ for initial and deformed cavity.

To study the effect of cavity deformation under hot (in presence of electron beam) condition, we have revisited the non-linear, time dependent, multimode theory of the gyrotrons presented in Section 3.5. Maintaining the same beam parameters with zero velocity spread, gyrotron device performance with the deformed RF interaction cavity is obtained. The field amplitude profile and power levels in various modes are calculated. Comparisons of hot cavity field amplitude profiles and the output power levels in the operating modes $TE_{6,2}$ for initial and deformed cavity with tolerable limits are plotted in Figures 3.25 and 3.26. It can easily be noted a reduction of ~ 2 kW in RF output power in the case for the deformed cavity from the initial cavity gyrotron device.

3.7. Conclusions

In the present chapter, the design, analysis and PIC simulations of RF interaction cavity of gyrotron operating $TE_{6,2}$ mode at 95GHZ for generation of 100kW of RF power has been presented. Considering the velocity spreads and misalignments of the beam axis with respect to the cavity axis, the structures have been simulated in the Commercial "CST studio suite". In addition, the effect of ohmic losses due to RF generation has been evaluated by the thermal studies with the help of a commercial PIC tool "COMSOL Multiphysics". It is observed that, the beam axis shift and tilt are affecting majority on RF power level and mildly on the operating frequency. Secondly, for small transverse dimensions structures, the thermal losses are significant and needs an efficient cooling system for longer life and reliable operation. Though, $TE_{6,2}$ is one of suitable mode in the 95GHz regime for gyrotrons, but observing the effects of misalignments and thermal losses on the frequency of operation, the interest has been raised to see the use of volumetric modes as the operating mode and its effects on the RF performance and thermal studies under some practical considerations like beam shift. Beam tilt and velocity spreads.

After the beam-wave interaction behaviour study of the gyrotron, the thermo-mechanical study of the RF interaction cavity, its effects on the RF power generation have been carried out for a $TE_{6,2}$, 95 GHz, 100 kW gyrotron. Thermal system design has been validated using a commercial PIC tool, which was not found in the published literature to the authors, using "COMSOL Multiphysics" commercial tool. Implementation of this code has been found simpler than those previously reported though equally accurate. For stable device operation, with the help of the design relationships, radial cooling fins design for the cavity has been presented. Further, describing the approach, an optimum thermal system has been designed and

performance got simulated. Thermo-mechanical behaviour of the interaction cavity structure for various cavity thicknesses, and convective heat transfer coefficient values under without fins and with radial fins conditions have also been investigated. Considering water as coolant at room temperature ~293 K, the range of hydraulic diameter and flow rates have been determined for the optimum convective heat transfer coefficient values from 14000 - 16000 W/m2.K. An optimized simple cooling system thus designed keeps the maximum RF cavity radius deformation (increase) ~ 3.2 μm maintaining the average cavity outer surface temperature of 308 K. Furthermore, a nonlinear time-dependent multimode analysis has also been carried out to observe the RF output behaviour of the gyrotron under such condition. A decrease in its resonance frequency of 48 MHz and a decrement of 20 in the diffractive quality factor of the RF interaction cavity with the reduction of 2 kW of RF output power have been observed in the case for the deformed cavity from those of the initial cavity gyrotron device, which are within the tolerance limit of such devices. We hope that the thermo-mechanical analysis, radial cooling fins and cooling system design, its optimization as well as description of simpler simulation technique using commercial code "COMSOL Multiphysics" for the gyrotron RF interaction cavity carried out here would be useful not only to the tube designers but also to the high power microwave system developers.

Keeping above mentioned points for the gyrotron in our mind and in order to mitigate the thermo-mechanical issues; in the upcoming Chapter, Chapter 4, the same rating gyrotron device operating at a relatively high order mode will be investigated. As we know that the RF structure of the device operating at the higher order mode will be larger. Hence it is expected that here thermo-mechanical issues will get relaxed. Such gyrotron device design, its RF analysis that includes nonlinear section including thermo-mechanical analysis will be carried out and presented in Chapter 4.

CHAPTER 4

DESIGN, ANALYSIS AND BEAM-WAVE INTERACTION STUDIES OF FIXED FREQUENCY (95 GHZ 100KW CW, $TE_{10,4}$ MODE) GYROTRON OPERATED IN THE VOLUMETRIC MODE

4.1. Introduction

In Chapter 3, the gyrotron device design constraints, linear theory and nonlinear theory used for the design and analysis of the cylindrical tapered interaction cavity gyrotrons have been described and demonstrated. As well as, the RF simulation study using commercial 3D PIC code "CST studio suite" and thermal studies using commercial PIC code "COMSOL Multiphysics" have been presented. It has been observed that, the thermal effects due to ohmic losses limits the margins of cavity dimensions tolerances and that necessitates the presence of cooling maintenance system for the high power devices. As well as, the shifts in the beam sources, i. e., misalignment of the beam axis with respect to cavity axis, are also found to limit the operation. Since, the dimensional and beam radius variations are also get scales with operating modes, so lower order mode gives small margin of tolerances, even though mode like, $TE_{6,2}$ is widely used at 95GHz frequency for 100 kW gyrotron, but observing these effects, we wants to investigate the advantages as well as challenges by operating this specification gyrotron device in the higher order volumetric modes, which is so far not fully explored and reported in the published literature, at least not accessible to us.

Considering the challenges and issues related to thermal and misalignments, in this chapter, Chapter 4, we designed, analyzed and simulated an RF interaction cavity for the same rating device that operates in a relatively high order mode $TE_{10,4}$- that allows a wide transverse dimensions thereby more relaxation regarding thermal issues as well can be upgraded to high power levels too. In the literature, Krishna *et al.* (2011), have started the mode selection and the analysis of RF interaction cavity in the absence of electron beam but not much details about the beam wave interaction studies that includes RF analysis and thermal analysis as well the post interaction components, like, nonlinear taper, and RF window designs were not reported. Considering this gap,

additionally the goals mentioned in the Chapter 3, in the present work, the design, analysis and simulated the interaction cavity that gives the desired power in the operating mode $TE_{10,4}$- and larger dimension relaxes the thermal issues is presented. After the design of interaction cavity by adding the nonlinear taper section, the beam wave interaction studies are revisited using time dependent multimode theory with uniform profile of magnetic field. The detailed design methodology, beam wave interaction studies are described in this chapter.

With the help of the theories presented in Chapter 3, the design constraints values for the various modes of the design beam parameters, the mode selection and the identification of the compete modes are determined as per the beam parameters Later on, using Vlasov approximation the RF cavity dimension was got determined.

In addition, the nonlinear taper that acts as impedance matching unit between interaction structure and the collector circuits and allows the transmission of generated RF power to the RF window with minimum mode conversion, is presented. In the present design, the NLT is designed such that quasi-optical mode converters can be used for transmitting interaction cavity mode TE_{mn} into free space Gaussian beam mode TEM_{00}.

Like the beam wave interaction studies in the interaction cavity region presented in Chapter 3, for the current design, by adding the nonlinear taper region, the beam wave interaction studies are performed. As well, the beam misalignment effects are incorporated into the time dependent multimode theory, the structures are analyzed. The NLT is confirmed through Vlasov approximation as well beam wave interaction studies allowing a constant uniform magnetic field profile. For the same, the 3D PIC

simulations, both for RF interaction as well as thermo-mechanical analysis are also performed integratedly here using a single tool "CST Studio Suite".

The Chapter has been organized as follows. Starts with the calculations of design constraints and the RF cavity dimensions using linear theories presented in Chapter 3, the beam wave interaction studies are performed using both analysis and 3D PIC simulation. The misalignment effects are added in the time dependent theory and the analysis is carried out for various beam widths. Followed by the design and analysis of the nonlinear taper (NLT) section and the beam wave interaction studies including NLT are presented. For the optimized cavity and NLT section, and the thermo-mechanical studies are reported.

4.2 Design Constraints and Mode Selection of Gyrotron

In Table 4.1, the design goals and constraints for the 95GHz, 100kW is outlined. Starting with the calculation of design constraints mentioned in Chapter 3, the suitable operating mode selection is carried out.

Table 4.1: Design goal and technical constraint values

Parameter	**Value**
Frequency f	95±0.1 GHz
Output power P_{out}	> 100 kW
Diffractive quality factor Q_{diff}	~2000
Beam current I_b	5 A
Beam voltage V_b	58 kV
Magnetic field at the cavity B	3.65±0.3 T
Pitch factor α	1.3-1.5
Harmonic number, s	1
Interaction efficiency η	>35%
Wall losses dP_{loss}/dA	< 2 kw/cm^2

Considering such design constraints and requirements of the device, a suitable operating mode selection is required for the achievement of the targeted goals. Sometimes, it is not feasible for modes to maintain all the design constraint within the limits and trade-off among constraints needs to be considered

In the present design, we are intending for the larger transverse dimension that relaxes the mode converter design as well further reduces ohmic losses that relaxes the need of the thermal management system thereby assurance of reliable device operation over longer period.

Table 4.2: Design constraints values for different modes

m	**n**	R_c **(mm)**	R_b **(mm)**	V_d **(kV)**	I_L **(A)**	**Peak ohmic loss** dP/dA **(kW/cm^2)**	m/X_{mp}	Δf_1	Δf_2
0	1	1.9256	0.9252	0.8198	49.841	6.188	0	51.9	109.1
2	1	1.5348	0.9252	0.5662	72.17	17.056	0.654	39.719	74.56
4	2	4.6649	2.1113	0.8868	46.08	1.295	0.430	13.651	8.039
5	2	5.2868	2.6723	0.7631	53.54	1.060	0.475	11.763	5.23
6	2	5.8975	3.2242	0.6754	60.49	0.893	0.511	10.354	3.31
6	3	7.6731	3.2242	0.9698	42.13	0.460	0.393	8.390	4.47
7	2	6.4993	3.7698	0.6092	67.07	0.768	0.541	9.259	1.93
7	3	8.3070	3.7698	0.8837	46.23	0.405	0.423	7.630	3.42
8	2	7.0939	4.3109	0.5571	73.34	0.671	0.566	8.382	0.910
8	3	8.9325	4.3109	0.8149	50.14	0.360	0.450	7.002	2.595
8	4	10.6689	4.3109	1.0136	40.31	0.234	0.376	6.063	3.07
9	2	7.6825	4.8484	0.5148	79.36	0.595	0.588	7.661	0.122
9	3	9.5510	4.8484	0.7584	53.88	0.324	0.473	6.475	1.932
9	4	11.3083	4.8484	0.9473	43.13	0.213	0.400	5.654	2.532
10	2	8.2661	5.3832	0.4797	85.17	0.532	0.608	7.059	0.494
10	3	10.1633	5.3832	0.7108	57.48	0.294	0.494	6.025	1.391
10	**4**	**11.9412**	**5.3832**	**0.8912**	**45.85**	**0.195**	**0.420**	**5.30**	**2.074**
10	5	13.6607	5.3832	1.0417	39.22	0.142	0.367	4.748	2.344
10	6	15.3455	5.3832	1.1718	34.87	0.109	0.327	4.309	2.436

A systematic procedure for suitable mode selection is adapted by considering a group of modes where azimuthal and radial indexes modes of up to 10. Considering effective length of the interaction cavity as 30.00 mm, at the design parameters listed in the above Table 4.1, using expressions (3.1) - (3.5) from Chapter 3, the design constraints for various modes are calculated and tabulated in Table 4.2.

Observing design constraints values for different modes, $TE_{0,1}$, and $TE_{2,1}$ modes can be eliminated owing to their smaller dimensions whose diameters are in the order of operating wavelengths, excessive Ohmic losses, respectively. There are several lower and higher order modes that can be suitable as an operating mode for the present design. But as stated above, in order to investigate the advantages of the larger transverse dimension of the RF interaction cavity structure on the RF performance, the asymmetric volume modes are suitable as the operating modes for the present problem. Considering low ohmic losses, larger transverse dimension and possibility of the implementation of the internal mode converters for the radial RF output coupling, $TE_{10,4-}$ mode is chosen as operating mode for the present study/design, where '-' and '+' indicates co-rotating and counter-rotating modes.

The limiting current I_L and voltage depression V_{dep} curves for the $TE_{10,4-}$ mode over a range of normalized beam radius values are calculated for the beam parameter listed in Table 4.1 and is plotted as Figure 4.1.

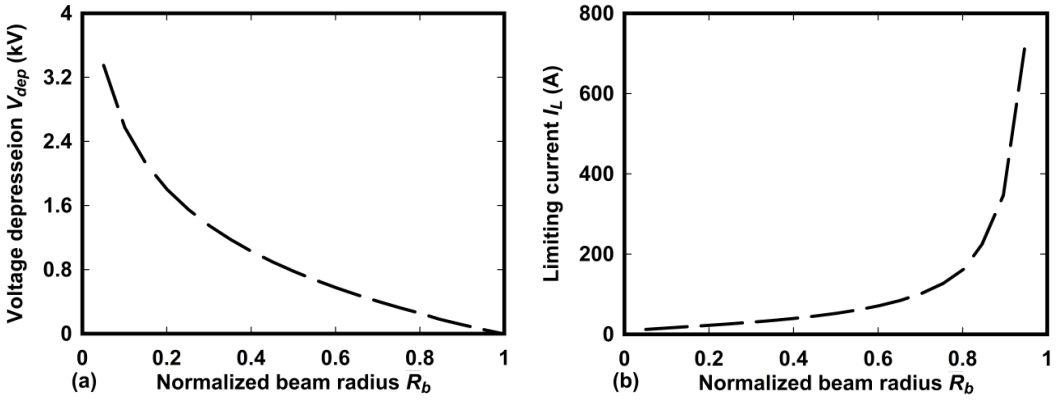

Figure 4.1: (a) Voltage depression V_{dep} (kV) versus normalized beam radius $\overline{R_b}(=R_b/R_c)$, and (b) Limiting current I_L (A) versus normalized beam radius $\overline{R_b}(=R_b/R_c)$ for $TE_{10,4-}$ mode.

After the selection of operating mode, the RF interaction cavity that provides space for the beam wave interaction has to be designed. The role of the interaction structure is to allow the growth of the operating mode at desired frequency of oscillation while suppressing the mode conversion when subjected to the beam parameters. The background analysis required for the RF cavity design and the selection of the cavity dimensions are presented in the following subsection.

4.3. Design of RF Interaction Cavity

As considered in Chapter 3.2, in the present design also, a conventional tapered cylindrical structure as RF interaction cavity is taken .The design of interaction cavity requires knowledge of axial RF field profile $V_{mp}(z)$, resonating frequencies f_{res}, and its quality factor Q_{diff}. By solving the Vlasov approximation equation using Numerov's methods, the interaction cavity geometries have been determined for several combinations.

Table 4.3: RF cavity parameter for various cavity combinations

Parameter	Set#1	Set#2	Set#3
L_d (mm)	15	15	15
L_c (mm)	28	30	32
L_{up}(mm)	10/15/20	10/15/20	10/15/20
θ_d	2^0	2^0	2^0
θ_{up}	1.8^0	1.8^0	1.8^0
L_{ds} (mm)	4	4	4
L_{us}(mm)	4	4	4
f_{res} (GHz)	95.035	95.01	94.985
Q_{diff}	1580	2250	2620

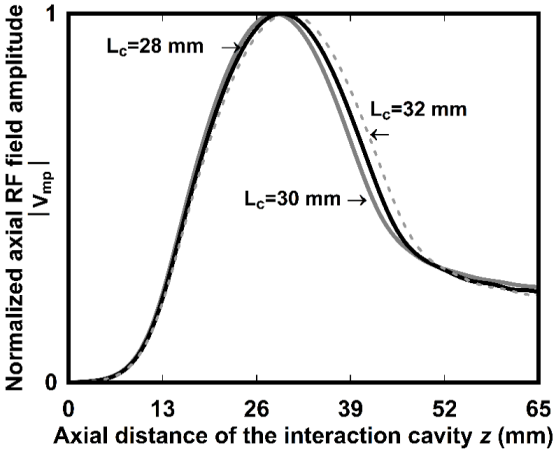

Figure 4.2: Normalized axial RF field amplitude profiles for various uniform section lengths: L_c= 28.00 mm (solid light), 30.00 mm (solid) and 32.00 mm (dashed light)

As described in Chapter 3, using a systematic cavity design procedure [Kalaria *et al.* (2016)], calculations is performed for various cavity geometry combinations. The suitable combinations and the corresponding cavity parameters in the cold condition (beam absent) i.e., J_{mp}= 0 are tabulated in Table 4.3.

The normalized axial RF field amplitude profiles for various uniform section lengths (L_c) are plotted in Figure 4.2. Longer cavity length provides longer interaction region, requiring lower beam current, however it results in larger quality factor Q_{diff}. Considering the advantages of lower beam current of operation and longer interaction

space over larger Q_{diff} values, the optimized interaction cavity dimensions are listed in Table 4.4.

Table 4.4: Optimized tapered RF cavity dimensions

Parameter	Value
Cavity radius R_c	11.94 mm
Down taper length L_d	15 mm
Middle section Length L_c	30 mm
Up taper length L_u	20 mm
Parabolic smoothing L_{ds}	4 mm
Parabolic Smoothing L_{us}	4 mm
Down taper angle θ_d	2^0
Up Taper angle θ_{up}	1.8^0
Resonant Frequency f_{res}	95.01 GHz
Diffractive quality factor Q_{diff}	2250

Following the determination procedure of probable RF cavity dimension, the designed beam parameter needs to be optimized such that accomplishment of desired operation with the minimum mode competition is achieved. Using the coupling coefficient and the start oscillations curves, the optimum beam radius and the possible compete modes are suitably identified. The values are calculated using the expressions (3.8) – (3.10), from Chapter 3 and the corresponding values are mentioned below.

The optimum beam radius is taken, such that, achieving maximum coupling and have significant distance away from both the walls as well axis of the structure. Considering various modes, the Coupling coefficient C_{mp} curves for various modes with respect to normalized beam radius $\overline{R_b} = R_b / R_c$ are shown in Figure 4.3. It can be observed that the maximum coupling for the desired mode $TE_{10,4}$- occurs at normalized beam radius $\overline{R_b}$ = 0.451, accordingly electron beam radius is selected as 5.38 mm.

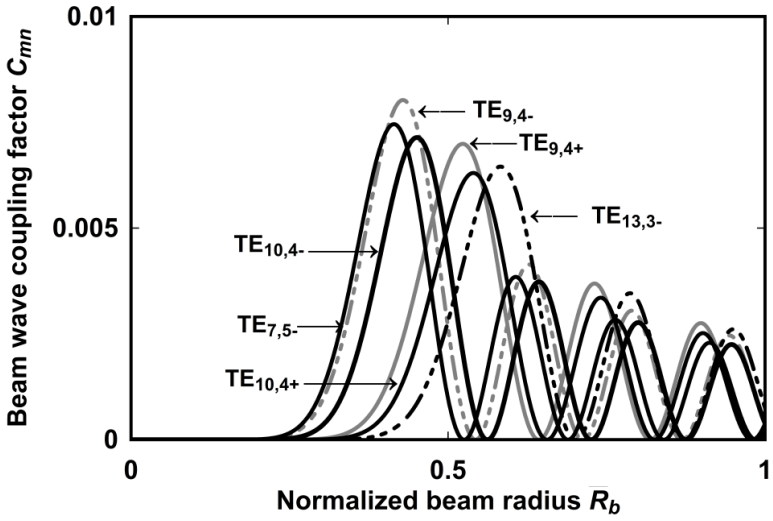

Figure 4.3: Beam wave coupling factor C_{mp} curves versus normalized beam radius ($\overline{R_b}$) for various modes.

Considering the beam parameter as mentioned in Table 4.1, the start oscillations curves for various modes for a range of magnetic fields from expressions (3.4) to (3.10) are calculated and are plotted in Figure 4.4.

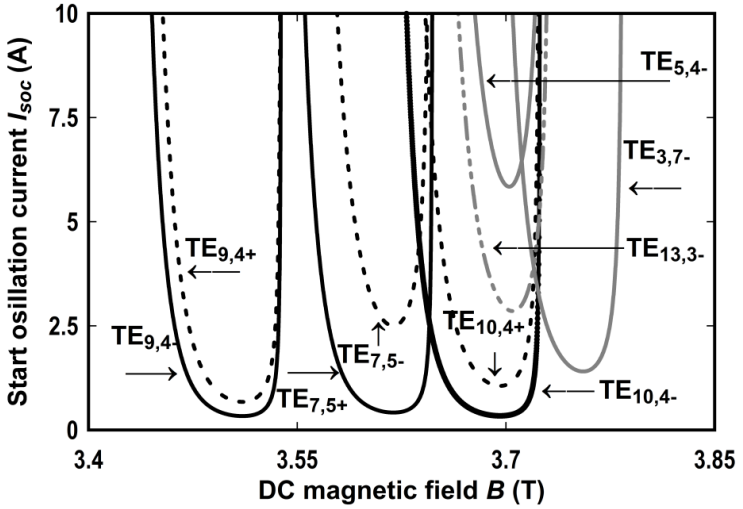

Figure 4.4: Start oscillation current I_{soc} (in amperes) versus DC magnetic field B in (Tesla) plots for different operating modes.

From the start oscillation current I_{soc} curves, it can be observed that $TE_{7,5+}$ is one of the main competing mode for the $TE_{10,4-}$, however a suitable selection of DC magnetic field can reduce its significance and are further examined during electron-beam and RF-wave interaction studies.

After determining the probable interaction cavity dimensions, the next step is to perform the beam wave interaction analysis that confirms whether the cavity is suitable and able to generate the desired power with suitable frequency. In the following section, using the time dependent multimode analysis mentioned in Chapter 3, the beam wave interaction analysis has been carried out and are explained in detail in the following section.

4.4. Beam-Wave Interaction Study

Taking the probable set of beam parameter and cavity dimension as obtained from Section 4.2, by studying the electron beam and RF wave interaction mechanism for operating mode along with competing modes, the design is to be confirmed with the optimized parameters. In the present section the beam wave interaction mechanism has been studied analytically using time dependent multimode analysis as well as through PIC simulation by CST studio suite.

4.4.1. Time-dependent multimode analysis with misalignment effects

In Chapter 3, the self-consistent time-dependent multimode nonlinear analysis developed by Fliflet *et al.* (1991) used for the study of the electron-beam and RF-wave interaction mechanism in the gyro devices is presented in detailed. In the theory the whole analysis has been carried out by considering axial symmetric gyrotrons i.e. both the beam and interaction cavity axis are sharing the same axis of symmetry as well are concentric to each other i.e., same centers. Practically, there might be situation where the concentricity does not meet, means beam axis either shifts or tilts with respect to the cavity frame. Hence, the beam wave interaction has to be studied considering these factors too for an efficient design. As in Chapter 3, these effects are investigated by 3D

PIC simulation but analytically using time dependent multimode theory has not been investigated.

The linear theory of the gyrotron with marginal shift of the beam axis with respect to cavity axis was developed and then generalized to coaxial cavities by Nusinovich *et al.* (2004), and Dumbrajs *et al.* (1995). Later, considering the beam tilt case, the theory was updated by Dumbrajs *et al.* (2013), and has discussed the effects with the help of self-consistent theory. With the help of this, we have updated/incorporated the addition factor that resulted due to the beam misalignments in the nonlinear, time dependent multimode theory developed by Fliflet *et al.* (1991), and the beam wave interaction studies are carried out. Secondly, the theory presented in Chapter 3 for multimode behaviour study in the interaction cavity, in the present chapter, by extending it to Nonlinear taper section, the after cavity interactions are by incorporating the original $h(z)$ profile function derived by solving the Vlasov approximation equation.

The RF generations in the high power microwave sources, are strongly influenced by the coupling between electron beam and the rotating TE_{mpq} waves. For the strong synchronization, both the electron beam optical system axis and the microwave circuit axis, i. e., interaction cavity axis are in concentric to each other and any misalignments severely effects on the RF performance. In the present section, the role of misalignments on the beam wave coupling are studies and later these factors are incorporated in the time dependent multimode theory presented in the Chapter 3.

In axially symmetric gyrotrons, the coupling of electrons gyrating about a guiding center with a radial coordinate R_b to rotating TE_{mp} waves can be determined by the L_s and given by

$$L_s = J_{m-s}(k_t R_b) e^{-i(m-s)\psi} \quad . \tag{4.1}$$

Here, R_b is the radial coordinate of the guiding center in the cavity frame and ψ is the guiding angles of the beam. As describe in the Figure 3.7, the coordinates of the electron guiding centres in the cavity frame (R_b, ψ) and in the beam frame (R_0, ψ_0) in case of electron beam axis displacement of d with respect to cavity radius and are related as

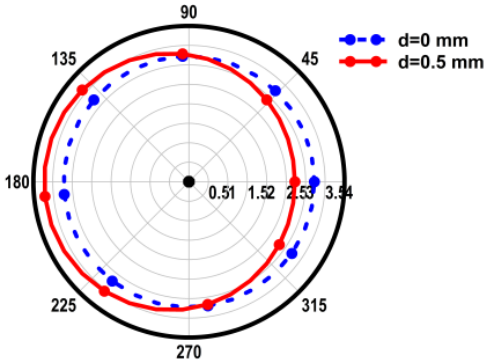

Figure 4.5: Beam misalignments effects: Location of beam lets for d = 0 mm and d = 0.5 mm.

$$R_0^2 = R_b^2 - 2dR_b \cos\psi + d^2 \ . \tag{4.2}$$

The coupling of the beam with $TE_{m,p}$ wave in the case of displaced beam is given by:

$$L_S = \sum_{m_a=-\infty}^{\infty} J_{m_a}(k_\perp d) J_{m-s-m_a}(k_\perp R_b) \mathrm{e}^{-i(m-s-m_a)\psi} \quad . \tag{4.3}$$

In the case of the parallel shift of the beam axis, the value of d is constant and independent of axial coordinate z. As well, assuming that the distance between two axes is always smaller than a wavelength, we can take account in the equation 4.3 only a limited number of terms, i. e., m_a value limits to few integer. In case of tilt in the beam axis, d varies with axial coordinate z and is given by :

$$d = \sqrt{(x_{00} + z\tan\alpha_x)^2 + (y_{00} + z\tan\alpha_y)^2} \quad , \tag{4.4}$$

where x_{00} and y_{00} are the transverse coordinates of the beam frame origin with respect to the origin of the resonator frame at the entrance and the angles $\alpha_{x,y}$ are the tilt angles in corresponding directions. Since x and y axes can be chosen arbitrarily, we can assume without a loss of generality that the beam is tilted in any one direction.

Hence, to describe the beam wave interaction in gyrotrons with a tilted beam by equations similar to those for a symmetric gyrotron, it is sufficient to introduce just one new function, which is the ratio of the beam coupling in a gyrotron with misaligned beam to that in a gyrotron with a concentric beam in the resonator mid-plane [Dumbrajs *et al.* (2013)]

$$T(z,\psi) = (\sum_{m_a} J_{m_a}\left[k_\perp(z)d(z)\right] J_{m-s-m_a}\left[k_\perp(z)R_0(z)\right] e^{im_a\psi}) / J_{m-s}(k_{\perp 0}R_{00}) \quad , \tag{4.5}$$

and

$$k_t(z)R_0(z) = k_{\perp 0}R_0\frac{R_c}{R(z)}\sqrt{\frac{B_{0,\max}}{B_0(z)}} \quad , \tag{4.6}$$

where $R_0\ (z)$ is the beam radius in case of the misalignment and R_{00} is the beam radius under no misalignment.

By revisiting the Chapter 3 from, the electron trajectory equations (3.14) – (3.16) and the mode field phase and amplitude equations (3.17) – (3.19), the beam wave coupling factor f_n is updated with the new term resulted by equations (4.5) and (4.6).

Now, considering the misalignment effects, the normalized mode amplitude is updated by:

$$f_n = \frac{|e|}{m_e c^2} x_n' C_n J_{m_n - s}\left(k_{nt} r_b\right) a_n\left(t_0\right) |T(z,\psi)| \tag{4.7}$$

and the phase terms in the equations (3.14) – (3.16) gets an additional term $\angle T(z,\psi)$.

4.4.1a Multimode analysis with ideal beam conditions

As mentioned in Chapter 3, the coupled equations are numerically integrated using fourth order Runge-Kutta method. Considering a ramp type of DC beam voltage source from 35 kV to 58 kV with rise time duration of 150 ns is taken. DC beam voltage is applied to a uniformly distributed gyrating electron beam having 32 beamlets with 32 electrons in each beamlets. For the operating and its neighboring modes, like, $TE_{7,5}$+, $TE_{7,5}$-, $TE_{9,4}$+, $TE_{9,4}$-, $TE_{10,4}$-, and $TE_{10,4+}$ beam-wave interaction behaviour is observed and its temporal power growth P_m are determined (plotted as Figure 4.6). It can observed here that initially $TE_{7,5}$+ mode dominates and after 300 ns it dies out completely whereas the desired operating mode $TE_{10,4}$- starts growing upto a stable RF power of ~123 kW; while all the competing modes reaches to a minimal value after 320 ns. An electronic efficiency of 40% is achieved at DC magnetic field of 3.65 T. Further, a parametric study is also performed analytically for range of applied DC magnetic fields and is discussed at the end of the section.

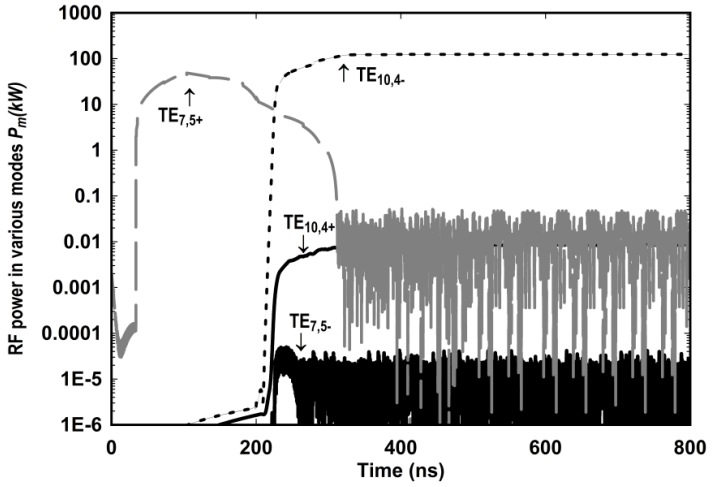

Figure 4.6: Temporal growth of output RF powers P_m (kW) in various modes through time dependent multimode analysis.

4.4.2. 3D Particle in cell (PIC) simulation

In addition, 3D Particle in Cell (PIC) simulation of the electron-beam and RF-wave interaction region of the device is performed reconfiguring a commercial code "CST Studio Suite". In the present study, taking OFHC copper as the cavity material with conductivity of 5.8×10^7 S/m, the RF interaction structure of the device is modeled. The lower conductivities yields more ohmic losses thereby challenges in the thermal system design which are discussed in detail in the thermal analysis section at the end of this Chapter. Like Chapter 3, A particle circular source is taken for forming the gyrating electron beam with designed beam parameters, and an external axial magnetic field profile *B(z)* is applied. To observe the temporal behaviour of modes, various 2D and 3D field monitors are placed with suitable boundary conditions.

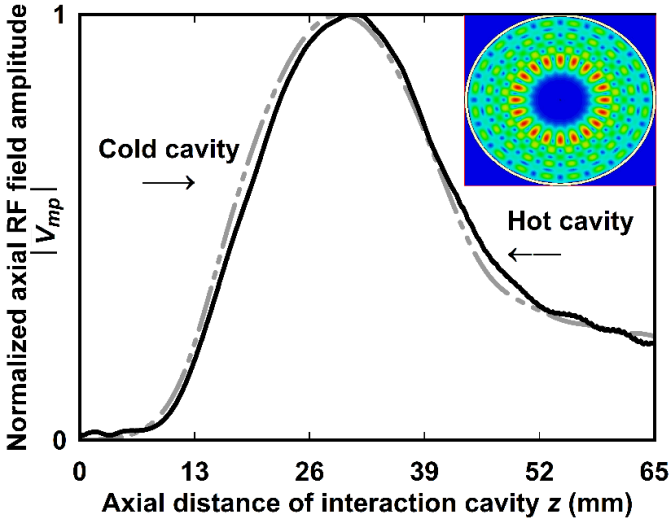

Figure 4.7: PIC simulation results: Comparisons of Normalized axial RF field amplitude profiles in the cold and hot conditions along with vector field distribution.

After the RF interaction cavity design, the desired axial electric field profile and mode excitation inside the cavity in the cold condition (absence of the electron beam) is ensured. Thereafter, by introducing the electron beam, the beam wave interaction

behaviour is investigated. The simulated interaction cavity axial RF electric field profile versus axial cavity position, for the cold (beam absent) and the hot (beam present) conditions, as vector plot is shown in Figure 4.7. It can be observed that here the field profile gets slight upward shift due to the beam loading. The time varying field amplitudes of various modes is also observed using 3D *E*-field monitors. Out of all the modes, the only significant amplitudes of the operating $TE_{10,4}$- mode and the main competing mode $TE_{7,5+}$, at magnetic field B = 3.65 T are plotted in Figure 4.8. Here, one can observe that for $TE_{10,4}$- operating mode RF signal growth stabilizes in 400 ns and competing $TE_{7,5+}$ mode decay to a minimal value in ~ 450 ns.

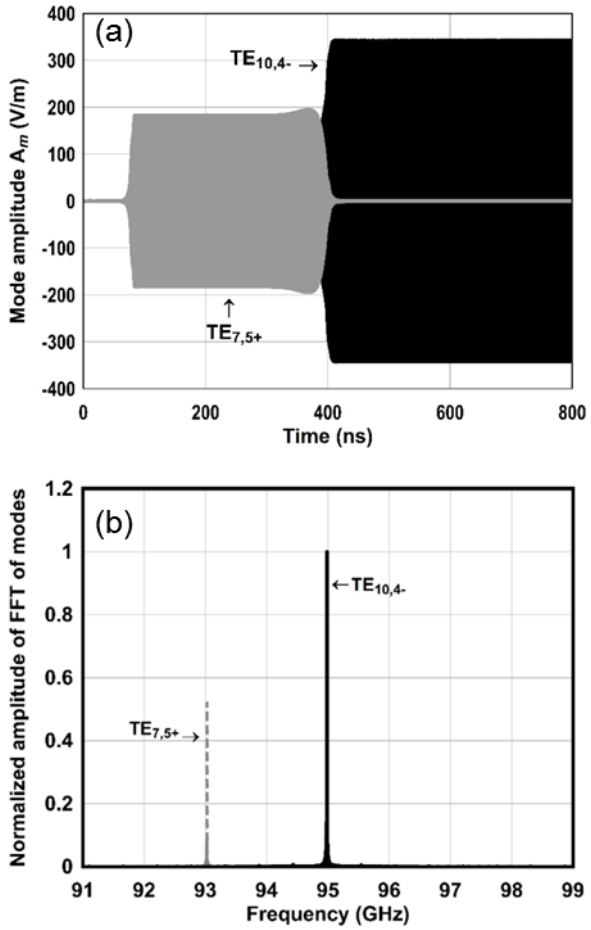

Figure 4.8: 3D PIC Simulation results- Temporal growth of operating and competing mode amplitudes A_m (V/m) from PIC Simulation study (b). Frequency response of the operating and compete modes.

In the next step, the post processing of the temporal power growth is performed for the $TE_{7,5+}$ and $TE_{10,4-}$ modes and correspondingly their frequency responses are observed. The frequency response of the modes is determined by performing Fast Fourier Transform (FFT) action on the mode amplitude signals and the resultant response for the modes are shown in the Figure 4.8. It is observed that the FFT responses of the main mode $TE_{10,4-}$ and compete mode $TE_{7,5+}$ are significantly different both w.r.to to frequency as well amplitude levels. The oscillation frequency of the competing mode $TE_{7,5+}$ is significantly away from desired frequency of operation. A 2.0 GHz frequency separation from the main operating mode is observed and that confirms the mode competition is reduced through proper selection of the background DC magnetic field. As well from the peaks of the amplitudes of the FFT signals confirms that the $TE_{10,4-}$ is dominant.

The temporal power growth in the gyrotron device for $TE_{7,5+}$ and $TE_{10,4-}$ modes are shown in Figure 4.9, where one can readily observe that power transfer from the electron-beam to the RF-wave in different modes with time during device operation. Around 117 kW stable RF power is generated at oscillation frequency 94.98 GHz in at the desired operating $TE_{10,4-}$ mode, while RF power generated in all the competing modes is less than a percent. A better view of the energy exchange from the electron beam to the RF wave can be observed from the wave particle power transfer with respect to time, as shown in Figure 4.10, which indicates the transfer of electron beam power to the RF wave in the time axis.

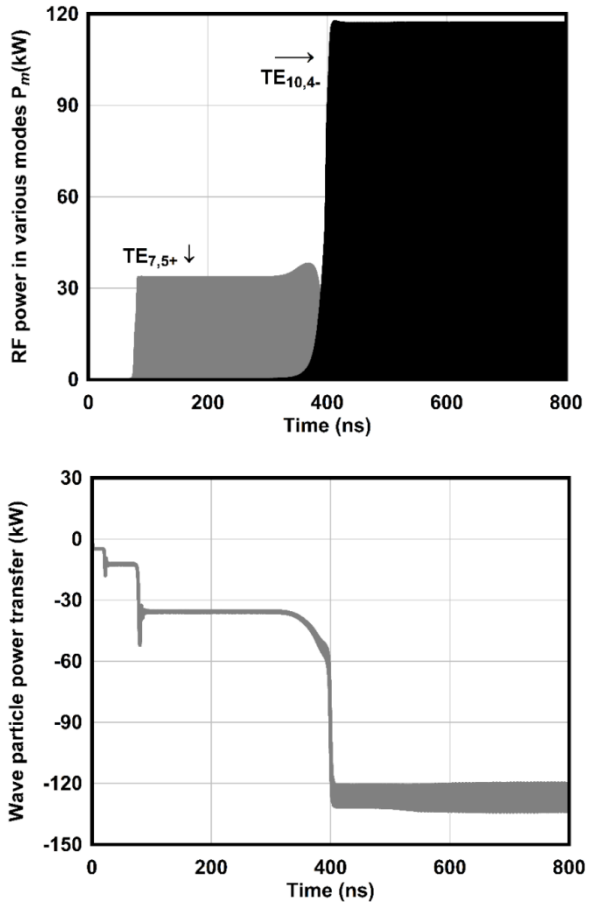

Figure 4.9: 3D PIC Simulation results-(a)Temporal growth of RF powers in the operating and competing modes P_m resulted from PIC simulation (b) Wave particle power transfer (kW) versus time (ns).

It can be further observed that from the start of simulation onwards, the electron beam loses its net power to the RF wave due to beam wave interaction continuously and reaches to a saturation level of more than >120 kW power to the RF wave after 400 ns. By correlating Figures 4.7 and 4.9, one can also observe that initially the beam losses its majority of the power/energy to the compete mode of the design, i. e., to $TE_{7,5+}$ time interval in between 100 ns to 300 ns until, the main mode $TE_{10,4+}$ is in the silent state. While in the transition period from 300 ns to 400 ns, the electron beam starts losing much more power to the RF wave growth simultaneously the mode $TE_{7,5+}$ also starts decaying where as the main mode starts growing and reaches to a stabilized value after 400ns. In order to show the stability as well less mode conversion of the

design, the beam wave interaction mechanisms through PIC simulation is carried out till 800 ns and found device saturated RF power as 117 kW.

4.4.3 Effect of the electrons velocity spread

The device performance is often required to be evaluated under non-ideal but in practical situations. Velocity spread in the electron beam is always present in the electron-beam devices and causes deviations in the beam characteristics and affects device performance. Even though, in present days, the device fabrication and beam launching technologies as well as facilities are considerably improved, which has reduced the amount of velocity spread but certain percentage of beam velocity spread is always present in the practical devices. In our study considering velocity spreads of 0%, 5% and 8%, its effect on the device performance is also evaluated. Using PIC simulation, the RF power and frequency of oscillations are calculated and tabulated in the Table 4.5. It is observed that the velocity spread effects much on the power level but its effect on oscillation frequency deviation is mild.

Table 4.5: RF power and frequencies for different velocity spreads

Velocity spread	RF power (kW)	Frequency (GHz)
0 %	117	94.98
5 %	112	94.968
8%	94.8	94.954

To strengthen the design study, a parametric analysis of device operation is also carried out for a range of the applied DC magnetic field. The RF output power generated versus applied DC magnetic field is performed both analytically and also compared for its validation with PIC simulated values (Figure 4.10). As magnetic field increases the RF power levels in the main mode are decreases in both analytical and

simulated results. Furthermore, an agreement within 7% is observed between the analytical and PIC simulation results.

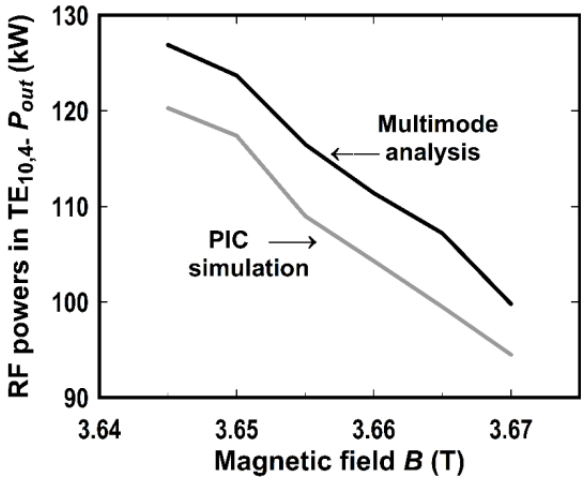

Figure 4.10: Comparisons of output RF powers in the main mode $TE_{10,4-}$ through multimode analysis and PIC simulation study.

By this, the RF cavity designed for the generation of 95 GHz, 100kW operating $TE_{10.4-}$ mode has been studied under ideal beam and velocity spread conditions.

In this chapter, the beam wave interaction studies for the proposed RF cavity with $TE_{10,4-}$, 95 GHz gyrotron are carried out for no misalignment and with misalignment by analytical approach as well PIC simulations with a uniform magnetic field profile along the interaction cavity.

With the help of the analysis mentioned in Section 4.4.1, the beam wave interaction studies in the presence of misalignment of beam axis with respect to cavity axis is performed by updating the time dependent multimode analysis as well as through simulations using 3D PIC commercial code.

The misalignment of beam axis from 0.00 mm to 0.50 mm with 0.25 mm are induced and the beam wave interactions behaviour got studied using analytical expressions and the observed figures in the main mode are calculated and tabulated in

Table 4.6. It's been observed that as the shift of the misalignment increases from 0.00 mm to 0.50 mm, the RF power in the desired mode reduces in a big way as well the efficiency too.

Table 4.6: RF power in the main with various beam misalignments

Beam shift d (mm)	RF power Analytical	RF power PIC code
0	123kW	109 kW
0.25	117 kW	115kW
0.5	106.5 kW	104 kW

4.5 Design and Analysis with the Nonlinear Taper

After the design and analysis of RF interaction structure, the generated RF power is carried to outside via nonlinear taper (NLT), quasi optical mode converter (radial output coupling) and RF window while the spent electron beam is collected by using a collector. Usually, for the preliminary design study of gyrotron oscillators, typical resonator geometry is being used that contains a down taper followed by a uniform mid-section and a linear uptaper. But to guarantee stable operation of the device, NLT should also be included in the calculations as an integral part of the resonator cavity and the NLT part should be designed carefully to minimize the mode conversion. Since, the QOMC converter follows the NLT section, and the launcher radius is usually related to mid-section radius by $1.07R_c$ to $1.1R_c$ times.

Coming to the design of nonlinear taper section used in gyrotrons, a raised cosine type of nonlinear section, with input radius a_1, end radius a_2 of length L_{NLT} and shape factor s_h are used in gyrotron oscillators and is given by

$$R(\mathbf{z}) = a_1 + \frac{(a_2 - a_1)}{2}\left\{-1 + 2\left(\frac{z}{L_{NLT}}\right)^{s_h} + \frac{1}{\pi} sin\left(\pi\left[-1 + 2\left(\frac{z}{L_{NLT}}\right)^{s_h}\right]\right)\right\} + \frac{(a_2 - a_1)}{2} \quad .$$

(4.8)

In the present work, by fixing the end radius of nonlinear taper as R_{NLT} = 13.134 mm, i. e., 1.1R_c, and applying the Vlasov approximation theory presented in Chapter 3, on the combination of interaction cavity and the NLT, for various combinations of shape factors and NLT section lengths, the cold cavity field profiles and the corresponding cavity features i.e., resonant frequency and diffractive quality factors are calculated. Even, the uptaper lengths determined from the above section are varied so that achieving the energy conversion with optimum dimensions in less time.

By using the time dependent multimode theory reported in Chapter 3, for the RF cavity and NLT combinations, the beam wave interactions behaviour that is after cavity interactions are investigated analytically as well through 3D PIC simulation code. The calculations have been performed by allowing the radius profile as well complete cold cavity field profile $h(z)$ with uniform magnetic field profile $B(z)$.

By solving the Vlasov approximation equation, we determined few combinations of RF cavity and raised cosine type NLT profiles that can results the desired operation and are tabulated in Table.4.6.The time dependent multimode theory has been used for the after cavity interaction studies considering various compete modes. As well, it has been observed that the three cavities are resulting almost same diffractive quality factor and cold cavity resonating frequency combinations.

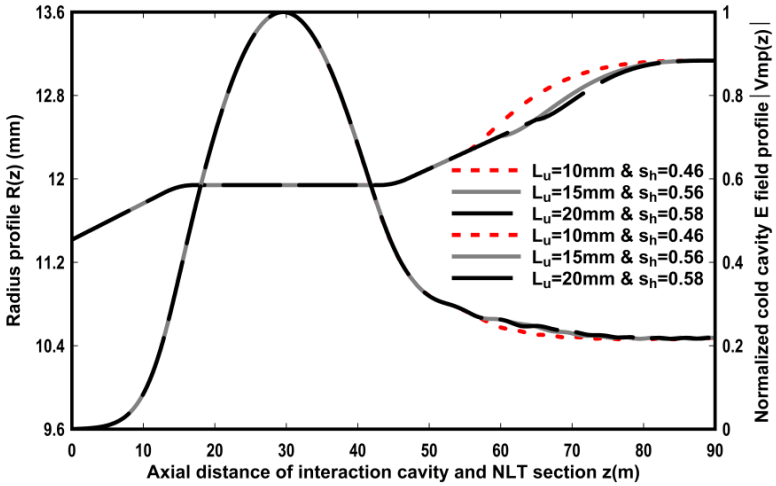

Figure 4.11: Normalized axial cold cavity field profiles and the corresponding radius profiles that include NLT section vs axial distance of the device.

Table 4.7: RF interaction cavity and NLT specifications

Parameter	**Values**		
R_C (mm)	11.94		
L_d (mm)	15		
L_c (mm)	30		
θ_d (°) / θ_{up} (°)	2/1.8		
L_u (mm)	20	15	10
L_{NLT} (mm)	25	30	35
Shape factor, s_h	0.58	0.58	0.46
R_{NLT}(mm)	13.134		
Q_{diff} / f_{res} (GHz)	2250 /95.054		

The beam wave interaction analysis has been carried out for the above three profiles that looks suitable for the corresponding design. The RF power develop in the main mode along with the optimum radius profile based on the power growth and the less mode competition, the uptaper length has been chosen as 10 mm and are shown in Figure 4.12.

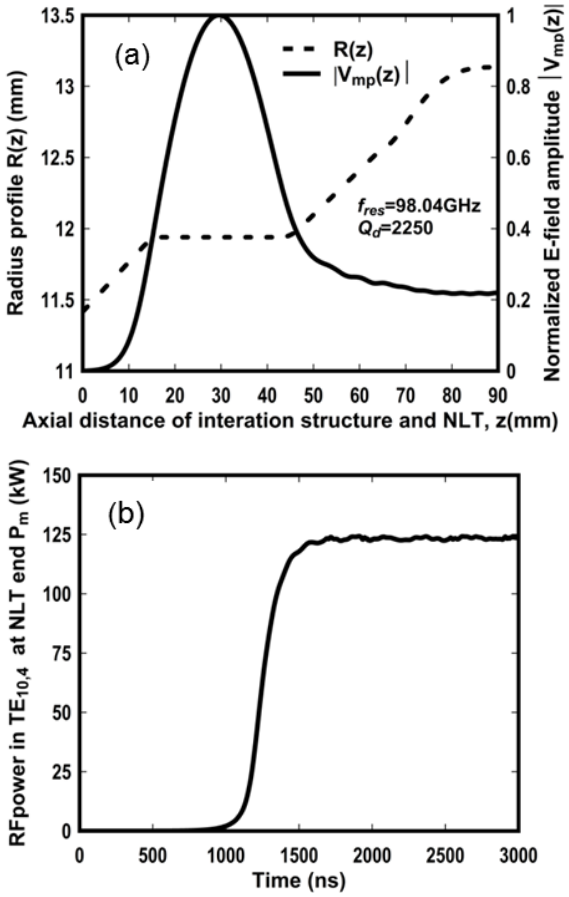

Figure 4.12: Analytical results: (a) normalized axial cold cavity field profiles and the corresponding radius profiles that include NLT section vs axial distance of the device (b) RF power versus time.

The 3D PIC simulation studies using Commercial CST Studio Suite after inclusion of NLT section to the RF interaction cavity with uniform magnetic profile are presented below. It has been observed that with uptaper of 10 mm and L_{NLT} = 35.00 mm, the beam wave interaction mechanism shows a quick growth in the desired mode as well a less time of compete mode presence in the simulation duration. The hot (electron beam present) cavity axial *E* field profile along with the vector field plot of the $TE_{10,4}$- mode is shown in Figure 4.13.

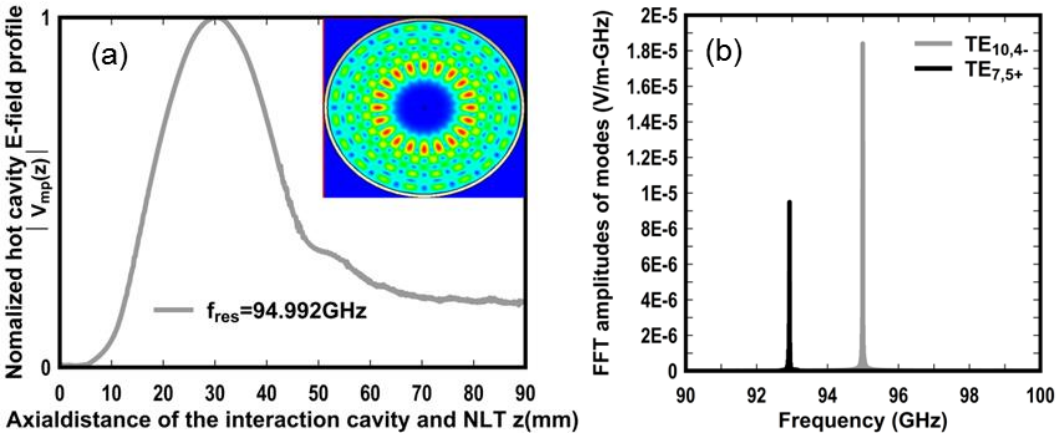

Figure 4.13: (a). Normalized axial E field profile in hot (beam present condition) along with 2D vector field pattern of $TE_{10,4-}$ mode (b). FFT field amplitudes of $TE_{10,4-}$ (Light shade) and $TE_{7,5+}$ (dark shade)modes.

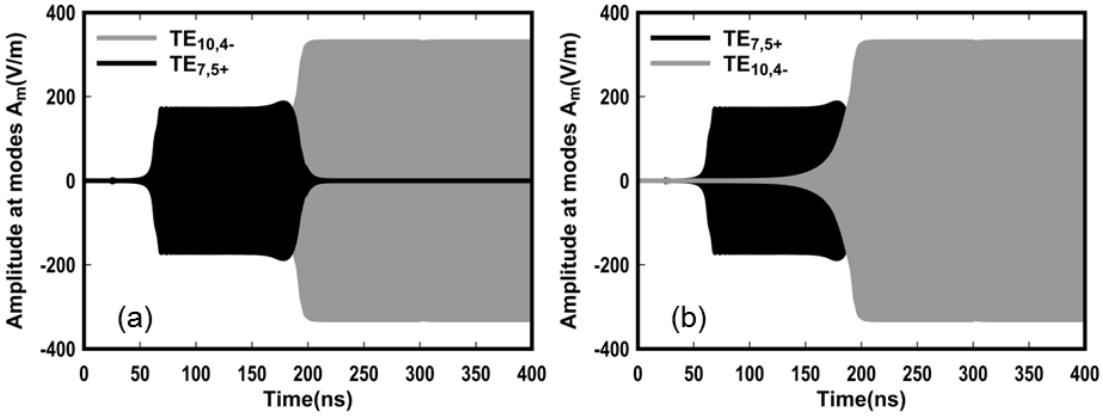

Figure 4.14: 3D PIC Simulation results- temporal growth of amplitudes across various modes A_m(V/m) (a) : $TE_{7,5+}$ overrides $TE_{10,4-}$ (while plotting) (b) vice versa.

It is observed that the desire mode oscillating with frequency of 94.99GHz as well the oscillating frequency of compete mode is far of more than 2GHz from operating frequency. The temporal growth of mode amplitudes and the corresponding RF power developed across various modes with respect to time has been calculated by post processing the results and are plotted in Figures 4.14 and 4.15.

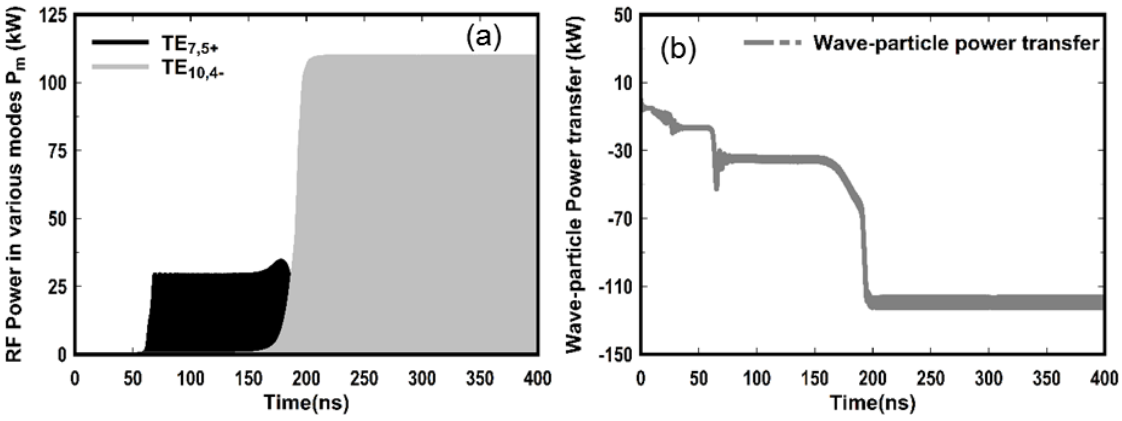

Figure 4.15: 3D PIC Simulation results- (a) temporal growth of mode powers and (b) wave particle power transfer versus time.

4.6. Thermo-Mechanical Analysis

As reported in Chapter 3 that thermo-mechanical analysis was simulated separately using commercial code "COMSOL Multiphysics". However, the thermo-mechanical analysis for the present case of the $TE_{10,4-}$ 100kW gyrotron including nonlinear taper section is performed using a single code "CST Studio Suite". With the experience of the Chapter 3, the analysis is carried out here also for two different electrical conductivities by considering two different electrical conductivities of the cavity material i.e., for 5.8e7 S/m and 2.9e7 S/m. The analysis is started by calculating the ohmic loss profile that acts as heat load of the structure by using the design parameters mentioned in Table 4.6, using equations (3.27). In the present design, the thermal effects are studied. Since, the value of the ohmic loss magnitude are varies as per the conductive nature of the cavity material, the present structure has been analysed for the both values. As per equation (3.27), the wall loading profiles along the interaction structure are plotted below Figure 4.16.

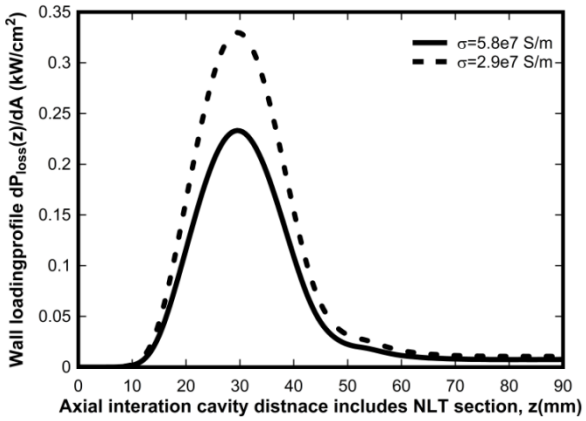

Figure 4.16: Ohmic loss profile for both the electrical conductivities for the cavity and NLT section.

Later on, by considering the cavity material with the properties as mention in Table 3.7, Chapter 3, the RF structure has been modelled. Initially, the structure has been subjected by various convective heat transfer coefficient *h* values and different cavity thickness *dR* values for determining the optimum combinations of *h* and *dR* values. Unlike in the Chapter 3, since for the measure of thermal effects the maximum inner radial deformations and outer surface temperatures are sufficient. Thereby, in the current analysis the effects are measured in terms of maximum values. Without much in detailed description like done in the Chapter 3, here, the thermal effects are calculated by modelling, suitable selection of boundary conditions.

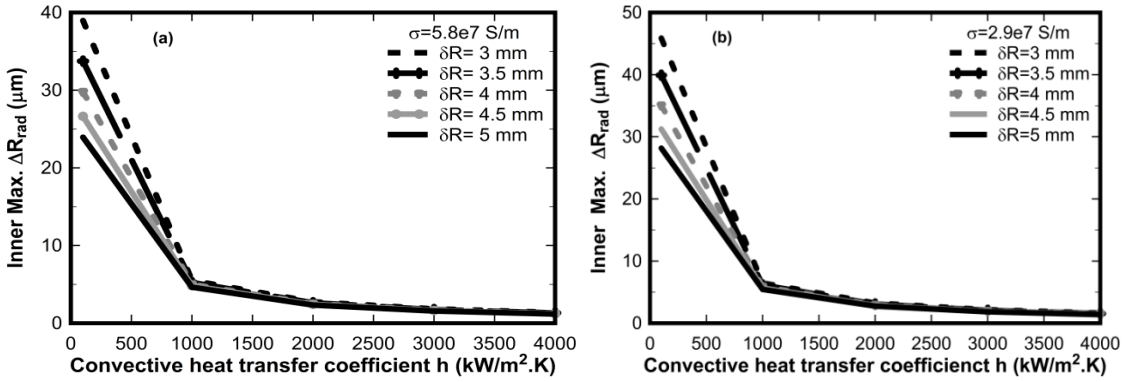

Figure 4.17: Inner maximum radial deformations versus convective heat transfer coefficient h for various cavity thickness δR_{rad} at electrical conductivities (a) 5.8e7 S/m (b) 2.9e7 S/m.

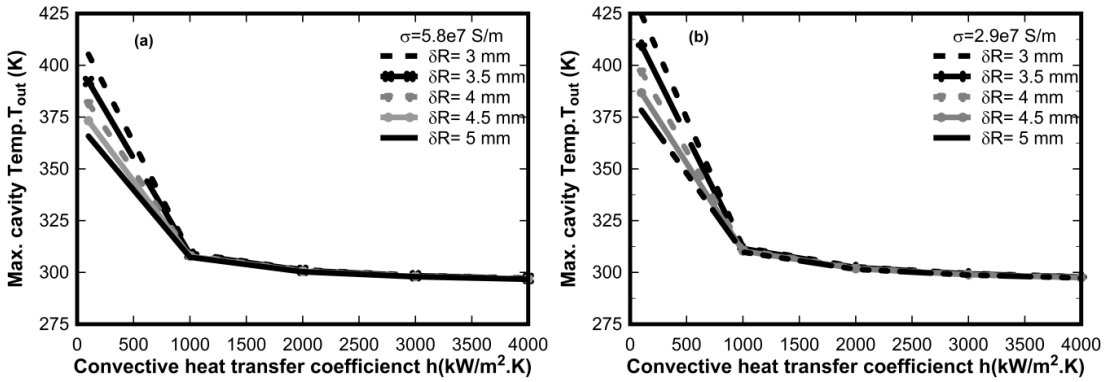

Figure 4.18: Outer maximum radial cavity temperatures T_{out} (K) versus convective heat transfer coefficient h at various cavity thickness δR_{rad} at electrical conductivities (a) 5.8e7 S/m (b) 2.9e7 S/m.

The Maximum deformations ΔR_{rad} at the inner surface and the temperatures T_{out} at the outer surfaces for various combinations of convective heat transfer coefficient h and cavity thickness δR values for the electrical conductivities σ = 5.8e7 S/m and 2.9e7 S/m are plotted in Figures 4.17 and 4.18. It can be observed from these figures that with $h \geq 1000$ and for any combination of δR value, the maximum radial deformation for both conductivities is near by 5 micrometres as well the maximum outer surface temperature is 310ºK whose values are quite promising as compared to $TE_{6,2}$ mode gyrotron, as discussed in Chapter 3. Since, in the present design, a max of 0.1 GHz frequency shift happens for the radial deformation of ~13 micrometres, keeping in mind about the nonlinear section module, the optimum cavity thickness is chosen as minimum of 4.5micrometers as well the optimum h is chosen around 2000 that results a maximum temperature of ~302 K and 2.5micrometers of inner deformations which are in tolerable limits.

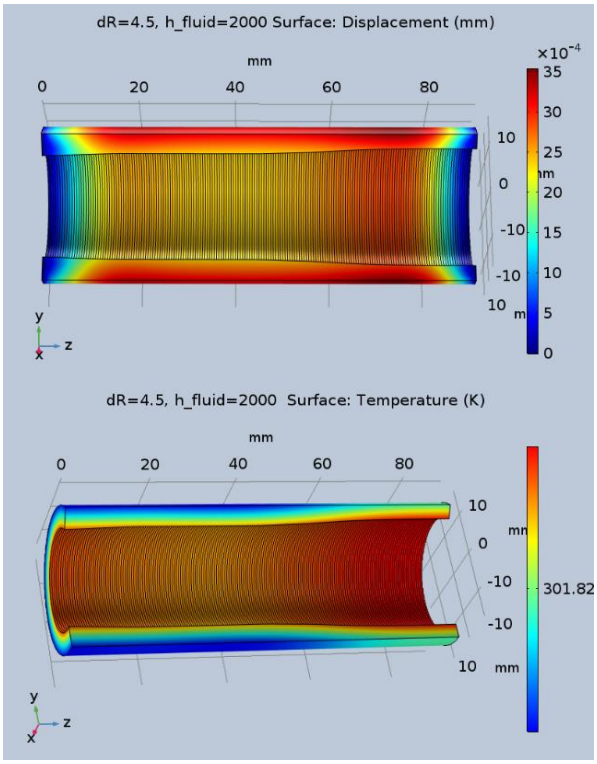

Figure 4.19: 3D view of surface displacements and surface temperatures for heat transfer coefficient h=2000 (W/m^2.K) and cavity δR= 4.5 mm.

Comparing with the $TE_{6,2-}$ mode, 95 GHz gyrotron, the $TE_{10,4-}$ mode operated gyrotron has less thermal effects on the system performance as well a very simple cooling system design requirements which even managed without any extended heat surfaces called Fins. With minimum/low values of thermal system parameters, the cooling system can be provide for reliable device performance which can reduce the complexity as well cost of the thermal system. Since, the thermal effects are very much under desire limits that's why its effects on the RF behaviour after optimized cooling system has not been discussed.

4.7. Conclusion

Keeping the goal of design and analysis of the gyrotron oscillator that able to generate 100kW at 95GHz that operates in the high order volumetric mode and does not require additional cooling system for its thermal management. The device is designed

for its operation at a higher order mode so as its RF interaction cavity structure dimension becomes larger and heat loading problem get relaxed. The operating mode selection has been carried out by inspecting the various design constraints. Later, using Vlasov approximation, the RF interaction cavity has been determined such that it able to provide desired sustainable growth of RF signals. Using time dependent multimode theory and simulations using PIC codes for the beam wave interaction studies has been carried out and able to observe that the desired performance at the end of the interaction cavity. To determine the optimum interaction cavity dimension as well the quasi optical mode launcher design, the cavity has been extended by adding a raised cosine type NLT section that acts as impedance matching unit between the RF cavity and the quasi optical mode converter and allows the RF transmission with minimum mode conversion.

The Vlasov approximation analysis of single mode has been used for the determination of the NLT profile. The same profile has been confirmed using after cavity beam wave interaction studies by extending the time dependent multimode theory of Fillet *et al* (1991), while taking the complete $h(z)$ profile calculated resulted from the Vlasov approximations analysis.

For the same radius profile, using PIC simulation, the after cavities interactions with uniform magnetic profile are carried out and results have been in good agreement with the analytical values. Later, the misalignment of beam axis with respect to cavity axis has also been analyzed by updating the time dependent theory with the modified beam wave coupling term and also simulated using PIC code. Then the thermal behaviour of the current design is studied and the optimum cooling parameters are determined now using an integrated tool, CST Studio suite. Further, it has also been observed that by operating the device in high order mode, the sensitivity of the device

for misalignments has been reduced. As well the impact of ohmic losses has been reduced significantly thereby requirement and challenges of cooling system.

With this complete design, analysis and simulations for beam wave interaction behaviour, it has been established that the designed 100kW, 95GHz gyrotron operating at the $TE_{10,4-}$ mode does not require external cooling system. In other side, the structure is needed to be investigated with the non-uniform magnetic profile. As well, efficiency of the device is found ~35%.

CHAPTER 5

DESIGN APPROACH AND BEAM-WAVE INTERACTION STUDIES OF THE TUNABLE-FREQUENCY GYROTRONS FOR DNP-NMR SPECTROSCOPY APPLICATIONS

5.1. Introduction

As discussed in Chapter 1 of this thesis, gyrotron oscillators are the potential RF sources for various applications that require RF power at either single frequency or tunable frequency range. The inclusion of Dynamic Nuclear Polarization (DNP) mechanism makes the use of Nuclear Magnetic Resonance (NMR) spectroscopy very wide by enhancing the sensitivity of the signal. But the DNP driven NMR spectroscopy requires either a tunable NMR magnet or a tunable RF source. Comparatively, the design, development and maintenance of a tunable RF source have large and many benefits, like, simple and reliable over tunable NMR magnet systems. Gyrotron oscillators are capable of generating a low power over a band frequency tuning range and enhance the sensitivity and the realization of DNP-NMR spectroscopy more effectively.

Dynamic Nuclear polarization is a key technique which transfers unpaired electrons spin polarization into nuclear spins and is used for the enhancements of sensitivity of NMR spectroscopy study that enables faster data acquisitions in various sample characterization. For the enhanced sensitivity study of DNP-NMR spectroscopy, a RF source is required at the NMR frequencies. In addition to this, a DNP NMR spectroscopy requires either a super conducting NMR magnet with sweep coils or a tunable RF source for the study of various samples. Due to the complexities involved in the arrangements of a tunable NMR magnet, now the researches are also focussed on the development of various tunable RF microwave sources at various NMR frequencies.

Gyrotron is the most suitable RF source for this application. The gyrotron research is now getting focussed to play its role in DNP-NMR spectroscopy where a few watts to several tens of watts of CW RF power required over a tunable bandwidth. Several gyrotron oscillators for the DNP-NMR applications have been analyzed,

designed and experimentally investigated at electron frequencies 132 GHz, 260 GHz, 330 GHz, 460 GHz, etc[Hornstein,(2001)].

In this Chapter, the design of a tapered cavity RF interaction structure of gyrotron for 263 GHz for a 400 MHz NMR spectroscopy system is investigated. The operating mode is considered as $TE_{5,3,q}$ with a target of more than 2 GHz tunable bandwidth. The tunability of the device is studied by magnetic tuning as well as electrical tuning methods.

The presented chapter is organized as follows. Section 5.2 contains the various tunable techniques used in gyro-devices for achieving a tunability. In Section 5.3, the design of tapered cavity interaction structure along with its cold cavity analysis is presented. The beam wave interaction analysis using time dependent multimode theory given by Fliflet *et al.* (1991) for the proposed design is presented in Section 5.4 at various magnetic and beam voltage variations.

5.2. Tuning Techniques Used for the DNP Gyrotrons

The main aim of any tunable RF source is to provide desired amount of RF power over a wide range of frequencies. Generally, shift in the frequencies and power levels are achieved by varying the beam parameters. In the case of gyrotron oscillators, since the device is based on the CRM instability principle, where the exchange of power between RF wave and electron beam depends on the frequency of oscillation of the mode as well as the cyclotron frequency of oscillation. The operating frequency of gyrotron mainly depends on the resonating frequency of the RF interaction cavity and the cyclotron frequency of the electrons that are interacting with the RF fields generated by the noise inside the interaction structure. Hence, by allowing the variations in either resonating frequency of the interaction cavity mode or cyclotron frequency of the electrons, the tunability of the device can be achieved.

There are several techniques used in general for achieving the tunability of the device in gyrotrons, namely, mechanical and thermal tuning methods which affect the dimensions of the interaction cavity thereby resonating frequency of the mode, and by electrical and magnetic tuning methods which yields the variations in the cyclotron frequency of the electrons thereby shift in the operating frequency of the device. A brief description of these tuning techniques used in the gyrotrons is presented as follows [Dumbrajs *et al.* (2011)].

5.2.1. Mechanical Tuning

As the name indicates, in the mechanical tuning, the frequency tuning is achieved by inducing changes in the cavity dimension mechanically and simultaneously adjusting the strength of the magnetic field B(z) as well as the beam parameters. The DC magnetic field along the cavity is adjusted here in order to maintain the synchronism between the interaction mode and the electrons. Since, the variations in the cavity dimension directly effects the oscillating frequency of the mode thereby shifts in the operating frequency.

For a rigid cavity type, it is unattainable to change the transverse dimensions because of lack of provisions for altering the cavity dimensions and results in implementation of mechanical tuning impossible. However, an effective transverse dimension alteration can be made with a split cavity structure. Here, frequency tuning is achieved by sliding the wedge shaped pieces pneumatically, so that the two halves are moved apart or closer by the necessary amount to affect the transverse dimensions thereby the frequency of operation. But the presence of gap in the cavity restricts the operation of the device to azimuthally non-symmetric modes [Dumbrajs *et al.* (2011)]. Apart from limited modes of operation, the major challenge with the mechanical tuning is the handling of cooling system which is responsible for longer life of the RF cavity.

In high power gyrotrons, the resonators must be rigorously cooled so as to limit any uncontrollable changes of their dimensions due to overheating. It is difficult to maintain the mechanical changes of the cavity along with the cooling system. Due to this, the mechanical tuning method is limited to low power, and short pulse gyrotrons only where the role of cooling is minimal. In spite of this, implementation of mechanical tuning is easy in the quasi optical gyrotron where the distance between the mirrors to be modified which makes the Fabry-Perot resonator. So this type of tuning is most suitable for quasioptical gyrotrons and unfeasible for a tapered cavity and coaxial cavity gyrotrons.

5.2.2. Thermal Tuning

In thermal tuning method, the variations in the operating frequencies are achieved by allowing the variations in temperatures of the coolant along the interaction structure and thereby controlling the impact of the ohmic losses in the interaction cavity due to RF power generation that leads to mechanical deformations of the cavity, as discussed, in Chapter 3 and Chapter 4.

Alteration in temperature of the coolant, results in variation in the temperature of the interaction structure wall due to variable amount of heat exchange in the system. According to the property of thermal coefficient of expansion of the cavity material, there is contraction or expansion of the walls as per the temperature variations. These changes in the cavity dimensions result variation in the resonating frequency of the mode of the structure which in turn results in variation in the operating frequency of the device. The amount of tuning achieved via thermal technique mainly depends on the cavity material properties. Considering the tolerances in the cavity dimensions, the amount of frequency shift is very small.

It has been reported that a 4 MHz /^{o} C of frequency shift is obtained in the low power gyrotrons operating at 263 GHz [Glyavin *et al.* (2015)]. In the case of moderate lengths interaction structure, this technique is found suitable for tuning since, operation on high order axial modes are limited. For 140 GHz gyrotron reported by Joye *et al.* (2006) mentioned that they achieved frequency tuning via thermal variations. The thermal and mechanical tuning techniques directly affects the resonating frequencies of the mode and do not affect the cyclotron frequencies of the electrons.

5.2.3. Electrical Tuning

In electrical tuning, the DC voltage of the electron beams varied thus the cyclotron frequency of the electrons are get altered that results shift in the frequency of energy exchange, i. e., the operating frequency of the device. It is one of the most widely used techniques for achieving the frequency tenability in the gyrotrons. The variations in the beam accelerating potential leads to the changes in the relativistic factor, γ, and is given by as follows [Edgcombe (1993)]:

$$\gamma = 1 + \frac{V_b}{m_e c^2}, \tag{5.1}$$

where V_b is the beam voltage, m_e is the rest mass of electron and c is velocity of light in free space. The variations in the relativistic mass factor γ effects the cyclotron frequency of the electrons and is known by

$$\Omega = \frac{eB_0}{m_e \gamma_0} \approx 28s \frac{B_0[\mathrm{T}]}{\gamma}[\mathrm{GHz}], \tag{5.2}$$

where s is the harmonic number, B_0 is the external DC magnetic field. From the above equations (5.1) and (5.2), it is obvious that the variation in the accelerating voltage result the variations in relativistic factor there by the variations in the cyclotron frequency. As the energy exchange depends on the synchronous condition between

cyclotron frequency of the electron beam and the resonating frequency of the mode, these variations affects the operating frequency.

Percentage variation in the relativistic factor with the variations in DC beam voltage is determined by

$$\frac{d\gamma}{\gamma_0}\times 100 \approx \frac{dV_b}{511+V_{b0}}\times 100 \ . \tag{5.3}$$

Here, γ_0 and V_{b0} are the initial relativistic mass factor and beam voltages. The percentage of variation in cyclotron frequency for the variations in beam voltage is given by

$$\frac{d\Omega}{\Omega_0}\times 100 \approx -\frac{dV_b}{511+V_{b0}}\times 100 \ . \tag{5.4}$$

Here, Ω_0 is the initial cyclotron frequency of electrons and negative sign in equation (5.4) indicates the increase in beam voltages yields reduction in cyclotron frequency. Equations (5.3) and (5.4) specifies that the amount of variations in the cyclotron frequency is not only depends on the amount of variation in the beam voltages but also on the starting values of beam voltage.

Figure 5.1 shows the effect of the beam voltage variations on the relativistic factor and cyclotron frequency of the device with the start value of beam voltage is 15 kV (random value). It is observed that typically for this case, 1 kV change of beam voltage nearly yields a 0.175% change in both cyclotron frequency as well as relativistic factor keeping the rest of beam parameters as constant. Since the intensity of electric fields can be changed very rapidly which results smaller switching times means that faster electrical tuning. But it requires a very sensitive and expensive power supplies which makes the realization of frequency tunability through the electrical tuning complex.

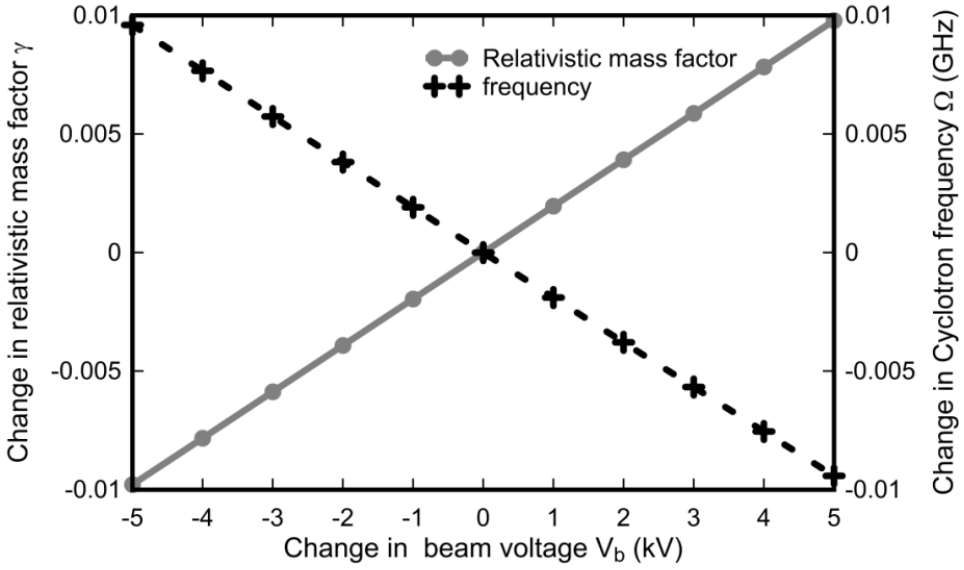

Figure 5.1: Dependence of relativistic factor and cyclotron frequency with respect to beam voltage.

5.2.4. Magnetic tuning

Similar to electrical tuning, the magnetic tuning also yields variation in cyclotron frequency of electrons thereby variations in the operating frequency of the device by altering the magnetic field B along the interaction structure.

Equation (1.2), indicates that the variations in cyclotron frequency are directly proportional to the variations in magnetic field. Thus, magnetic tuning is simple and more effective to achieve higher tunable frequency because of the ease of varying magnetic field though having the longer switching times between different magnetic field values. The percentage of variation in cyclotron frequency for the variations in beam voltage is given by

$$\frac{d\Omega}{\Omega_0}\times 100 = \frac{dB}{B_0}\times 100 \quad . \tag{5.5}$$

Here, B_0 means the starting value of B from which the variations starts. The equation (5.5), indicates that the amount of variations in the cyclotron frequency is not only

depends on the amount of variation in the magnetic field but also on the starting values of beam voltage.

The percentage variation in the cyclotron frequency with the magnetic field is shown in figure 5.2. It can be observed that 1% of change in cyclotron frequency is produced with the change of magnetic field of 0.01 Tesla with the reference value of B_0 = 1 T, which has a strong effect on frequency compared to the beam voltage.

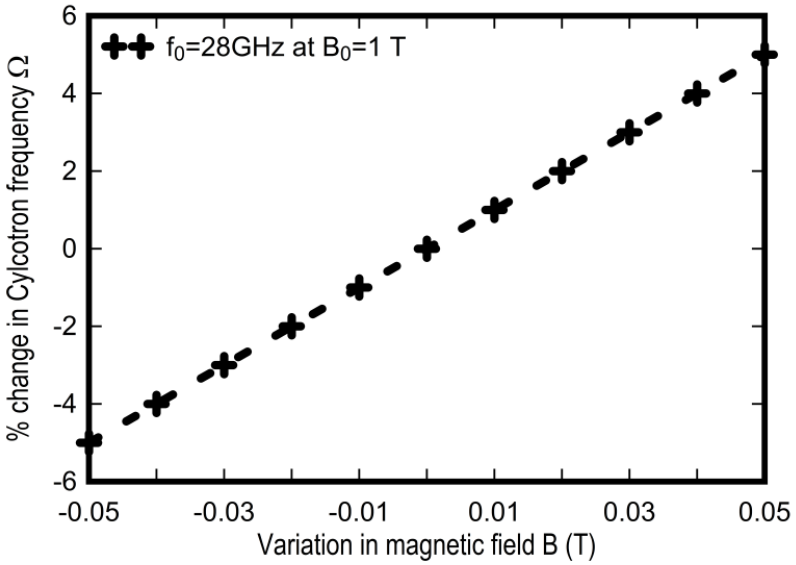

Figure 5.2: Percentage change of cyclotron frequency versus magnetic field B (T).

In this Chapter, a tapered cylindrical RF cavity is designed for achieving a continuous tunable bandwidth using both the magnetic and electrical tuning for a 400MHz NMR spectroscopy applications.

5.3. Design Constraints and Mode Selection for the Tunable Frequency Gyrotrons

Like in the high power gyrotrons discussed in Chapter 3 and Chapter 4, for the low power tunable gyrotron purposes also, a cylindrical tapered RF section has been considered as the interaction structure of the gyrotron. In the continuous tunable gyrotrons, tunability has been achieved by incorporating different tunable techniques as

discussed above, through exciting device in the high order axial mode indices with fixed azimuthal and radial variations. For the generation of high order axial modes, long interaction cavity sections needed usually, of the order of few tens of operating wave length. As well, the diffraction losses that results the RF power reduces as the axial mode index increases and which needs a proper selection of beam parameters along with suitable cavity geometry.

In the Chapter, the design and analysis of the RF interaction cavity structure for the 400MHz DNP enhanced NMR spectroscopy applications presented. The $TE_{5,3,q}$ mode, at the 263 GHz operating frequency along with beam parameters have been taken from the experimental data [Glayvin *et al.* (2015)], here *q* indicates the number of axial variations in the field across interaction cavity. The design investigation is carried out with the aim of a tunable bandwidth greater than 2 GHz via magnetic, electrical tuning.

In this Chapter, as mentioned above, the operating mode is chosen as $TE_{5,3,q}$ [Glayvin *et al.* (2015)]. With the help of coupling coefficient curves, the optimum beam radius that allows maximum coupling between beam and RF wave has been chosen and are plotted in figure 5.3 for various normalized beam radius $\overline{R_b} = R_b / R_c$.

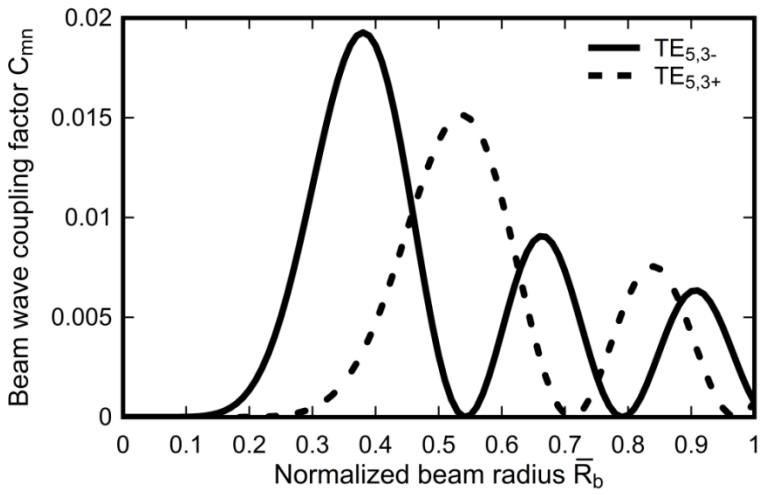

Figure 5.3: Beam wave coupling factor C_{mn} versus normalized beam radius $\overline{R_b} = R_b / R_c$

Observing beam wave coupling dependence of the mode, the beam radius is taken as 0.96 mm which is at the first radial maximum and will be optimized by the inspection of beam wave interaction studies in the following sections.

5.3.1. Design of Tunable RF Cavity Structure

The design parameters are taken from the Glyavin *et al.* (2015) and are tabulated in Table 5.1. The optimization of axial RF cavity dimensions are calculated by solving the single mode Vlasov approximation equation for various cavity dimensions as discussed in Chapter 3. Dimensions of the tapered cylindrical RF cavity are optimized for $TE_{5,3,q}$ choosing cavity interaction length 22.49 mm (~20 λ), and the optimized dimensions are tabulated in Table 5.2.

Table 5.1: Design constraints

Parameter	Value
Frequency	263
Tunable bandwidth	>2GHz
Pitch factor	1.5
Beam voltage	10-15kV
Beam current	20-50 mA
Magnetic field	9.6-9.7
Beam radius	0.96 mm

Table 5.2: RF Interaction parameters

Parameter	Value
Down taper angle θ_d (^{0})	2
Uptaper angle θ_{up} (^{0})	0.8
Down taper length, L_d (mm)	15
Uptaper length, L_{up} (mm)	25
Middle section length L_c (mm)	22.49
Cavity radius (mm)	2.54

Table 5.3: Q_{diff} and f_{res} for various axial mode indices q of TE_{53q}

Axial Mode index, q	Frequency, GHz	Q_{diff} factor
1	262.9780	14500
2	263.182	3510
3	263.527	1660
4	264.005	950
5	264.621	605
6	265.377	436

The normalized axial field profiles for various high order q along the interaction structure are plotted in Figure 5.4. The corresponding Q_{diff} and resonating frequencies f_{res} are determined and tabulated in Table 5.3. It is observed that as the q increases, the value $Q_{diff,q}$ reduces as well the oscillating frequency of the mode increasing.

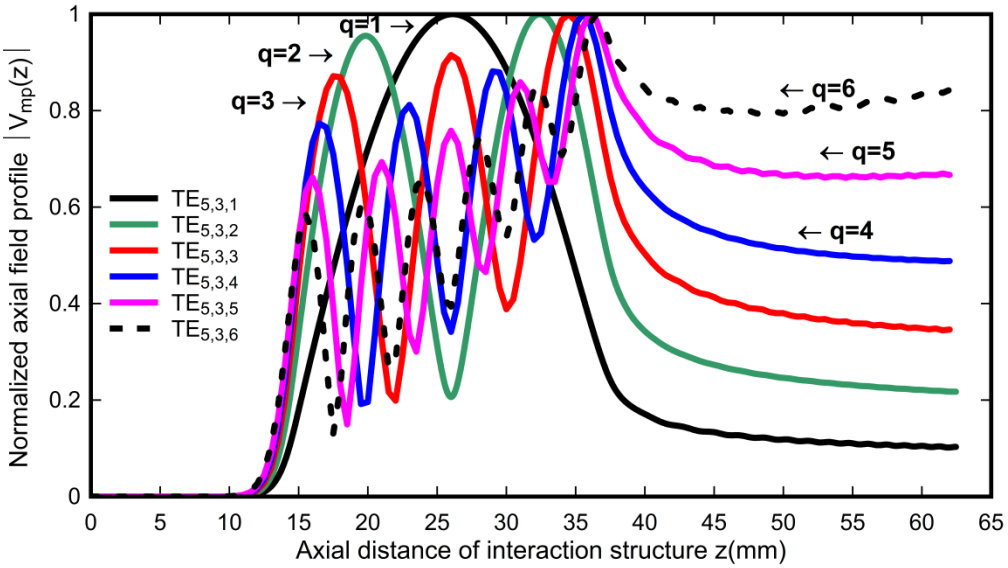

Figure 5.4: Axial mode profiles at beam absent conditions for various q of proposed RF interaction cavity.

5.3.2. Start Oscillation Currents for the Higher-Order Axial Mode Indices

Now, like in the previous chapters, the start oscillation curves used for determining compete modes as well the minimum currents needed for the growth of several modes at various magnetic fields are determined. Unlike, single axial mode index i.e., q = 1, the I_{soc} curves are determined using (3.9) and (3.10) equations, but for the present work, the device should operate in various axial mode indices for tunability. Hence, the field profile used for deriving equations (3.9) and (3.10) are need to modify that results calculation of I_{soc} for q >1 values. According to Torrezan *et al.* (2010), the I_{soc} for various high order axial mode indices q are determined by using the following expressions.

$$I_{soc} = -\frac{1}{2}\left(\frac{m_e \varepsilon_0 c^3}{e}\right)\left(\frac{\gamma_0}{Q}\right)\left(\frac{s!2^s}{s^s}\right)^2 \frac{\beta_{\perp 0}^{2(3-s)}}{C_{m,p}} \frac{\left(\frac{\pi^2}{\lambda}\right)\int_0^L |h(z)|^2 dz}{\left(s+\frac{\partial}{\partial \Delta}\right)\left|\int_0^{\mu} h(\zeta)\exp\left(j\int_0^{\zeta}\Delta d\zeta'\right)d\zeta\right|^2} \quad (5.6)$$

where, s gives harmonic number, C_{mp} is the coupling coefficient, and the rest of the parameters are already defined in Chapter 3 of this thesis; h (z) indicates the axial field profile in the interaction cavity. By providing the h (z) profiles evaluated from Vlasov approximation equations, the I_{soc} curves are determined for the various axial mode indices. The diffractive quality factor Q values are also updated as for the q. The start oscillation current I_{soc} are calculated for the beam parameters mentioned in Table 5.4 by varying magnetic fields 9.5 to 9.9 T and are plotted in Figure 5.5. It has been detected that the operated mode is significantly differ from various compete mode and shows a promise for more tunability with respect to magnetic tuning. As well, it is observed that a minimum beam current of 20 mA, will excites the axial modes q = 1 to 6. All the modes are distinguished curves with respect to magnetic field that gives the confirmation about the oscillation of various modes along the interaction structure.

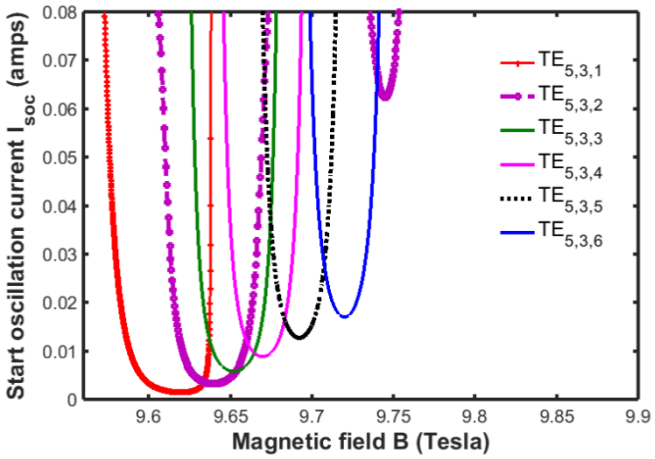

Figure 5.5: Start Oscillation currents for $TE_{5,3,q}$ mode q = 1 to 6 versus magnetic field.

Later, the voltage depression V_{dep} for various beam currents is determined and the % percentage of V_{dep} with respect to the beam voltages V_b is plotted in Figure 5.6. It is observed that as the beam current increases the amount of voltage depression also increase though all are in very much lower to the maximum allowed limit.

From the design and analysis of RF cavity, it has been observed that the proposed RF cavity can be operated over a various axial modes and allows a tuning bandwidth of 2.4 GHz. Though, the proposed RF cavity supports growth of various axial mode indices, but it is the responsibility of the beam parameters (especially V_b) and magnetic fields (B(z)) to make it possible. In the present work, by incorporating the electrical tuning, magnetic tuning as well the hybrid tuning, the proposed cavity has been investigated for various input parameters (combinations of beam voltage, magnetic field as well both) . Since, considering the limitations of time and complexities with computational resources available, for the present work, the beam wave interaction studies are carried out with help of the time dependent multimode theory and are discussed in detail in the following section.

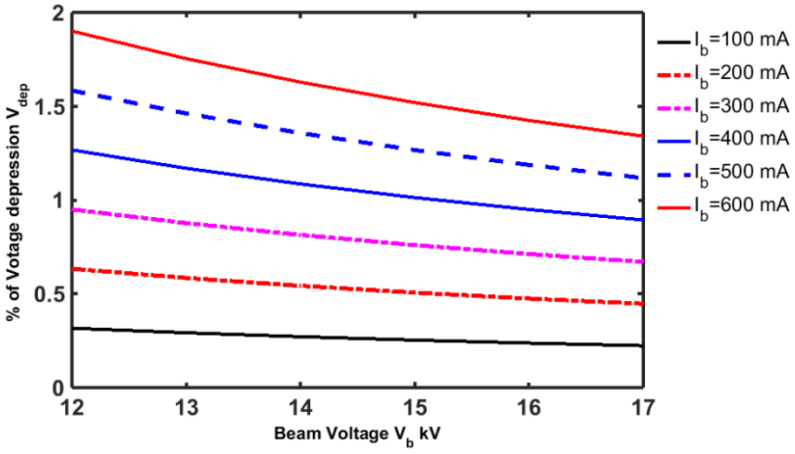

Figure 5.6: % of voltage depression versus beam voltages for the various beam current values.

5.4. Analytical Studies of the Beam-Wave Interaction

The cold cavity analysis in the former section confirms that the interaction structure is suitable for generating the high order axial mode profiles of q = 1 to 6. The mode profile of various axial variations with the resonating frequencies mentioned in table that allows a possible tunable bandwidth of > 2.3 GHz. In the present work, the beam wave interaction studies for the proposed cavity have been performed using the nonlinear time dependent multimode theory discussed in Chapter 3. For the beam interaction studies, considering the field profile h (z) at various q, the multimode analysis theory has been carried out performed for various beam parameters. With beam current of 400 mA, the initial beam wave interaction studies are done and later on the beam current have been reduced in the steps and finally the beam currents are settled to 20 mA.

5.4.1. Investigations via Magnetic Tuning

Like presented in chapter 3 and Chapter 4, the beam wave interaction studies are carried out by considering 32 beamlets and 32 electrons for each beam let. The investigation are started by providing beam currents, I_b = 0.4 A, the tunability of proposed RF interaction of gyrotron are investigated by magnetic as well as electrical tuning for 400 MHz DNP-NMR spectroscopies.

Considering the magnetic tuning first, the magnetic fields along the interaction structure is varied in order to tune the mode of operation at different frequencies. The output power developed in the interaction mode, $TE_{5,3,q}$ for q =1 to 6 for the interaction structure tabulated in Table 5.2 are performed. In Figure 5.7, in addition to RF output power level, the oscillation frequencies of various axial modes are also shown with respect to the magnetic field. Initially, considering I_b = 400 mA, the beam wave interactions are carried out. Later, the beam currents are reduce in steps and the RF

power levels and corresponding frequencies at beam current 20 mA are calculated and are plotted in Figure 5.8.

Table 5.4: Magnetic tuning parameters at I_b = 400 mA

Axial Variation, q	Frequency (GHz)	Magnetic Field (T)	Beam Voltage (kV)	RF Output Power (kW)	$Q_{diff,q}$ Quality factor
1	262.9780	9.6050	15	1.0516	14500
2	263.1817	9.6120	15	1.001	3510
3	263.523	9.6255	15	0.9891	1560
4	264	9.64159	15	0.9871	890
5	264.620	9.6675	15	0.881	562
6	265.370	9.7005	15	0.490	412

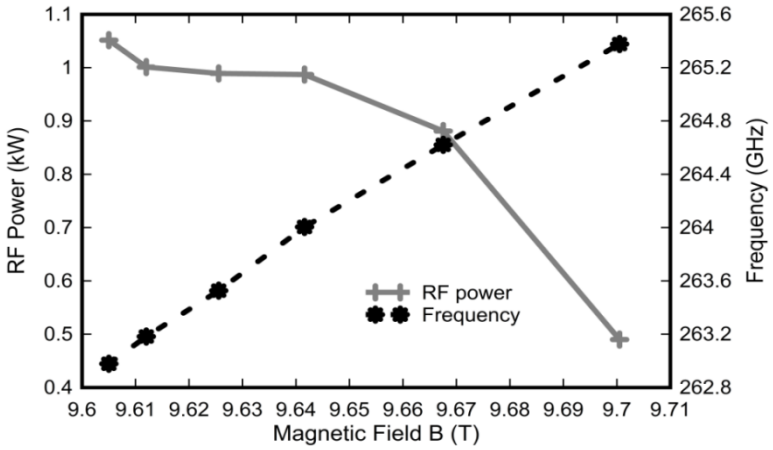

Figure 5.7: Operating frequencies and RF power levels for various axial variations, q =1 to 6 in magnetic tuning at I_b = 400mA.

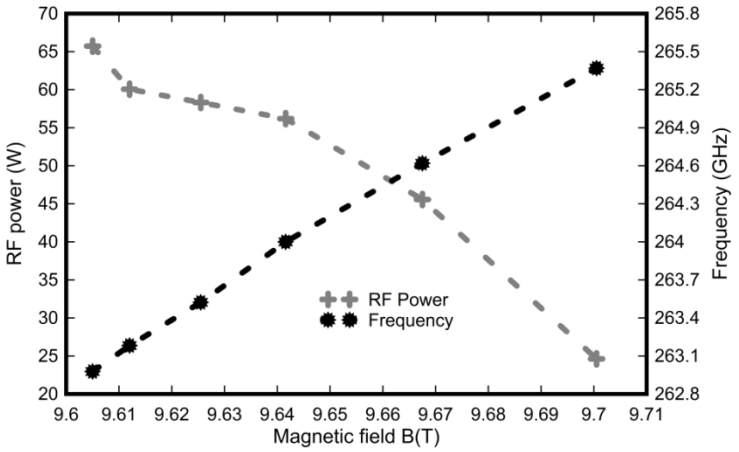

Figure 5.8: Operating frequencies and RF power levels for various axial variations, q = 1 to 6 in magnetic tuning at I_b = 20 mA.

5.4.2. Investigations via Electrical Tuning

Secondly, the tunability of the proposed design is studied for beam voltage variations namely electrical tuning. As per the beam voltage variations, the RF power developed in interaction cavity mode $TE_{5,3,q}$, from q = 1 to 6, is tabulated in Table 5.5, which gives the various RF power levels for different axial variation modes at various oscillating frequencies.

Table 5.5: Electrical tuning parameters

Axial Mode q	Frequency (GHz)	Magnetic Field (T)	Beam Voltage (kV)	RF Output Power (kW)	Q_{diff} Quality factor
1	262.9780	9.605	15	1.0516	14500
2	263.1817	9.605	14.590285	0.9862	3510
3	263.523	9.605	13.904195	0.9732	1560
4	264	9.605	12.9538	0.9079	890
5	264.620	9.605	11.734129	0.8085	562
6	265.370	9.605	10.244976	0.7039	412

It can be observed from Figures 5.9 and 5.10 that variations in the RF power output as well as oscillating frequencies with respect to the variations in the beam voltage at I_b = 400 mA as well I_b = 25 mA.

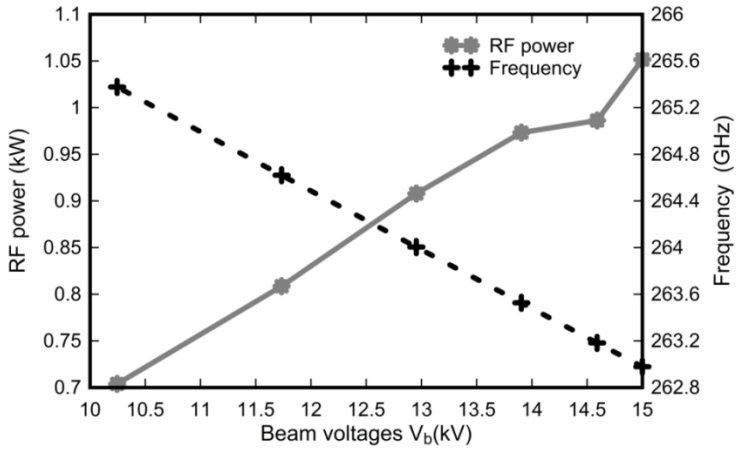

Figure 5.9: Resonant frequencies and RF power levels for various axial variations, q =1 to 6 in electrical tuning at I_b= 400 mA.

It can be further observed that, the magnetic tuning results good amount of power over electrical tuning even though both tuning mechanisms resulting a significant amount power more than 490 W at I_b = 400 mA as well around 50W threshold power at I_b = 0.02A.

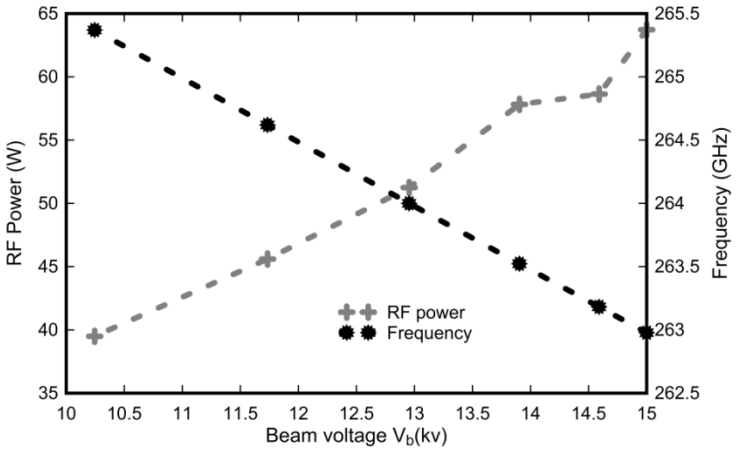

Figure 5.10: Resonant frequencies and RF power levels for various axial variations, q = 1 to 6 in electrical tuning at Ib = 20 mA.

5.5. Output RF Window

For the present work too, a single disc type RF window has been chosen for transmitting the generated RF power in the device to the output transmission line. Considering the broadband tunability nature of RF output, the design has been carried for several disc thicknesses d_w. As well, since the generated RF power does not cause any thermal deformations so no cooling has been necessary. For the present case, a SiO_2 Corning 7980 UV has been chose as a window material. The material properties have been tabulated in Table 5.6 [Mandal *et al.* (2015) and Gray *et al.* (2008)].

Table 5.6: SiO_2 Window for $TE_{5,3,q}$ mode

Material	**Window radius R_{win}**	**Permittivity**	**Loss tangent**	**d_0, disk thick ness at N=1**
SiO_2	25.75 mm	3.9	115×10^{-5}	0.2888 mm

By means of the analysis presented in Chapter 2, the transmission T(dB) and reflection characteristics R (dB) of output RF window versus frequencies at various disc thicknesses d_w has been investigated .

The disc thickness is given by

$$d_w = N\frac{c}{2f\sqrt{\varepsilon_r}}, \quad \text{where } d_0 = \frac{f}{2f\sqrt{\varepsilon_r}} \quad , \tag{5.7}$$

where N is an integer and varies, 1, 2, 3, 4, ... etc.

In the present work, N has been has been varied from 1 to 8 for identification of suitable disc thickness. The window has been designed by assuming the generated RF power is in TEM_{00} mode at the RF window. The radius of the window is chosen as 25.75 mm, even though the radius of the RF window does not effect in case of TEM_{00} mode.

The resulted reflection and transmission characteristics versus frequency for various thicknesses are plotted in Figures 5.11 and 5.12.

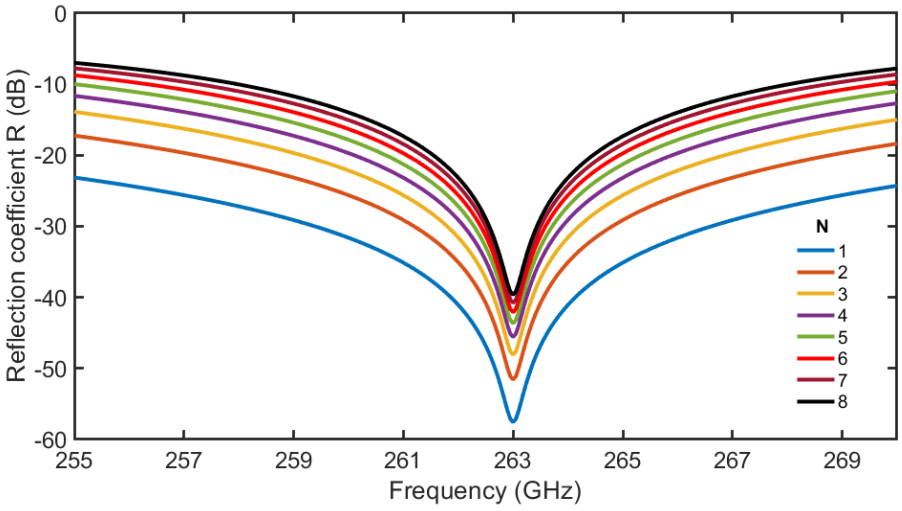

Figure 5.11: Reflection characteristics R (dB) versus frequency (GHz) at various disc thickness $d_w = N^* d_0$ of window radius thickness.

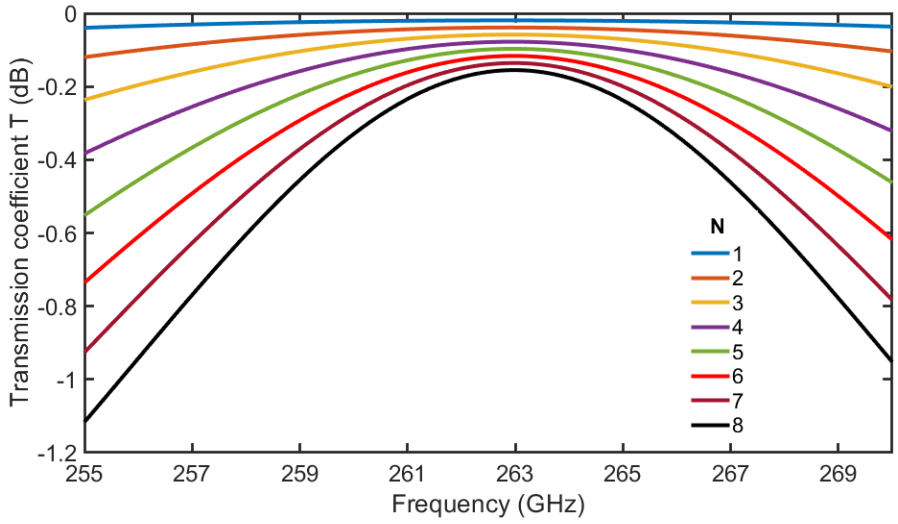

Figure 5.12: Transmission characteristics T (dB) versus frequency (GHz) at various disc thickness $d_w = N*d_0$.

It can be observed that the variation in the disc thickness are effecting the transmission characteristics of maximum variation of 0.25dB per d_0 variation multiple whereas the reflection characteristics all are having minimum value at 263 GHz and the amount of reflection increases with the disc thickness. By observing, the window thickness has been chosen for $N = 4$, i. e., $d_w = 1.155$ mm for the window radius of 25.75 mm.

5.6. Conclusions

The design constraints, design and analysis of RF interaction cavity structure of the tunable gyrotrons for the DNP-NMR spectroscopy applications are presented. Initially, for the operated mode $TE_{5,3,q}$, the RF interaction structure has been determined by solving single mode Vlasov approximation for various cavity geometries and are optimized. Later, for identifying the minimum beam currents and various competing modes, the linear theory of gyrotrons has been used and the corresponding parameters

for various axial mode indices of the operating mode are determined. As of now, the time dependent multimode theory has been used for deciding the working modes with single axial mode index, i. e., $q = 1$. By amending necessary changes to the time dependent multimode theory, i. e., updating Gaussian profiles to the actual *h(z)* profiles for various axial mode, variations of the beam wave interactions are carried out. The magnetic and electrical tuning techniques have been implemented for achieving the broadband tunability. In case of magnetic tuning, by varying a *B(z)* from 9.6005 T to 9.7005 T, a continuous frequency band of 2.4 GHz has been observed. For the case of electrical tuning technique, by down shifting the beam voltage from 15 kV to 10.245 kV, a continuous tunability of 2.4 GHz has been achieved with threshold of output power >20 W. All the analysis has been carried out considering zero spread in the beam as well no misalignments in between the beam optical axis and microwave circuit axis. Since, the generated output power is very less that it does not cause severe deformations in the structure by ohmic losses so the thermal analysis has not been performed.

As well as, the output RF window that acts as shielding between the vacuumed and outside transmission system has been designed using SiO_2, Corning 7980 UV as material. For various cavity thicknesses, the reflection and transmission characteristics of the window versus frequency have been performed and the optimized window parameters are determined.

CHAPTER 6

DESIGN MODIFICATION IN RF INTERACTION CAVITY OF A 140GHZ GYROTRON TO ACHIEVE WIDE TUNABLE BANDWIDTH FOR DNP-NMR SPECTROSCOPY APPLICATIONS

6.1. Introduction

As discussed in Chapter 5, Dynamic Nuclear polarization (DNP) enhanced NMR spectroscopy desires to have a wide tunable RF source for better sensitivity required for material characterization. Keeping this as our goal, using the knowledge acquired in Chapter 5, in the current Chapter, we have revisited an experimental reported gyrotron device that operates on $TE_{0,3}$ mode at 140GHz for 212MHz DNP-NMR applications by Joyce *et al.* 2006. It has been reported that the tunability of the RF source had been achieved by magnetic as well thermal tuning techniques. In addition, it was observed that, the gun is able to generate the maximum beam current of 25mA as well the device has been operated upto second order axial mode $q = 2$ mode in the ideal condition. For low power tunable gyrotrons, the device can be operated in the axial mode index q from 1 to 6, that able to generate a minimum threshold power over a wide continuous frequency range without variation of m and p indices of the mode. For this, one possible way is to design longer interaction cavities thereby achieving magnetic as well electrical tuning techniques.

In this Chapter, an experimentally demonstrated low power gyrotron operating with beam voltage 12.3 kV and current 25mA at 140GHz for 212 MHz DNP NMR spectroscopy reported by Joyce *et al.* 2006 is revisited and its RF cavity design is suitably modified to enhance device tunable bandwidth by magnetic tuning. By the help of the concepts described in Chapter 5 of this thesis, for the reported RF cavity geometry with the beam parameters, the cold cavity RF characteristics and the beam wave interaction behaviour is studied as well as through PIC simulation studies are also performed using a commercial PIC code "CST Studio Suite".

As the reported gyrotron has a limited tunable bandwidth via magnetic tuning and only thermal tuning is used. From the knowledge of the Chapter 5 about lengthy

interaction space, with the aim of achieving wider device tunable bandwidth, the tapered cylindrical RF interaction cavity is suitably modified such that in addition to thermal tuning, the magnetic tuning can also be achieved by operating the device in the high order axial operating modes using the same beam parameters. The operating mode is considered here as $TE_{0,3,q}$ with a target of more tunable bandwidth through magnetic tuning as well. With the modified RF cavity, the cold cavity analysis and its electron-beam and RF-wave interaction behaviour studies through analysis as well as PIC simulations at various beam currents and magnetic fields are carried out.

Chapter 6, is organized as follows: for confirmation about the possible axial operating modes q, the cold cavity analysis and the start oscillation current I_{soc} curves that provide information for the state of the mode oscillation at various magnetic fields are done. Followed by the determination of RF field profiles, diffractive quality factors and resonant frequency calculations under beam absent conditions for the reported cavity and the modified cavity. The beam wave interaction mechanism in the RF cavities for various modes are studied using time dependent, non-linear, multimode theory and the same the beam wave interaction mechanisms are simulated through PIC simulation code of Commercially CST and presented. A conclusion that summarizes the current chapter is presented at the end.

6.2. RF Interaction Cavity Design Modification

An RF source generates the RF energy by interacting with DC electron beam. Suitable environments are required for the successful and sustainable RF radiations with desired characteristics conditions that include selection of appropriate beam parameters, and the space that allows the interaction between electron beam and RF wave, i.e., Interaction region.

A conventional, tapered cylindrical RF interaction cavity is taken as the interaction structure in the present design. As discussed in Chapter 5, the design and optimization of an RF interaction cavity requires the knowledge of axial RF field profiles $V_{mp}(z)$, resonating frequencies f_{res}, and its diffractive quality factor Q_{diff} that gives the information about the amount of RF power diffracted from cavity.

For broadband tunable gyrotrons, it is advantageous to design the RF cavity which operates in the mode over a range of frequency, i.e., $TE_{m,p,q}$, where the axial mode index q changes usually from 1, 2, 3 etc. This kind of implementation eases the design of the post RF interaction cavity components, i.e., nonlinear taper, collector and the RF window for the collecting and guiding the generated RF power simpler since the mode has same azimuthal and radial variations. Usually a longer interaction cavity section is chosen with Lc is of few tens of wavelengths for the smooth transitions over axial mode indices as frequency varies. Longer interaction cavities yield higher Q values. The diffractive quality factor $Q_{diff,q}$ for the various axial mode indices are related to fundamental $Q_{diff,1}$ as [Hornstein *et al.* (2004)]

$$Q_{diff,q} \approx \frac{Q_{diff,q=1}}{q^2} \quad . \tag{6.1}$$

As the axial mode indices increases, the corresponding diffractive quality factor reduces by a factor of $\sim q^2$ and it indicates about the amount of power generation is reduces too that makes the generation of stable power over tunable band of frequencies challenging. In the present work, as stated above, the RF interaction cavity designed for the 212 MHz DNP-NMR spectroscopy applications is considered; the beam and geometrical parameters are given in Tables 6.1 and 6.2. The axial RF field profiles $V_{mp}(z)$, resonating frequencies and corresponding diffractive quality factors Q_{diff}, under

beam absent conditions are determined by solving Vlasov approximation equations like done so far.

Table 6.1: Design beam parameters of Joye *et al.* (2006)

Parameter	**Value**
Frequency f	139.65 GHz
Output power P_{out}	> 10 W
Beam voltage V_b	12.3 kV
Magnetic field at the cavity B_0	5.06 -5.12 T
Pitch factor α	1.6
Harmonic number, s	1
Beam current I_b	25 mA

Table 6.2: RF Interaction cavity dimensions of Joye *et al.* (2006)

Parameter	**Value**
Cavity radius R_c	3.48 mm
Down taper length L_d	5.5 mm
Down taper angle θ_d	1^0
Up taper length L_u	36.25 mm
Up Taper angle θ_{up}	2^0
Middle section Length L_c	28.25 mm
Resonant Frequency f_{res}	139.65 GHz
Diffractive quality factor Q_{diff}	6950

The normalized axial RF field profiles, for various possible axial modes of the reported parameters, q = 1, 2, and 3 with resonant frequencies along radius profile $R(z)$

are shown in Figure 6.1. The calculated and reported resonant frequencies f_{res} as well diffractive quality factors Q_{diff} for various axial mode indices are tabulated in Table 6.3. Even though there was no mention about the existence of the axial mode index 3 but we observed the existence of it through our calculation and the corresponding details are tabulated too.

Table 6.3: Tailored RF cavity parameters

Mode	Reported f_{res} (GHz)	Calculated f_{res} (GHz)	Reported Q_{diff}	Calculated Q_{diff}
TE_{031}	139.650	139.647	6950	6950
TE_{032}	139.870	139.841	1750	1750
TE_{033}	Not stated	140.241	Not stated	810

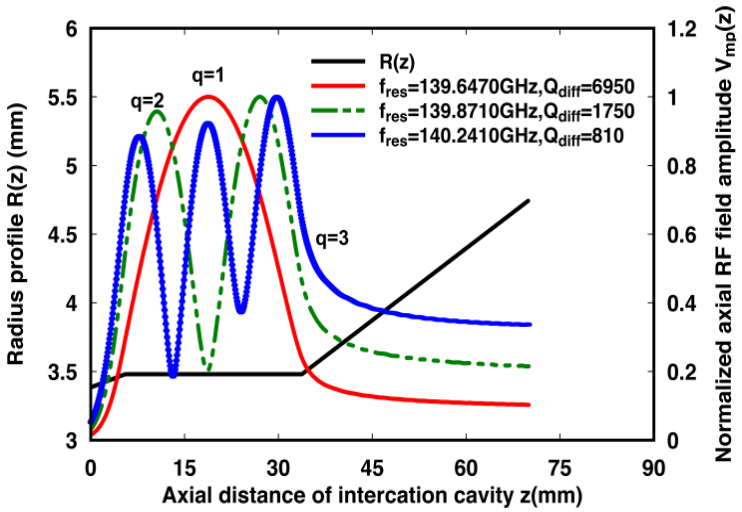

Figure 6.1: Normalized cold cavity axial RF field amplitude profiles for various axial mode indices $TE_{0,3,q}$, where q = 1, 2, 3 of Joye *et al.* (2006).

The possibility of oscillation of various modes in the cavity with respect to magnetic fields, subjected to the given beam parameters are assessed by calculating the start oscillation current curves I_{soc}. By varying the background DC magnetic field from 5 T to 5.2 T, the start oscillation current curves I_{soc} values for the operating mode $TE_{0,3,q}$

at various axial indices q are calculated and are plotted in Figure. 6.2. It can be observed that the minimum current required for oscillation of the TE_{03q}, at q = 1 and q = 2, is less than 20 mA, whereas for the q = 3 mode is above 35 mA. Since, the electron gun under consideration is limited to supply the beam current of maximum 25 mA so it confirms the oscillation and growth of the high order axial modes are unattainable of mode $TE_{0,3}$ with q = 3 due to magnetic tuning and even for the excitation of q = 2 mode is also challenging with given dimensions and beam parameters. Due to this limitation, the tuning of the device was achieved by varying the temperature of the coolant at the outer walls of the cavity thereby changes in the radius profile of the structure R (z) and that affects the operating frequency, i.e., via thermal tuning. It was mentioned that 0.2MHz/K is observed as per thermal cooling technique for the present design.

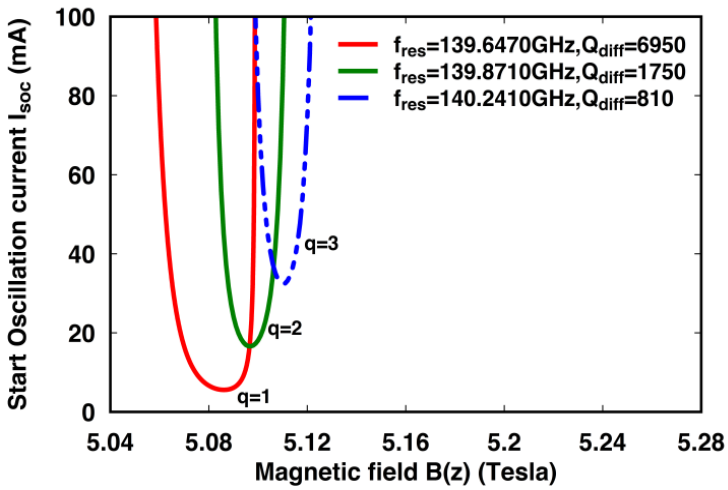

Figure 6.2: Start oscillation current I_{soc} (mA) versus DC magnetic field B (T) plots of $TE_{0,3,q}$ for different axial mode indices q of Joye *et al.*(2006).

But if we are able to operate the device even in high order axial modes (q > 2), the tunable bandwidth of the device can be improved. Targeting the enhancement of the tunable bandwidth as the priority, the dimensions of the RF interaction cavity can be modified keeping the same beam parameters, such that the device is able to operate in high order axial mode indices further. Considering the fact of longer cavities allows device to operate with low beam currents as well scope for exciting the high order axial

modes by with the surrendering the longer Q values. Since, the electron gun is limited of beam voltage 12.3 kV and beam current up to 25mA, the tailoring the cavity dimensions such that the device is able to operate for low beam currents I_b as well high axial mode operation.

The RF interaction cavity analysis using Single mode Vlasov approximation in the absence of beam is carried by considering various cavity geometrical combinations and the optimized modified dimensions are listed in Table 6.4. The corresponding RF characteristics, namely, f_{res}, Q_{diff} of the various axial modes are tabulated in Table 6.5 and compared with the cold cavity characteristics reported by Joye *et al.* (2006).

Table 6.4: Modified RF interaction cavity parameters

Parameters	**Value**
Cavity radius R_c	3.48 mm
Down taper length L_d	10.5 mm
Down taper angle θ_d	1^0
Up taper length L_u	36.25 mm
Up taper angle θ_{up}	1^0
Middle section length L_c	35.25 mm
Resonant frequency f_{res}	139.62 GHz
Magnetic field B	5.05 -5.20 T

Table 6.5: Resonating frequency f_{res} and diffractive quality factor Q_{diff} of modified cavity

Mode	Reported f_{res} (GHz)	Calculated Q_{diff}
TE_{031}	139.62	10100
TE_{032}	139.771	2570
TE_{033}	140.0207	1152
TE_{034}	140.368	652

The cold cavity axial RF field profiles $V_{mp}(z)$ along with radius profile $R(z)$ of the modified cavity geometry are shown in Figure 6.3. Assigning the same beam parameters, for the modified interaction cavity, the start oscillation current curves I_{soc} are calculated over a range of magnetic fields B and are plotted in Figure. 6.4. It can be observed from the analysis that the minimum current required for the oscillation of the axial mode indices for q = 1, 2 and 3 is less than 20mA whereas for the axial mode q = 4, it is at the verge of 25mA.

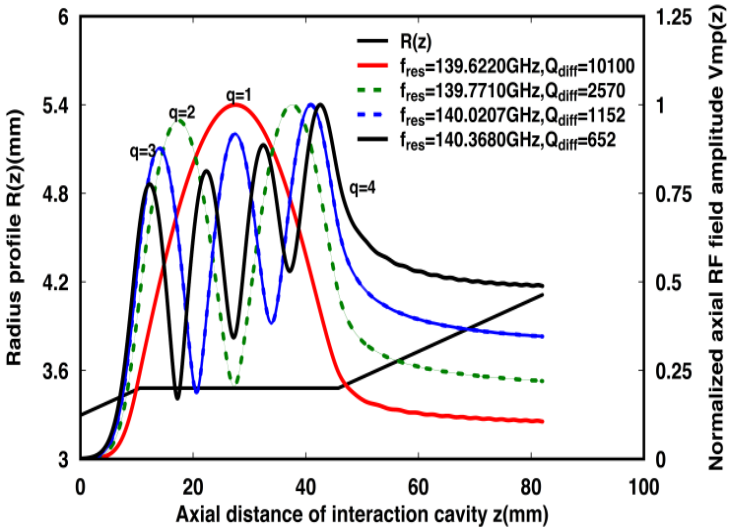

Figure 6.3: Normalized cold cavity axial RF field amplitude profiles of modified cavities for various axial mode indices $TE_{0,3,q}$, for q = 1, 2, 3, and 4.

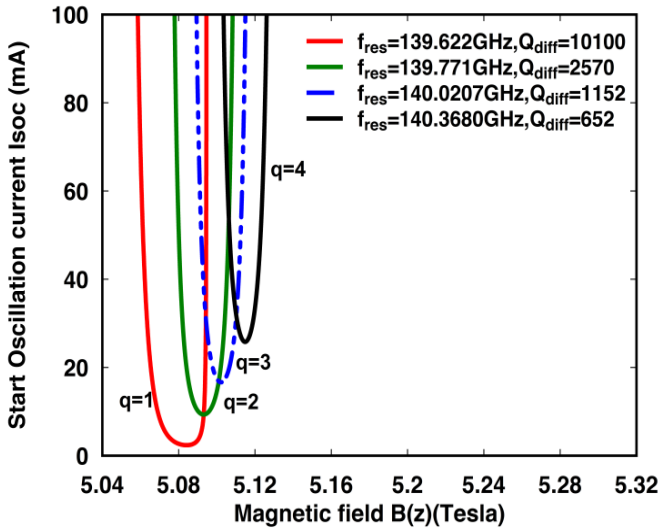

Figure 6.4: Start oscillation current Isoc (A) versus DC magnetic field B in (T) plots for different axial operating modes of $TE_{0,3,q}$ for modified RF cavity dimensions.

From the curves, it can be observed that the minimum values of I_{soc} are reduced as compared with those reported by Joye *et al.*(2006), as well the excitation of axial mode index up to q = 3 is achievable since the minimum current required is well less than 25 mA. The longer interaction cavities allow more interaction space thereby chances of more electron beam and RF wave interaction results higher output power with proper tailoring of the cavity dimensions. These are examined by studying the beam wave interaction behaviour that gives information about the temporal growth of the RF power using time dependent multimode theory as well obtained through 3D PIC simulation codes. A commercially available code "CST studio suite" is reconfigured and used for this purpose. The details of the electron beam-wave interaction studies for both the interaction cavities are carried and presented in in the following section**.** Though, the uptaper angle is less than the reported cavity, but the generated RF power from the RF cavity is transmitted by choosing a suitable NLT section, QOMC sections and is kept out of the scope of the present research work.

6.3. Beam-Wave Interaction Exploration

As discussed in the previous chapters about the beam wave interaction importance and the procedure to calculate it, using the same theory and way the beam wave interaction analysis and PIC simulations are carried out for both the reported and the modified cavity dimensions with the same beam parameters. The main details of our finding are discussed as follows.

6.3.1. Time-dependent multimode analysis

In the present study, selecting a uniform background DC magnetic field profile B(z) along the interaction length, the coupled equations are numerically integrated using fourth order Runge-Kutta method. A 12.3 kV DC voltage is applied to a uniformly distributed gyrating electron beam carrying a current of 25mA having 16 beamlets with 16 electrons in each beamlets. For the operating and its neighbouring modes, like, $TE_{2,3}$, $TE_{0,2}$, the beam-wave interaction calculations are done. Taking various magnetic field values, the temporal growth of RF powers in the output mode for both the designs with respect to the time has been determined. The temporal growth of RF power in the main mode $TE_{0,3,1}$ for both the cavities are determined analytically and plotted in Figure.6.5. The RF powers of the operating modes for various magnetic fields are calculated while providing the various axial mode index profiles with the corresponding frequencies for both the designs and are plotted in Figure. 6.5. For both cavities designs, the analytical calculations are carried out by taking the beam current 25mA.

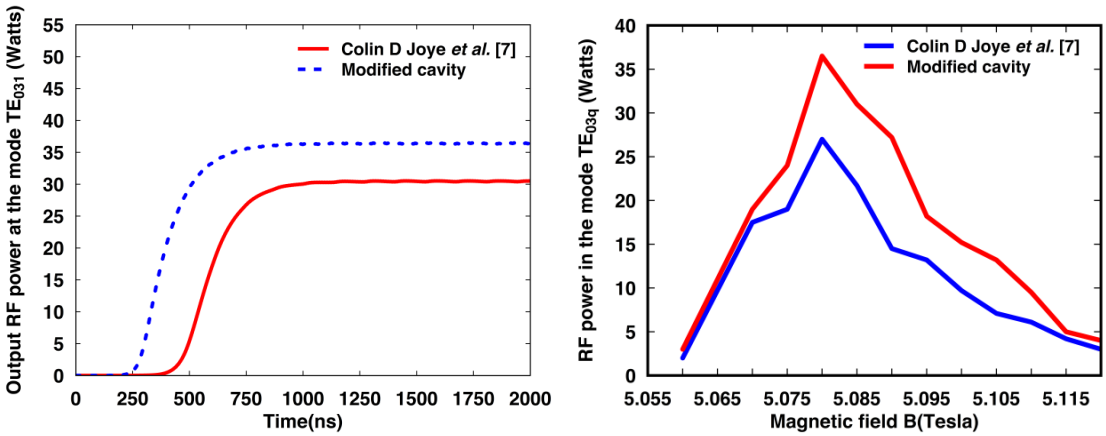

(a) (b)

Figure 6.5: Comparisons of RF power (a) versus time using multimode analysis and (b) with respect to magnetic fields for cavities of Joye et al. (2006) and modified design.

6.3.2. PIC simulation of the gyrotron

In addition to the non-linear multimode analysis, like in the Chapter 3 and 4, using 3D particle in cell solver, simulation of the electron beam and RF-wave interaction mechanisms of the device is performed reconfiguring a commercial code "CST Studio Suite" for both the cavity geometries. In the present study, the modelled is designed in CST studio suite selecting OFHC copper as the cavity material with conductivity of 2.9×10^7 S/m by assigning suitable boundary conditions. A DC particle source is taken for forming the gyrating electron beam with assigned parameters, and a uniform magnetic field profile is applied along the device structure axis.

For observing the time varying behaviour of modes, various 3D E-field and H-field monitors are placed with suitable boundary conditions. The PIC simulation has run for 1000 ns and after the simulation time, by performing post processing steps, the necessary information for confirmation of the device design has been carried out.

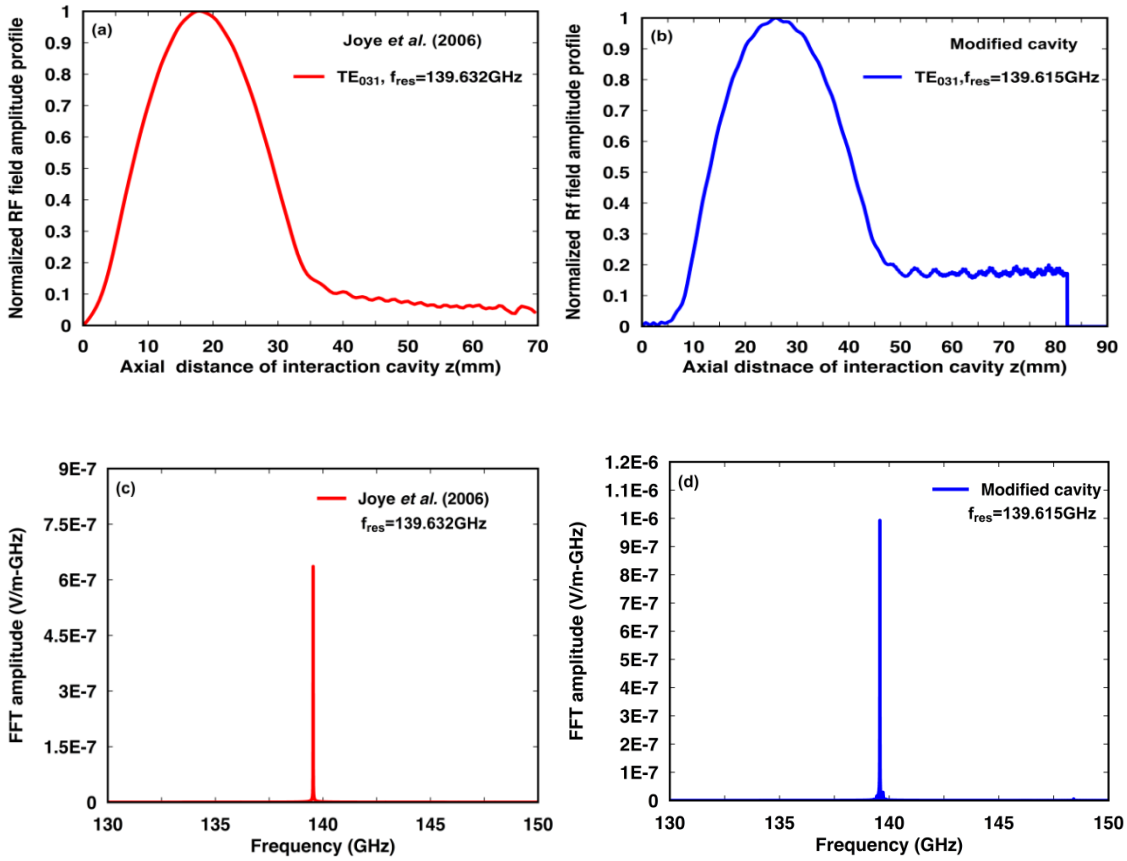

Figure 6.6: PIC Simulation results - (a-b) hot axial RF field profiles (c-d) frequency response of the operating mode $TE_{0,3,q}$ with axial index q = 1 for cavities of Joye et al.(2006) and modified designs, respectively.

The PIC simulated results for both the designs at beam current I_b = 25 mA and magnetic field 5.08 T are shown in Figures 6.9 and 6.7. The axial RF field profile in the presence of the electron beam along with the fast Fourier transform of the mode is shown in Figure 6.6. The temporal growth of mode amplitudes and the peak power generated in the mode $TE_{0,3,1}$ mode is shown in Figure 6.7.

It is found that the operating mode oscillates at 139.63 GHz for the reported cavity dimensions and able to generate power of ~ 23W whereas for the modified cavity it has been observed that a stable RF power of more than ~ 27W oscillating at 139.59 GHz in the fundamental axial mode of TE_{031} for a beam current of 25 mA at magnetic

field 5.08 T. The results are shown for the external magnetic field of a 5.08 T uniform magnetic field along the interaction structure.

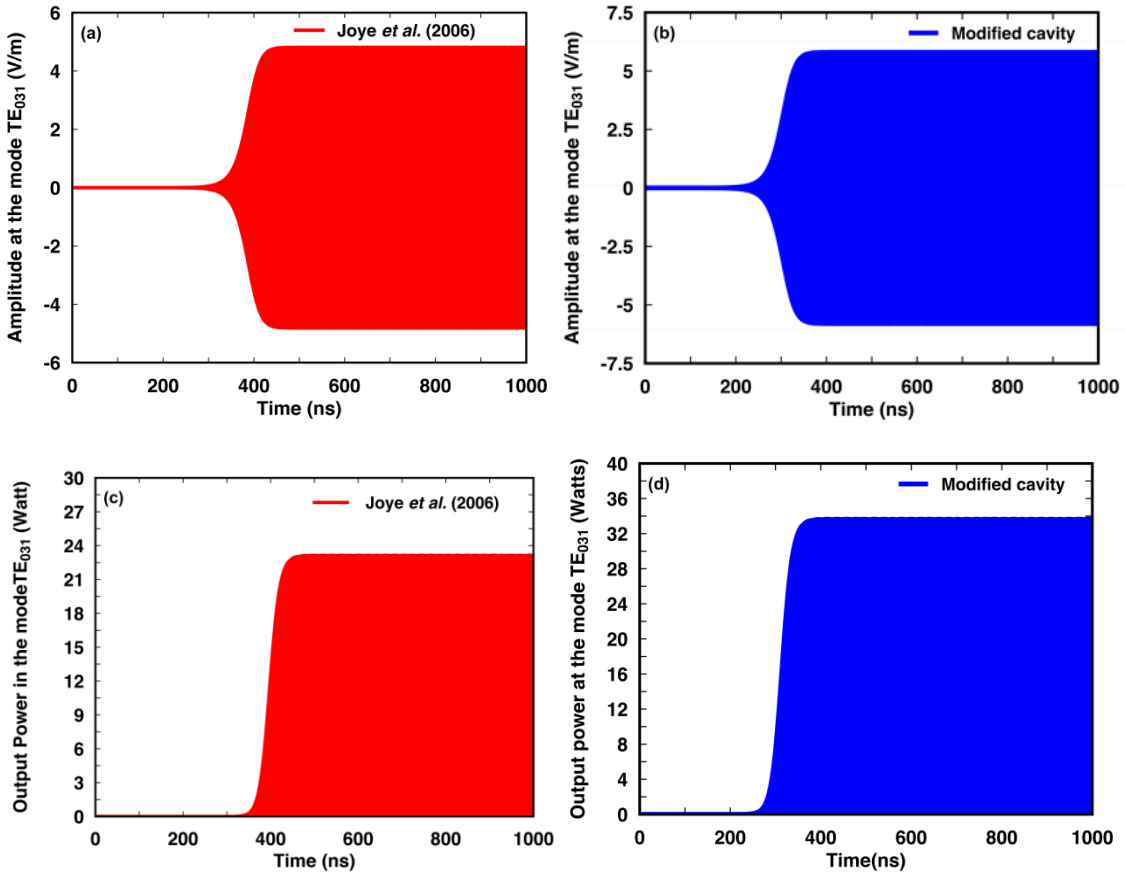

Figure 6.7: PIC Simulation results - Temporal growth of mode $TE_{0,3,1}$ (a - b) amplitudes (c - d) power values for cavities reported design by Joye *et al.* (2006) and as per our modified design, respectively.

Even an amount of more than 15W power is observed in the second axial mode index of $TE_{0,3,2}$ oscillating at 139.76 GHz for beam current of 25 mA at magnetic field of 5.11 T. By operating the device in the high order axial modes, through magnetic tuning, the operating bandwidth found to be enhanced.

6.4. Conclusions

A low power, tunable gyrotron operating in a $TE_{0,3,q}$ mode for 140 GHz DNP NMR spectroscopy applications is explored to facilitate wider bandwidth with magnetic tuning. The RF interaction cavity design has been tailored such that it can operate in the

high order axial modes. The beam absent as well as beam present RF wave behaviour, both analytical and Particle-in-Cell (PIC) simulation studies have been presented. Gyrotron beam-wave interaction behaviour explored using time dependent non-linear multi-mode analysis for various beam currents and magnetic fields and more than >15W of RF power over a tunable bandwidth of 400MHz has been achieved through magnetic field tuning for the tailored the interaction cavity. More than 15W RF power output over a band of 400 MHz through magnetic tuning has been attained solely apart from thermal tuning at beam currents of around 25 mA. The thermal tuning behaviour for the modified cavity is kept beyond the scope of the present research. In addition, a 3D PIC simulation for fundamental modes TE_{031}, at beam currents 25mA for both the designs have been carried out and it was found that the modified design gives more power compared with reported design due to lengthy interaction space. Further, it was also observed that, the time required for the growth of RF power gets reduced for the modified cavity. This tunable bandwidth gyrotron design provides important application for the enhancement of sensitivity of the DNP NMR spectroscopy.

Though, the cavity has been tailored for enhancement of bandwidth, but the suitable after cavity components are also need to be designed such that the generated RF quantity and is to carried to the output transmission system. Due to the tunability nature of the RF quantity, the design of nonlinear taper, Quasi-optical mode converter as well RF window becomes little bit complex and these are not kept within the scope of the present research work.

CHAPTER 7

SUMMARY, CONCLUSION, AND FUTURE SCOPE

7.1. Summary and Conclusion

7.2. Limitations of the Present Work and Scope for Further Studies

7.1. Summary and Conclusion

In the present dissertation, the design and analytical investigations of single frequency as well tunable frequency gyrotron oscillators, a kind of fast wave device, operating in the millimeter and sub millimeter frequency regime, have been carried out. Design study of the gyrotron using tapered cylindrical type RF interaction structures operating for the single frequency, medium power level gyrotrons operating in whispering gallery mode and volumetric mode have been presented. The device designs for its electron-bean and RF-wave interaction performance as well as thermal effects have been studies through analysis and simulation. For the first time, we have used single simulation tool for the gyrotron beam wave interaction and thermal studies. We have also suggested modified device design to mitigate the thermo-mechanical effect and its effect on the device RF performance are investigated. Followed by, the design and analysis of post interaction cavity components, like, the nonlinear taper section, quasi optical mode launcher and the output RF windows for transmission of the generated power in the interaction cavity to output transmission system have been described. An afetrcavity interaction study for single frequency gyrotron oscillator has also been carried by considering uniform axial magnetic field profiles. In addition, the design and frequency tuning studies of low power, tunable frequency gyrotrons for DNP enhanced NMR spectroscopies with electrical and magnetic tunings have been described in detail. Necessary steps required for the device parameters selection, tapered cavity RF interaction structure design of the tunable frequency gyrotrons have been presented. Further, the RF window used for the tunable frequency RF extraction has also been discussed.

In Chapter 1, with the introduction of gyro-devices evolution and literature review of high and low power gyrotrons operating in the single frequency and tunable frequency, respectively. Operating principle, and sub-assemblies of the gyrotron oscillators have been

presented. Thereafter, various output couplings used in the gyrotrons and their advantages as well challenges have been presented. The applications of various power level gyrotrons generating RF radiation at single and tunable frequencies are discussed. The motivation of the present research and the organization of the thesis are drawn at the end.

With the knowledge of the implementation of the radial output type couplings in high power, high frequency gyrotron oscillators, in Chapter 2, the components, i.e., quasi optical mode converters that are responsible down converting interaction mode into low free space Gaussian like mode TEM_{00} for radial output couplings have been presented. Starts with the brief theory for the representation of interaction cavity mode TE_{mn} into group of rays used for the design of the quasi optical launcher, a part of mode converter followed by various types of QOM converters, i.e., Vlasov type and Denisov type are discussed. The dimensions of the Vlasov launchers for the 95GHz, 100kW TE_{62} and $TE_{10,4}$ modes gyrotrons, a single frequency medium power level rating, to be presented in the Chapter 3 and 4 of this thesis are determined. Observing the limitations and design considerations of Vlasov type converters, in the present work, Denisov type launchers have been chosen for radial output couplings. A brief notes on the coupled mode theory used for the analysis of Denisov type launchers have also been presented.

Usually, the quasi optical mode converters used for the radial output couplings are designed and optimized by widely accepted commercial software's LOT and SURF3D developed Calabaza's Creek. Considering its unavailability with respect to cost with researcher, we developed our own numerical code in the Matlab domain based on the theories available in various literatures for the study of quasi optical launchers as of now. The code has been validated by calculating the mode variation profiles and the wall intensity field for the $TE_{22\ 6}$, 110GHz gyrotron developed by Blank (1994). Thereafter, the optimization of the Denisov launchers for the $TE_{10,4}$, 95GHz 100kW by inspecting the mode variation profiles

along the launcher followed by wall field intensity profiles have been performed successfully, with ~ 99% accuracy.

Further in this Chapter 2, the analysis and design of single disc type output RF windows for various type of operating modes, i. e., TE_{mn}, TM_{mn} and TEM_{00} have been presented in detail. Then, considering several window materials, the RF window for $TE_{10,4}$-, 95GHz has been designed by inspecting the transmission and reflection characteristics versus frequency at various disc thicknesses.

By knowing the role of gyrotron oscillators in security applications as a potential RF source for active denial system applications that operates in W-band; in Chapter 3, design and analysis of a tapered cylindrical cavity gyrotron oscillator has been presented. Considering the operating mode $TE_{6,2}$ as well as beam parameters by VGB 8095 gyrotron, given by CPI, USA, the design and analysis of RF interaction structure has been presented. By solving the single mode Vlasov approximation equation, the suitable interaction cavity dimensions are obtained and verified with published data. Thereafter, for the interaction cavity combinations, using non-linear, time dependent multimode analysis reported by Fliflet *et al.*, widely accepted theory for the beam wave interaction studies of gyrotrons, a self-consistent code has been indigenously developed and used for the analytical study of the designed gyrotron. For the same beam and cavity combinations, using PIC solver code of Commercial "CST Studio Suite", the gyrotron model has been designed. The beam wave interactions are investigated for different combinations of input parameters by considering a uniform axial magnetic field profile. The generated RF power and efficiency curves of the designed interaction cavity are found in good agreement. In practical circumstances, the occurrence of velocity spreads in the beam as well beam misalignments are inevitable though in small amounts. Considering this, the beam wave interaction studies are carried out using 3D PIC simulation. It has also been observed that a small shift in the beam optical axis affects severally on the performance

of the system and limits the margin of dimensional tolerances. By RF studies, the interaction cavity dimensions that are responsible for the growth of RF power with desire qualities of 100kW at 95GHz are determined and optimized. But, due to metallic nature of the cavity walls, the generated RF power leads ohmic losses in the structure that acts as heat load there by thermal effects that causes mechanical deformations of structure which plays critical role in the RF performance of device. Therefore, for the present medium power level, the thermo-mechanical effects and its effect on the RF performance are investigated considering the cavity material conductivity as 5.8e7 S/m (an ideal value). The thermo mechanical effects and design of optimized cooling system parameters are determined by COMSOL Multiphysics by providing the generated ohmic losses as heat load. For the present work, instead of allowing coolant with different velocities and temperatures on the outer walls, by varying convective heat transfer coefficient, and providing extended heat surfaces called fins over the middle section the cavity, the cooling system has been optimized. The required coolant parameters for achieving the optimized heat transfer coefficient are determined. The RF studies of interaction cavity after taking the optimized thermal system effects are studied and the variations in the RF performance are under tolerable limits of the design.

In Chapter 3, the RF simulation study using commercial 3D PIC code "CST Studio Suite" and thermo-mechanical studies using commercial PIC code "COMSOL Multiphysics" have been carried out. It has been observed that, the thermal effects due to ohmic losses limits the margins of cavity dimensions tolerances and that necessitates the presence of cooling maintenance system for the high power devices. As well as, the shifts in the electron beam, i. e., misalignment of the beam axis with respect to cavity axis, have also been found to limit the device performance. Since, the dimensional and beam radius variations are also get scales with operating modes, so lower order mode gives small margin of tolerances, even though mode like, $TE_{6,2}$ is widely used at 95GHz frequency for 100 kW gyrotron, but observing

these effects, we wants to investigate the advantages as well as challenges by operating this specification gyrotron device in the higher order volumetric modes, which is so far not fully explored and reported in the published literature, at least not accessible to us.

Considering the challenges and issues related to thermo-mechanical deformations and misalignments, in Chapter 4, we designed, analyzed and simulated the same rating gyrotron device that operates in a relatively higher order mode $TE_{10,4}$- that allows a wide transverse dimensions thereby more relaxation regarding thermal issues as well as it could also be upgraded to higher power levels too. In the literature, Krishna *et al.* (2011), have started the mode selection and the analysis of RF interaction cavity in the absence of electron beam though not dealt with the beam-wave interaction studies that includes RF analysis and thermo-mechanical analysis as well the post interaction components, like, nonlinear taper, and RF window designs were not reported. Considering this gap, as well as the goals mentioned in Chapter 3, in the present work, the design, analysis and simulated the device and its RF interaction cavity that gives the desired power in the operating mode $TE_{10,4}$ and larger dimension relaxes the thermo-mechanical issues are presented.

After the RF interaction cavity design, to ensure stable device operation at the desired oscillation frequency, the beam wave interaction studies of the cavity by adding a raised cosine type non-linear taper (NLT) has been carried-out for the axial uniform magnetic profile. By extending the single mode Vlasov approximation equation, the suitable nonlinear taper section has been determined by inspecting the cold cavity RF field profile (in the beam absent condition). Then, the RF cavity and NLT section has been optimized through the beam wave interaction studies. Since, the time dependent multimode theory proposed by the Fliflet *et al.*, have been used so far considering the uniform section of the cavity with ideal Gaussian beam. In the present work, we extended it by incorporating the actual field profile and is calculated by solving the Vlasov approximation equation to the combined RF cavity and NLT

geometry. For the same, using the PIC code of Commercial CST Studio Suite, the beam wave interaction simulations are carried out with uniform DC magnetic field profile. The analytical results calculated from the updated time dependent theory as well from the simulations are found in good agreement. Observing the beam wave interaction calculations after adding the NLT section, it is found that a less uptaper with longer NLT section results early growth of RF power. In addition, observing the effect of beam misalignments on the beam coupling to the TE_{mn} mode, the additional coupling term has been incorporated to the time dependent multimode theory that allows successfully, the effect of misalignments on the beam wave interactions. The analytical and the simulated results for various offset in the beam axis with respect to the cavity axis are calculated and both results are found in good agreement. And it was found that for $TE_{10,4}$ mode, the effect of beam widths on the RF performance are very much less compared to that for the $TE_{6,2,}$ 95GHz gyrotron design. Instead of performing the thermo-mechanical calculations using the code COMSOL Multiphysics, for the present case, the thermo-mechanical analysis has been carried using Steady state thermal solver as well Mechanical solver using single code, i.e., available in the CST Studio Suite. As we targeted at the start of this chapter, Chapter 4, it was found the amount of ohmic losses are very much less than that for the $TE_{6,2}$ mode design though the calculations are done by considering two different conductivities, and as well the design of thermal system requires heat transfer coefficient value of 2000 with cavity thickness of 5 mm with no cooling fins present, which can be achieved very easily. It has been found that the frequency deviation in the gyrotron oscillation frequency without any cooling system in the case of $TE_{10,4}$ mode gyrotron operation are within the operational limit of the device. Though to achieve the targeted power in the higher order mode, one needs to sacrifice with the device efficiency to some extent. However, in future, by upgrading the design to high power levels the compensation for the efficiency can be mitigated by no additional need of a thermal

cooling system as well as less sensitivity to the electron beam misalignments and more geometrical tolerances.

With the knowledge of studies made and reported Chapters 3 and 4 of this dissertation, we shifted our research focus towards the design of low power tunable gyrotrons for the DNP enhanced NMR applications by operating the device in the higher order axial modes and are presented here in Chapter 5. Various tuning techniques used in gyrotrons are discussed. In the present work, we have described the design methodology and designed an RF interaction structure that is able to generate a minimum RF power of 20W over a band of 2.4GHz for $TE_{5,3}$, 263GHz gyrotron for the 400MHz DNP NMR spectroscopy applications. In order to operate the device in higher order axial mode, a longer length interaction cavity section are required that results a high quality factors at the same lowers the starts oscillation currents of the modes. Considering the operating mode $TE_{5,3,q}$ from the literature and the design and analysis of RF interaction cavity are presented. In this Chapter too, by allowing the actual field profiles calculated for the RF interaction cavity geometry from the Vlasov approximation for the high order axial modes, the time dependent multimode theory has been carried out at two beam currents 400mA and 20mA via electrical and magnetic tunings. It was found that the designed cavity is able to generate the RF power levels of >20 W over a band of 2.4GHz centered at 263GHz. Then considering a SiO2, as window material, a single disc type RF window for the tunable frequency range has been designed by allowing various disc thicknesses. Further. It was found that smaller disc thickness results good transmission and reflection characteristics versus frequencies, however in the present case disc thickness of 1.155 mm.

It has been seen and presented in Chapter 5 that longer integration cavities lower the start oscillation current of mode excitation as well allows the excitation of high order axial modes. An experimentally demonstrated low power tunable gyrotron operating in $TE_{0,3}$ at

140GHz, has been revisited and reported in Chapter 6 of this dissertation. Here, for this device, its beam wave interaction studies by time dependent analysis as well as simulation using PIC code of Commercial CST studio suite have been carried out. Later, keeping the same beam parameters, and tailoring the reported RF interaction cavity such that excitation of the higher order mode via magnetic tuning that results increment in the tuning bandwidth has been demonstrated. It was found that an increment of 400MHz of bandwidth via magnetic tuning can easily be achieved through such modifications in the device RF interaction cavity.

In the last chapter, Chapter 7, the work embodied in the present thesis are summarized and the significant conclusions are drawn from the major findings. The limitations of the present study are discussed pointing out the scope for the future work.

7.2. Limitations of the Present Work and Scope for Further Studies

In the present work, the mirror section of the quasi optical mode converter is not studied analytically even though several theories are available to explore. But, one key way is by solving the Stratton Chu integrals for the calculation of radiated fields from the launcher on the mirrors, with the suitable numerical methods for fast and accurate calculations. Though the RF window has been designed, the cavity thickness and type of window material can be optimized furthermore by investigating the thermo mechanical behavior of the RF windows due to the losses resulted from the generated RF power propagation. However the time dependent multimode theory has been given for the tapered magnetic field type for the interaction cavity, since, we have extended it for the after cavity interaction studies by taking a uniform magnetic field profile, incorporating a magnetic field profile more accurate beam wave interactions can be achieved. As well, instead of single tuning techniques, the design can be investigated by allowing a hybrid tuning for the enhancement of tunable bandwidth.

As well by incorporating the PBG type interaction actions, the tunability of the device can be increased.

AUTHOR'S RELEVANT PUBLICATIONS

1. **Rao S.V.**, Thottappan M, P.K. Jain PK, "Design modifications in RF interaction cavity of a 140 GHz Gyrotron to achieve wide tunable bandwidth for DNP NMR Applications," *International Journal of Engineering and Advanced Technology*, ISSN: 2249-8958, vol. 9, no. 1, pp.6456-6462, October 2019 .

2. **Rao S.V.**, Thottappan M, P.K. Jain PK, "Thermo-mechanical analysis and its effect on Rf behaviour of a tapered cavity of the W-band gyrotron oscillator," *International Journal of Innovative Technology and Exploring Engineering (IJITEE*), ISSN: 2278-3075, vol. 8, no. 9, pp. 1170-1178, July 2019.

3. **Rao S.V**., Jain P.K., "PIC Simulation of a W-band Gyrotron Oscillator," National Workshop on Vacuum Electron Devices & its Applications (VEDA-2015), Bengaluru, India, 20-21 December 2015.

4. **Rao S.V**., Jain P.K., "Quasi Optical Mode Launcher for a millimeter CW Gyrotron," National Workshop on Vacuum Electron Devices & its Applications (VEDA-2014), Indore, India, 20-21 March 2015.

5. **Rao S.V**., Jain P.K, "Design and development of 95GHz Gyrotron: A Review," *International Conference on Innovative Advancements in Engineering and Technology* (IAET-2014), Jaipur, India, 7-8 March 2014.

REFERENCES

Abrams, R.H., Levush, B., Mondelli, A.A. and Parker, R.K., "Vacuum electronics for the 21st century," *IEEE Microwave magazine*, vol. 2, no. 3, pp.61-72, 2001.

Amboss, K., "The current art of millimeter-wave solid state and tube type power sources," In *Conference Proceedings Military Microwaves*, MM-80, London, pp. 520-546, 1980.

Andronov, A. A., Flyagin, V. A., Gaponov, A. V., Goldenberg, A. L., Petelin, M. I., Usov, V. G., and Yulpatov, V. K., "The gyrotron: high power sources of millimeter and submillimeter waves," *Infrared Physics*, vol. 18, no. 5-6, pp. 385-393, 1978.

Baird, J. M., "Survey of fast wave tube developments," In *Proceedings of Electron Devices Meeting Technical Digest*, vol. 25, pp. 156-163, 1979.

Bajaj, V.S., Farrar, C.T., Hornstein, M.K., Mastovsky, I., Vieregg, J., Bryant, J., Elena, B., Kreischer, K.E., Temkin, R.J. and Griffin, R.G., "Dynamic nuclear polarization at 9 T using a novel 250 GHz gyrotron microwave source," *Journal of Magnetic Resonance*, vol. 160, no. 2, pp.85-90, 2003.

Barker, R. J. and Schamiloglu, E. Ed., *High-Power Microwave Sources and Technologies*, IEEE Press, New York, USA, 2001.

Barker, R. J., Booske, J. H., Luhmann Jr., N. C. and Nusinovich, G. S. Ed., *Modern Microwave and Millimeter-Wave Power Electronics*, IEEE Press, New Jersey, USA, 2004.

Barker, R.J., Luhmann, N.C., Booske, J.H. and Nusinovich, G.S., *Modern microwave and millimeter-wave power electronics*, John Wiley & Sons Publication and IEEE Press, USA, 2005.

Benford, J., and Swegel, J. Ed., *High Power Microwaves*, Artech House, Boston, USA, 1992.

Blank, M, "High efficiency quasi-opticalmode converters for overmoded gyrotrons," Ph.D. Thesis, Massachusetts Institute of Technology, USA, 1994.

Blank, M., Danly, B.G., Levush, B., Calame, J.P., Nguyen, K.T., Pershing, D.E., Petillo, J., Hargreaves, T.A., True, R.B., Theiss, A.J. and Good, G.R., "Demonstration of a high power W-band gyroklystron amplifier for radar applications," In *IEEE International Conference on Plasma Science*, cat. no. 99CH36297, p. 185, 1999.

Born, M. and Wolf, E., *Principles of Optics*, Cambridge University Press, 7th expanded edition, UK, 2009.

Bratman, V., Glyavin, M., Idehara, T., Kalynov, Y., Luchinin, A., Manuilov, V., Mitsudo, S., Ogawa, I., Saito, T., Tatematsu, Y. and Zapevalov, V., "Review of

subterahertz and terahertz gyrodevices at IAP RAS and FIR FU," *IEEE Transactions on Plasma Science*, vol. 37, no. 1, pp.36-43, 2008.

Bratman, V.L., Kalynov, Y.K. and Manuilov, V.N., "Large-orbit subterahertz and terahertz gyrotrons," *Radiophysics and Quantum Electronics*, vol. 52, no. 7, p.472, 2009.

Braz, O., Dammertz, G., Kuntze, M. and Thumm, M., "D-band frequency step-tuning of a 1 MW gyrotron using a Brewster output window," *International journal of infrared and millimeter waves*, vol. 18, no. 8, pp.1465-1477, 1997.

Bryant, J.H., "The first century of microwaves-1886 to 1986, Part II: The Hertzians and their work," *IEEE Transactions on Microwave Theory and Techniques*, vol. 36, no. 5, pp.830-858, 1988.

Bykov, Y., Eremeev, A., Glyavin, M., Kholoptsev, V., Luchinin, A., Plotnikov, I., Denisov, G., Bogdashev, A., Kalynova, G., Semenov, V. and Zharova, N., "24-84-GHz gyrotron systems for technological microwave applications," *IEEE Transactions on Plasma Science*, vol. 32, no. 1, pp.67-72, 2004.

Caryotakis, G., "Development of X-band klystron technology at SLAC," In *Proceedings of the Particle Accelerator Conference*, (Cat. No. 97CH36167), vol. 3, pp. 2894-2898, 1997.

Caryotakis, G., "The klystron: A microwave source of surprising range and endurance," *Physics of Plasmas*, vol. 5, no. 5, pp.1590-1598, 1998.

Chatterjee, R., *Microwave, Millimetre-Wave and Submillimetre-Wave: Vacuum Electron Devices*, Affiliated East-West Press, New Delhi, India, 1999.

Cheng, J., Xu, X., Lawson, W.J., Calame, J.P., Castle, M., Hogan, B.P., Granatstein, V.L., Nusinovich, G.S. and Reiser, M., "Experimental studies of a high power, X-band, coaxial gyroklystron," *IEEE transactions on plasma science*, vol. 27, no. 4, pp.1175-1187, 1999.

Choi, J.J., Ganguly, A.K., Blank, M., Calise, F., Danly, B.G., Kyser, R.H., Levush, B., Latham, P., Park, G.S. and Parker, R.K., "35 GHz gyroklystron amplifier development at NRL," In *IEEE International Conference on Plasma Science*, p. 265, 1996.

Chu, K.R., "The electron cyclotron maser," *Reviews of modern physics*, vol. 76, no. 2, p.489, 2004.

Chu, K.R., "Theory of electron cyclotron maser interaction in a cavity at the harmonic frequencies," *The Physics of Fluids*, vol. 21, no. 12, pp.2354-2364, 1978.

Collin, R. E., *Foundations for Microwave Engineering*, McGraw-Hill, New York, USA,1966.

Collins, G.B. ed., *Microwave magnetrons*, McGraw-hill Book company, New York, USA, 1948.

Curie, N. C., and Brown, C. E., Ed., *Principle and Applications of Millimeter-Wave radars,* Artech House, Boston, USA, 1989.

Dammertz, G., Arnold, A., Heidinger, R., Jin, J., Koppenburg, K., Leonhardt, W., Neffe, G., Piosczyk, B., Rzesnicki, T., Schmid, M. and Thumm, M., "High Power Gyrotron Development at Forschungszentrum Karlsruhe for Fusion Applications," In *IEEE International Conference on Plasma Science,* pp. 110-110, 2005.

Danly, B.G. and Temkin, R.J., "Generalized nonlinear harmonic gyrotron theory," *The Physics of fluids*, vol. 29, no. 2, pp.561-567, 1986.

Denisov, G.G., Kuftin, A.N., Malygin, V.I., Venediktov, N.P., Vinogradov, D.V. and Zapevalov, V.E., "110 GHz gyrotron with a built-in high-efficiency converter," *International journal of electronics*, vol. 72, no. 5-6, pp.1079-1091, 1992.

Denisov, G.G., Petelin, M.I. and Vinogradov, D.V., "Converter of high-mode of a circular waveguide into the main mode of a mirror line," *PCT Gazette,* vol. 16, pp.47-49, 1990.

Doane, J.L., "Polarization converters for circular waveguide modes," *International Journal of Electronics Theoretical and Experimental*, vol. 61, no. 6, pp.1109-1133, 1986.

Doane, J.L., "Propagation and mode coupling in corrugated and smooth-wall circular waveguides," *Infrared and millimeter waves*, vol. 13, pp.123-170, 1985.

Drumm, O., "Numerical optimization of a quasi-optical wave type converter for a frequency-tunable Gyrotron," Ph.D. Thesis, Universität Karlsruhe, Germany, FZKA, 6754, 2002.

Dumbrajs, O. and Koponen, J.P.T., "Generalized gyrotron theory with inclusion of electron velocity and energy spreads," *Physics of plasmas*, vol. 6, no. 6, pp.2618-2621, 1999.

Dumbrajs, O. and Nusinovich, G.S., 2013. "Effect of electron beam misalignments on the gyrotron efficiency," *Physics of plasmas*, vol. 20, no. 7, pp.073105, 2013.

Edgcombe, C. J. Ed., *Gyrotron Oscillators: Their Principles and Practice*, Taylor & Francis, London, UK, 1993.

Emerson, D. T., "The Work of Jagadis Chandra Bose: 100 Years of Millimeter-Wave Research," *IEEE Transaction on Microwave Theory and Techniques*, vol. 45, no. 12, pp. 2267-2273, 1997

Esfahani, N.N., Tayarani, M. and Schünemann, K., "Design and simulation of a π/2-mode spatial-harmonic magnetron," *AEU-International Journal of Electronics and Communications*, vol. 67, no. 5, pp.426-432, 2013.

Feinstein, J., and Felch, K., "Status review of research on millimeter-wave tubes," *IEEE Transaction on. Electron Dev*ices, vol. 34, no. 2, pp. 461-467, 1987.

Felch, K., Blank, M., Borchard, P., Cahalan, P., Cauffman, S., Chu, T.S. and Jory, H., "Demonstration of a 95 GHz, 100 kW, CW gyrotron oscillator," In *Fifth IEEE International Vacuum Electronics Conference,* IEEE cat. no. 04EX786, pp. 63-64, 2004.

Felch, K.L., Danly, B.G., Jory, H.R., Kreischer, K.E., Lawson, W., Levush, B. and Temkin, R.J., "Characteristics and applications of fast-wave gyrodevices," *Proceedings of the IEEE*, vol. 87, no. 5, pp.752-781, 1999.

Flamm, J.H., Jin, J. and Thumm, M.K., "Wave propagation in advanced gyrotron output couplers," *Journal of Infrared, Millimeter, and Terahertz Waves*, vol. 32, no. 7, p.887, 2011.

Fliflet, A.W., Lee, R.C., Gold, S.H., Manheimer, W.M. and Ott, E., "Time-dependent multimode simulation of gyrotron oscillators," *Physical Review A*, vol. 43, no. 11, p.6166, 1991.

Flyagin, V.A., Gaponov, A.V., Petelin, I. and Yulpatov, V.K., "The gyrotron," *IEEE Transactions on Microwave Theory and Techniques*, vol. 25, no. 6, pp.514-521, 1977.

Gandhi, O. P., *Microwave Engineering and Applications*, Pergamon Press, New York, USA, 1981.

Gaponov, A. V., and Granatstein, V. L., Ed., *Application of High Power Microwaves*, Artech House, Boston, USA, 1994.

Gaponov, A.V., Gol'Denberg, A.L., Grigor'ev, D.P., Pankratova, T.B., Petelin, M.I. and Flyagin, V.A., "Experimental investigation of centimeter-band gyrotrons," *Radiophysics and Quantum Electronics*, vol. 18, no. 2, pp.204-211, 1975.

Garin, P., Jedar, E., Jendrzejczak, G., Mourier, G., Payen, F. and Teyssier, L., "Symmetric and non-symmetric mode in a 200 kW, 100 GHz gyrotron," In *12th International Conference on Infrared and Millimeter Waves*, pp. 194-195, 1987.

Gere, J. M., and Timoshenko, S. P., *Mechanics of Materials*, India, CBS Publishers & Distributors PVT. LTD, 2004.

Gilmour, A. S. Jr., *Microwave Tubes*, Artech House, Boston, USA, 1986.

Gold, S. H., and Nusinovich, G. S., "Review of high-power microwave source research," *Review of Scientific Instruments*, vol. 68, no. 11, pp. 3945-3974, 1997.

Grantstein, V. L., and I. Alexeff, Ed., *High Power Microwave Sources*, Artech House, Boston, USA, 1987.

Harrington, R.F., *Time-harmonic electromagnetic fields*, McGraw-Hill, USA, 1961.

Hirshfield, J. L., and Granatstein, V. L., "Electron cyclotron maser — an historical survey," *IEEE Transaction on Microwave Theory and Techniques*, vol. 25, no. 6, pp. 522-527, 1977.

Hornstein, M. K., "Design of a 460 GHz second harmonic gyrotron oscillator for use in dynamic nuclear polarization," Ph.D. Thesis, Massachusetts Institute of Technology, USA, 2001.

Hornstein, M.K., Bajaj, V.S., Griffin, R.G., Kreischer, K.E., Mastovsky, I., Shapiro, M.A., Sirigiri, J.R. and Temkin, R.J., "Second harmonic operation at 460 GHz and broadband continuous frequency tuning of a gyrotron oscillator," *IEEE Transactions on Electron Devices*, vol. 52, no. 5, pp.798-807, 2005.

Hornstein, M.K., V. S. Bajaj, R. G. Griffin, K. E. Kreischer, I. Mastovsky, M.A. Shapiro, and R. J. Temkin, "Design of a 460 GHz second harmonic gyrotron oscillator for use in dynamic nuclear polarization," in Conf. Digest, 27th Int.Conf. on Infrared and Millimeter Waves. Piscataway, NJ: IEEE, 2002, pp. 1934.

Idehara, T., Saito, T., Ogawa, I., Mitsudo, S., Tatematsu, Y., and Sabchevski, S., "The potential of the Gyrotrons for bridging the THz power gap," FIR Center Report, FIR, Fukui University, Japan, 2008.

Idehara, T., Tsuchiya, H., Watanabe, O., Agusu, L. and Mitsudo, S., "The first experiment of a THz gyrotron with a pulse magnet," *International journal of infrared and millimeter waves*, vol. 27, no. 3, pp.319-331, 2006.

Incropera, F. P., Lavine, A. S., Bergman, T. L., and DeWitt, D. P., *Principles of Heat and Mass Transfer*, USA, Wiley, 2013.

Industrial microwave heating application, Published by EPRI center for materials fabrication, vol. 4, no.3, 1993

Joye, C.D., Griffin, R.G., Hornstein, M.K., Hu, K.N., Kreischer, K.E., Rosay, M., Shapiro, M.A., Sirigiri, J.R., Temkin, R.J. and Woskov, P.P., "Operational characteristics of a 14-W 140-GHz gyrotron for dynamic nuclear polarization," *IEEE Transactions on Plasma Science*, vol. 34, no. 3, pp.518-523, 2006.

Kalaria, P.C., Avramidis, K.A., Franck, J., Gantenbein, G., Illy, S., Pagonakis, I.G., Thumm, M. and Jelonnek, J., "Systematic cavity design approach for a multi-frequency gyrotron for DEMO and study of its RF behavior," *Physics of Plasmas*, vol. 23, no. 9, p.092503, 2016.

Kartikeyan, M. V., Borie, E., Drumm, O., Piosczyk, B., and Thumm, M., "Design of a 42 GHz, 200 kW gyrotron operating at the second harmonic," *IEEE Transaction on Microwave Theory and Techniques*, vol. 52, no. 2, pp. 686–692, 2004.

Kartikeyan, M.V., Borie, E. and Thumm, M., "A 250 GHz, 50 W, CW second harmonic gyrotron," *International Journal of Infrared and Millimeter Waves*, vol. 28, no. 8, pp.611-619, 2007.

Kartikeyan, M.V., Borie, E., and Thumm, M., *Gyrotrons: high-power microwave and millimeter wave technology*, Germany, Springer Science & Business Media, 2013.

Kartikeyan, M.V., Kumar, A., Kamakshi, S., Jain, P.K., Illy, S., Borie, E., Piosczyk, B. and Thumm, M.K., "RF behavior of a 200-kW CW Gyrotron," *IEEE Transactions on Plasma Science*, vol. 36, no. 3, pp.631-636, 2008

Kasugai, A., Sakamoto, K., Takahashi, K., Kajiwara, K. and Kobayashi, N., "Steady-state operation of 170 GHz–1 MW gyrotron for ITER," *Nuclear Fusion*, vol.48, no. 5, p.054009, 2008.

Köhler, R., Tredicucci, A., Beltram, F., Beere, H.E., Linfield, E.H., Davies, A.G., Ritchie, D.A., Iotti, R.C. and Rossi, F., "Terahertz semiconductor-heterostructure laser," *Nature*, vol. 417, no. 6885, p.156, 2002.

Koner, J., and Sinha, A.K., "Wall loss and thermal analysis of 200 kW (CW), 42 GHz Gyrotron cavity," *International Journal of Microwave Optical Technology*, vol. 4, no. 1, pp.18-20, 2009.

Krishna, P.V., Kartikeyan, M.V. and Thumm, M., "Mode selection and resonator design studies of a 95 GHz, 100 KW, CW Gyrotron," In *IEEE International Vacuum Electronics Conference (IVEC)*, pp. 293-294, 2011.

Kumar, A., Kumar, N., Singh, U., Khatun, H., Vyas, V. and Sinha, A.K., "Thermal and structural analysis and its effect on beam-wave interaction for 170-GHz, 1-MW gyrotron cavity," *Journal of fusion energy*, vol. 31, no. 2, pp.164-169, 2012.

Kumar, A., Kumar, N., Singh, U., Vyas, V. and Sinha, A.K., "RF behavior and cavity design for 0.3 THz, 4 kW gyrotron for material processing application," *Infrared Physics & Technology*, vol. 55, no. 4, pp.337-344, 2012.

Kumar, N., Singh, U., Kumar, A. and Sinha, A.K., "A feasibility study of beam-wave interaction in 670 GHz gyrotron for radioactive material detection application," *Japanese Journal of Applied Physics*, vol. 51, no. 7R, p.076705, 2012.

Kumar, N., Singh, U., Kumar, A. and Sinha, A.K., "Design of 95 GHz, 100 kW gyrotron for active denial system application," *Vacuum*, vol. 99, pp.99-106, 2014.

Kumar, N., Singh, U., Kumar, A., Khatun, H., Singh, T.P. and Sinha, A.K., "Design of 35 GHz gyrotron for material processing applications," *Progress In Electromagnetics Research*, vol. 27, pp.273-288, 2011.

Kumar, N., Singh, U., Singh, T.P. and Sinha, A.K., "A review on the applications of high power, high frequency microwave source: Gyrotron," *Journal of fusion energy*, vol. 30, no. 4, pp.257-276, 2011

LeVine, S., *The Active Denial System. A Revolutionary, Non-lethal Weapon for Today's Battlefield*, Technical Report, Center for Technology and National Security Policy, National Defense University, Washington DC, 2009.

Lhermitte, R.M., "Cloud and precipitation remote sensing at 94 GHz," *IEEE transactions on geoscience and remote sensing*, vol. 26, no. 3, pp.207-216, 1988.

Liao, S. Y., *Microwave Electron Tubes*, Prentice-Hall, New Jersey, USA, 1988.

Liebe, H.J., "MPM—An atmospheric millimeter-wave propagation model," *International Journal of Infrared and millimeter waves*, vol. 10, no. 6, pp.631-650, 1989.

Lindsay, P.A., "Gyrotrons (electron cyclotron masers): Different mathematical models," *IEEE Journal of Quantum Electronics*, vol. 17, pp.1327-1333, 1981.

Lindsay, P.A., "Self-consistent large-signal interaction in a TWT gyrotron," *International Journal of Electronics Theoretical and Experimental*, vol. 51, no. 4, pp.379-393, 1981.

Litvak, A., Sakamoto, K. and Thumm, M., "Innovation on high-power long-pulse gyrotrons," *Plasma Physics and Controlled Fusion*, vol. 53, no. 12, p.124002, 2011.

Litvak, A.G., Denisov, G.G., Myasnikov, V.E., Tai, E.M., Azizov, E.A. and Ilin, V.I., "Development in Russia of megawatt power gyrotrons for fusion. Journal of Infrared," *Millimeter, and Terahertz Waves*, vol. 32, no. 3, pp.337-342, 2011.

Liu, Q., Liu, Y., Chen, Z., Niu, X., Li, H. and Xu, J., "Investigation on heat transfer analysis and its effect on a multi-mode, beam-wave interaction for a 140 GHz, MW-class Gyrotron," *Physics of Plasmas*, vol. 25, no. 4, p.043101, 2018.

Liu, Q., Liu, Y., Niu, X., Chen, Z., Li, H., Xu, J. and Zhao, J., "Thermoanalysis and Its Effect on the Multimode Beam-Wave Interaction for a 0.24-THz, Megawatt-Class Gyrotron," *IEEE Transactions on Electron Devices*, vol. 65, no. 2, pp.704-709, 2018.

Manheimer, W.M., "On the possibility of high power gyrotrons for super range resolution radar and atmospheric sensing," *International journal of electronics*, vol. 72, no. 5-6, pp.1165-1189, 1992.

Mark Baird, J. and Lawson, W., "Magnetron injection gun (MIG) design for gyrotron applications," *International Journal of Electronics Theoretical and Experimental*, vol. 61, no. 6, pp.953-967, 1986.

Mead, J.B., Pazmany, A.L., Sekelsky, S.M. and McIntosh, R.E., "Millimeter-wave radars for remotely sensing clouds and precipitation," In *Proceedings of the IEEE*, vol. 82, no. 12, pp.1891-1906, 1994.

Mehdi, I. and Siegel, P., "THz semiconductor-based front-end receiver technology for space applications," In *Proceedings. IEEE Radio and Wireless Conference*, IEEE Cat. No. 04TH8746, pp. 127-130, 2004.

Michel, G., "Feldprofilanalyse und-synthese im Millimeterwellenbereich," Ph.D. Thesis, Universität Karlsruhe, Wissenschaftliche Berichte/Forschungszentrum (Karlsruhe), FZKA, 6216, 1998.

Morse, P.M. and Feshbach, H., *Methods of theoretical physics: Part* 1, International series in pure and applied physics. McGraw-Hill, 1953

Neilson, J., "Surf3d and LOT: Computer codes for design and analysis of high-performance QO launchers in gyrotrons.," In *Infrared and Millimeter Waves, and 12th International Conference on Terahertz Electronics*, pp. 667-668, 2004.

Neilson, J., Read, M. and Ives, L, "Design of a permanent magnet gyrotron for active denial systems," In *International Conference on Infrared, Millimeter, and Terahertz Waves*, pp. 1-2, 2009.

Nickel, H.U., "Plane transverse waveguide windows: survey of formulas for reflection, transmission, and absorption," In *16th International Conference on Infrared and Millimeter Waves*, vol. 1576, p. 157667, 1991.

Numerov, B., "Note on the numerical integration of d2x/dt2= f (xt)," *Astronomische Nachrichten*, vol. 230, p.359, 1927.

Nusinovich, G. S., *Introduction to the Physics of Gyrotrons*, Johns Hopkins Univ. Press, Baltimore, Maryland, 2004.

Nusinovich, G.S., Thumm, M.K. and Petelin, M.I., "The gyrotron at 50: Historical overview," *Journal of Infrared, Millimeter, and Terahertz Waves*, vol. 35, no. 4, pp.325-381, 2014.

Parker, R. K., R. H. Abrams, Jr., B. G. Danly, and Baruch Levush, "Vacuum electronics," *IEEE Trans. Microwave Theory Tech.*, vol. 50, no. 3, pp. 835-845, 2002.

Piosczyk, B., Iatrou, C.T., Dammertz, G. and Thumm, M., "Single-stage depressed collectors for gyrotrons," *IEEE transactions on plasma science*, vol. 24, no. 3, pp.579-585, 1996.

Rao, S. V., and Jain, P. K., "PIC Simulation of a W-band Gyrotron Oscillator," in *National Workshop on Vacuum Electron Devices & its Applications. VEDA*, Bangalore, India, 2015.

Sakmoto, K., "Gyrotron and millimeter wave technology", *IEEE Transaction on Plasma Science*, vol. 34, pp. 635, 2006.

Salvi, D., Boldor, D., Ortego, J., Aita, G.M. and Sabliov, C.M., "Numerical modeling of continuous flow microwave heating: a critical comparison of COMSOL and ANSYS," *Journal of Microwave Power and Electromagnetic Energy*, vol. 44, no. 4, pp.187-197, 2010.

Singh, A. and Jain, P.K., "Beam-wave interaction behavior of a 35 GHz metal PBG cavity Gyrotron," *Physics of Plasmas*, vol. 21, no. 9, p.093101, 2014.

Singh, A., Ravi Chandra, B. and Jain, P.K., "Multimode behavior of a 42GHz, 200kW Gyrotron," *Progress In Electromagnetics Research*, vol. 42, pp.75-91, 2012.

Singh, A., "High Studies on gyrotrons using metallic PBG structures as RF cavity," Ph.D. Thesis, IIT (BHU) Varanasi, INDIA, 2012.

Singh, V.V.P., Arnold, A., Borie, E., Braz, O. and Thumm, M., "Thermal modelling of edge-cooled single disc gyrotron windows using a one-dimensional finite difference computer code," *International journal of infrared and millimeter waves*, vol. 19, no. 11, pp.1451-1469, 1998.

Smith, L., and Carpentier, M., Ed., *The Microwave Engineering Handbook*: *Microwave Components*, vol. 1, Chapman and Hall, London, UK, 1993.

Sobol, H., "Microwave communications-an historical perspective," *IEEE Transactions on microwave theory and Techniques*, vol. 32, no. 9, pp.1170-1181, 1984.

Sousa, A. C., "Frequency-tunable second-harmonic submillimeter-wave gyrotron oscillators," Ph.D. Thesis, Massachusetts Institute of Technology, USA, 2010.

Srivastava, A., "Numerical design of a 100 W, 38 dB gain, W-band multi-section serpentine waveguide vacuum electronic TWT," *AEU-International Journal of Electronics and Communications*, vol. 82, pp.145-151, 2017.

Symons, R.S. and Jory, H.R., "Cyclotron resonance devices," *Advances in Electronics and Electron Physics*, Academic Press, vol. 55, pp. 1-75, 1981.

Tatsukawa, T., Maeda, T., Sasai, H., Idehara, T., Mekata, M., Saito, T. and Kanemaki, T., "ESR spectrometer with a wide frequency range using a gyrotron as a radiation power source," *International journal of infrared and millimeter waves*, vol. 16, pp.293-305, 1995.

Thumm, M., "MW gyrotron development for fusion plasma applications," *Plasma Physics and Controlled Fusion*, vol. 45, no. 12A, p.A143, 2003.

Thumm, M., "State-of-the-Art of High Power Gyro-Devices and Free Electron Masers," Update 2017, *KIT Scientific Reports KIT Scientific Publishing*; vol. 7750, 2018.

Thumm, M., *State- of- the- art of high power gyro-devices and free electron masers update 2004*, FZK, KIT, Germany.

Thumm, M., *State-of-the-Art of High Power Gyro-Devices and Free Electron Masers*, update 2009, KIT Scientific Reports 7540, 2010.

Thumm, M.K. and Kasparek, W., "Passive high-power microwave components," *IEEE transactions on plasma science*, vol. 30, no. 3, pp.755-786, 2002.

User's Manual, CST-Particle Studio, Darmstadt, Germany, 2016.

VGB8095 Gyrotronoscillator https://www.cpii.com/docs/datasheets/0/vgb8095.pdf.

Vlasov, S.N., "Transformation of a whispering gallery mode, propagating in a circular waveguide, into a beam of waves," *Radio Engineering and Electron Physics*, vol. 21, pp.14-17, 1975.

Weinstein, L.A., *Open Resonators and Open Waveguides*, Golem Press, 1969.

Wien, A., Ein Beitrag zur Analyse von quasi-optischen Wellentypwandlern in Hochleistungsgyrotrons, Ph.D. Thesis, Universität Karlsruhe, Wissenschaftliche Berichtedes Forschungszentrums, FZKA 5797, 1995.

Zhang, T., Yu, S., Liu, Y., Zhang, Y., Yang, Y. and Zhao, Q., "Analysis of a Denisov Launcher for 420 GHz High Order Mode Gyrotron," *Journal of Fusion Energy*, vol. 34, no. 4, pp.751-758, 2015.